N° D'ordre NNT : 2015-23

**THESE DE DOCTORAT DE L'UNIVERSITÉ DE LYON**

**Opérée au sein de l'Ecole Centrale de Lyon**

**Ecole doctorale Matériaux (EDML)**

**Spécialité de Doctorat**

**Discipline : Science des Matériaux**

**Soutenue le 29 Septembre 2015 par**

**KOSHIGAN Komlavi Dzidula**

# Understanding the influence of environment on the solid lubrication processes of carbon-based thin films

*"Compréhension de l'influence de l'environnement sur les mécanismes de lubrification solide des couches minces à base carbone"*

**Devant un Jury Composé de :**

| | | | |
|---|---|---|---|
| DONNET Christophe | Professeur | Université Jean Monet, Saint Etienne | Président |
| DENAPE Jean | Professeur | Ecole Nationale d'Ingénieur de Tarbes | Rapporteur |
| MISCHLER Stefano | Professeur | Ecole Polytechnique de Lausanne | Rapporteur |
| CARPICK Robert W. | Professeur | University of Pennsylvania | Examinateur |
| DIENWIEBEL Martin | Docteur | Karlsruhe Institute of Technology | Examinateur |
| FONTAINE Julien | Docteur | Ecole Centrale Lyon | Co-Directeur de thèse |

# ACKNOWLEDGEMENTS

It has been exactly three years now since this wonderful adventure began In Lyon. Just like in all the places where my studies and research life drove me to, throughout these six past years, I was pleased to meet you, lovely people during this PhD and I believe I will remember this adventure as one of the most enriching experiences of my life.

My profound and deepest gratitude goes to my Father KOSHIGAN Komla Atoni and my Mother KLU Adzowoa Delali. I owe you more than words can express. Thank you for your support and vote of confidence that carried me in every single moment and everywhere I have been to.

To you Honorine ISHIMWE, my sweetheart, for having honoured my need of time and space yet being always there in that original and discrete way of yours. We made It! Thank you for all!

Many thanks to you, my brothers (Attisso, Eklou, Agbessi) and sisters (Edem, Obubé, Nyedewofe) you offered me a wonderful environment to grow up in as your youngest sibling. To all the other brothers and sisters that life gave me, you deeply enriched me in many ways through my many adventures that have been part of my academic and personal experiences.

Brandon McClimon, Prathima Nalam, Filippo Mangolini, I will forever be grateful for your time, intelligence and the remarkable efforts you have put in reading my manuscript. I learnt a lot from you.

Thank you Pr. Robert W. Carpick for the warm welcome you offered me during my rewarding six months' stay in your group. It was an enriching experience either scientifically or humanely thanks to you and your Group. What a great time in Philadelphia!

For your technical and personal support, Michel Belin, Thierry Le Mogne, Matthieu Guibert, Thibaut Durand, Nasario Morgado.

To my office colleagues and buddies, Eloi Kewes, Julien Bonnaventure, Thomas Touche. To my generous and precious friends Gerard Jeanningros and "the wise" soeur Annie, things would not have happened in this way if only you were not there.

Last but not least, I would like to thank my supervisors, Sandrine Bec, Fabrice Dassenoy and Julien Fontaine.

Dear Julien, thank you for being such a supporting supervisor and collaborator during these three years. Things have not always been easy but we managed to “deliver the baby”. Thank you for the trust you placed in me and for all the fruitful discussions we had.
I cannot express enough my gratefulness to everyone who made this long trip worth living: from Togo, Algeria, France, Vietnam, USA and all over, my academic and personal trip was built up with many human encounters that reminded me all the way to always remember what really matters in life.

*“Ce que nous faisons pour nous même disparait avec nous.*

*Ce que nous faisons pour les autres et le monde est immortel et demeure reste”*

**Albert Pine**

*Je dedie cette these à*

*Mon Papa KOSHIGAN Komla Atoni,*

*Ma Maman KLU Adzowoa Delali,*

*Et à ma tendre fiancée ISHIMWE Honorine*

# Table of Contents

# List of Figures

**Chapter 1. Literature review**

**Chapter 2. Experimental Approach**

**Chapter 3. Influence of environment on the tribological behavior of a-C:H:Si:O**

**Chapter 4. Influence of environment hydrogen, oxygen and water vapor on the tribological behavior of a-C:H:Si:O**

**Chapter 5. Influence of environment and structural evolutions on the tribological behavior of a-C:H:Si:O: proposition of a model**

**Appendix**

# List of Tables

# List of Abreviations

| | |
|---|---|
| **a-C** | **amorphous carbon,** |
| **a-C:H** | **amorphous hydrogenated carbon** |
| **AFM** | **atomic force microscopy** |
| **CCD** | **charge coupled device** |
| **CEAT** | **controlled-environment analytical tribometer** |
| **CVD** | **chemical vapor deposition** |
| **DLC** | **Diamond-Like Carbon** |
| **ECR-CVD** | **electron cyclotron resonance chemical vapor deposition** |
| **FFM** | **friction force microscopy** |
| **HOPG** | **highly oriented pyrolitic graphite** |
| **HFS** | **hydrogen forward scattering spectroscopy** |
| **MW** | **muliwavelength** |
| **NCD** | **nanocrystalline diamond** |
| **NEXAFS** | **near-edge X-ray adsorption fine structure** |
| **NSLS** | **national synchrotron light source** |
| **OLFs** | **onion-like fullerenes** |
| **PECVD** | **plasma enhanced chemical vapor deposition** |
| **PEEM** | **photoelectron emission microscopy** |
| **PEY** | **partial electron yield** |
| **PVD** | **physical vapor deposition** |
| **RH** | **relative humidity** |
| **RBS** | **rutherford backscattering spectroscopy** |
| **SIMS** | **secondary ions mass spectroscopy** |
| **ta-C** | **tetrahedral amorphous carbon** |
| **UNCD** | **ultrananocrystalline diamond** |
| **XPS** | **x-ray photoelectron spectroscopy** |

# List of Symbols

| | |
|---|---|
| **$\mu$** | **coefficient of friction** |
| **$\pi$** | **pi chemical bonds** |
| **$\pi^*$** | **pi chemical antibonding** |
| **$\sigma$** | **sigma chemical bonding** |
| **$\sigma^*$** | **sigma chemical antibonding** |
| **H** | **hardness** |
| **E*** | **reduced elastic modulus** |

# *Introduction*

One could define tribology as an area of research that focuses on friction, wear and lubrication challenges. Tribology requires a multidisciplinary approach including mechanical engineering, material science and chemistry. One main discipline of tribology is lubrication of mechanical parts. Respectively in 1966, 1977 and 1983, United Kingdom (UK), United States of America (USA) and Germany published studies estimating the cost due to unawareness of tribology in their industrial system. These cost has been estimated at US$16.25 billion for USA or 1.3 to 1.6% of German GDP[1]. Mang *et al.*[1] recently published a study summarizing the cost related to tribology all around the world in 2008. In those studies, it was reported that tribological unawareness costs every year, 303, 186 and 68 US$ billion respectively to European Union, United States and China. Energy savings and increasing environmental issues are another main challenge related to tribology mainly in transportation industries, especially the automotive one. In fact, due to the increasing use of vehicles, carbon dioxide emissions are increasing exponentially. Recently in 2012, Holmberg *et al.*[2] published a work focused on the global energy consumption due to friction in passenger cars. They estimated that enhancing tribological parts in car engines could generate by 2030, 385 billions liters and 1 billion tons of fuel and $CO_2$ savings respectively.

Improving engines in order to create outstanding and environment-friendly ones thanks to tribology is thus a critical economic and environmental issue. Different solutions are being explored since long, including enhancing the engines' lubricants. In boundary lubrication regimes however (when the lubricant does not cover all the asperities of the engine parts), the lubricant alone could not sustain engines' efficiency. There is therefore a need to develop solid lubricants as coatings for steel parts in the engine. Diamond-Like Carbon (DLC) coatings are one of solid lubricants used for that aim. For better design of DLC coatings and optimization of their efficiency the fundamental interactions between DLCs and their tribological environment should be given a particular attention and that is the main focus of this thesis.

DLC coatings are consisting in amorphous hydrogenated or non-hydrogenated metastable carbon networks. They are mainly deposited using CVD (chemical vapor deposition) or PVD (physical vapor deposition)[3] methods and exhibit outstanding tribological behavior (ultra-low friction in some conditions[4] and very low wear). To impart new properties or to modify existing ones while keeping the characteristic amorphous structure of a-C:H films, different elements such as Si, O, F, N, or metals[5–7] can be incorporated into the amorphous carbon network.

The incorporation of oxygen together with silicon in a-C:H films leads to the development of a new class of coatings, *i.e.* silicon oxide-doped hydrogenated amorphous carbon (a-C:H:Si:O), sometimes referred to as Diamond-Like Nanocomposite (DLN) or SiO-doped Diamond-Like carbon. a-C:H:Si:O films are so far generally described as a fully amorphous film consisting of two interpenetrating and interbonded networks, one being a silica glass ($SiO_x$) network and the second one, an amorphous hydrogenated carbon network (a-C:H).

a-C:H:Si:O exhibit impressive durability, *i.e.* mechanical properties, thermal stability, and tribological performances[8–13]. In order to develop a fundamental physically-based understanding of the tribo-mechanical and structural durability of a-C:H:Si:O films, a collaboration, named MADDiLiN (Mechanics And Durability of Diamond Like Nanocomposites), has been built between researchers at Laboratoire de tribologie et Dynamique des Systemes (Ecole Centrale Lyon, France) and University of Pennsylvania (Philadelphia, PA, USA). In order to address the key question "what exactly is responsible for the beneficial properties of a-C:H:Si:O" the collaboration is based on the synergy of the two institutions' expertise while using a multidisciplinary, multi-scale and multi-technique experimental approach as well as research stays of the team members between the two institutions. Three main research directions are explored in this collaboration:

- Material design
- Characterization of the material's properties
- Tribological behavior of the material.

This thesis is part of the MADDiLiN project and focuses on the fundamental understanding of the tribological behavior of a-C:H:Si:O by addressing these questions:

- What are the main structural changes that occurs upon sliding a-C:H:Si:O film against 52100 steel ?
- What is the influence of environment of the macroscale tribological behavior of a-C:H:Si:O ?

To answer these questions, this manuscript is presented in five chapters. In the first chapter, a discussion of existing literature on carbon-based materials, from their structure to their tribological behavior is presented, with and emphasis on the tribology of diamond-like carbon solid lubricant. The second chapter describes the experimental approach we used to reach our goal, from tribological experiments to the study of the coatings' surfaces. In the third chapter, we discuss the influence of water vapor and oxygen on the tribological behavior

of a-C:H:Si:O by using an ambient air tribometer equipped with a gas blowing system, thus allowing a quick change of the sliding environment. The fourth chapter discusses the influence of oxygen, hydrogen and water vapor pressure on the tribological behavior of a-C:H:Si:O while using a environment-controlled analytical tribometer. Finally, in chapter five, a model is proposed for describing the fundamental tribological process, including tribochemical reactions that occurs when sliding a-C:H:Si:O.

# Introduction

La tribologie est une science multidisciplinaire conjuguant la mécanique du contact, la science des matériaux et la physico-chimie pour étudier les phénomènes de frottement, d'usure et de lubrification, principalement pour répondre aux enjeux de lubrification des systèmes mécaniques. Respectivement en 1966, 1977 et 1983, le Royaume Uni, les Etats-Unis et l'Allemagne ont publié des données relatives à la négligence des aspects liés à la tribologie dans l'industrie. Le coût de cette négligence a été estimé à 16,25 milliards de dollars pour les Etats-Unis ou 1,3 à 1,6% du Produit National Brut pour l'Allemagne[1]. Un peu plus récemment, en 2008, une étude de Mang *et al.*[1] a montré que le coût annuel des pertes d'origine tribologique dans l'industrie s'évaluerait à 303, 186 et 68 milliards de dollars respectivement pour l'Union Européenne, les Etats-Unis et la Chine.

Par ailleurs, l'industrie des transports, en particulier l'industrie automobile, fait dorénavant face à des problématiques grandissantes de réduction des consommations énergétiques et d'impact environnemental, qui renforcent le besoin d'une meilleure considération des aspects tribologiques. L'augmentation du nombre de véhicules contribue pour une grande part aux émissions de dioxyde de carbone (gaz à effet de serre). En effet, une étude menée par Holmberg *et al.*[2] en 2012, a démontré que si les solutions tribologiques adéquates étaient mises en œuvre dès la conception des moteurs de voiture, il y aurait, d'ici 2030, une réduction de consommation de 385 milliards de litres de carburant, correspondant à une diminution des émissions de $CO_2$ d'un milliard de tonnes.

Si l'amélioration des propriétés des lubrifiants fluides est une des pistes pour diminuer les pertes dans les moteurs à combustion interne, elle ne suffit pas à répondre aux enjeux de lubrification de contact de plus en plus sévères, favorisant les régimes de lubrification mixte et limite, pour lesquels le film de lubrifiant ne sépare pas entièrement les aspérités de surface des pièces en contact. Il est alors indispensable d'améliorer non seulement l'huile, mais également les surfaces en contact, pour améliorer le rendement énergétique et la durabilité des systèmes mécaniques. En outre, tous les contacts ne peuvent pas être lubrifiés par une huile ou un fluide, que ce soit pour des raisons opérationnelles (faibles vitesses, fortes pressions, grandes variations thermiques…), ou environnementales (fonctionnement sous vide, en microgravité, en ambiance propre…).

Ainsi, le recours à des lubrifiants solides ou des matériaux anti-usure en couche mince se généralise dans l'industrie, pour protéger et lubrifier les systèmes mécaniques. Parmi les matériaux de choix pour ces applications figurent les couches minces à base de carbone

amorphe, connues sous le terme générique *Diamond–Like Carbon* (DLC). Dans une perspective d'optimisation de la structure et des performances de ces couches DLC, il convient de porter une attention particulière aux interactions physico-chimique pouvant intervenir entre ces revêtements en couche mince et leur environnement de fonctionnement. C'est dans ce cadre que s'inscrit cette thèse.

Les revêtements en couche mince DLC sont constitués d'un réseau amorphe et métastable de carbone, hydrogéné ou non. Ils sont déposés principalement par des procédés physiques (PVD : Physical Vapor Deposition) ou chimiques (CVD : Chemical Vapor Deposition)[3] en phase vapeur, et présentent des propriétés tribologiques exceptionnelles[14], associant faible frottement (coefficient de frottement contre acier inférieur à 0,01 dans certaines conditions) et faible usure. Afin d'améliorer certaines propriétés de ces revêtements tout en maintenant leur structure amorphe, différents éléments d'addition peuvent être incorporés dans la structure initiale de carbone amorphe, notamment le silicium, l'oxygène, le fluor ou des éléments métalliques[5,6,15].

Dans le cas d'une incorporation de silicium et d'oxygène dans la couche amorphe de carbone, on obtient un revêtement couramment dénommé *Diamond-Like Nanocomposite* (DLN) ou plutôt *silicon-oxide containing hydrogenated diamond-like carbon* (a-C:H:Si:O).

Les a-C:H:Si:O présentent une très bonne durabilité, c'est à dire, de bonnes propriétés mécaniques, une bonne stabilité thermique et un bon comportement tribologique[8–13]. Afin de développer une compréhension fondamentale des phénomènes tribo-mécaniques et des modifications structurales de ces revêtements, une collaboration internationale a été mise en place entre le *Laboratoire de Tribologie et Dynamique des Systèmes* (LTDS) de l'*École Centrale de Lyon* et le departement *Mechanical Engineering and Applied Mechanics* (MEAM) de l'*Université de Pennsylvanie* (Philadelphie, USA). Ce partenariat scientifique dénommé MADDiLiN (Mechanics And Durability of Diamond Like Nanocomposites) avait pour objectif principal de répondre à la question « *comment expliquer les propriétés exceptionnelles des revêtements a-C:H:Si:O ?* ».

Dans le cadre de cette thèse, nous nous sommes focalisés sur le troisième axe du projet, notamment la compréhension fondamentale du comportement tribologique d'un revêtement a-C:H:Si:O, autour de certains questionnements :

- *Quels sont les principaux changements structuraux qui peuvent intervenir lors d'une sollicitation tribologique des a-C:H:Si:O ?*
- *Quelle est l'influence de l'environnement sur le comportement tribologique du a-C:H:Si:O à macro-échelle ?*

Ce manuscrit, qui vient apporter des éléments de réponse à ces questionnements, s'organise en cinq chapitres.

Le premier chapitre propose une étude approfondie de la littérature existante sur les revêtements en couche mince à base carbone en général et leur comportement tribologique.

Dans le deuxième chapitre sont décrites les démarches expérimentales mises en œuvre tant sur l'aspect tribologie que pour les caractérisations pré- et post-essais tribologiques.

Le troisième chapitre met en évidence les rôles respectifs de la vapeur d'eau et de l'oxygène sur le frottement et l'usure des a-C:H:Si:O, grâce un tribomètre linéaire alternatif fonctionnant dans l'air ambiant mais équipé d'un système de soufflage de gaz autour du contact, permettant ainsi un changement rapide de l'environnement d'essai.

Une étude approfondie de l'influence de la vapeur d'eau, de l'oxygène et de l'hydrogène sur le comportement tribologique des a-C:H:Si:O, réalisée sur un tribomètre linéaire alternatif fonctionnant sous vide poussé, est présentée dans le quatrième chapitre.
Toutes ces investigations nous ont permis de proposer un modèle expliquant les mécanismes tribologiques fondamentaux des a-C:H:Si:O, présenté dans le cinquième et dernier chapitre.

## References


1. Wiley: Industrial Tribology: Tribosystems, Friction, Wear and Surface Engineering, Lubrication - Theo Mang, Kirsten Bobzin, Thorsten Bartels. at <http://eu.wiley.com/WileyCDA/WileyTitle/productCd-3527320571.html>
2. Holmberg, K., Andersson, P. & Erdemir, A. Global energy consumption due to friction in passenger cars. Tribol. Int. **47,** 221–234 (2012).
3. Robertson, J. Diamond-like amorphous carbon. Mater. Sci. Eng. R Rep. **37,** 129–281 (2002).
4. Fontaine, J., Loubet, J. L., Mogne, T. L. & Grill, A. Superlow Friction of Diamond-Like Carbon Films: A Relation to Viscoplastic Properties. Tribol. Lett. **17,** 709–714 (2004).
5. Sánchez-López, J. C. & Fernández, A. in Tribology of Diamond-Like Carbon Films (eds. Donnet, C. & Erdemir, A.) 311–338 (Springer US, 2008). at <http://link.springer.com/chapter/10.1007/978-0-387-49891-1_12>
6. Tripathi, R. K., Panwar, O. S., Srivastava, A. K., Rawal, I. & Chockalingam, S. Structural, nanomechanical, field emission and ammonia gas sensing properties of nitrogenated amorphous carbon films deposited by filtered anodic jet carbon arc technique. Talanta **125,** 276–283 (2014).
7. Panwar, O. S. et al. Effect of high substrate bias and hydrogen and nitrogen incorporation on spectroscopic ellipsometric and atomic force microscopic studies of tetrahedral amorphous carbon films. Surf. Coat. Technol. **205,** 2126–2133 (2010).
8. Neerinck, D. et al. Diamond-like nanocomposite coatings (a-C:H/a-Si:O) for tribological applications. Diam. Relat. Mater. **7,** 468–471 (1998).
9. Neerinck, D. et al. Diamond-like nanocomposite coatings for low-wear and low-friction applications in humid environments. Thin Solid Films **317,** 402–404 (1998).
10. Scharf, T. W. & Singer, I. L. Monitoring Transfer Films and Friction Instabilities with In Situ Raman Tribometry. Tribol. Lett. **14,** 3–8 (2003).
11. Scharf, T. W. & Singer, I. L. Role of Third Bodies in Friction Behavior of Diamond-like Nanocomposite Coatings Studied by In Situ Tribometry. Tribol. Trans. **45,** 363–371 (2002).
12. Yang, W. J., Sekino, T., Shim, K. B., Niihara, K. & Auh, K. H. Microstructure and tribological properties of SiOx/DLC films grown by PECVD. Surf. Coat. Technol. **194,** 128–135 (2005).
13. Yang, W. J. et al. Structural characteristics of diamond-like nanocomposite films grown by PECVD. Mater. Lett. **57,** 3305–3310 (2003).

# *Chapter 1.*

# *Literature review*

*Thinking of solid lubrication as proposed by Bowden et al.[16], low friction is promoted by low shear strength interfacial material and thus one might be tempted to argue that only soft materials could serve as lubricants. Indeed, the fundamental lubrication mechanism of soft solid materials such as transition metal dichalcogenide compounds ($MoS_2$ and $WS_2$), graphite, polymers (PTFE) and other soft metals (silver, tin, indium, gold etc.) have been widely studied in literature[17]. But hard carbon-based materials such as Ultra Nano Crystalline Diamond (UNCD) and Diamond-Like Carbon (DLC) thin films have shown superior tribological properties. DLC films also find a wide range of commercial applications as thin films, thanks to their mechanical properties together with outstanding tribological behavior and chemical inertness. A substantial body of literature is dedicated to understand the lubrication mechanisms for these "contradictory" materials (hard modulus, solid but lubricious)[18] but there is still a considerable amount of investigation required to gain a fundamental understanding of their tribological mechanisms. In this chapter, we give first a short overview of the main components of DLC coatings, namely, carbon, in its different states. Later, a brief summary of the literature on different DLC coatings and their tribological behavior are presented. In the last part of this chapter, the latest developments in addition element DLC coatings especially for silicon oxide containing amorphous carbon films (a-C:H:Si:O) – the material under investigation in this thesis – are given.*

# Table of contents: Chapter 1. Literature review.

# 1. Carbon atom and its hydridization states

Hybridization of an atomic orbital is defined by Riichiro Saito et al.[19] as the mixing of atomic orbitals which possess different angular momenta so as to change the direction of the chemical bonds and to lower the total energy of the molecule.

Carbon is the sixth element in the periodic table and the sixth most abundant element in the universe[20] but its chemistry is one of the most complex. In its neutral electrical state, a carbon atom has six electrons, which occupy $1s^2$, $2s^2$, $2p^2$ atomic orbitals in the ground state. Two of the 6 electrons (named core electrons) are strongly bonded in the orbital 1s whose one-electron energy is about 285 eV below vacuum level[19]. The four other electrons (valence electrons), which occupy the $2s^2$ and $2p^2$ orbitals, are the ones, which contribute to the chemical bonding.

In the crystalline phase, the valence electrons give rise to 2s, $2p_x$, $2p_y$ and $2p_z$ orbitals which are important in forming covalent bonds in carbon materials. Due to the relatively small energy difference between the upper 2p energy level and the lower 2s energy level in carbon (4 eV)[19], in comparison with the energy gain in forming the chemical bonds, the electronic wavefunctions for the four valence electrons have a capability to reorganize and enhance the binding energy of the carbon atom with its neighboring atoms. A hybrid $sp^n$ orbital is made of a mix between a single 2s orbital and n (n= 1, 2 or 3) 2p orbitals thus resulting in sp, $sp^2$ and $sp^3$ hybridization structures of carbon (Figure 1.1).

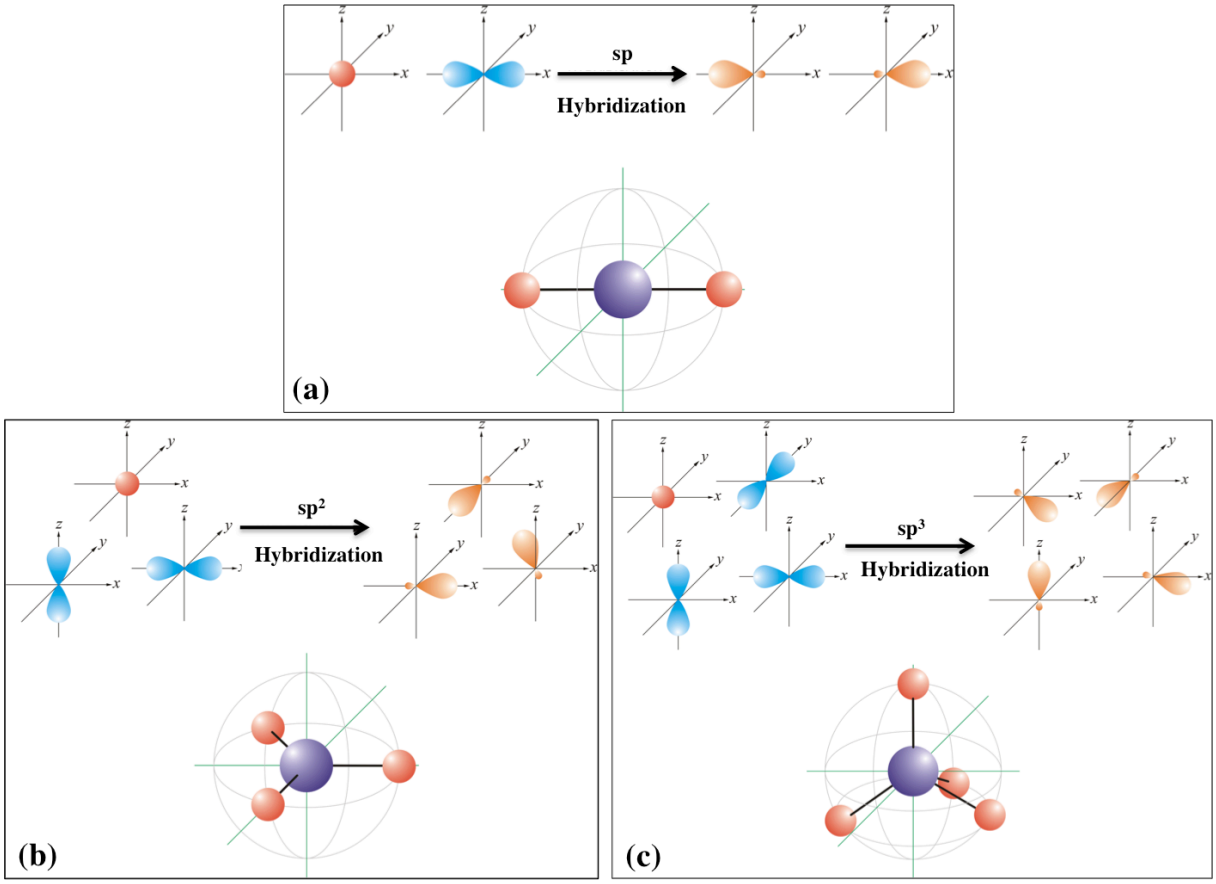


***Figure 1.1. Schematic of the three different hybridization of carbon: (a) sp, (b) $sp^2$ and (c) $sp^3$ from Chemistry Glossary***

In case of sp configuration, two linear 2sp orbitals are formed, leaving two non-hybridized 2p orbitals. The overlapping of these two sp orbitals with the neighboring atoms generates linear σ bonds. The remaining two non-hybridized 2p overlap to create 2 π bonds. Acetylene ($C_2H_2$) is a typical example of this configuration. Similarly, $sp^2$ hybridization leads to three $2sp^2$ hybrid orbitals while one 2p orbital remains unhybridized. This remaining p orbital on each carbon atom can form a π bond by overlapping with the orbital of the neighboring atom. This is the case of ethylene ($C_2H_4$) molecule. Finally in $sp^3$ hybridization, carbon forms four equivalent $2sp^3$ hybrid orbitals that are tetrahedrally oriented and thus forming equivalent tetrahedral σ bonds neighboring atoms[21]. Ethane ($C_2H_6$) molecule is an example of $sp^3$ hybridization where overlapping of $sp^3$ orbitals creates C–C σ bonds and three C-H σ bonds are formed on each carbon atom. The bond angle of the hybrid $sp^n$ orbital can be obtained by $\cos^{-1}(-1/n)$ resulting in bond angles of 180°, 120° and 109,47° for sp, $sp^2$ and $sp^3$ hybridizations, respectively. Furthermore, except carbon, none of the other group IV elements present different hybridization states since the electron-electron repulsion between their inner

and outer electronic shells facilitating only $sp^3$ hybridization. Being in the same group as carbon, Silicon shares the bonding versatility of carbon with its four valence electrons. The most common compound of silicon is $SiO_2$, commonly kwon as sand, which is the most abundant chemical compound on earth.

# 2. Crystalline carbon materials

Crystalline forms of carbon materials are commonly related to a polycyclic saturated hydrocarbons[22] which organization and interbondings are responsible for the physical and chemical properties of the material. Thermodynamic stability and the configuration of the polycyclic saturated hydrocarbon determine the different crystalline forms of carbon materials such as graphite, diamond, fullerenes, carbon nanotubes, *etc.,* for example.

## 2.1. Graphite

### 2.1.1. Structure of Graphite

Graphite is the most common and thermodynamically-stable crystalline form of carbon under ambient conditions and room temperature. It is structurally related to polycyclic benzenoid aromatic hydrocarbon, which forms a two dimensional three-connected (2D3C) benzenoid $sp^2$ bonding network with bond angles of 120° and bond lengths of 1.42 Å[22]. There are covalent bonds between carbon atoms coupled with delocalized electrons which are free to move anywhere within the sheet. Nevertheless, there is no direct contact between delocalized electrons the different sheets.

Graphite commonly exists in Hexagonal (ABABAB) or configuration. Graphite has a layered structure linked by weak van der Walls interactions, produced by delocalized π-orbitals. Graphite can also be found in Rhombohedral (ABCABC) configuration (Figure 1.2). The Rhombohedral structure of graphite is less stable than ordinary graphite. Proportion of Rhombohedral graphite in single crystals graphite can either be reduced or enhanced by deformation processes such as grinding (typically from few percent to approximately 20%) or by high temperature heat-treatment and quenching[23], respectively.

Geim and Novosely[24] recently were able to extract, by exfoliation method, a single layer of graphite from a bulk sample resulting in a two-dimensional (2D) honeycomb lattice of graphene. The authors were granted the Nobel Prize in Physics in 2010 by royal Swedish Academy of sciences for this discovery.

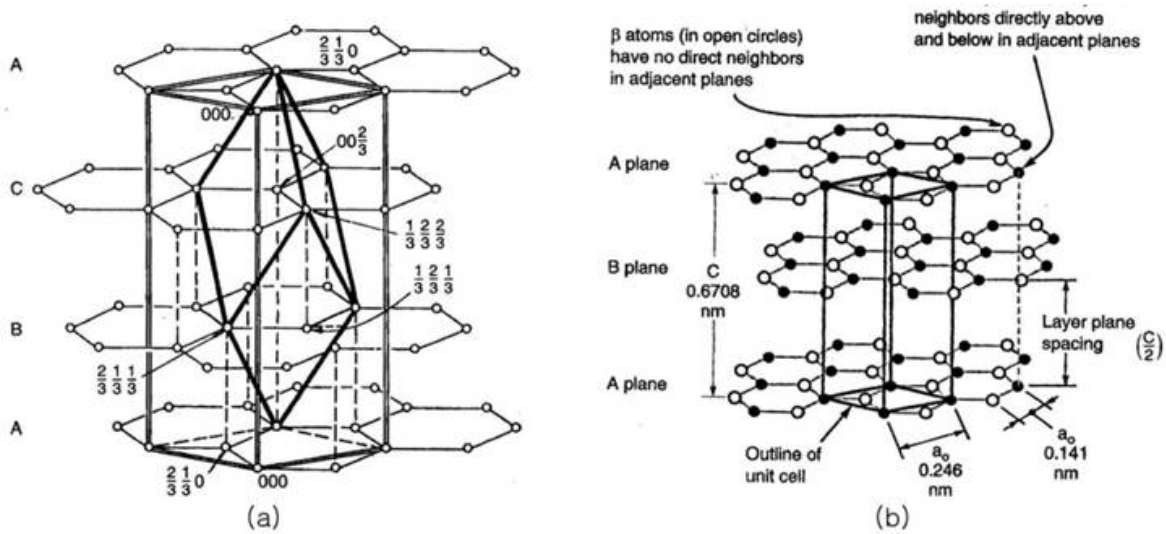


***Figure 1.2. (a)Rhombohedral and (b)Hexagonal unit cell structure of graphite (b) from Pierson et al.[25]***

### 2.1.2. Mechanical properties of Graphite

Graphite is a very anisotropic material. There is a very strong bonding between the in plane carbon atoms (stronger bonding than in diamond thanks to the delocalized electrons). Therefore, graphite is a soft material that can easily be exfoliated into single layered graphene structures. Mechanical properties of graphene depend on the number of layers used for measurement. Due to the complexity in measuring the hardness such thin graphene layers, different values are reported in the literature. Using nanoindentation Zhang *et al.*[26] have reported hardness and elastic modulus of graphene at 950 and 305 GPa respectively for a monolayer of graphene or 190 and 410 GPa for a four layers graphene, whereas WenXing *et al.*[27] while using both experiments and molecular dynamic simulations estimated the elastic modulus of graphene at 1033 and 1025 GPa respectively (measurements were carried out in a sample with 3 graphene layers).

### 2.1.3. Tribological behavior of Graphite

It is known that graphite has poor intrinsic lubrication properties[28]. Its frictional response is rather due to its ability to adsorb vapors such as water or hydrocarbons as demonstrated early in 1948 by Savage *et al.*[29]. They have shown that a minimum amount of water vapor is needed to promote the sliding of graphite lamellas against each other and thus lead to low friction. Berman *et al.*[30,31] have recently shown that the presence of graphene (the single monolayer of graphite mentioned in the previous section) at the sliding interface of self-mated steel surfaces can reduced friction by ~ an orders and wear by 3-4 orders of

magnitude, respectively, comparing to self-mated steel contacts. One has to notice that in their experiments, graphite was chemically suspended in ethanol.

It seems rather unlikely that graphene sheets alone could induce such low coefficient of friction as observed in these studies mainly because of the surface roughness. Another mechanism could be a generation of a third body made of mixture of graphene and environment species that promotes low friction. Further studies could be made to clarify the actual mechanisms.

## 2.2. Diamond

### 2.2.1. Structure of Diamond

Diamond is also related to the family of polycyclic saturated hydrocarbons, which forms a highly rigid three -dimensional four connected (3D4C) carbon network. Diamond is the second most thermodynamically stable allotrope of carbon with all carbon atoms forming tetrahedral $sp^3$ bonding with bond angles of 109.5 ° and bond length of 1.54 Å as in alkanes[22]. The nearest neighbors of each carbon atom can be imagined to be placed at the fourth of the eight cornered cube and these cubes are stacked to form a cubic lattice structure of diamond[32]. The second possible configuration for diamond – called hexagonal or lonsdaleite diamond– the nearest neighboring $sp^3$ carbons define a triangular prism to form hexagonal lattice. Figure 1.3 shows both cubic and hexagonal structural configuration of diamond.

The density of Diamond is 50% higher than that of graphite and therefore a conversion from graphitic structure to diamond structure is possible at high temperatures[33]. As a comparison, table 1.1 summarizes some relevant thermodynamic properties of diamond and graphite.

| *Property, 298K, 1 bar* | *Graphite* | *Diamond* |
|---|---|---|
| ***Enthalpy, ΔH°*** | *0* | *1.895 kJ/mole* |
| ***Free energy, ΔG°*** | *0* | *2.900 kJ/mole* |
| ***Entropy, S*** | *5.740 J/mole K* | *2.377 J/mole K* |
| ***Heat capacity, Cp*** | *8.527 J/mole K* | *6.113 J/mole K* |
| ***Density*** | *2.26 g/cm$^3$* | *3.515 g/cm$^3$* |

***Table 1.1. Comparison of thermal properties of Diamond and Graphite from Pierson et al.[25]***

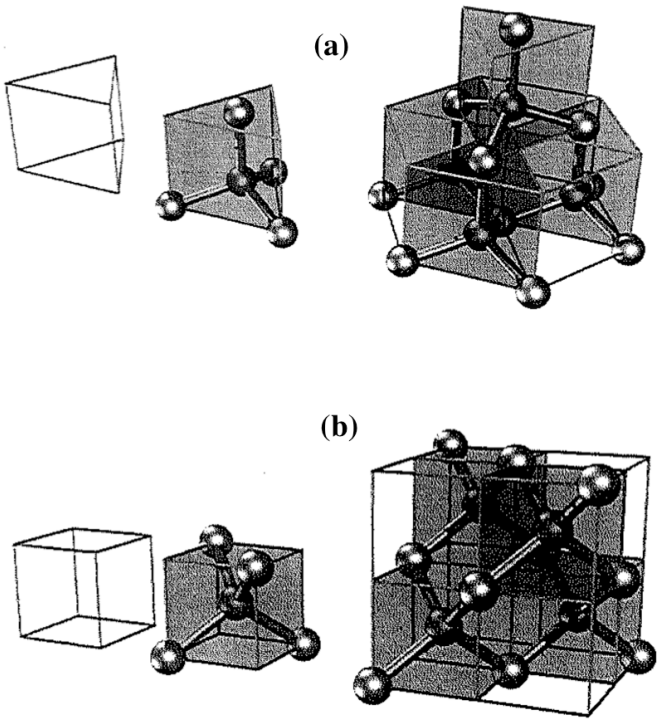


***Figure 1.3. Schematic representation of (a) hexagonal and (b) cubic diamond structures as proposed by Di Fisica et al.[32]***

At 1200 °C, a slow transition from diamond to graphite can be observed and the free-energy transformation of diamond into graphite has been reported to occur at -10.05 kJ/mol[25]. At higher temperatures, this transformation is accelerated. Environment can also play a key role in this phase transformation, for instance, diamond can be transformed into graphite

already at 500°C in presence of cobalt while it remains stable until 2000°C under hydrogen environment or until 1700°C under ultra-high vacuum.

The thermal conductivity of an impurity-free diamond is five times higher than that of copper making this allotropic form of carbon as the highest solid thermal conductor at room temperature.

### 2.2.2. Mechanical properties of Diamond

Diamond, is known as the hardest solid material on earth. The Knoop test provides the most accurate measurements for estimating the mechanical properties of crystalline materials. This test employs a hard diamond tip as indenter. Thus it is hard to have an accurate measurement of mechanical properties of Diamond or harder materials. Therefore different values of diamond's hardness and elastic modulus can be found in the literature, namely, from 57 GPa to 104 GPa and 1050 GPa respectively[25].

Nevertheless in the last few years, a several novel and synthetic hard materials have been synthetized and it has been shown that a combination of Hall-Petch effect and quantum confinement effects can be used to obtain boron nitride nanocomposites with similar hardness values as a single crystal or polycrystalline diamond. In 2009, Zicheng Pan *et al.*[34] have reported the hardness of wurtzite boron nitride (w-BN) and lonsdaleite (hexagonal diamond) via total energy calculations, as higher than diamond. They propose that such high hardness values for w-BN and lonsdaleite result from higher indentation strengths on their cleavage planes due to the generation of a stress-induced structural phase transformation[34]. Under the similar conditions, the computed hardness values of diamond, w-BN and lonsdaleite were reported as 97±1 GPa, 114±1 GPa and 152±1 GPa respectively.

Figure 1.4shows the hardness of diamond compared to other reference materials such as aluminum oxide ($Al_2O_3$), tungsten carbide (WC), silicon carbide (βSiC), Boron nitride (BN) and wurtzite boron nitride (w-BN).

One has to notice that the mechanical properties computed for these new materials (w-BN) has been estimated on defect free materials. Values for actual physical materials could be different.

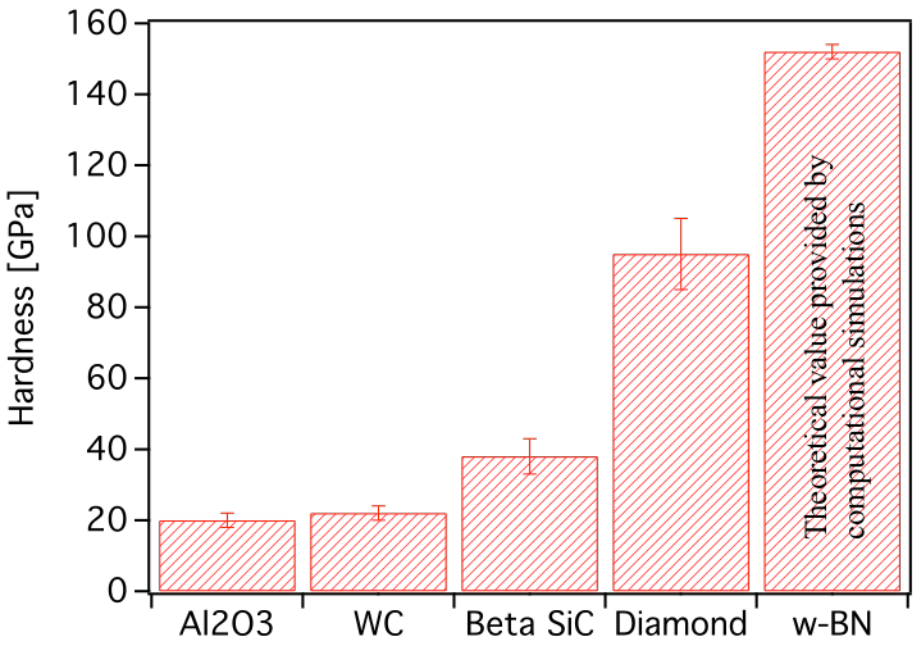


***Figure 1.4. Hardness of few hard materials compared to Diamond adapted from Dubrovinskaia and Pan. Z[34,35]***

### 2.2.3. Tribological behavior of Diamond

Diamond displays a low friction (under specific conditions), low wear, and high erosion resistance and thus is extensively used for industrial applications, mainly for cutting tools. Thus understanding the friction and wear mechanisms of diamond has been a long-term research topic[36–39]. The literature indicates two key phenomena explaining the fundamental tribological mechanisms for diamond as re-hybridization and passivation.

- ***Rehybridization***

The work of E. M. Wilks and J. Wilks attempts to understand the resistance of diamond to abrasion[36,37,40]. In 1972, they published a paper explaining the "surprising feature" in diamond machining, by a microscopic cleavage process[36]. They observed the cutting process of natural diamond frequently used for jewelry making and proposed that the rate of removal of diamond during machining depends on both crystallographic orientation of the material and the direction of the abrasive tool. Several authors have also supported rehybridization process[41,42]. Erdemir *et al*[42] explained that rehybridization is a phase transformation that occurs at the surface of nanocrystalline diamond. This transformation is induced or assisted by local contact pressures and temperatures generated between two asperities in rubbing contact resulting in graphitization. Later in this chapter we will further discuss the

graphitization hypothesis proposed by Erdemir *et al.*[42]. Recently in 2010, the work of Pastewka *et al*[39] from Fraunhofer Institute for Mechanics of Materials published an article entitled "*How to soften diamond?*", where they reported several new insights in the understanding of the friction and wear mechanisms of diamond. Their molecular dynamic simulations showed that the polished diamond undergoes a $sp^3$- to $sp^2$- bonded carbon transformation at the interface thus resulting in the generation of an amorphous layer whose growth rate depends on the surface orientation. These findings go against the graphitization hypothesis previously proposed by Erdemir *et al.*

- ***Passivation***

High vacuum tribometry experiments on polycrystalline diamond, performed by Gardos *et al.*[43] showed high friction coefficient, which was attributed to the interactions between carbon dangling bonds at the interface. In the same study, the friction coefficient was observed to decreases in presence of hydrogen. This phenomenon has been interpreted as a consequence of the "*tribo-catalytically enhanced dissociative chemisorption of molecular hydrogen"* on the carbon dangling bonds. Konicek *et al.*[44,45] have given further evidence of passivation of carbon dangling bonds for ultranonocrystalline diamond (UNCD) in presence of water vapor. In facts, by using spatially resolved near-edge x-ray absorption fine structure (NEXAFS) spectroscopy, the evidence of dissociation of water vapor as OH and H was observed, which leads to the passivation of the carbon dangling bonds creating C-OH bonds, while sliding UNCD in humid environment. As a consequence, the friction coefficients for UNCD showed a decrease from 0.6 in vacuum to 0.008 in humid environments. Furthermore, first-principles simulations and gas phase lubrication tribometry performed by De Barros *et al.*[46] concur with the passivation phenomena as described by Konicek *et al.*[44,45]. Both their experimental and simulation results revealed enrichment of the worn region of diamond with hydrogen and hydroxyl groups when sliding under hydrogen and water environments, respectively. In their hypothesis, the build-up of the chemical bonds in the worn region can result in the decrease of adhesion between the two sliding surfaces and thus might result in the prevention of generation of covalent bonds across the interface and therefore leading to lower friction coefficients. Passivation hypothesis is thus a proven mechanism that explains the low coefficient of friction of diamond in presence of chemical radicals such as OH or H.

## 2.3. Fullerene

Unlike the two previously described crystalline forms of carbon, *i.e.* graphite and diamond, which are infinite network solids, fullerenes are considered as a major allotrope of carbon which are stable, finite in their discrete molecular form[25]. They generally are arranged in the form of a geodesic spheroids, named after the inventor of the geodesic dome M. Buckminster Fuller[25]. Even though, they were randomly discovered at first in 1985, by Smalley and Kroto[47] (Nobel prize in Chemistry in 1996) while performing mass-spectroscopy analysis of carbon vapor, Kratschmer and Huffman[48] were the ones who demonstrated the practical synthesis of fullerenes as solid aggregates in 1990, and thanks to them, fullerenes are now available in large quantities, allowing detailed studies and their evaluations for practical applications.

### 2.3.1. Structure of Fullerenes

Fullerenes are a family of molecular, geodesic structures in the form of cage-like spheroids consisting of a network of five-membered rings and six-membered rings[49]. The uniqueness of fullerenes resides in the fact that, in order to be closed into a spheroid, the geodesic structures must have exactly twelve pentagons along with a variable number of hexagons.

The hybridization states in fullerenes molecules is not fixed but varies depending on the number of carbon atoms it contains. In order to account for the bonding of carbon atoms in a fullerene molecule, the hybridization must be a modification of the $sp^3$ hybridization of diamond and $sp^2$ hybridization of graphite in such a way that the sigma orbitals no longer contain all of the s-orbital character and the $\pi$ orbitals are no longer of the purely p-orbital character as they are in graphite[25].

Theoretically, there can be many possible structures for fullerene but only $C_{60}$, $C_{70}$, $C_{76}$, $C_{78}$ and $C_{84}$ have been characterized so far. $C_{60}$ was the first stable fullerene to be discovered. It contains sixty carbon atoms arranged in the way that they form twenty hexagons and twelve pentagons, giving it the appearance of a soccer ball as shown in Figure 1.5. Each carbon atom is shared by one pentagon and two hexagons generating thus the spheroidal shape of fullerenes. The intermolecular bonding in fullerenes is dominated by van der Waals forces.

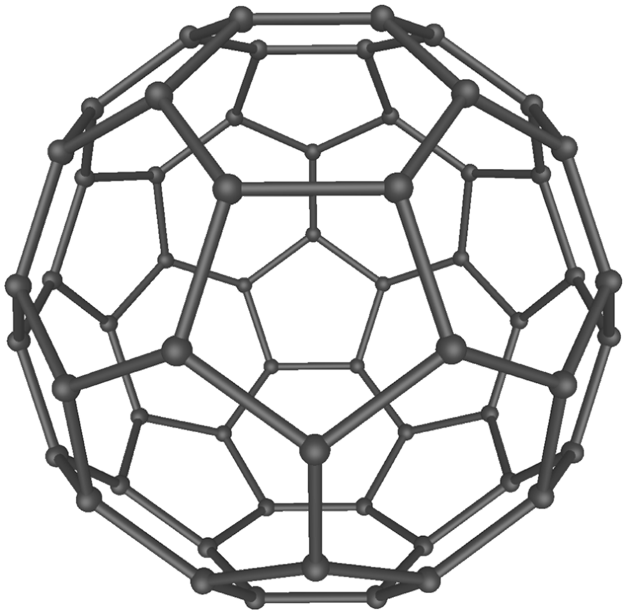

***Figure 1.5. Structure of Fullerene C60 from Bhushan et al.[50]***

Pentagons or heptagons are required to generate the curved surface. For a different number of pentagons, many other forms of fullerenes can be obtained such as carbon nanotubes, bucky-Onions etc. Depending on the ordering between layers, the clustered carbon based material can be either graphitizable *i.e.* can undergo thermally activated transformation into graphite, partially graphitizable or non-graphitizable. This renders difficult the understading of tribologically-induced structural evolution of clustered carbon based materials.

### 2.3.2. Mechanical properties of Fullerenes

$C_{60}$ has been considered for long, as the softest solid phase of carbon until Curl and Smalley[51] demonstrated that fullerenes can become even harder than diamond when they are compressed to less than 70% of its original volume. Unlike graphite, which can undergo a transformation into diamond at high temperature and high pressure, fullerenes can instantaneously transform into polycrystalline diamond at room temperature when a non-hydrostatic compression of approximately 20 GPa is applied on $C_{60}$[52]

### 2.3.3. Tribological behavior of Fullerenes

Thanks to the weak van der Waals interatomic interactions between fullerenes layers[49], which result in low shearing stresses making fullerenes a good possible candidate for solid lubricants. Thanks to their high hardness, onion-like fullerenes present a “roll bearing” effect as well as sliding between layers that increases their lubricating properties[53].

# 3. Diamond-Like Carbon (DLC)

DLC films are amorphous hydrogenated or non-hydrogenated metastable carbon networks made of sp-, $sp^2$- and $sp^3$- bonded carbon.  shows a molecular dynamic simulation representing hydrogenated DLC with carbon atoms in blue and hydrogen in red. It can easily be seen that the film is made of carbon in different hybridization states as well as bonded and free hydrogen. They are mainly deposited by CVD and PVD methods. DLC films show good tribological properties making them excellent candidates for solid lubrication. DLC films already applied as protective coatings in outstanding engines, biomedical implants, watch *etc*.

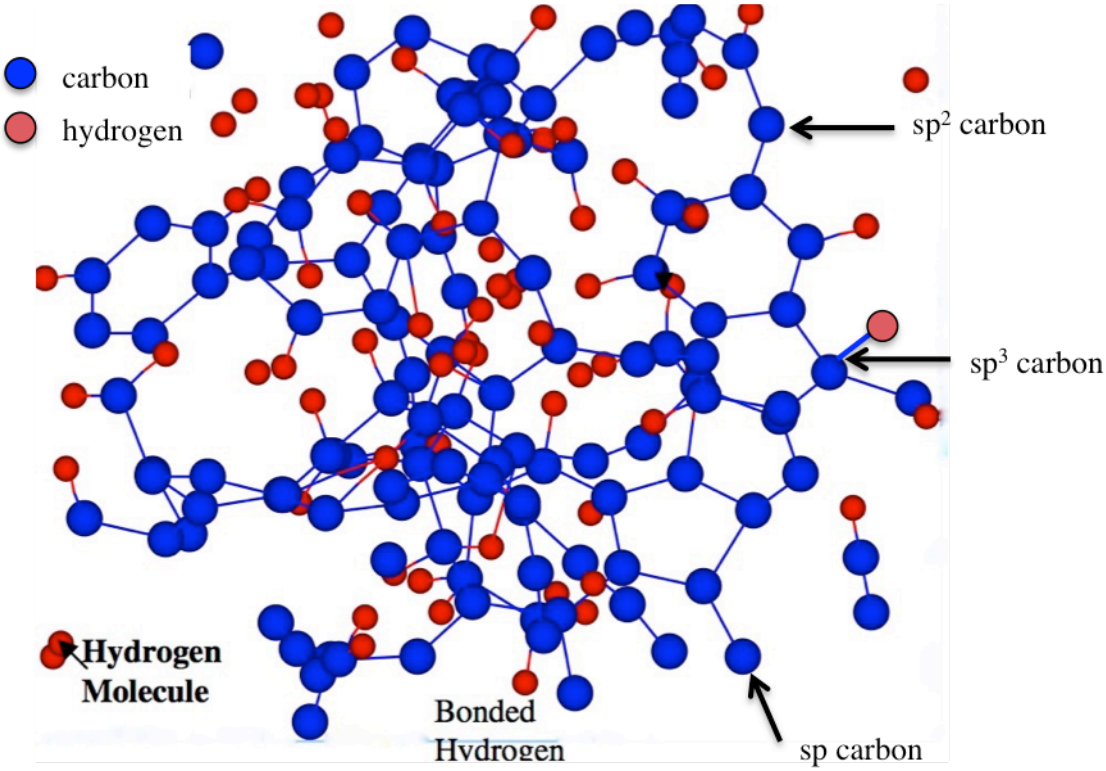


***Figure 1.6. Schematics of molecular dynamics simulation showing atomic structure of hydrogenated DLC adapted from Erdemir et al.[54]***

## 3.1. Different types of DLC coatings: structure and deposition methods

Depending on the deposition method and control parameters, the hybridization state of carbon atoms and the hydrogen content in the deposited films can be varied. The classification of the different existing DLC coatings in the literature has been provided by Jacob and Moller[55] *via* a pseudo ternary phase diagram and from the work of Robertson[3].

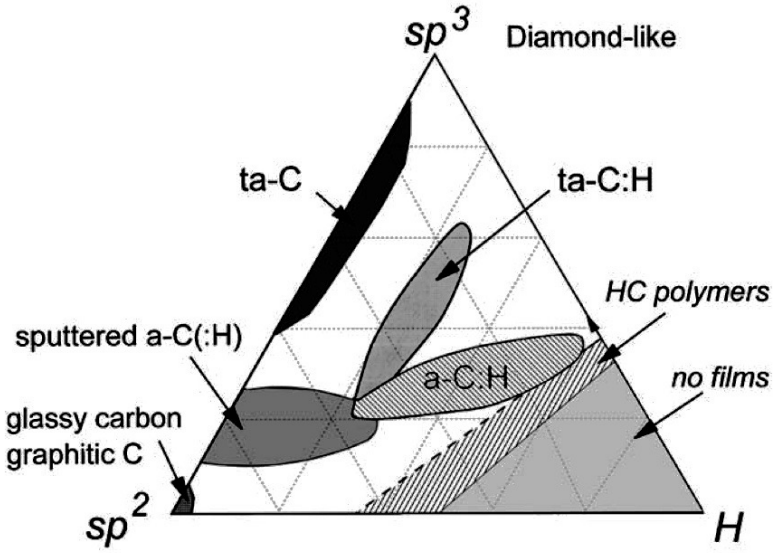


***Figure 1.7. Pseudo ternary phase diagram describing different types of diamond-like carbon coatings as described by Robertson et al.[3]***

The extreme top and the left-bottom of the triangle (Figure 1.6) represent 100% diamond and graphite, respectively. *ta*-C films (tetrahedral amorphous carbon) coatings are mostly rich in $sp^3$-bonded carbon and these films possess beneficial properties similar to diamond such as high mechanical hardness, chemical and electrochemical inertness[3]. On other end, *a*-C (amorphous carbon) coatings are mostly rich in $sp^2$-bonded carbon. In the center of the phase diagram, *ta*-C:H and *a*-C:H films (respectively for tetrahedral amorphous hydrogenated carbon and amorphous hydrogenated carbon) are composed of both carbon and hydrogen at varying concentrations. The increase in hydrogen content results mostly in a decrease in the mechanical properties of the coatings.

Various deposition techniques are used to deposit amorphous carbon thin films on required substrates. They can be divided in two different categories:

- *Deposition techniques using a solid carbon source such as physical vapor deposition (PVD), ion beam sputtering, cathodic arc deposition, laser evaporation etc. These techniques are used for depositing a-c and ta-C films.*
- *Deposition techniques using hydrocarbon gas source such as chemical vapor deposition (CVD), plasma-enhanced chemical vapor deposition (PECVD), electron cyclotron resonance chemical vapor deposition (ECR-CVD) etc. These techniques are used to deposit a-C:H and ta-C:H films.*

Figure 1.8 illustrates the schematics of some of the deposition techniques. Full description of these techniques can be found elsewhere[3,18,54,56]. PECVD is one of the most popular techniques used to deposit DLC coatings. This technique can be described in four steps[50]:

- *The plasma decomposes the hydrocarbon precursors into hydrocarbon species and ions.*
- *The hydrocarbon free radicals react with one another resulting in polymerization.*
- *Polymers adsorbe onto the substrate, generating thus chemical bonds with atoms on the surface*
- *densification of the radicals onto the surface with high energy ion.*

As mentioned in the previous section, the structure and properties of the coatings are dependent on the deposition techniques and coating parameters. It is well established that harder and denser coatings can be obtained using high-energy surface bombardment techniques[50] thus resulting in higher $sp^3/sp^2$ fraction until a threshold in ion energy is reached. A good balance has then to be found between the incident ions (with enough energy to penetrate the surface atomic layer) while minimizing thermal dissipation energy[57].

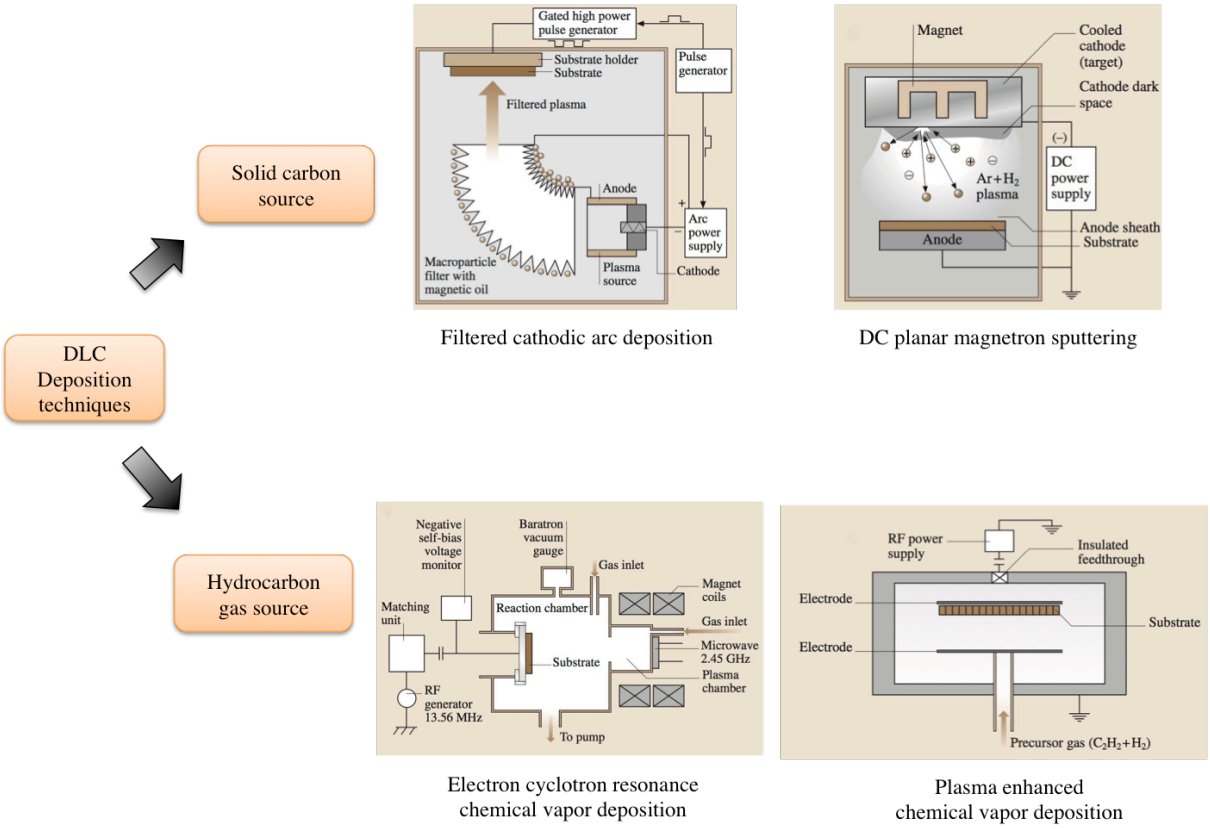


***Figure 1.8. Examples of DLC deposition techniques using either solid carbon precursor or hydrocarbon gas source. The schematic is adapted from Bhushan et al.[50]***

## 3.2. Mechanical properties of DLCs

Similar to the structural properties, the mechanical properties of DLC coatings strongly depend on the deposition method and therefore on the $sp^3/sp^2$ fraction and the amount of hydrogen in the coating. As demonstrated by Gao *et al.*[58] while using molecular dynamics simulations, along with $sp^3/sp^2$ fraction and hydrogen content, the tridimensional configuration of the carbon network is responsible for the mechanical response of DLC coatings[3,50]. Thus, a wide range of hardness ($10<H<80$) and elastic modulus ($100<E<500$) for DLC coatings can be found in the literature. Experimental proof of the tridimensional configuration of the carbon network and its consequences on the tribological behavior of DLC coatings have been provided by Fontaine *et al.*[4] while working on DLC coatings with various hydrogen content. They have shown that direct correlation could not be established between hydrogen content in DLC coating and their mechanical properties, namely hardness. They rather demonstrated that DLC coatings could exhibit viscoplastic behavior with increasing hydrogen content. Furthermore they were able to show that superlow friction (coefficient of friction <0.01) could be obtained only for coatings with significant viscoplastic behavior. This

shows the direct correlation between the relaxation properties of DLC coatings and their tribological behavior, viscoplasticity being controlled by the network relaxation.

## 3.3. Tribology of DLCs

A wide range of tribological behavior is observed for DLC coatings, which are directly related to the structural properties in the coatings and also on the employed tribological conditions. In a comprehensive review paper on DLC coatings A. Erdemir and C. Donnet[54] classified the different parameters that influence the tribological response of DLC, described in Figure 1.9.

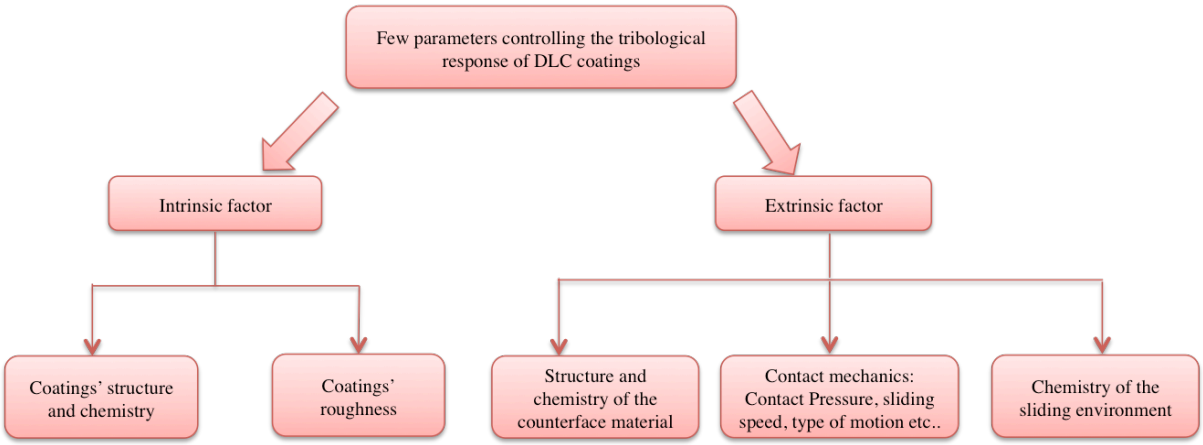


***Figure 1.9. Illustration of the different parameters that influence the tribological properties of DLC coatings. The schematic adapted from Erdemir et al.[54]***

Intrinsic factors are mainly related to the structure and chemistry of the coatings as well as the roughness of the coatings. On the other hand extrinsic factor involve structure and chemistry of the counterface material, the contact mechanical conditions and the chemistry of the sliding environment. It is important to note that $sp^3/sp^2$ fraction together, the three-dimensional structure and hydrogen content[58] of the film are paramount in determining its tribological response. In the following sections, we will mainly discuss the mechanically-induced structural changes in DLC coatings.

### 3.3.1. Fundamental structural and chemical changes during sliding of DLC coatings

Similar to the tribology of diamond, DLC films also show two main structural changes while sliding: rehydridization[44,59–65] (conversion from $sp^3$- to $sp^2$-bonded carbon) and passivation[66–70] (functionalization or interactions with external environment).

***a) Rehybridization***

Le Huu *et al.*[59] have shown that upon rubbing hydrogenated amorphous carbon thin film, a transition from $sp^3$- to $sp^2$-bonded carbon occurs. This phenomenon is attributed to the desorption of hydrogen from the DLC, leaving dangling bonds and followed by the formation of energetically more favorable π bonds assisted by increased interfacial temperatures. According to their studies, such processes result in a "thin graphitic" layer at the sliding interface which promotes low friction coefficients. Later, Konicek *et al.*[44] have refuted the temperature induced graphitization hypothesis proposed by Le Huu *et al.*[59] and Erdemir *et al.*[40], based on NEXAFS evidence of enrichment in $sp^2$-bonded carbon in the extreme surface of ta-C and UNCD. Kunze *et al.*[65] work on rehybridization hypothesis shows that when self-mated surfaces of *ta*-C slide against each other, there is a stress-induced transition from $sp^3$- to $sp^2$-bonded carbon. In addition, the newly generated $sp^2$-rich surface is strained due to the mechanical stress in the contact. Their results were also supported by the molecular dynamic simulations[65]. Other authors[61,63] have also supported the hypothesis of stress-induced rehybridization for ta–C coatings upon sliding using molecular dynamic simulations as described in Figure 1.10. As illustrated on Figure 1.10.a, while sliding ta–C in unlubricated self-mattered contact in vacuum conditions, a transfer of material occurs from ta-C (1) to ta–C (2). Figure 1.10.b represents the corresponding chemical states of Figure 1.10.a. In the initial state, both ta-C films are made of $sp^3$- (grey), $sp^2$-(green) and sp-(yellow) bonded carbon. Upon sliding, rehybridization occurs, leading to a more $sp^2$-bonded carbon material at the interface.

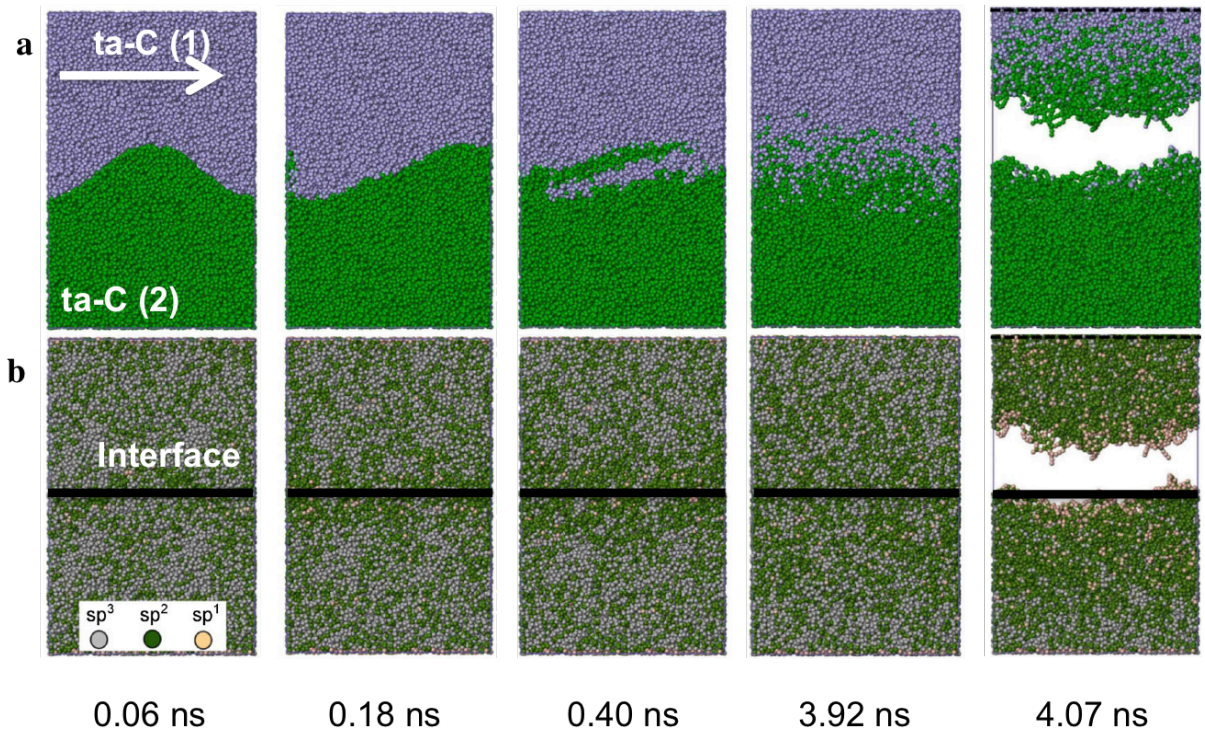


***Figure 1.10. Molecular dynamics simulations illustrating (a) transfer and (b) rehybridization upon sliding of self-mated ta-C coatings in vacuum, from Romero et al.[71]***

It has been thus proposed[54,72–74] that the high friction coefficients observed for hydrogen free DLC coatings (*ta*-C or *a*-C) when sliding under vacuum conditions is a consequence of the rehybridization phenomenon, since the interaction between the free and active covalent bonds (as called carbon dangling bonds) could generate high friction under vacuum conditions.

Thanks to these studies (both experimental and simulations) is it now well established that upon sliding DLC films, mechanically induced rehybridization (conversion from $sp^3$- to $sp^2$ bonded carbon) occurs generating carbon dangling bonds. In absence of reactive environmental elements, interactions between dangling bonds results in high friction.

***b) Passivation***

In presence of gaseous species it has been established[45,65,69,70,73,74] that dangling carbon bonds in the sliding contact of DLC films are passivated. Several authors including Fontaine *et al.*[66], Donnet *et al.*[67] and Erdemir *et al.*[68] have investigated the role of passivation of dangling carbon bonds, in hydrogen environment, on the tribological behavior of hydrogenated amorphous carbon films. They proposed that the intrinsic hydrogen trapped in the coating during deposition or the native hydrogen present in the sliding environment can serve as a reservoir for passivation and thus prevents the direct interaction between the dangling bonds. Therefore, according to Erdemir *et al.*[54], a dipole configuration is created at

the sliding interface, which gives rise to short-range repulsion between the hydrogen-terminated sliding surfaces, and therefore lower friction coefficients can be obtained (Figure 1.11.a). While working on *ta*-C coatings, in presence of glycerol, Matta *et al.*[69] proposed that the –OH bonds generated from glycerol decomposition passivates carbon dangling bonds on the surface and thus resulting in lower friction coefficients (Figure 1.11.b).

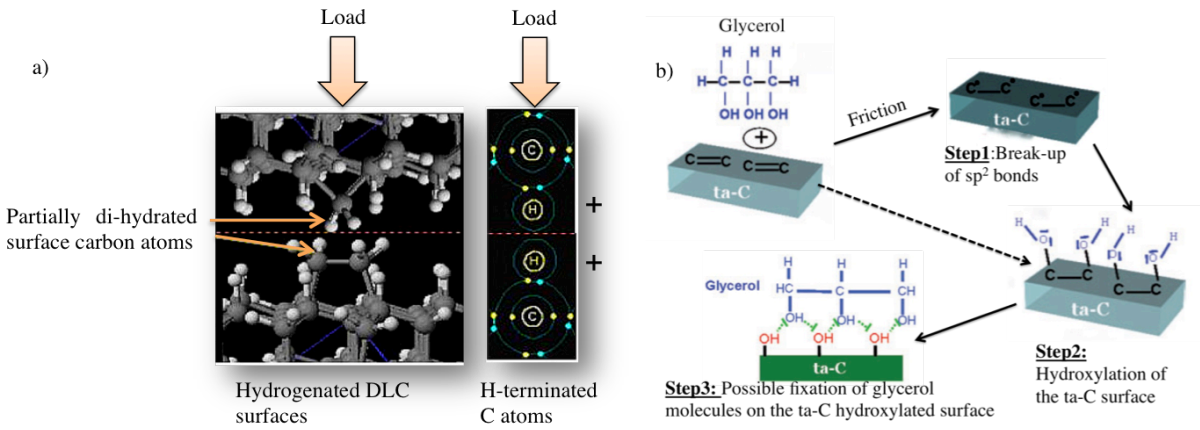


***Figure 1.11. Proposed model for the passivation of carbon dangling bonds by hydrogen for hydrogenated DLC coatings from Erdemir et al.[54](a) and (b)model of passivation of carbon dangling bonds by -OH groups from ta-C films, from Matta et al.[69])***

More recently, Konicek *et al.*[64] have investigated the friction behavior of *ta*-C coatings in presence of water vapor and further evidence of passivation of dangling bonds by H or -OH groups generated from decomposition of water vapor is observed.

### 3.3.2. Role of the third body in the tribological behavior of DLC coatings

As pointed out in the beginning of this chapter and proposed by Scharf *et al.*[11], the high hardness of DLC coatings can seem to contradict with their low friction properties. Such a contradiction can be explained using a "Third Body Approach". The Third body Approach was first proposed by Godet *et al.*[75,76] who defined the third body as the "material formed by the relative motion of the two parent (first bodies) materials in the sliding contact".

From an exclusive mechanical point of view, the properties of third body can be characterized by its rheology by being indifferent to the composition of the film while from an exclusive chemistry approach, the third body can be characterized via its chemical composition, by remaining indifferent to its rheology. Combining this dual approach, Singer *et al.*[77] proposed a shear strength approach, which bridges the gap between the chemistry of

the third body and its rheology (shear strength). Thus the shear strength of a given third body depends on its chemistry, which is influenced by the chemical species in the sliding environment. Ronkainen *et al.*[78] have also demonstrated the predominant role of the shear strength of the third body in the frictional response of *a*-C:H films while sliding against steel or alumina surfaces.

On the other hand, the chemistry, structure and stickiness of the third body is influenced by the counterface material. Erdemir and Donnet[54] reported that counter-body made of materials known to be carbide-forming such as titanium, iron, tungsten and silicon, for example, generate tribofilms at a much higher growth rate in comparison to other non-carbide forming surfaces. Several other authors[10,11,17,78–82] have also reported the crucial role of the third body in controlling the frictional response of DLC coatings. Also, Erdemir *et al.*[82] highlighted the influence of the interfacial materials' structure in controlling the frictional response between *a*-C:H and sintered MgO-PSZ. They emphasized the so-called "graphitic third body" generated at the sliding interface which played a crucial role in reducing the friction. According to them, mechanically induced thermal heating leads to graphitization and this further explains the reduced rates of graphitization with relative humidity. As mentioned above, the graphitization hypothesis has recently been ruled out by Konicek *et al.*[64] while working on UNCD and ta-C. They found that the increased temperatures at the contact are not sufficient enough to promote graphitization but rather stress-assisted transformation can increase the amount of $sp^2$-bonded carbon in ring-like structure.

In summary, given the evidences provided by works based on stress-induced rehybridization followed or not by passivation, depending on the sliding environment, mechanically-induced thermal heating followed by graphitization seems unlikely to occur during tribological test on DLC coatings. Rehydridization and passivation hypothesis is so far, more valid. However, only few studies have presented spectroscopic evidence of these two phenomena while mainly working on UNCD or ta-C. As well, no previous studies have clearly verified these hypotheses for addition elements containing DLC coatings. Further work has to be accomplished in order to provide new evidence of the validity of these hypotheses for addition elements containing DLC coatings. Among other things, this thesis will overcome that shortcoming.

## 3.4. Different addition elements containing DLCs

In order to broaden the range of properties achieved with DLC coatings or to enhance the existing ones, different elements such as B, N, O, F, Si, P, Ca and metals[6,15,83–87] can be incorporated into the carbon network as illustrated in Figure 1.12.

Panwar *et al.*[84] have conducted a comparative study on the influence of boron and phosphorous inclusions in DLC coatings and they found that incorporating 2 at.% of boron in DLC decreased the $sp^3$ fraction by ~ 4%, while incorporation of phosphorous ~ 2 at.% leads to a 30 % decrease in $sp^3$ fraction.

Presence of elemental nitrogen in the amorphous carbon network improves the hardness and anti-corrosion properties[87]. Liu *et al.*[86] have highlighted the influence of nitrogen incorporation in the mechanical properties of hydrogenated amorphous carbon films. Papakonstantinou *et al.*[88] work on the effect of nitrogen incorporation in DLC, quantify the threshold of nitrogen content in the films that enhances the mechanical properties. While small amounts of nitrogen incorporation (2 *at.*%) reduces the clustering of $sp^2$-bonded carbon and increases the mechanical properties of the coating, the higher contents of nitrogen (19 at.%) increases the amount of $sp^2$-bonded carbon clusters thus lowering the hardness and elastic modulus *i.e.* 56 and 573 GPa respectively – for 2 *at*.% of nitrogen – down to 2 and 44 GPa respectively for 19 at.% of nitrogen.

Fluorination of DLC was reported to induce an increase in $–CF_2$ and $-CF_3$ groups and thus reduce the mechanical properties of the coating. Donnet *et al.*[89] have reported that high percentages of fluorine incorporation in DLC (*i.e.* greater than 20 *at.*%) can enhance the crosslinking of the network and therefore increase the wear resistance compared to low fluorine containing DLCs.

As seen for the other dopants, Calcium and Oxygen (Ca-O) incorporation in the amorphous carbon network also promotes and increase of amount of $sp^2$-bonded carbon nanoclusters. Incorporation of Ca-O in the amorphous carbon network can increased the biological acceptance as shown as shown by Doner-Reisel *et al.*[90] while working on mouse cells.

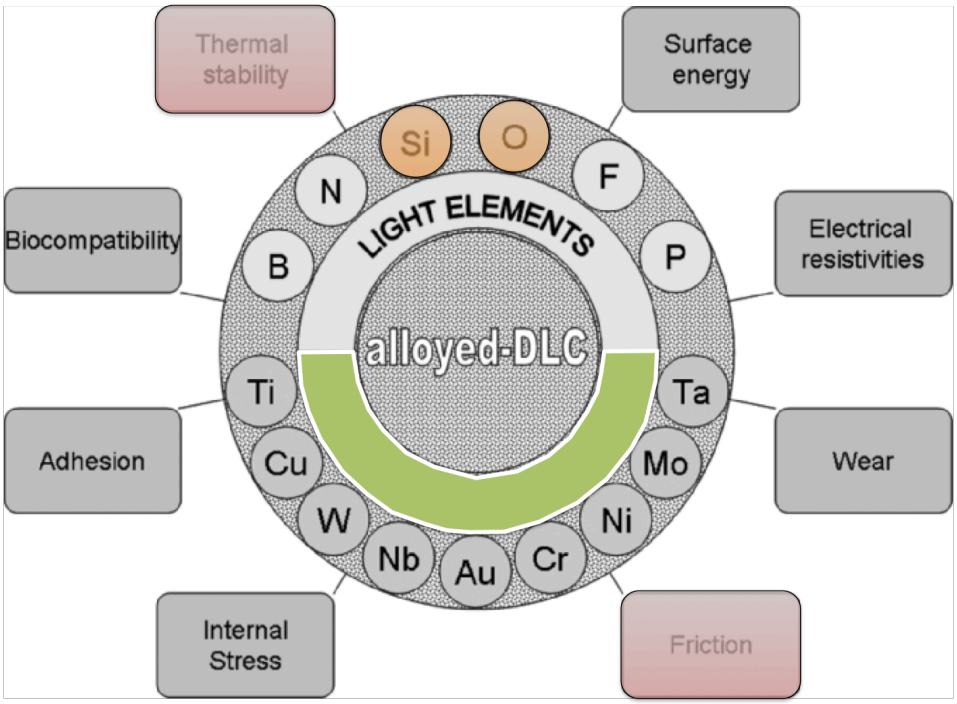


***Figure 1.12. Schematic of different addition elements incorporated into amorphous carbon network for enhancing properties from Sanchez-Lopez et al.[83]***

### 3.4.1. Silicon and oxygen incorporation in DLC: a-C:H:Si:O films

#### *3.4.1.1. Structure*

The incorporation of Oxygen together with Silicon in amorphous hydrogenated (a-C:H) films lead to the development of a new class of coatings, *i.e.* silicon oxide containing hydrogenated amorphous carbon (a-C:H:Si:O), sometimes referred to as diamond-like nanocomposite (DLN) or SiO-containing diamond-like carbon. a-C:H:Si:O films are generally deposited using PECVD method with a siloxane precusors[8,91–94]. They are generally described as a fully amorphous films consisting of two interpenetrating and inter-bonded networks, one being a silica glass ($SiO_x$) network and the other an amorphous hydrogenated carbon network (a-C:H) as described in Figure 1.12. Randeniya *et al.*[95] have shown that depending on the silicon content, the network could either exhibit an amorphous single phase structure -for silicon content lower than ~ 13 at.% – or double phase structure ($SiO_x$-DLC network and $SiO_x$ segregated phase) – for silicon content higher than ~ 13 at.%.

SiO-based DLC coatings usually exhibit lower internal stresses (typically less than 1 GPa[9,91]) than a:C-H. The drop in the compressive residual stress in a-C:H:Si:O films has been ascribed by Neerinck *et al.*[8] to the presence of Si–C bonds, which are longer that C-C bonds (Si–C bond length = 1.89 Å vs. C–C bond length = 1.54 Å).

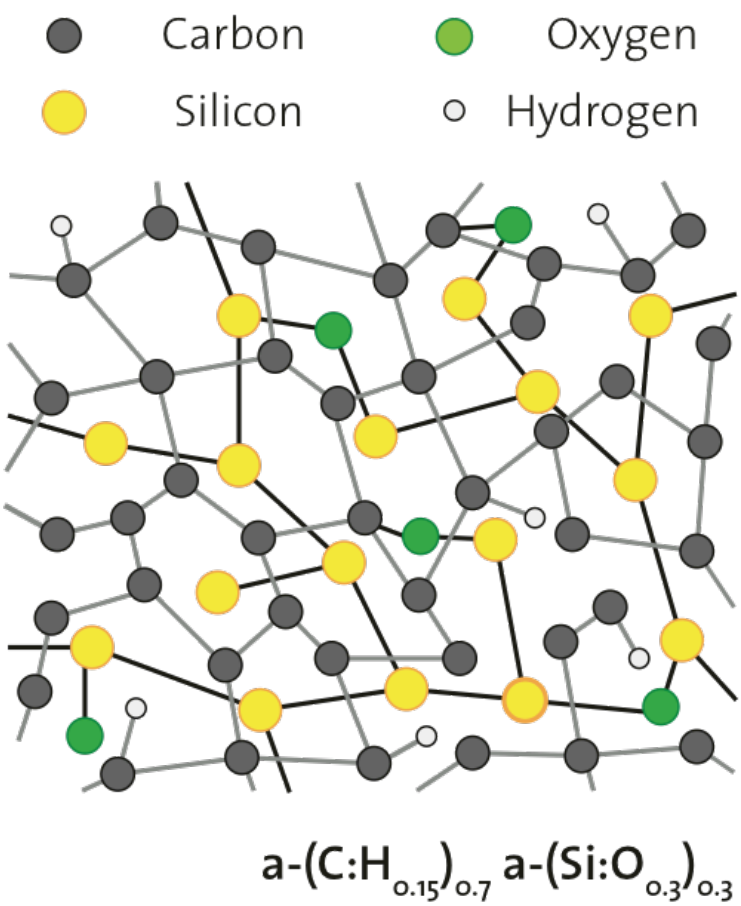


***Figure 1.13. Schematic of atomical structure of Diamond-Like Nanocomposite films from Scharf et al.[96]***

***3.4.1.2. Main advantages of a-C :H :Si :O* vs *a-C:H***

As a consequence of their low internal stresses, a-C:H:Si:O coatings exhibit lower delamination while deposited onto various types of substrates in comparison to a-C:H coatings[12,97]. The thermal stability of a-C:H:Si:O films has been found to be higher than that of a-C:H. This occurs from the fourfold coordination of Si atoms with Carbon thereby stabilizing the carbon atoms in the $sp^3$ hybridization state and inhibiting their conversion into threefold-coordinated $sp^2$-bonded carbon at high temperature. This would imply that the activation energy required for the conversion of $sp^3$- to $sp^2$-bonded carbon atoms in a-C:H:Si:O is higher than in a-C:H, which has been estimated by Mangolini *et al.*[98] to be 3.5 ± 0.5 eV. However, no experimental evidence to explain the effect of the incorporation of silicon and oxygen in the amorphous carbon matrix on the thermal stability of the resulting structure has been reported yet. Some of this aspect will also be investigated in this thesis as well as the tribological behavior of annealed a-C:H:Si:O.

Concerning their tribological behavior it has been shown that incorporation of Si reduces the extent to which the frictional properties of DLCs are dependent on the environmental conditions[99,100]. In particular, Gilmore and Hauert[85] demonstrated that the incorporation of approximately 4 at. % of Si into the amorphous carbon network can render its friction response less dependent on the sliding environment especially while sliding against steel counterface. Fundamental understandings of the role of silicon in enhancing the tribological properties of Si-containing DLC coatings are still missing.

#### *3.4.1.3. Fundamental tribological mechanisms of a-C:H:Si:O*

Even though the coefficient of friction for a-C:H:Si:O coatings is less dependent on the external environment in comparison to pure DLC, different values can be obtained from the literature as illustrated by Meskinis *et al.*[101]. In fact, in 1989, Sugimoto *et al.*[81] reported a coefficient of friction of 0.007 for a silicon containing a-C:H film under vacuum conditions which they attributed to a "transfer of hydrocarbon species from the coating to the steel counterbody". While working in humid environments (50 % RH and 90 % RH) Neerinck *et al.*[9] have reported coefficients of friction of 0.04 and 0.08 respectively for a-C:H:Si:O while pure a-C:H exhibited a coefficient of friction of 0.15. A fundamental understanding of the tribological behavior of a-C:H:Si:O coatings have been proposed by Scharf *et al.*[96], using the third body hypothesis as proposed by Sugimoto *et al.*[81]. They demonstrated that the friction mechanism of a-C:H:Si:O is mainly governed by the interfacial sliding between the a-C:H:Si:O coating and the friction-induced tribofilm formed on the silicon nitride or steel counterface. Moreover, the environment plays a major role on the composition and mechanical properties of this interfacial film: while in dry environment the interfacial film mainly consists of carbon and has a low shear strength (9 GPa), under humid conditions the interfacial film consists of silica-rich fragments and exhibits a high shear strength (78 GPa).

Further analysis of the fundamental tribological mechanism of a-C:H:Si:O is thus needed in order to provide complementary information or a better understanding of the influence of environment on the tribological behavior of a-C:H:Si:O films.

# 4. Summary

Diamond-like carbon (DLC) coatings are amorphous carbon solid lubricant with a wide range of exciting applications. By incorporating elements into the amorphous carbon network, mechanical and tribological properties of the films can be altered according to the requirement in a specific application. Silicon oxide containing hydrogenated amorphous carbon (a-C:H:Si:O) coatings are known for their lower environment dependences of friction properties than pure DLC films. Although several groups proposed different tribological mechanisms to explain this behavior, there still is a lack in the fundamental understanding of the friction mechanisms of a-C:H:Si:O coatings. This thesis will attempt to address the mechanism behind the enhanced tribological properties of a-C:H:Si:O coatings by understanding the fundamental physical and chemical phenomenon that occur at the interface upon tribological testing.

# 5. Résumé Chapitre 1

Les revêtements *Diamond-Like Carbon* (DLC) sont des lubrifiants solides de structure amorphe très attractifs dans différents domaines d'application. Afin de modifier les propriétés mécaniques de ces revêtements et d'améliorer leurs performances tribologiques, différents éléments peuvent être incorporés dans le réseau amorphe de carbone.

Dans ce chapitre nous rappelons d'abord les bases des phénomènes d'hybridation de l'atome de carbone afin de mieux présenter la structure des matériaux à base carbone en général, notamment le diamant, le graphite, les fullerènes, pour ensuite focaliser sur les revêtements DLC, leur structure, leurs propriétés intrinsèques et leur comportement tribologique.

Un parallèle est établi entre les principaux mécanismes tribologiques observés dans la littérature pour les revêtements diamant et DLC. Il ressort de cette analyse bibliographique – menée autant sur les travaux expérimentaux que sur les travaux de simulation – que trois phénomènes principaux interviennent dans le comportement tribologique des revêtements en couche mince à base carbone :

- *La réhybridation $sp^3$–$sp^2$ (conversion des carbones hybridés $sp^3$ en carbones hybridés $sp^2$) ;*
- *La passivation (recombinaison entre les carbones réhybridés et les éléments ou groupements chimiques réactifs de l'environnement) ;*
- *Le rôle joué par le tribofilm (le troisième corps généré lors du frottement des deux corps initiaux, par transfert de matière et interactions avec l'environnement).*

Ce chapitre aborde également les différents éléments d'addition pouvant être incorporés dans le réseau amorphe de carbone hydrogéné afin de modifier certaines propriétés. L'accent est mis sur le matériaux qui a fait l'objet de ce travail de thèse, le a-C:H:Si:O. En effet, il est prouvé que les revêtements de carbone amorphe hydrogéné contenant du silicium et de l'oxygène (a-C:H:Si:O) présentent une réponse tribologique moins sensible à leur environnement de fonctionnement comparativement aux revêtements DLC purs. Bien que des équipes de recherche aient apporté quelques éléments de réponse à la compréhension de cette différence de comportement des a-C:H:Si:O, les mécanismes fondamentaux pouvant l'expliquer et les interactions physico-chimiques entre les a-C:H:Si:O et leur environnement de fonctionnement manquent encore. C'est donc dans cette perspective que s'inscrit ce travail de thèse.

# 6. References


1. Bowden, F. P. & Tabor, D. Friction, lubrication and wear: a survey of work during the last decade. Br. J. Appl. Phys. **17,** 1521 (1966).
2. Scharf, T. W. & Prasad, S. V. Solid lubricants: a review. J. Mater. Sci. **48,** 511–531 (2012).
3. Donnet, C. & Erdemir, A. Tribology of Diamond-like Carbon Films: Fundamentals and Applications. (Springer Science & Business Media, 2007).
4. Yasuda, E. Carbon Alloys: Novel Concepts to Develop Carbon Science and Technology. (Gulf Professional Publishing, 2003).
5. Heiserman, D. Exploring Chemical Elements and Their Compounds. (McGraw-Hill Companies,Incorporated, 1991).
6. Burchell, T. D. Carbon Materials for Advanced Technologies. (Elsevier, 1999).
7. Wang, J.-T., Chen, C. & Kawazoe, Y. New Carbon Allotropes with Helical Chains of Complementary Chirality Connected by Ethene-type π-Conjugation. Sci. Rep. **3,** (2013).
8. Fahy, S., Louie, S. G. & Cohen, M. L. Pseudopotential total-energy study of the transition from rhombohedral graphite to diamond. Phys. Rev. B **34,** 1191–1199 (1986).
9. Geim, A. K. & Novoselov, K. S. The rise of graphene. Nat. Mater. **6,** 183–191 (2007).
10. Pierson, H. O. Handbook of Carbon, Graphite, Diamonds and Fullerenes: Processing, Properties and Applications. (William Andrew, 2012).
11. Zhang, Y. & Pan, C. Measurements of mechanical properties and number of layers of graphene from nano-indentation. Diam. Relat. Mater. **24,** 1–5 (2012).
12. WenXing, B., ChangChun, Z. & WanZhao, C. Simulation of Young's modulus of single-walled carbon nanotubes by molecular dynamics. Phys. B Condens. Matter **352,** 156–163 (2004).
13. Sliney, H. E. Solid lubricant materials for high temperatures—a review. Tribol. Int. **15,** 303–315 (1982).
14. Savage, R. H. Graphite Lubrication. J. Appl. Phys. **19,** 1–10 (1948).
15. Berman, D., Erdemir, A. & Sumant, A. V. Few layer graphene to reduce wear and friction on sliding steel surfaces. Carbon **54,** 454–459 (2013).
16. Berman, D., Erdemir, A. & Sumant, A. V. Reduced wear and friction enabled by graphene layers on sliding steel surfaces in dry nitrogen. Carbon **59,** 167–175 (2013).
17. Di fisica, S. italiana. The Physics of Diamond. (IOS Press, 1997).
18. Scandolo, S., Bernasconi, M., Chiarotti, G. L., Focher, P. & Tosatti, E. Pressure-Induced Transformation Path of Graphite to Diamond. Phys. Rev. Lett. **74,** 4015–4018 (1995).
19. Pan, Z., Sun, H., Zhang, Y. & Chen, C. Harder than Diamond: Superior Indentation Strength of Wurtzite BN and Lonsdaleite. Phys. Rev. Lett. **102,** 055503 (2009).
20. Dubrovinskaia, N. et al. Superhard nanocomposite of dense polymorphs of boron nitride: Noncarbon material has reached diamond hardness. Appl. Phys. Lett. **90,** 101912 (2007).
21. Wilks, E. M. & Wilks, J. The resistance of diamond to abrasion. J. Phys. Appl. Phys. **5,** 1902 (1972).
22. Wilks, E. M. The relative hardness of the hard directions in diamond. Philos. Mag. **6,** 701–705 (1961).
23. Casey, M. & Wilks, J. The friction of diamond sliding on polished cube faces of diamond. J. Phys. Appl. Phys. **6,** 1772 (1973).
24. Pastewka, L., Moser, S., Gumbsch, P. & Moseler, M. Anisotropic mechanical amorphization drives wear in diamond. Nat. Mater. **10,** 34–38 (2011).
25. Wilks, E. M. & Wilks, J. The resistance of diamond to abrasion. Philos. Mag. **4,** 158–170 (1959).
26. Gardos, M. N. & Soriano, B. L. The effect of environment on the tribological properties of polycrystalline diamond films. J. Mater. Res. **5,** 2599–2609 (1990).
27. Erdemir, A. et al. Tribological properties of nanocrystalline diamond films. Surf. Coat. Technol. **120–121,** 565–572 (1999).
28. Gardos, M. N. Re(de)construction-induced friction signatures of polished polycrystalline diamond films in vacuum and hydrogen. Tribol. Lett. **4,** 175–188 (1998).
29. Konicek, A. R. et al. Origin of Ultralow Friction and Wear in Ultrananocrystalline Diamond. Phys. Rev. Lett. **100,** 235502 (2008).
30. Konicek, A. R. et al. Influence of surface passivation on the friction and wear behavior of ultrananocrystalline diamond and tetrahedral amorphous carbon thin films. Phys. Rev. B **85,** 155448 (2012).
31. De Barros Bouchet, M.-I. et al. Friction of Diamond in the Presence of Water Vapor and Hydrogen Gas. Coupling Gas-Phase Lubrication and First-Principles Studies. J. Phys. Chem. C **116,** 6966–6972 (2012).
32. Hare, J. P. & Kroto, H. W. A postbuckminsterfullerene view of carbon in the galaxy. Acc. Chem. Res. **25,**

106–112 (1992).
33. Huffman, D. R. & Kratschmer, W. Solid $C_{60}$. (1991). at <http://inis.iaea.org/Search/search.aspx?orig_q=RN:23056034>
34. Pierson, H. O. in Handbook of Carbon, Graphite, Diamonds and Fullerenes (ed. Pierson, H. O.) 356–373 (William Andrew Publishing, 1993). at <http://www.sciencedirect.com/science/article/pii/B9780815513391500207>
35. Bhushan, B. in Nanotribology and Nanomechanics 843–899 (Springer Berlin Heidelberg, 2008). at <http://link.springer.com/chapter/10.1007/978-3-540-77608-6_16>
36. Curl, R. F. & Smalley, R. E. Probing C60. Science **242,** 1017–1022 (1988).
37. Regueiro, M. N., Monceau, P. & Hodeau, J.-L. Crushing C60 to diamond at room temperature. Nature **355,** 237–239 (1992).
38. Full Text PDF. at <https://tel.archives-ouvertes.fr/tel-00790813/document>
39. Erdemir, A. & Donnet, C. Tribology of diamond-like carbon films: recent progress and future prospects. J. Phys. Appl. Phys. **39,** R311 (2006).
40. Jacob, W. & Möller, W. On the structure of thin hydrocarbon films. Appl. Phys. Lett. **63,** 1771–1773 (1993).
41. Robertson, J. Diamond-like amorphous carbon. Mater. Sci. Eng. R Rep. **37,** 129–281 (2002).
42. Grill, A. Diamond-like carbon: state of the art. Diam. Relat. Mater. **8,** 428–434 (1999).
43. Robertson, J. Deposition mechanisms for promoting sp3 bonding in diamond-like carbon. Diam. Relat. Mater. **2,** 984–989 (1993).
44. Fontaine, J., Loubet, J. L., Mogne, T. L. & Grill, A. Superlow Friction of Diamond-Like Carbon Films: A Relation to Viscoplastic Properties. Tribol. Lett. **17,** 709–714 (2004).
45. Gao, G. T., Mikulski, P. T., Chateauneuf, G. M. & Harrison, J. A. The Effects of Film Structure and Surface Hydrogen on the Properties of Amorphous Carbon Films. J. Phys. Chem. B **107,** 11082–11090 (2003).
46. Le Huu, T., Zaidi, H., Paulmier, D. & Voumard, P. Transformation of sp3 to sp2 sites of diamond like carbon coatings during friction in vacuum and under water vapour environment. Thin Solid Films **290–291,** 126–130 (1996).
47. Ma, T.-B., Wang, L.-F., Hu, Y.-Z., Li, X. & Wang, H. A shear localization mechanism for lubricity of amorphous carbon materials. Sci. Rep. **4,** (2014).
48. Gao, G. T., Mikulski, P. T. & Harrison, J. A. Molecular-Scale Tribology of Amorphous Carbon Coatings: Effects of Film Thickness, Adhesion, and Long-Range Interactions. J. Am. Chem. Soc. **124,** 7202–7209 (2002).
49. Gao, F., Erdemir, A. & Tysoe, W. T. The Tribological Properties of Low-friction Hydrogenated Diamond-like Carbon Measured in Ultrahigh Vacuum. Tribol. Lett. **20,** 221–227 (2005).
50. Schall, J. D., Gao, G. & Harrison, J. A. Effects of Adhesion and Transfer Film Formation on the Tribology of Self-Mated DLC Contacts. J. Phys. Chem. C **114,** 5321–5330 (2010).
51. Konicek, A. R. et al. Influence of surface passivation on the friction and wear behavior of ultrananocrystalline diamond and tetrahedral amorphous carbon thin films. Phys. Rev. B **85,** 155448 (2012).
52. Kunze, T. et al. Wear, Plasticity, and Rehybridization in Tetrahedral Amorphous Carbon. Tribol. Lett. **53,** 119–126 (2014).
53. Fontaine, J., Le Mogne, T., Loubet, J. L. & Belin, M. Achieving superlow friction with hydrogenated amorphous carbon: some key requirements. Thin Solid Films **482,** 99–108 (2005).
54. Donnet, C., Fontaine, J., Grill, A. & Mogne, T. L. The role of hydrogen on the friction mechanism of diamond-like carbon films. Tribol. Lett. **9,** 137–142 (2001).
55. Erdemir, A. The role of hydrogen in tribological properties of diamond-like carbon films. Surf. Coat. Technol. **146–147,** 292–297 (2001).
56. Matta, C. et al. Tribochemistry of tetrahedral hydrogen-free amorphous carbon coatings in the presence of OH-containing lubricants. Lubr. Sci. **20,** 137–149 (2008).
57. Martin, J.-M. et al. Gas-Phase Lubrication of ta-C by Glycerol and Hydrogen Peroxide. Experimental and Computer Modeling. J. Phys. Chem. C **114,** 5003–5011 (2010).
58. Romero, P. A., Pastewka, L., Lautz, J. V. & Moseler, M. Surface passivation and boundary lubrication of self-mated tetrahedral amorphous carbon asperities under extreme tribological conditions. Friction **2,** 193–208 (2014).
59. Andersson, J., Erck, R. A. & Erdemir, A. Friction of diamond-like carbon films in different atmospheres. Wear **254,** 1070–1075 (2003).
60. Miyoshi, K., Wu, R. L. C., Garscadden, A., Barnes, P. N. & Jackson, H. E. Friction and wear of plasma-deposited diamond films. J. Appl. Phys. **74,** 4446–4454 (1993).
61. Chandrasekar, S. & Bhushan, B. The role of environment in the friction of diamond for magnetic recording head applications. Wear **153,** 79–89 (1992).
62. Scharf, T. W. & Singer, I. L. Role of Third Bodies in Friction Behavior of Diamond-like Nanocomposite Coatings Studied by In Situ Tribometry. Tribol. Trans. **45,** 363–371 (2002).

63. Godet, M. The third-body approach: A mechanical view of wear. Wear **100,** 437–452 (1984).
64. Godet, M. Third-bodies in tribology. Wear **136,** 29–45 (1990).
65. Singer, I. L. in Fundamentals of Friction: Macroscopic and Microscopic Processes (eds. Singer, I. L. & Pollock, H. M.) 237–261 (Springer Netherlands, 1992). at <http://link.springer.com/chapter/10.1007/978-94-011-2811-7_13>
66. Ronkainen, H., Likonen, J., Koskinen, J. & Varjus, S. Effect of tribofilm formation on the tribological performance of hydrogenated carbon coatings. Surf. Coat. Technol. **79,** 87–94 (1996).
67. Singer, I. L., Dvorak, S. D., Wahl, K. J. & Scharf, T. W. Role of third bodies in friction and wear of protective coatings. J. Vac. Sci. Technol. A **21,** S232–S240 (2003).
68. Vihersalo, J., Ronkainen, H., Varjus, S., Likonen, J. & Koskinen, J. in Tribology Series (ed. D. Dowson, C. M. T., T. H. C. Childs, M. Godett and G. Dalmaz) **27,** 337–344 (Elsevier, 1994).
69. Iwao Sugimoto and Shojiro Miyake. Oriented hydrocarbons transferred from a high performance lubricative amorphous C:H:Si film during sliding in a vacuum. at <http://scitation.aip.org/content/aip/journal/apl/56/19/10.1063/1.103072>
70. Scharf, T. W. & Singer, I. L. Monitoring Transfer Films and Friction Instabilities with In Situ Raman Tribometry. Tribol. Lett. **14,** 3–8 (2003).
71. Erdemir, A., Bindal, C., Pagan, J. & Wilbur, P. Characterization of transfer layers on steel surfaces sliding against diamond-like hydrocarbon films in dry nitrogen. Surf. Coat. Technol. **76–77, Part 2,** 559–563 (1995).
72. Sánchez-López, J. C. & Fernández, A. in Tribology of Diamond-Like Carbon Films (eds. Donnet, C. & Erdemir, A.) 311–338 (Springer US, 2008). at <http://link.springer.com/chapter/10.1007/978-0-387-49891-1_12>
73. Panwar, O. S. et al. Effect of high substrate bias and hydrogen and nitrogen incorporation on spectroscopic ellipsometric and atomic force microscopic studies of tetrahedral amorphous carbon films. Surf. Coat. Technol. **205,** 2126–2133 (2010).
74. Tripathi, R. K., Panwar, O. S., Srivastava, A. K., Rawal, I. & Chockalingam, S. Structural, nanomechanical, field emission and ammonia gas sensing properties of nitrogenated amorphous carbon films deposited by filtered anodic jet carbon arc technique. Talanta **125,** 276–283 (2014).
75. Panwar, O. S. et al. Characterization of Boron- and Phosphorous-Incorporated Tetrahedral Amorphous Carbon Films Deposited by the Filtered Cathodic Vacuum Arc Process. Jpn. J. Appl. Phys. **48,** 065501 (2009).
76. Gilmore, R. & Hauert, R. Control of the tribological moisture sensitivity of diamond-like carbon films by alloying with F, Ti or Si. Thin Solid Films **398–399,** 199–204 (2001).
77. Liu, F.-X., Yao, K.-L. & Liu, Z.-L. Raman spectroscopy of a-C:H:N films deposited using ECR-CVD with mixed gas. Appl. Surf. Sci. **253,** 6957–6962 (2007).
78. Irmer, G. & Dorner-Reisel, A. Micro-Raman Studies on DLC coatings. Adv. Eng. Mater. **7,** 694–705 (2005).
79. Papakonstantinou, P. & Lemoine, P. Influence of nitrogen on the structure and nanomechanical properties of pulsed laser deposited tetrahedral amorphous carbon. J. Phys. Condens. Matter **13,** 2971 (2001).
80. Donnet, C. et al. Wear-resistant fluorinated diamondlike carbon films. Surf. Coat. Technol. **94–95,** 531–536 (1997).
81. Dorner-Reisel, A. et al. KALZIUM-SAUERSTOFF-MODIFIZIERTE AMORPHE UND NANO-KRISTALLINE KOHLENSTOFFSCHICHTEN ALS BIOMATERIAL. Biomed. Tech. Eng. **47,** 393–396 (2002).
82. Neerinck, D. et al. Diamond-like nanocomposite coatings (a-C:H/a-Si:O) for tribological applications. Diam. Relat. Mater. **7,** 468–471 (1998).
83. Damasceno, J. C., Camargo Jr, S. S., Freire Jr, F. L. & Carius, R. Deposition of Si-DLC films with high hardness, low stress and high deposition rates. Surf. Coat. Technol. **133–134,** 247–252 (2000).
84. Baek, S., Shirafuji, T., Saito, N. & Takai, O. Adhesion property of SiOx-doped Diamond-like Carbon Films Deposited on Polycarbonate by Inductively Coupled Plasma Chemical Vapor Deposition. Thin Solid Films **519,** 6678–6682 (2011).
85. Chen, L.-Y. & Hong, F. C.-N. Diamond-like carbon nanocomposite films. Appl. Phys. Lett. **82,** 3526–3528 (2003).
86. Tóth, A., Mohai, M., Ujvári, T. & Bertóti, I. Nanomechanical properties of silicon-, oxygen- and nitrogen-containing a-C:H films prepared by RF plasma beam CVD. Thin Solid Films **482,** 188–191 (2005).
87. Randeniya, L. K., Bendavid, A., Martin, P. J., Amin, M. S. & Preston, E. W. Molecular structure of SiOx-incorporated diamond-like carbon films; evidence for phase segregation. Diam. Relat. Mater. **18,** 1167–1173 (2009).
88. Neerinck, D. et al. Diamond-like nanocomposite coatings for low-wear and low-friction applications in humid environments. Thin Solid Films **317,** 402–404 (1998).
89. Scharf, T. W., Ohlhausen, J. A., Tallant, D. R. & Prasad, S. V. Mechanisms of friction in diamondlike nanocomposite coatings. J. Appl. Phys. **101,** 063521–063521–11 (2007).

90. Yang, W. J., Sekino, T., Shim, K. B., Niihara, K. & Auh, K. H. Microstructure and tribological properties of SiOx/DLC films grown by PECVD. Surf. Coat. Technol. **194,** 128–135 (2005).
91. Mori, H. & Tachikawa, H. Increased adhesion of diamond-like carbon–Si coatings and its tribological properties. Surf. Coat. Technol. **149,** 224–229 (2002).
92. Mangolini, F., Rose, F., Hilbert, J. & Carpick, R. W. Thermally induced evolution of hydrogenated amorphous carbon. Appl. Phys. Lett. **103,** 161605 (2013).
93. K. Oguri and T. Arai. Low friction coatings of diamond-like carbon with silicon prepared by plasma-assisted chemical vapor deposition. J Mater Res Vol 5 No 11 (1990).
94. K. Oguri and T. Arai. Two different low friction mechanisms of diamond-like carbon with silicon coatings formed by plasma-assisted chemical vapor deposition. J Mater Res Vol (1992).
95. Meškinis, Š. & Tamulevičienė, A. Structure, Properties and Applications of Diamond Like Nanocomposite (SiOx Containing DLC) Films: A Review. Deimanto Tipo Anglies Nanokompozicinių SiOx Turinčių Deimanto Tipo Anglies Plėvelių Struktūros Cheminės Sudėties Savybių Ir Taikymo Sričių Apžv. **17,** 358–370 (2011).

# *Chapter 2.*

# *Experimental approach*

*In this chapter we will highlight the details of our experimental approach, from the full characterization of the as-received material as well as the annealing-induced structural changes, the tribological method and the details of characterization of the worn material. In fact, in order to meet the primary objectives of this thesis presented in the general introduction, namely, understanding the fundamental interactions between the chemical species in the sliding environment and a-C:H:Si:O upon tribological testing and the influence of the annealing-induced structural changes of a-C:H:Si:O coatings on their tribological behavior, experiments were performed on commercially available a-C:H:Si:O coatings. Prior to the tribological investigations, a complete characterization of the coatings (structure, chemistry and mechanical properties) has been jointly conducted at LTDS and in the Carpick Research Group at the University of Pennsylvania.*

*The role of the environment on the tribological behavior of as-received a-C:H:Si:O has been investigated using two approaches:*

- *Ambient air tribological tests with gas blowing facility, allowing rapid cycling of the sliding environment,*
- *High vacuum and controlled-environment tribological tests, allowing precise control of a static sliding environment.*

*In order to study the influence of chemical and structural changes on the tribological response of a-C:H:Si:O, modifications of a-C:H:Si:O were obtained through annealing of samples under high vacuum. Tribological behavior of annealed samples was investigated in dry conditions using an ambient air linear alternative tribometer equipped with a gas blowing system. After annealing and tribological testing, the morphology, structure and chemistry of the worn materials have been analyzed using electron microscopy and surface analysis techniques.*

# Table of contents: Chapter 2. Experimental approach

# 1. Material of interest

## 1.1. As received a-C:H:Si:O

The Diamond-Like Carbon (DLC) coating investigated here is a silicon oxide-doped amorphous hydrogenated carbon (a-C:H:Si:O) coating. The films were deposited on silicon (100) wafers by Sulzer-Metco Inc. (Winterthur, Switzerland, now Oerlikon Metco) using a proprietary plasma-enhanced chemical vapor deposition (PECVD) process, whose details are described in the literature[8,9,96,102]. Briefly, a plasma discharge is formed from a siloxane precursor by means of a hot filament, whose temperature ranged between 2073 and 2273 K. In order to favor interactions between the plasma and the surfaces to coat, thus promoting the deposition, a negative radio frequency (RF) bias voltage between -300 and -500 V is applied to the substrates. Although the substrate temperature is not deliberately increased during the deposition process, it may locally increase due to ion impingement on the surface; the temperature rise is expected to be no more than 200 K above room temperature. The typical deposition rate for a-C:H:Si:O films ranges between 0.5 and 1.5 μm/h[103]. The residual stresses in a-C:H:Si:O films are compressive and usually in the range of 200 to 300 MPa[104]. The thickness, topography, mechanical properties, chemical and structural analysis of the coating have been analyzed and details of the results will be presented in the next chapter.

## 1.2. Annealing induced structural changes of the a-C:H:Si:O

To investigate the structural evolution of a-C:H:Si:O upon annealing in vacuum, heating experiments were performed inside an XPS chamber. Details of the XPS will be given in section 2.3.8. The samples (6 x 6 $mm^2$) were mounted in a holder (RHK Technology, Inc., Troy, MI, USA) that included a tungsten filament for radiative heating and a K-type thermocouple in contact with the sample for recording specimen temperature.

The films were annealed at 150°C, 250°C, 350°C and 450°C for one hour under UHV and cooled after each annealing (heating and cooling rate: 10°C/min).

# 2. Tribological approach

## 2.1. Measuring the tribological response of two materials in contact

When two solids in contact slide against each other, the coefficient of friction between them is defined as the ratio of the tangential force and the normal force. The device that is used to measure this coefficient is called a tribometer. The friction coefficient is not an intrinsic parameter of the materials in contact, but it strongly depends on contact conditions, such as stress, motion and environmental conditions[105] (vacuum or ambient air, relative humidity, temperature) and it usually evolves with sliding cycles. Studying the tribological behavior of two bodies in contact can be of technological interest for a variety of applications including energy savings and decrease of $CO_2$ emissions for car engine[2] optimization of biomedical prostheses[106], etc…or for fundamental insights such as understanding the action mechanisms of antiwear additives[107] or probing the kinetics of fullerene nanoparticle friction[108,109].

Depending on the targeted application, the following contact parameters could be totally different thus determining the type of tribometer that can be used[110]:

- *The contact geometry: point contact (pin-on-disk, ball on flat or ball and inner ring configuration), line contact (cylinder on plane or cylinder on cylinder configuration), areal contact (plane on plane)…*
- *The type of motion: sliding, rolling, spin, impact or a combination of these with a sequence of motions that can be back and forth, unidirectional or intermittent.*
- *Velocities*
- *Load and loading time*
- *Temperature*

Appropriate tribometers can be chosen to best simulate the technologically-relevant operating parameters. In the following, we will focus on two of the most commonly used tribometers in academic laboratories, namely, rotating pin-on-disk and linear reciprocating pin-on-flat tribometers.

### 2.1.1. Rotating pin-on-disk tribometer

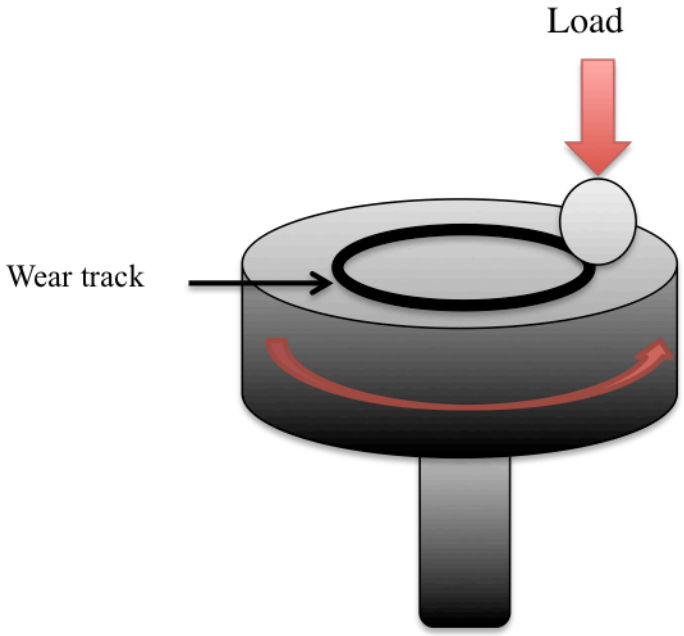


***Figure 2.1. Schematic of a rotating pin-on-disk tribometer***

In this type of system, as illustrated in Figure 2.1 a motor induces a rotation of the disk, while the pin does not move (or vice versa). This leads to a relative motion between the pin and the disk. The friction is measured through a tangential force sensor. The total motion of the pin in one cycle is thus: $2\pi R$ (where R is the radius of the wear stroke).

A primary advantage of the pin-on-disk system is that the velocity of the pin is constant, allowing an equivalent exposure time to the environment for all the points along the wear track on the disk[105]. In terms of friction and wear mechanism, the sliding direction being the same, any eventual wear debris is likely to be pushed outside the contact when we are in rotating disk configuration[111].

There are several disadvantages to using a pin-on-disk tribometer, including a misalignment of the disk during the motion that could induce a displacement of the contact point on the ball. Due to the radius of the wear track, a larger specimen is required with a very limited number of tracks. Changing the radius of the track's trajectory can result in varying the sliding speed.

### 2.1.2. Linear reciprocating pin-on-flat tribometer

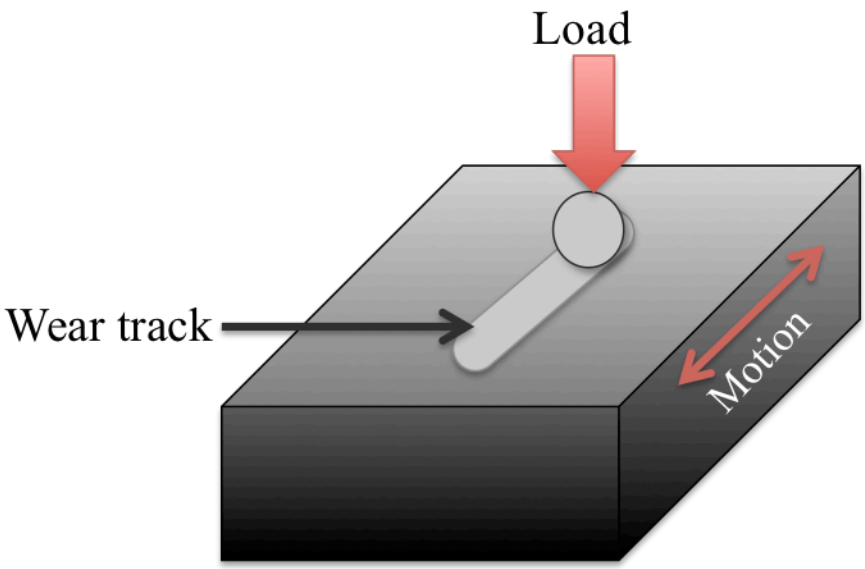


***Figure 2.2. Schematic of a linear reciprocating pin-on-flat tribometer***

In the pin-on-flat configuration as illustrated in Figure 2.2, a motor induces a motion of the flat while the pin is kept stationary. The total travel of the pin in one cycle is thus: 2L (where L is the length of the wear stroke).

In this configuration, the amplitude and frequency of the reciprocation can be varied as desired and the friction force must be measured in both sliding directions. Unlike the pin-on-disk configuration, the sliding pin – or ball – stops at the ending points of the wear track. When changing the sliding direction, the tangential force applied by the actuator will increase progressively, first leading to an overall strain of the tribometer due to its finite stiffness and static friction of the contact, until full sliding occurs inside the contact. These ending points can thus be used for calculating the static coefficient of friction, while the average kinetic coefficient of friction is calculated only in the center of the track length. Another consequence of the variation of the sliding speed in the reciprocating configuration in opposition to the pin-on-disk is that leading edge wear debris can be shed at the end of the contact whereas in rotating tribometry, leading edge wear debris builds up continuously until it is shed out the sides of the contact, and this could lead to a different wear mechanism for the same tribopairs depending on the type of tribometer that is used.

### 2.1.3. Partial conclusion

For a given radius of the wear stroke in pin-on-disk configuration (R) equal to the length of the wear stroke in pin-on-flat configuration and an equal number of sliding cycles, the travel of the ball is larger in the pin-on-disk configuration than in pin-on-flat configuration. Thus, the linear reciprocating pin-on-flat tribometer offers more severe tribological conditions for the flat than in the rotating one. This allows reducing the number of sliding cycles required to obtain equivalent structural changes in the material, that might have occurred upon sliding during a higher number of cycles in the rotating pin-on-disk configuration.

In summary, the followings are the main advantages of linear reciprocating tribometer relative to the pin-on-disk method:

a) *The more severe tribological conditions for the flat specimen allow a shorter duration of the friction test for obtaining similar stress-induced structural changes in the material.*
b) *It is possible to generate a larger number of different wear tracks with the same kinematics on the same sample, thus allowing more efficient post-processing and analysis of the wear tracks.*
c) *Pin-on-flat tribometers, since their stroke lengths can be reduced to very small values, can be built compactly, which allows their introduction to confined chambers. The small linear amplitude of the stroke also allows a homogeneous exposure of the wear track to any gas flow system.*

These reasons motivated our decision to utilize the linear reciprocating configuration as our primary tribological investigation tool in this thesis. In the next section, the two linear tribometers that have been used are described: an ambient air operating tribometer, equipped with a gas blowing system, and a tribometer placed inside a vacuum chamber, allowing careful control of the sliding environment.

## 2.2. Ambient air tribometer with gas blowing system

### 2.2.1. Tribometer Design

The linear reciprocating tribometer that we used operates in ambient air and is in the ball-on-flat configuration (Figure 2.3). The flat is mounted on a linear reciprocating arm, connected to an electrodynamic actuator that induces the motion in the X direction. The ball is first mounted in a ball holder, which is then mounted on a horizontal arm through which the

normal load is applied and the tangential force is measured. This ball holder allows easier handling of the ball, especially for analyses of the wear scar.

The horizontal arm holding the ball consists of two stages: a stage with an assembly of dual leaf springs providing low stiffness in the Z direction, while preserving high stiffness in the X and Y direction, and a stage separating the arm from the tribometer's frame by a piezoelectric force transducer, allowing the measurement of the tangential force. This arm is connected to the frame through a Y-Z micrometer stage, the Y direction allowing a precise positioning of the parallel wear tracks, the Z direction allows for bringing the ball into contact. Once the position of the track is chosen, the normal load is applied with a dead weight, placed on top of the ball holder.

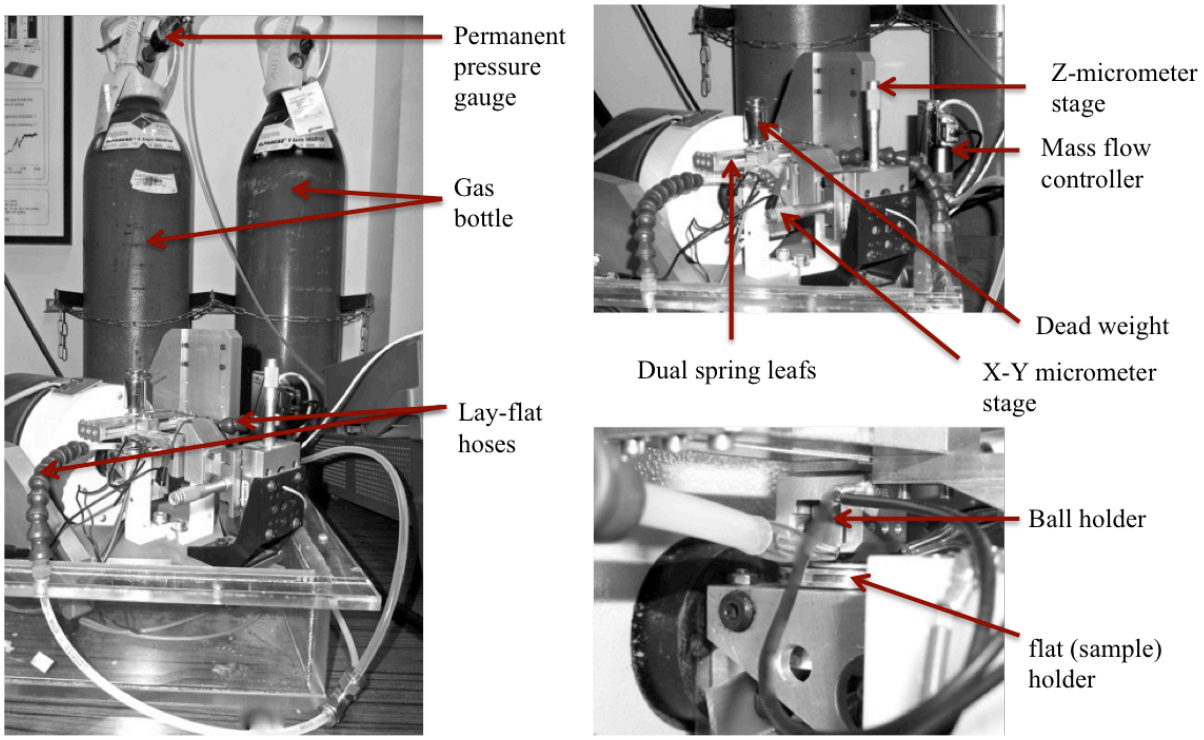


***Figure 2.3. Detailed description of the ambient air linear reciprocating tribometer with the gas flow equipment***

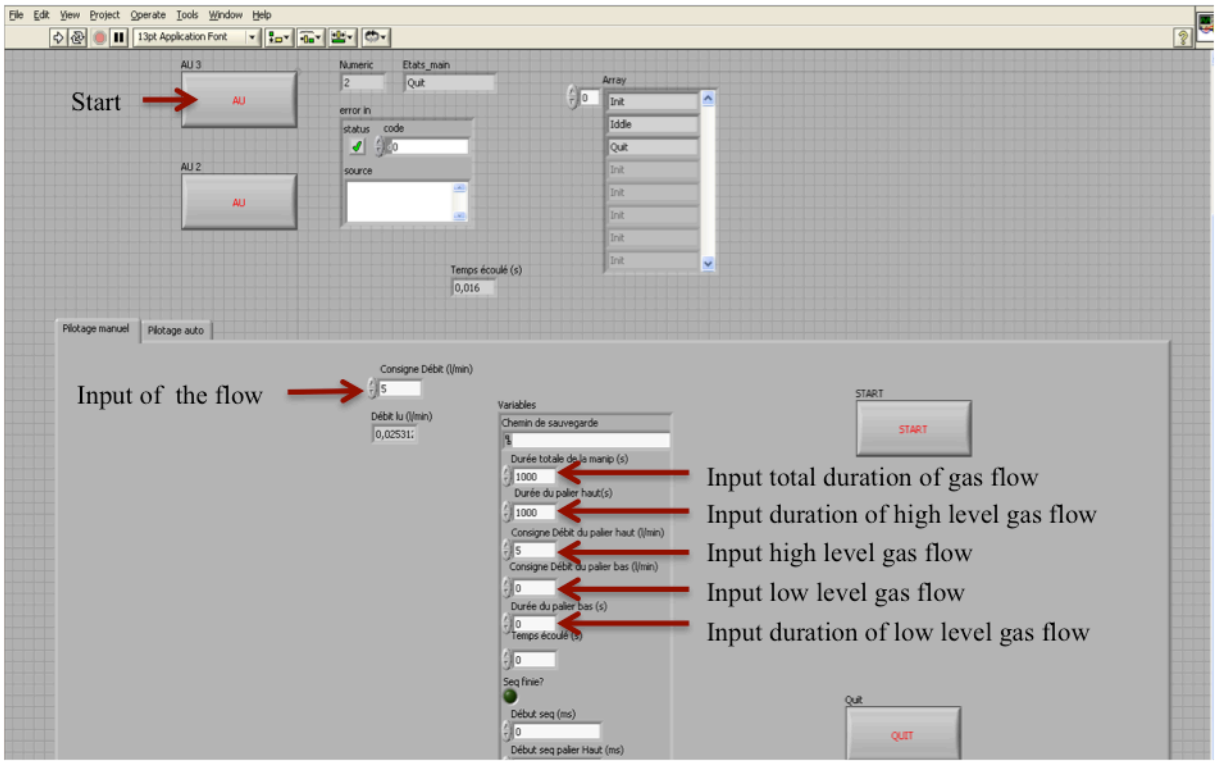


***Figure 2.4. Interface of the Labview software developed to control the mass flow controller***

In order to evaluate the influence of the sliding environment on the tribological behavior of our tribopairs, we equipped the tribometer with a gas blowing system that allows a precise control of a gas flow, oriented toward the contact.

The gas is blown through two lay-flat hoses connected to the output port of a mass flow regulator (Bronkhost El-Flow F-201CV, Bronkhost hight-Tech B.V, Neederlands,). The input port of the regulator is connected to the gas bottle through a permanent pressure gauge. Details of the tribometer's layout and the gas blowing system are given in Figure 2.3

We also developed a LabVIEW (National Instruments Corporation, Austin, USA) code to communicate with the mass flow controller in order to be able to precisely adjust the flow of gas blown toward the contact. The software offers several options, namely, we can either run the tribological test under a constant gas flow or alternate between a high and low level of gas flow with adjustable duration, as shown in Figure 2.4. This allows a rapid change in the environment for a precise duration.

The mass flow regulator controller was factory calibrated for dry argon and can deliver gas flows ranging from 0,1 l/min to 5 l/min. For the results shown in the following chapters, different gases (dry nitrogen, dry air and dry argon) have been successively blown toward the contact at 5 l/min in order to quickly induce changes in the sliding environment. One must

notice that due to the calibration with dry argon, the effective nitrogen and dry air flow was evaluated at 4.2 l/min.

In order to ensure that the gas flow was not affecting the tribological experiment, especially by decreasing the applied load through lifting effect, we used the electrical contact resistance measurement system of the tribometer. The electrical contact resistance is calculated from the measurement of the bias voltage between the ball holder and the flat holder while applying a small current through the interface (approximately 3 mA), as described by Belin *et al*[112]. While varying the gas flow up to 5 l/min, no measurable change of the electrical contact resistance of a self-mated bronze contact, in linear reciprocating motion could be measured, indicating that the contact area and thus the normal load was not affected.

### 2.2.2. Experimental conditions

The tribological experiments were performed by sliding a 52100 stainless steel ball with a diameter of 6 mm against a flat silicon wafer specimen coated with an a-C:H:Si:O thin film, as described in section 2.1. The steel ball was ultra-sonically cleaned for 5 minutes successively in acetone and isopropanol. The a-C:H:Si:O specimen was also ultra-sonically cleaned in isopropanol and then glued with cyanoacrilate ("super glue") on top of a flat steel sample holder.

Both specimens are systematically observed with a digital microscope (Keyence, VHX-1000 series, Keyence digital microscope and imaging solution, OSAKA, JAPAN) in order to check their cleanliness before being mounted on the tribometer.

The constant-load friction tests were carried out while applying a dead weight of 1 N, corresponding to a maximum Hertzian contact stress of approximately 570 MPa and an apparent contact diameter of 60 µm. The sliding speed and stroke length were respectively 3 mm/s and 3 mm. Load dependence friction test have also been performed using 2 N and 5 N dead weights. Table 1 summarizes the different loads and corresponding contact pressure and contact area.

| *Load [N]* | *Maximum Hertzian contact pressure [MPa]* | *Mean Hertzian contact pressure [MPa]* | *Apparent contact diameter [µm]* |
|---|---|---|---|
| *1* | *570* | *380* | *60* |
| *2* | *715* | *480* | *70* |
| *5* | *970* | *650* | *100* |

***Table 2.1. Applied load with the corresponding Hertzian contact pressure and corresponding apparent contact diameter***

The relative humidity (RH) and the room temperature were collected at the beginning of each experiment with a hygrometer (Testo 645, Testo, Germany) with a measurement range of -20°C to 80°C and 2% to 100% RH and a resolution of ±1°C and 1% respectively for temperature and relative humidity.

Three types of tribological experiments were performed:

- *Ambient air tests at room temperature and constant relative humidity;*
- *Constant gas flow tests, with a 5 l/min flow of dry nitrogen, dry air or dry argon, leading to a measured relative humidity lower than 5% RH near the contact, at room temperature;*
- *Alternating tests with gas flow switching on and off after defined durations.*

After the experiments, the friction coefficient was determined for each cycle as an average between back and forth motion by considering only data from 1/15 to 14/15 of the stroke. In the manuscript, the friction coefficient at a given cycle will be reported as its average value ± the standard deviation. All experiments were repeated at list four times in order to check the reproducibility of the results.

## 2.3. Controlled-Environment Analytical Tribometer

### 2.3.1. Tribometer set-up

The Controlled-Environment Analytical Tribometer (CEAT) is a unique device located at LTDS. It has been designed for performing tribological experiments under high vacuum or under a precisely controlled environment, hence its name.

The CEAT consists of a linear reciprocating pin-on-flat tribometer placed inside a high vacuum (HV) chamber, which allows introduction of gases at controlled pressures up to 2 bars. The device has been extensively described previously[46,69,70,113–115]. As shown in figure 2.5, the tribometer chamber (in green) is coupled with a sample preparation chamber (in brown) and a X-ray Photoelectron Spectroscopy chamber (XPS, in blue).

In the tribometer chamber, the flat sample holder is mounted on a force measurement stage, while the hemispherical pin, placed inside a pin holder, is mounted on an actuating horizontal shaft. This shaft is connected to a XYZ micrometer feedthrough, with X and Z-axis motorized. The load is applied through the Z-axis while linear reciprocated motion is provided by the X-axis. The normal and tangential forces are measured with a dual stage displacement-based force sensor, placed between the flat sample holder and the frame of the tribometer. The stage for the normal force consists in two parallel thin metallic annular plates

with several slots, providing a vertical compliance. The sample holder is attached to the internal side of the annuli. The stage for the tangential force consists in four parallel beams with two width's reductions on each, thus combining a large vertical stiffness with a good lateral compliance. Both vertical and lateral displacements are measured with optical sensors. The force-displacement relations are calibrated by using dead weights applied directly on the sensor for the normal force and using a pulley for the tangential force.

The tribometer is computer-controlled through a customized LabVIEW (National Instruments Corporation, Austin, USA) user interface. This software controls the X and Z axis motions for applying the load and provide the motion, and monitors the tangential and normal force.

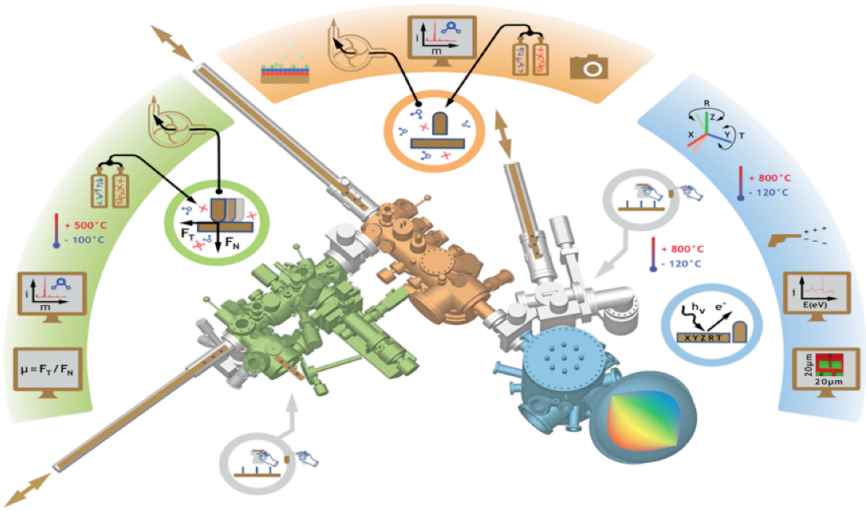


***Figure 2.5. Description of the Controlled Environment Analytical tribometer (green) equipped with a gas adsorption system (brown) and an XPS (blue). The tribometer is equipped with a mass spectrometer and a gas admission system. The sample holder's temperature can vary from -100°C up to 500°C.***

A time-averaging data-reduction method is applied for processing the friction coefficient data by averaging the data acquired during one sliding cycle. To avoid end-point effects, only the data corresponding to a slider position between 1/8 and 7/8 of the stroke length were considered for each cycle. The standard deviation of the values acquired during a cycle is also evaluated.

Introduction of different gases into the tribometer chamber is achieved through a leak valve, while the tribometer chamber can be isolated from the sample introduction chamber, equipped with a turbomolecular pump, thanks to a butterfly valve. The base pressure in the chamber is lower than $10^{-7}$ mbar. A Baratron gauge monitors the gas pressure in the chamber,

while a mass spectrometer (Transpector 2 Gas Analysis System, Inficon, NY, USA) installed in the sample introduction chamber monitors the gas purity in the tribometer chamber by taking samples of gases thanks to a leak valve placed between the two chambers.

#### 2.3.2. Experimental conditions

Tribological tests were performed at room temperature using 52100 steel pins with a radius of curvature of 8 mm, against polished silicon wafer specimens coated with the a-C:H:Si:O film. Before each experiment, the pins were mechanically polished leading to a root-mean square roughness lower than 30 nm (measured by white light interferometry) and then ultra-sonically cleaned successively in acetone and isopropanol during 5 minutes each. Experiments were run under an applied load of 3 N over a track length of 2 mm at a sliding speed of 2 mm/s. The contact conditions correspond to an initial maximum Hertzian contact stress of 430 MPa and an apparent contact diameter of 120 µm. At least three independent tribological tests were performed for each environmental condition to check reproducibility.

Oxygen and hydrogen gas used in this work were provided by Air Liquide (Air Liquide Creative Oxygen, France). The bottles (ALPHAGAZ 2) were limited to the following impurity levels ($H_2O$ < 0.5 ppm, $O_2$ < 0.1 ppm, $CO_2$ < 0.1 ppm, CO < 0.1 ppm, $C_nH_m$ < 0.1 ppm, $H_2$ < 0.1 ppm).

Water vapor was also introduced to the chamber, following a two-step process. First, deionized water was placed inside a hermetically sealed steel tube and connected to the vacuum chamber via a leak valve. Liquid nitrogen was used to freeze the water contained in the tube. It was then possible to pump down the tube to remove remaining gases. In a second step, the frozen water was heated and leaked into the vacuum chamber, in order to obtain the desired water vapor pressure in the tribometer chamber.

# 3. Characterization techniques

## 3.1. Surface observation, topography and mechanics

#### 3.1.1. Digital optical microscopy and scanning electron microscopy

A digital microscope (Keyence, VHX-1000 series, Keyence digital microscope and imaging solution, OSAKA, JAPAN) was used in order to check the cleanliness of the tribopairs and observe the wear tracks on the ball and the flat.

Two scanning electrons microscopes have been used: a JEOL 7500F (JEOL, USA) and an ESEM-FEG XL 30 (ESEM-FEG XL30, FEI-Philips, UK), providing a 2 nm resolution at

30 kV. These two systems are particularly useful for soft-matter studies. The JEOL 7500F is located in the Singh Center for Nanotechnology at the University of Pennsylvania and the ESEM-FEG, at the Centre Lyonnais de Microscopie (CLYM). Through a stage biasing system, referred to as the "gentle-beam" mode, the electron beam interacting with the sample may be reduced to a fraction of the accelerating voltage of the gun (down to 200 V), allowing for the imaging of soft or insulating samples without the need for carbon or metal coating. Good resolution SEM images have thus been take at low accelerating voltage (3 kV) while EDX analyses were carried out using an acceleration voltage of 8 kV, the minimum energy required to probe K$\alpha$ electrons of the silicon.

### 3.1.2. White light Interferometry

Figure 2.6 shows the schematic of an optical interferometer. Light incident from a laser source is split using a beam splitter into two separate beams: the reference and the object beams. The reference beam is reflected back to the beam splitter by a reference mirror at a constant distance $l_r$, while the object beam is also reflected back by the sample's surface on the beam splitter, but at a variable distance $l_o$. The reflected beams thus create an interference pattern on the detector (usually a CCD camera), which provide information about the surface topography with very accurate vertical resolution.

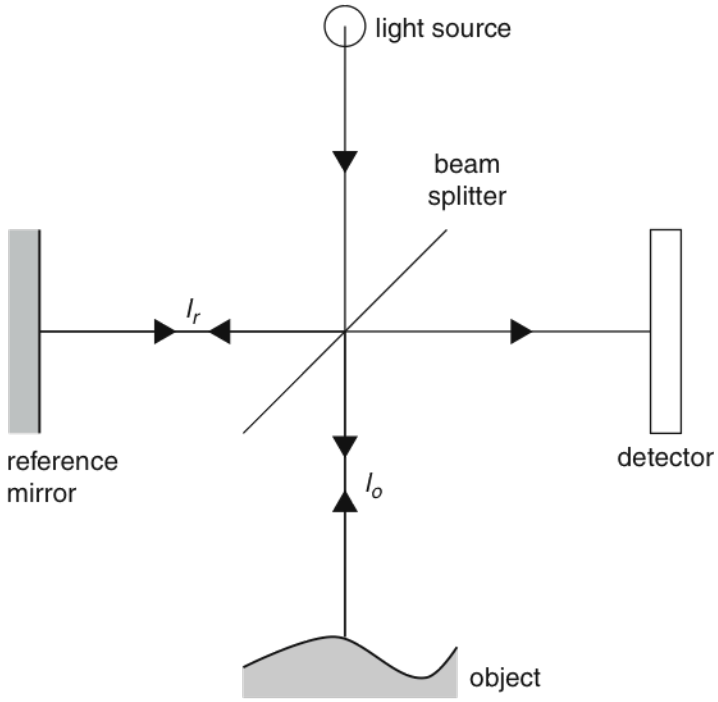


***Figure 2.6. Schematic of an optical white light interferometer: the beam emitted by the light source is divided in reference and objective beams by the beam splitter. The reflections of both beams are superposed on the detector where interference occurs. From Wiora et al.[116]***

This method allows a quick yet precise measurement of the surface topography. In particular, the very accurate Z resolution (< 1 nm) provides a detailed measurement of a wear track's depth. A significant advantage of optical interferometry is that it is a non-contact measurement, which will not affect the surface's topography or chemistry.

Interferometry measurements were carried out on a Bruker interferometer GT-K1 (Bruker Nano Surface Division, USA) equipped with two light sources (green and white) and two lenses (X5 and X50). The software of the device (Vision 64) allows selecting the Z-resolution of the measurement and the output format of the data.

Measurements were carried out using a vertical scanning interferometer mode with a Z-resolution of 0.5 nm. The white light was focused on the sample surface using the X5 lens and a numerical zoom of X2.

Quantifying the wear volume on a wear track was performed by sampling the wear track in 5 regions, then averaging the values. The first operation was to mask the wear track and then plane fit the data, excluding the masked wear track region, This resulted in all areas

outside of the wear track being centered near "zero height". The volume and depth of the wear track could then be easily determined by integrating or subtracting from this reference "zero" height. This operation is believed to be sufficiently accurate thanks to the low surface roughness of our samples (typically 1.2±0.1 nm rms over an area of 5 µ*5 µm)…After the plane fit, a depth profile can be taken across the wear track, allowing the computation of the wear depth or the worn volume.

### 3.1.2. Atomic force microscopy

#### *3.1.2.1. Brief description of the technique*

Atomic force microscopy (AFM) is a method of measuring the topography of a surface via the interactions between an atomically sharp tip and a surface, thus overcoming the diffraction limit of optical and electron microscopes and allowing for the observation of a surface in three-dimensional detail with sub-nanometer resolution. AFM can be used to image different types of materials (hard, soft, biological structures…) without any conductivity requirements unlike SEM[117].

Figure 2.7 shows the schematic of the interactions of a tip with a surface in AFM. There is an abundant literature on AFM topography measurements[117–119]. In brief, the apparatus is made of a sharp tip attached to a flexible microcantilever, which bends under the influence of interaction forces between the tip and the sample. The bending of the cantilever is measured by reflecting a laser beam on the cantilever and onto a photodiode split in four quadrant, which measures the position of the laser spot. The vertical movement of the laser spot, or the tip , (A+B) – (C+D) (Figure 2.7) provides information on the height of the surface (topography measurement)[117].

#### *3.1.2.2. Experimental details*

Two AFM have been used for our studies. The surface topography of the as-received material was measured using an Asylum Research MFP-3D AFM (Asylum Research, Santa Barbara, USA) located at the University of Pennsylvania. Measurements have been carried out using a Nanosensor Si cantilever with a normal spring constant of 0.06±0.01 $N.m^{-1}$ and a DLC coated tip. A normal load of 1.1±0.1 nN was applied while scanning an area ranging from 5 x 5 $\mu m^2$ down to 100 x 100 $nm^2$ with a resolution of 256 lines.

After tribological experiments, some wear tracks have been characterized using a Veeco V AFM (Veeco Instruments Inc., NY, USA) located at LTDS. Measurements were carried out with a diamond tip (Arrow-CONTR10) with a normal stiffness of 0.2 $N.m^{-1}$. A normal load of 10 nN was applied while scanning an area of 80 x 80 µm centered on the wear tracks with a resolution of 512 lines.

All observations were performed in ambient air at room temperature. Data processing was performed using Gwyddion (Czech Metrology Institute, Czech Republic).

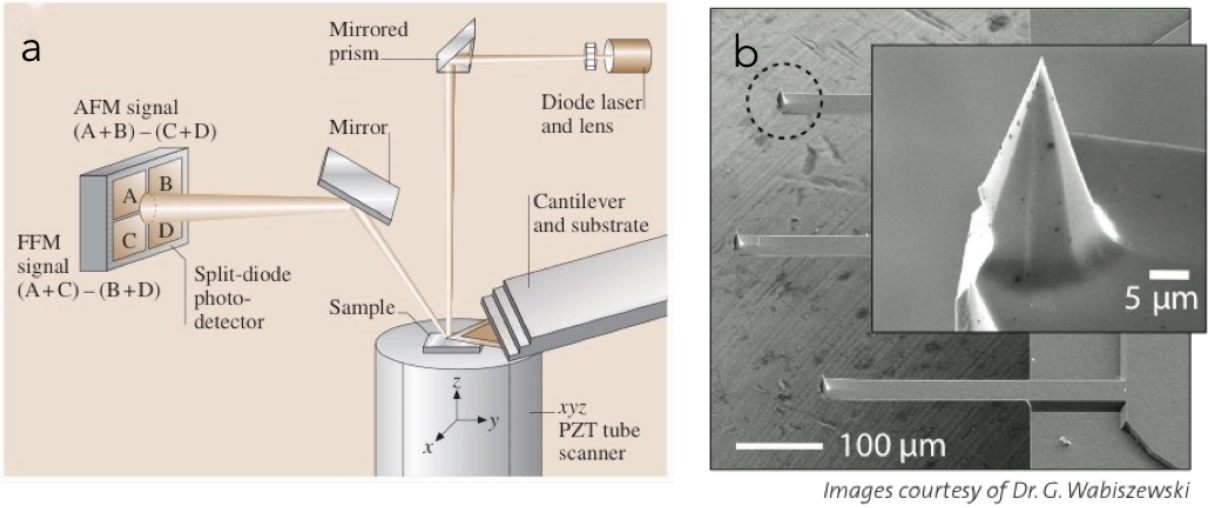


***Figure 2.7. Schematic of the basic principle of AFM and Friction Force Microscopy (FFM) (a) from Bhushan et al.[120](b) typical AFM tip on its cantilever.***

### 3.1.3. Friction force microscopy (FFM)

#### *3.1.3.1. Brief description of the technique*

This technique is derived from AFM and is used to measure lateral force (i.e. friction force) while sliding an AFM tip against a surface thus allowing tribological studies at the nanoscale. In order to do so, the sample is scanned back and forth in a direction orthogonal to the long axis of the cantilever beam[120] and the friction force between the tip and sample produces a twisting of the cantilever as described in the previous section for AFM. Therefore, there is an intensity difference between the laser signal received by the left hand (A+C) and the right hand (B+D) sectors of the photodiode as illustrated on Figure 2.7.a. This intensity difference is directly proportional to the magnitude of the friction force for small strains of the cantilever. One major advantage of this technique consists of measuring friction, adhesion and wear in one measurement. Since the friction data is directly related to the mechanical

properties (normal and lateral spring constant) of the cantilever, for reliable friction data measurements the tip must be carefully calibrated[121–123] .

### *3.1.3.2. Experimental details*

FFM was used to estimate the microscale tribological behavior of a-C:H:Si:O coatings while sliding against steel under dry and humid conditions. To that end, we used an environment controlled scanning probe microscope (RHK 350, RHK Technology, Michigan, USA) as illustrated in Figure 2.8 located at university of Pennsylvania. Experiments have been performed in humid (~ 50% RH) and dry (~ 1%) environment. Humid conditions were obtained by blowing humid nitrogen into the chamber while dry environment was obtained by introducing dry nitrogen to the chamber.

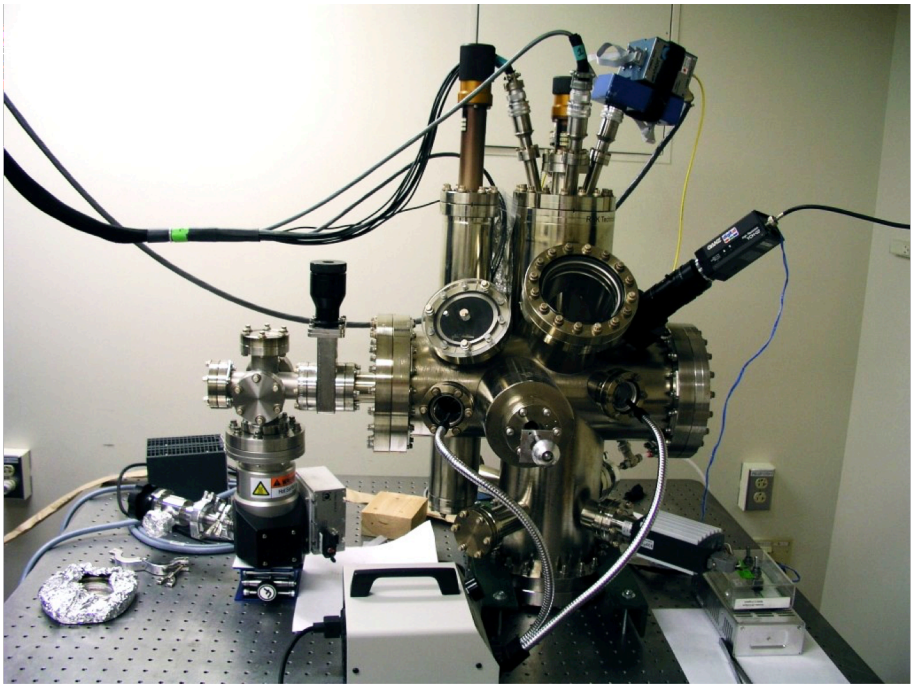

***Figure 2.8. RHK 350 Scanning probe microscope from Carpick Research Group carpick.seas.epenn.edu***

Since our interest resides in understanding the interactions between a-C:H:Si:O and steel at microscale and due to the lack of commercially available steel-tipped AFM probes, we used a customized AFM probe made of a steel colloid glued with a conductive epoxy silver glue (MG Chemicals, USA) onto a commercial tipless AFM cantilever using a micro-manipulator. Prior to the gluing process, the tipless cantilevers were calibrated (normal and lateral stiffness) using beam geometry[124]. Once the customized cantilever is ready for use, the roughness of the colloid is measured by scanning them with a standard sharp AFM tip.

Experiments have been performed using a 25±5 µm diameter colloid, an applied load of 1000 nN while scanning back and forth a 5 µm line (sliding stroke).

### 3.1.4. Nanoindentation

Measuring the mechanical properties of thin films or of volumes close to the surface cannot be performed accurately with conventional indentation tools. Indeed, the mechanical properties of materials in locally small regions and very close to the surface can be very different from that of the bulk material average having the same composition[125]. Nanoindentation is a method for measuring the mechanical properties down to the nanoscale range[125,126], which makes it very useful for probing thin films. Its technique consists of penetrating the sample with a stiff tip – usually diamond – and measuring the resulting interactions.

The following equations allow the determination of hardness $H$ and elastic modulus $E^*$ from the measurements performed in nanoindentation:

$$\boldsymbol{H = \frac{P}{A_c}} \qquad \textit{Eq 2. 1}$$

And

$$\boldsymbol{E_c^* = \frac{S}{2}\sqrt{\frac{\pi}{A_c}}} \qquad \textit{Eq 2. 2}$$

where $P$ is the applied load, $S$ the contact stiffness and $A_c$ the contact area.

Since the Pyramidal indenter with square or triangular base, are not axis symmetrical, it has been shown that equation 2 has to be corrected by a factor β (β=1.012 for Vickers tips and β=1.034 for Berkovich tips)[127]

Precise measurement of the applied load, the contact area and the contact stiffness is crucial for an accurate determination of the mechanical properties. In the next subsections we will describe the method that has been used to calculate the contact area and contact stiffness.

#### *3.1.4.1. Estimation of the contact area*

The contact area is related to the penetration depth but cannot be directly estimated, mainly because of the shape of the indent and the tip defect… We used Loubet's method, extensively detailed in reference[126,128] to estimate the contact area.

#### *3.1.4.2. Estimation of the contact stiffness*

There are two existing ways to calculate the contact stiffness; a static method and the continuous stiffness measurement method as detailed in the supplementary information.

For thin coating on substrate configuration, there are challenges in measuring the film's stiffness mainly because of the substrate effect. One main existing method that is used to get rid of the influence of the substrate is to limit the indentation depth typically to values 10 times lower than the thickness of the coating. It has been shown in the literature that even at this low penetration depth, the substrate effect can still influence the measurements[129,130]. There are several methods proposed to get rid of the substrate effect while indenting a thin film deposit on a substrate[131]. The one we used has been proposed by Bec *et al*[130] for a good estimation of the film stiffness and will be described in the next section.

#### *3.1.4.3. Determination of the contact stiffness using Bec et al method*

This new method consists of considering the substrate and the film as two springs connected in series as illustrated in Figure 2.9[130].

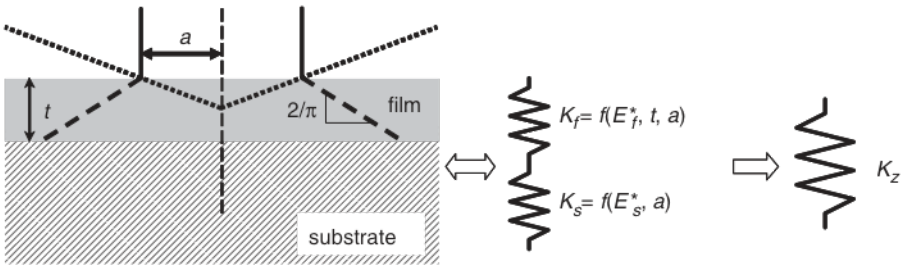


***Figure 2.9. Schematic of the spring model of substrate and coating proposed by Bec et al[130]. A is the tip radius, $E_f$*and $E_s$* the reduced young's modulus of the film coating and substrate respectively and t, the thickness of the coating.***

The global contact stiffness can thus be deduced as follows:

$$\frac{1}{K_z} = \frac{1}{1+\frac{2t}{\pi a}}\left(\frac{t}{\pi a^2 E_f^*} + \frac{1}{2aE_s^*}\right) \qquad \textbf{Eq 2. 3}$$

with $t$, the thickness of the coating, a, the radius of the indent, $E_f$*, and $E_s$* the reduced Young's modulus of the film and substrate respectively.

#### *3.1.4.4. Experimental details*

Nanoindentation test were performed using a MTS Nano Indenter XP following the continuous stiffness measurement (CSM) method described previously while using a Berkovich tip. During the test, the load was applied exponentially versus time, in order to keep a constant strain rate throughout indentation. P′/P was set at 0.03 Hz. Experiments were performed in ambient air, at room temperature. The reported values of the mechanical properties are an average of 9 different measurements at different locations (we were able to check the location of each indent on the surface, thanks to an integrated optical microscope). For each test the maximum applied load was 450 mN.

## 3.2. Chemical and structural analysis of a-C:H:Si:O

In order to understand the tribological behavior of the a-C:H:Si:O coatings, we need to understand the structural and chemical changes involved during sliding, both on the flat and on the ball surfaces. These materials are amorphous metastable thin films made of low atomic weight elements. It is thus necessary to cross-correlate the results of several techniques to obtain stronger insight into the structure and chemistry of our material, before and after the tribological experiments.

### 3.2.1. Raman spectroscopy

Raman spectroscopy consists of measuring the intensity of inelastically scattered light by a material as a function of the wavelength. Shifts in the wavelength of the scattered light occur due to interactions of the incident light with the material's vibrational modes[132]. Raman scattering occurs when a lattice vibrational mode causes a deformation in the electron cloud, thus affecting the polarizability (ability for a molecule to produce a dipole moment when exposed to an electromagnetic wave). The polarizability changes as the molecular bonds are altered by their vibrational motion.

#### *3.2.1.1. Single wavelength Raman*

Raman scattering from $sp^2$ hybridized carbon bonds is always a resonant process due to the relatively small optical gap of the π states from the conduction and valence band edges[132]. Raman can be a powerful non-destructive tool to investigate the structure of carbon-based materials. There are two characteristic peaks on Raman spectra of carbon-based materials using visible wavelength light: the G peak and the D peak located at around ~1560 $cm^{-1}$ and ~ 1360 $cm^{-1}$ respectively[87,133–137].

Visible Raman excitation are dominated by $sp^2$ bonded carbon atoms since the Raman cross-section of π states is more than fifty times higher than that of σ states[138]. The G peak is due to bond stretching of all pairs of $sp^2$ atoms in both rings and chains while the D peak is due to the breathing modes of $sp^2$ ring-like atoms[139].

Much information can be extracted from the position of the G and D peak. In fact, Ferrari *et al*[139] have shown that the variation in G peak position correlates with the disorder in the carbon amorphous network. An increasing G peak position is thus a consequence of short C=C bonded chains[139]. This means that the shift of the G peak position (Pos G) is proportional to the degree of disorder in the material. Pos G is due to a resonant selection of the $sp^2$ clusters with wider π band gaps. The ratio between the intensity of the D peak and the G peak gives information on the number of ordered $sp^2$ carbon rings in the material[133,139,140].

As illustrated in Figure 2.10, it is believed that an increasing ratio I(D)/I(G) together with a shift of the G peak toward higher wavenumbers can be understood as an increase of the number of clusters of ring-like $sp^2$ bonded carbon atoms.. Thus, a careful analysis of the position and intensity of the D and G peaks may provide information about the structural changes occurring during a tribological experiment on amorphous carbon coatings.

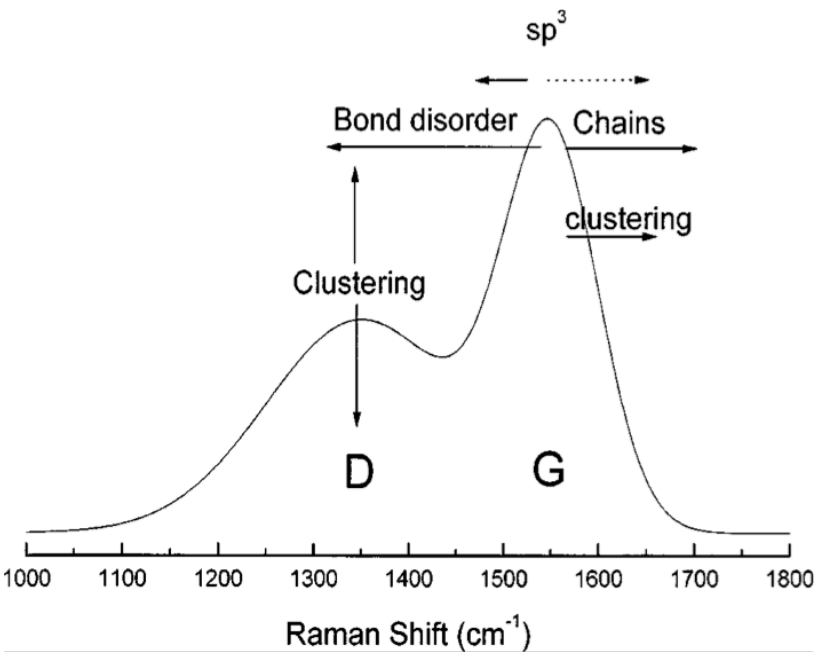


***Figure 2.10. Schematic diagram of structural changes affecting a Raman spectrum for carbon-based material. From Ferrari et al.[133]***

### *3.2.1.2. Multiwavelength (MW) Raman*

As mentioned in the section above, I(D)/I(G) measurements give us the amount of a specific size of $sp^2$ clusters for a given Raman wavelength, *i.e.* the ones where local band gaps are resonant with visible wavelengths as reported by several authors[133,137,138,140–142]. Therefore, each laser wavelength resonantly select a specific range of $sp^2$ clusters of a finite distribution of similar sizes and shapes[138]. High Raman excitation energies (lower wavelengths) could be used to probe smaller clusters since they are more resonant with UV excitations.

This means that I(D)/I(G) alone is not sufficient to probe the $sp^2$ fraction in the sample. Therefore, using multiwavelength Raman, it can be considered that the total distribution of the $sp^2$ clusters in the volume of a-C:H:Si:O probed by Raman is determined[138].

With a careful processing of the Multiwavelength Raman, one can thus deduce the remaining $sp^3$ bonded carbon fraction in the coating. Cui *et al*[142] proposed an empirical model to extract the $sp^3$ fraction by calculating the dispersion of the G peak, Disp (G), as a function of the excitation energy (Raman wavelength). The dispersion of the G peak is defined as follows[11]:

$$\boldsymbol{Disp(G)} = \left|\frac{\boldsymbol{Pos(G)\lambda_2 - Pos(G)\lambda_1}}{\boldsymbol{\lambda_2 - \lambda_1}}\right| \qquad \textbf{\textit{Eq 2. 4}}$$

with $\lambda_1$ *and* $\lambda_2$ two different Raman wavelengths and $Pos(G)\lambda_1$, $Pos(G)\lambda_2$ the corresponding positions of the G peak.

***3.2.1.3. Experimental conditions***

Two Raman devices have been used for characterizing the as-received and worn a-C:H:Si:O coatings. A single wavelength apparatus located at the University of Pennsylvania and a multiwavelength apparatus located at the "Laboratoire Hubert Curien" of Université Jean Monnet (Saint Etienne).

The single wavelength Raman is a near-field scanning Raman spectrometer (NT-MDT NTGRA™ Spectra Upright, NT-MDT Co., Moscow, Russia). A continuous wave diode-pumped solid-state laser (Compass 315M-100, Coherent Inc., Santa Clara, CA, USA) provides linearly polarized (transverse electromagnetic mode: $TEM_{00}$) light with wavelength and power of 532 nm and 22 mW, respectively. The laser output enters the spectrometer through a single-mode optical fiber. After being expanded, the laser beam is focused by a long-working-distance objective (magnification: 100X, numerical aperture: 0.7, Mutotuyo, Kanagawa, Japan) on the sample surface. Light scattered from the sample is collected by the same optics and directed into the grating of the Raman spectrometer. The point of analysis can be defined using a white-light CCD camera, which offers, together with the long-working-distance lens, a magnified live image of the sample surface. The laser beam has a spot size of 1 μm when focused on the sample. Data acquisition is performed using Nova Software (v.1.1.0.1812, NT-MDT Co., Moscow, Russia). In the present work, all Raman spectra were recorded with a laser power of 60 μW, to avoid any sample damage, and within a spectral range of 278-2676 $cm^{-1}$. A 600 lines/mm grating provided a spectral resolution better than 2 $cm^{-1}$.

The multivalength Raman device is an Aramis spectrometer (Aramis Jobin Yvon, Horiba, Japan), an integrated confocal micro-Raman system described elsewhere[35]. The confocal microscope is coupled to a 460 mm focal length spectrograph equipped with four PC-controlled interchangeable grating-turrets. Two internal lasers provide visible and near infrared wavelengths (488 nm and 633 nm respectively). The device is also equipped with two additional lasers that provide two wavelengths, one in UV (325 nm) and the second in visible (442 nm). Analysis can be thus performed at four different wavelengths from UV to IR.

The laser beam is focused on the surface towards a confocal objective (X40 for UV) and (X100) (Horiba, Japan) for visible an infrared wavelengths (442, 488 and 633 nm). In order to avoid damaging the sample, the laser power was regulated at 85±2 μW, 19±2 μW, 25±2 μW and 15±1 μW respectively at 633, 488, 442 and 325 nm. The acquisition time was set at 30 s

with 5 averaging measurements. The grating was set at 2400 l/mm for 325 nm and 600 l/mm for 442, 488 and 633 nm. The resulting wavenumber accuracy is less than 2 $cm^{-1}$.

Prior to the measurements on the samples, a pure silica calibration sample was analyzed and the Raman shift was corrected for all the wavelengths with the theoretical value for silica, 520 $cm^{-1}$.

### 3.2.2. Secondary Ion Mass Spectroscopy analysis

#### *3.2.2.1. Theoretical background*

As suggested by the technique's name, Secondary Ion Mass Spectroscopy (SIMS) analytical technique consists of recording secondary ions emitted from a surface due to interactions with a beam of bombarding primary ions as illustrated in Figure 2.11.

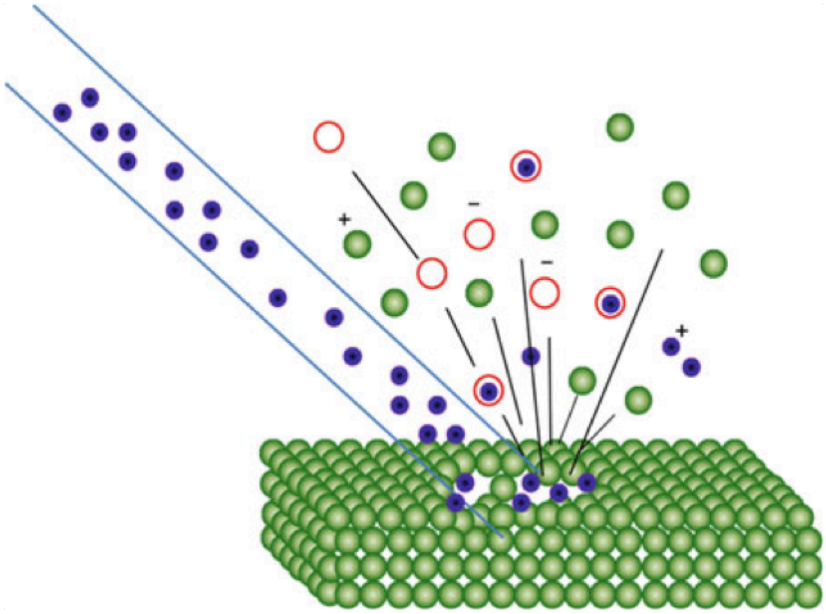

***Figure 2.11. Schematic of ion beam sputtering of a surface from reference[144]***

When the solid surface is sputtered with high-energy primary ions such as $CS^+$, $O_2$, $O^-$, $Ar^+$, $N_2^+$ and $Ga^+$ in the energy range from 1 to 30 keV[144], the primary ions transfer their energy to the lattice atoms. As a result, secondary electrons, neutral atoms or clusters of atoms, positively and negatively charged atoms or clusters (called secondary ions) as well as photons[145] issued from the collision cascade[146], emerge from the surface.

Analyzing the secondary ions with a mass spectrometer can provide chemical information about the target material. It is thus possible to identify elemental and molecular ions since the technique is based on the mass-to-charge ratio and ion counts per elements[144].

#### *3.2.2.2. Experimental details*

Deph-profiling SIMS performed by Evans Analytical Group (EAG, Sunnyvale California, USA) has been used to measure the distribution of carbon, hydrogen, silicon and oxygen within the coating. However, SIMS is not a quantitative technique: while it is useful to monitor any changes in the composition, it can't provide absolute values. It is thus necessary to couple this technique with quantitative ones to fully describe our material.

### 3.2.3. Rutherford Backscattering Spectroscopy / Hydrogen Forward Scattering

#### *3.2.3.1. Theoretical background*

RBS is an analytical technique based on the use of accelerators that provides a method to give quantitative composition of a solid material and the depth profile of the elements in ppm contained in the thin surface region of a sample. The technique is based on bombarding a desired target sample with high-energy ions (ion beam ranging from 0.5 to 4 MeV). $^{4}$He protons and sometimes lithium ions are often used as projectiles and the common backscattering angle is typically between 150° and 170°[147].

Figure 2.12 shows the schematics of a projectile having a charge $Z_1$ and a mass $M_1$ moving with a velocity of $v_1$ with a kinetic energy of $E_0$, scattered from a target nucleus having a charge $Z_2$ and a mass $M_2$.

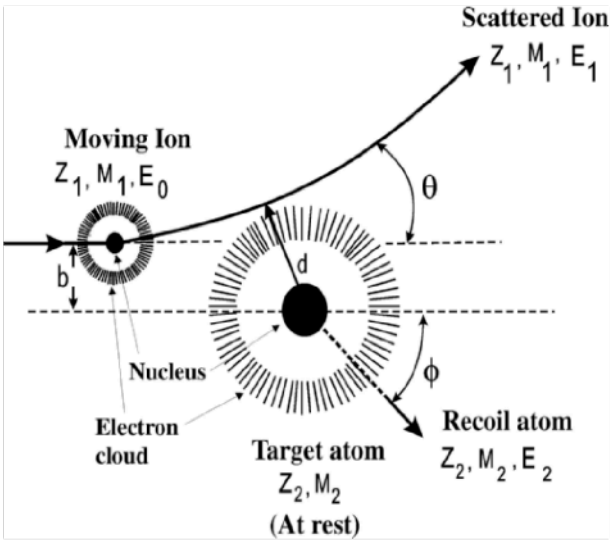


***Figure 2.12. Scattering of moving ion (Z1, M1, E0) by a target atom (Z2,M2) from Verma et al.[147]***

For backscattering to occur, the projectile and the target must get close enough together so that the distance of closest approach of the incoming particle, represented by "d" on Figure 2.12 is within the K-shell radius. "d" is given by:

$$d = \frac{Z_1 Z_2 e^2}{4\pi\varepsilon_o} \frac{1}{E_o} \qquad \textit{Eq 2. 5}$$

### *3.2.3.1. Experimental details*

RBS and HFS analysis have been performed by Evian Analytical Group (EAG$^{SM}$ EAG, Sunnyvale California, USA). As illustrated in Figure 2.13, RBS spectra are acquired at a backscattering angle of 160° and an appropriate grazing angle (with the sample oriented perpendicular to the incident ion beam). Experiments were carried out using Helium ($He^{++}$) ion beam which energy was set at 2.275 MeV, with a normal detector angle of 160° and a grazing Detector Angle of 100°. The sample is rotated with a small angle to present a random geometry to the incident beam. This avoids channeling in both the film and the substrate. The use of two detector angles can significantly improve the measurement accuracy for compositions when, like in our case, thin films are analyzed.

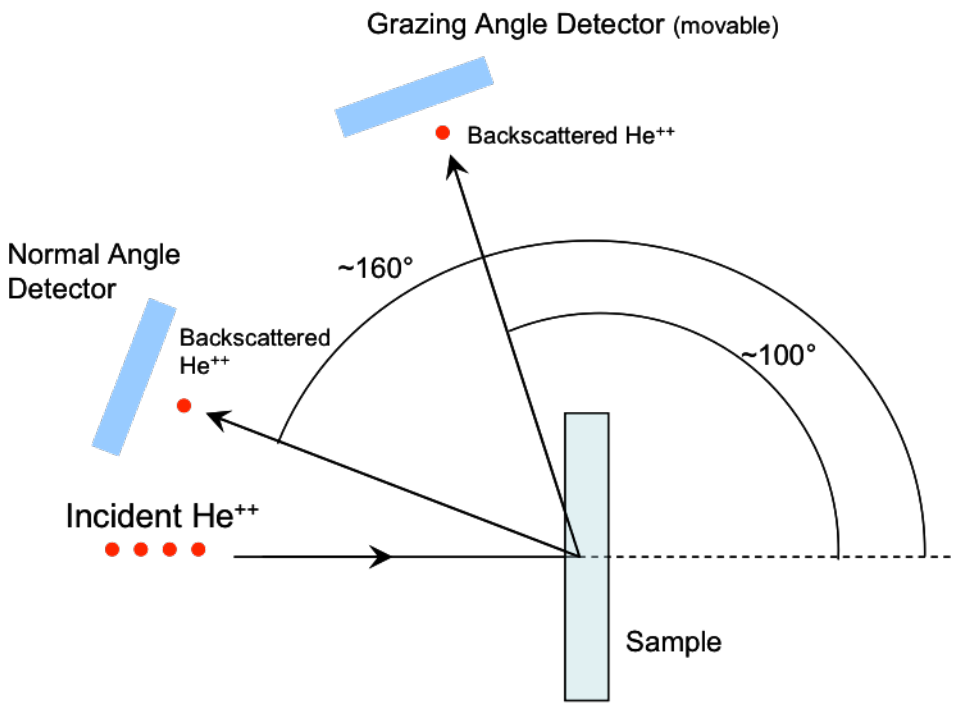


***Figure 2.13. Schematic showing a scattering geometry in a typical of RBS experimental setup***

When a thin (<100nm) amorphous or polycrystalline film resides on a single crystal substrate, "ion channeling" may be utilized to reduce the backscattering signal from the substrate. This result in improved accuracy in the composition of layers containing elements that overlay with the substrate signal, typically light elements, such as oxygen, nitrogen and carbon. Spectra were fitted by applying a theoretical layer model and iteratively adjusting elemental concentrations and thickness until good agreement was found between the theoretical and the experimental spectra.

In general, the physical thickness of films is checked with a direct measurement technique (cross section SEM in our case) prior to RBS measurement thus allowing a direct calculation of the real density of the coating. Conversely, if the density of the coating is known, RBS can provide accurate thicknesses evaluation. The equation governing the conversion from the RBS densities and thicknesses and real thicknesses to the real densities is:

$$\boldsymbol{D_{real} = (D_{RBS} \times \tau_{RBS}) / \tau_{real}} \qquad \textbf{\textit{Eq 2. 6}}$$

with $D_{real}$ and $D_{RBS}$ the real and RBS densities of the coating respectively, $\tau_{real}$ the physical thickness of the coating and $\tau_{RBS}$, the thickness determined with RBS.

In HFS experiments, a detector is placed 30° from the forward trajectory of the incident $He^{++}$ ion beam (operating energy of 2.275 MeV) and the sample is rotated so that the incident beam strikes the surfaces 75° from normal as illustrated in Figure 2.14. In this geometry it is possible to collect light atoms, namely hydrogen, forward-scattered from a sample after collisions with the probing $He^{++}$ ion beam. A thin absorber foil is placed over the detector to filter out $He^{++}$ ions that are also forward scattered from the sample.

Hydrogen concentrations are determined by comparing the number of hydrogen counts obtained from reference samples after normalizing by the stopping powers of the different materials. A hydrogen implanted silicon sample and a geological sample, muscovite, are used as references. The hydrogen concentration in the hydrogen implanted silicon sample is taken to be its stated implant dose of 1.6E17 ±0.2E17 atoms/cm$^2$. The muscovite (MUSC) sample is known to have ~6.5 ±0.5 atomic percent hydrogen.

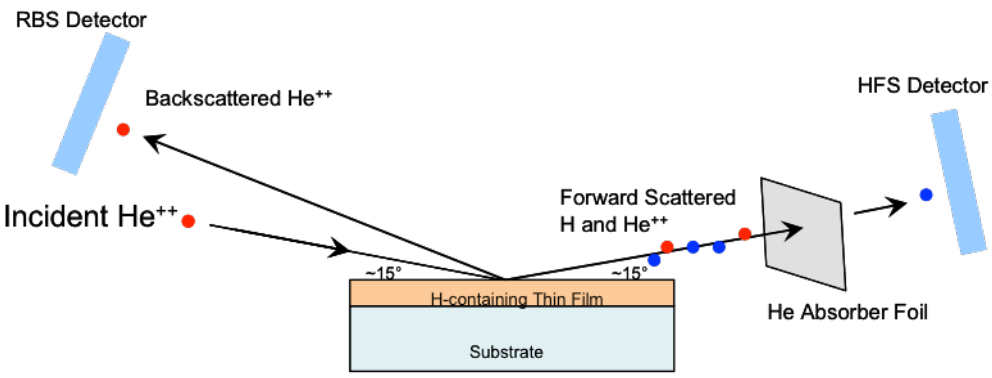


***Figure 2.14. Scanning geometry of an HFS experiment***

Samples are checked for hydrogen loss in the analyzed region. This is done by acquiring spectra for different acquisition times (initially a short exposure followed by a longer exposure to the He++ beam). Charge accumulations for 5 and 40 μC are used. Lower proportional signal in the 40 μC spectrum indicates hydrogen loss.

In those cases the shorter exposure is chosen for analysis at the expense of higher noise in the spectrum. To account for surface hydrogen due to residual moisture or hydrocarbon adsorption a silicon control sample is analyzed together with the actual samples and the hydrogen signal from the control sample is subtracted from each of the spectra obtained from the actual samples. During the HFS acquisition backscattering spectra are acquired using the 160° angle detector (with the sample in forward scattering orientation). The RBS spectra are used to normalize the total charge delivered to the sample.

### 3.2.4. XPS

#### *3.2.4.1. Theoretical background*

X-ray photoelectron spectroscopy is an "X-ray in, electron out" technique that is used to probe the outermost surface region of a material. XPS is one of the few techniques that can provide information about the chemical bonding of the top few nanometers of a surface[148]. The technique provides elemental information, except hydrogen and helium, of the top 10 to 200 Å of any solid that is vacuum compatible.

XPS is based on the photoelectric phenomenon (interaction between a photon and atomic orbital electrons) as illustrated in Figure 2.15.

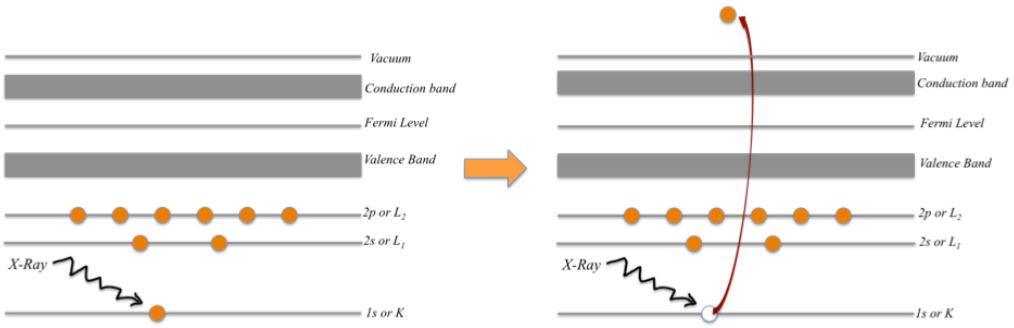


***Figure 2.15. Schematic of XPS principle***

In brief, when the incident photon interacts with the electronic structure of an atom, an electron is ejected from the atom whenever the photon energy is higher than the electron binding energy. The kinetic energy of the emitted electron is approximately equal to the difference between the photon energy and the electron's binding energy[149]. The binding energy of the electron can be written as follows:

$$\boldsymbol{E_b \approx h\nu - E_k} \qquad \textit{Eq 2. 7}$$

With $E_b$, $E_k$ the electrons bending energy and kinetic energy respectively, $h\nu$ is the photon energy.

### *3.2.4.2. Experimental details*

The chemistry of the near-surface region of the as received silicon oxide-doped hydrogenated amorphous carbon (a-C:H:Si:O) was investigated by X-ray photoelectron spectroscopy (XPS) using a customized XPS spectrometer, developed by Mangolini *et al*[150]. Briefly, the XP-spectrometer is equipped with a monochromatic Al Kα X-ray source with a X-ray spot size of 1 x 3 $mm^2$. The photoelectrons emitted from the specimen are collected with an electrostatic lens, whose axis is normal to the sample surface. After passing the hemispherical analyzer, the photoelectrons are detected by a two-dimensional MCP/CCD detector. In the present work, the X-ray source was run at 30 mA and 12 kV, whereas the analyzer was operated in constant-analyzer-energy (CAE) mode. Survey spectra were acquired with the pass energy and step size equal to 200 eV and 1 eV, respectively. For the high-resolution (HR) spectra, the pass energy and step size were, respectively, 100 and 0.05 eV (full width at half maximum (FWHM) of the peak height for the Ag3d5/2 equal to 0.57 eV). The curved slit at the entrance of the hemispherical analyzer has a width of 0.8 mm. The residual pressure in the analysis chamber was always below $1.10^{-6}$ Pa. The spectrometer was calibrated according to ISO 15472:2001 with an accuracy better than ±0.05 eV. The high-

resolution spectra were processed using CasaXPS software (v2.3.16, Casa Software Ltd., Wilmslow, Cheshire, U.K.). An iterated Shirley-Sherwood background subtraction was applied before peak fitting using a linear least-square algorithm[151].

No sample charging was ever observed, as determined by checking the position of the carbon (C1s) signal and of the valence band (this is expected since the samples have moderate electrical conductivity).

Chemical investigation of the worn material has been performed using a VersaProbe PHI XPS apparatus. The residual pressure in the analysis chamber was below $1.10^{-7}$ Pa. Extensive description of the apparatus can be consulted elsewhere [108,152,153]. The spectrometer was calibrated in energy using a gold sample (the $4f_{7/2}$ eletronic level for a binding energy of 83.95 eV).

In a first step, we performed a roughly resolved survey scan in order to identify the different elements present in the tribofilm. In a second step, a more resolved acquisition was carried out while focusing on C1s, N1s, O1s, Si2p and Fe2p signal. XPS data where processed using PHI Multipack software.

### 3.2.5. NEXAFS analyses

#### *3.2.5.1. Theoretical background*

NEXAFS (near edge X-ray absorption fine structure spectroscopy) is a synchrotron based spectroscopy technique that probes the structure and the electronic states of the surface of a material. The fact that this technique allows the investigation of the chemical changes and the chemical environment of an atom with a very high sensitivity makes it an important tool for studying the chemical changes that occurs in the near-surface region of our coatings (a-C:H:Si:O) following a tribological test. The technical basis of NEXAFS has been widely described by Gregory Hahner[154]. As with all synchrotron-based techniques, NEXAFS analysis uses the basic electromagnetic principle: radiations come from an acceleration of electric charges. As described in Figure 2.16, the synchrotron facility consist of 3 main parts[154]:

- *The booster: a ring equipped with highly powerful magnets where the electrons are injected at ~100 MeV and accelerated at ~ GeV in order to nearly reach the speed of light before being introduced in the storage ring.*
- *The storage ring: a second ring bigger than the booster and connected to it with a constant magnetic field, where the electrons issued from the booster are being*

*introduced. The radiation comes then from the electrons that are accelerated inside the storage ring.*

- *Beamline: they are lines issued from the storage ring and connected to the experimental chamber.*

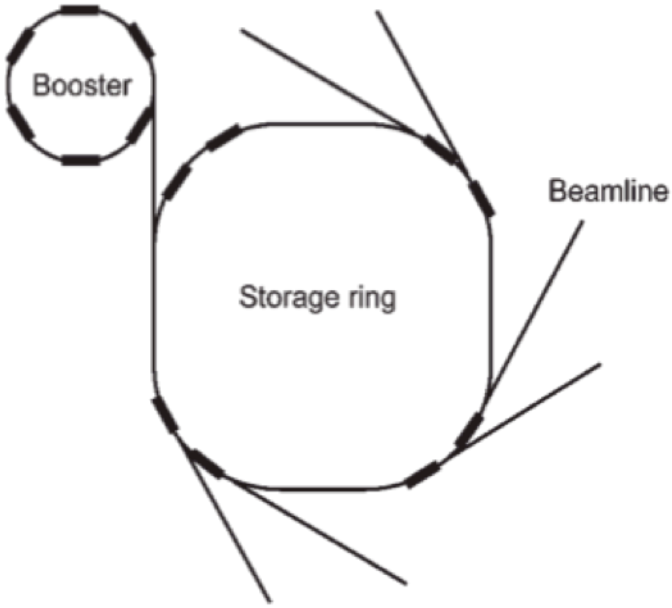


***Figure 2.16. Description of synchrotron facility from reference[154]***

Once in the beamline, a monochromator helps to select a single wavelength allowing a high-brilliance and tunable monochromatic X-ray source to be obtained with a high degree of polarization for the experimentalist.

Figure 2.17 shows a schematic of the interactions between the high energy X-rays and the material that is analyzed. The absorption of X-rays results in the emission of a photoelectron from an inner shell level to an unoccupied state leaving a hole (core hole). For light element such as carbon, nitrogen, oxygen and sulfur the photoionization results in the removal of a K-shell electron. The typical K-hole lifetimes are in the order of 1 to 10 fs[155]. There are two possible ways of filling the vacant hole:

- *Either another higher energy electron from the same atom fills the hole with the emission of a fluorescent photon (Figure 2.17.b)*
- *Or a higher energy electron from the same atom fills the hole with emission of an Auger electron (Figure 2.17.c)*

It is known that the Auger electron yield is much higher than the florescence yield for low-Z molecules (carbon, nitrogen, oxygen) and this mode provides a better surface sensitivity. For this reason, all NEXAFS spectra in this thesis were acquired in Auger detection mode.

Another possible way to enhance the surface sensitivity using NEXAFS is to apply a retarding voltage to the electrons before they enter the channeltron[156]. Thus, there are two possible measurement configurations:

- *Partial Electron Yield (PEY): lower kinetic energy electrons are suppressed and only electrons from the outermost surface (~ 3 nm[157]) are detected.*
- *Or Total Electron Yield (TEY): all the electrons that emerge from the surface can be detected.*

All the spectra in this thesis were acquired in PEY mode since it provides a better signal to background resolution than the TEY.

If the energy of the incoming photons matches the difference between the initial state and the unoccupied state, the enhanced resonant transitions are superimposed on the step-like shape[154], resulting thus in the NEXAFS spectra. A C1s to π* transition occurs at lower photon energies than a transition from C1s to σ* and this is characteristic of molecules with double and triple bonds.

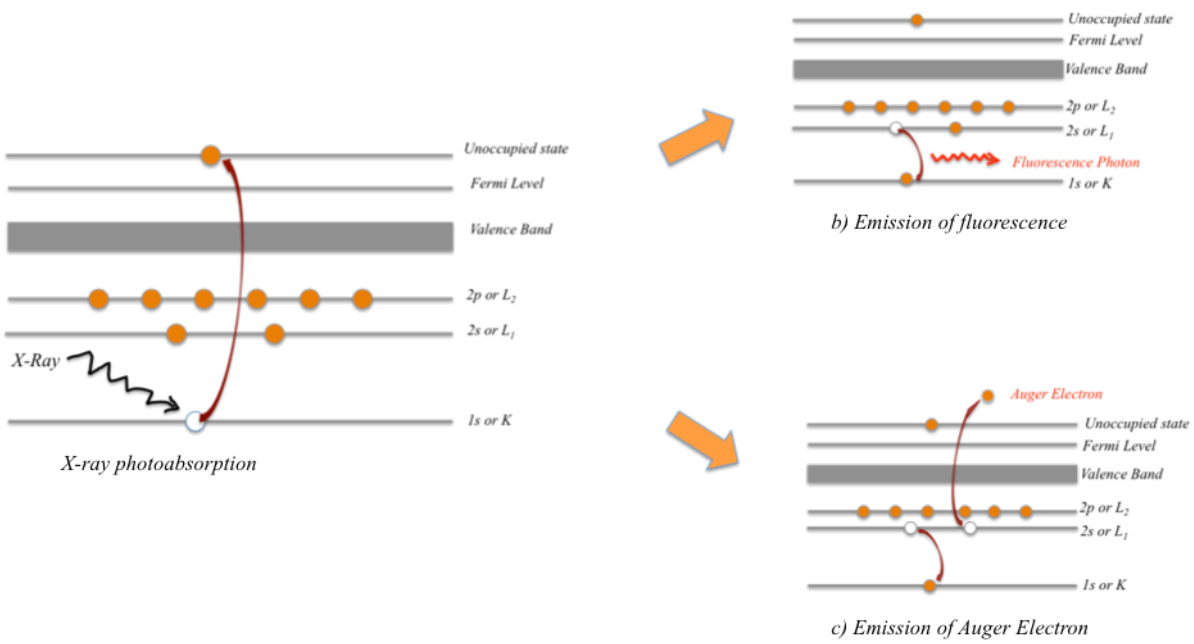


***Figure 2.17. Schematics of NEXAFS spectroscopy principles***

Unlike XPS measurement, which consists of a fingerprint of a direct excitation of the elastically scattered electrons, meaning that the core electron levels measured do not vary much depending on the type of bond and what the atom is bonded to, NEXAFS probes the unoccupied states. The shape of a NEXAFS spectrum depends on the local bonding state of the near surface region. NEXAFS is thus a powerful tool that allows for probing the chemical bonding states in the material. This means that many of the structural changes that might occurs during a tribological test could be detected by NEXAFS.

#### *3.2.5.2. Computing the $sp^2$ fraction in carbon materials using nexafs*

Figure 2.18 illustrates typical NEXAFS spectra that can be obtained for ultra nanocrystalline diamond (UNCD) and highly ordered pyrolytic graphite (HOPG).

For HOPG reference samples, there are two characteristic peaks:

- *A sharp peak located at 285.0 eV, due to the C 1s → π* transition for ordered $sp^2$-bonded carbon. It corresponds to a transition of an electron from a 1s core state to an unoccupied π anti-bonding state (referred as π*)*[105,156,158,159].
- *A peak located at ~292.0 eV, corresponding to C 1s → σ* transition (transition from a 1s core state to an unoccupied σ anti-bonding state, referred as σ*).*

For UNCD reference sample, two main peaks can be noticed:

- *The characteristic peak corresponding to C 1s → π* transition (located at 285 eV).Ideally, diamond should be composed of 100% $sp^3$ bonded carbon, making the presence of this peak questionable, but in fact, multiple sources of $sp^2$ bonded carbon are present in UNCD, namely, the grain boundaries and surface reconstruction.*
- *the large peak at ~289.0 eV followed by the ones at ~289.3 eV and 302.5 eV are all due to C 1s → σ* transition*[156,158,159].

For our a-C:H:Si:O sample, the two characteristic peaks are located at :

- *285.0 eV, corresponding to C 1s → π* for $sp^2$ bonded carbon*
- *289.0 eV corresponding to C 1s → σ* transition for (C-O, C-Si). More details about the characteristic peaks of a-C:H:Si:O coating, will be given in chapter 3.*

From the shape of the spectra, the fraction of $sp^2$ bonded carbon in our material can be calculated by integrating the intensity ratio of the C 1s → π* peak and the C 1s → σ* region for the investigated sample and a reference sample (usually freshly cleaved HOPG) as reported in the following formula [159–161] and illustrated in Figure 2.18.

$$f_{sp^2} = \frac{I_{sam}^{\pi^*} I_{ref}(\Delta E)}{I_{ref}^{\pi^*} I_{sam}(\Delta E)} \qquad \textbf{Eq 2. 8}$$

with $I_{sam}^{\pi^*}$ and $I_{ref}^{\pi^*}$ the areas under the π* peak of the sample and the reference respectively and $I_{sam}(\Delta E)$ and $I_{ref}(\Delta E)$ the areas calculated for the remaining part of the spectra which correspond to the contribution the σ* region.

#### *3.2.5.3. Experimental details*

Imaging near-edge X-ray absorption fine structure (NEXAFS) spectroscopic measurements were performed using the parallel processing imaging system at the NIST/Dow endstation of beamline U7A at the National Synchrotron Light Source (NSLS), Brookhaven National Laboratory (Upton, NY, USA). This imaging technique, which allows for the structural and chemical characterization of the near-surface region with a lateral resolution of 50 µm and a field of view of 18x13 $mm^2$, has been extensively described earlier[158]. The photon source for this beamline is a bending magnet, and covers an energy range from 100 to 800 eV. The photon flux is $2x10^{11}$ photons/second/0.1% bandwidth. In the present work, NEXAFS images were acquired in partial electron yield (PEY) mode using a photon energy range of 260-340 eV for the carbon K-edge (energy resolution of 0.1 eV). The entrance grid bias (EGB) of the channeltron detector was set to 50, 150, and 220 V for the carbon K-edge. Changing the EGB voltage allows NEXAFS measurements with different surface sensitivity to be performed[157].

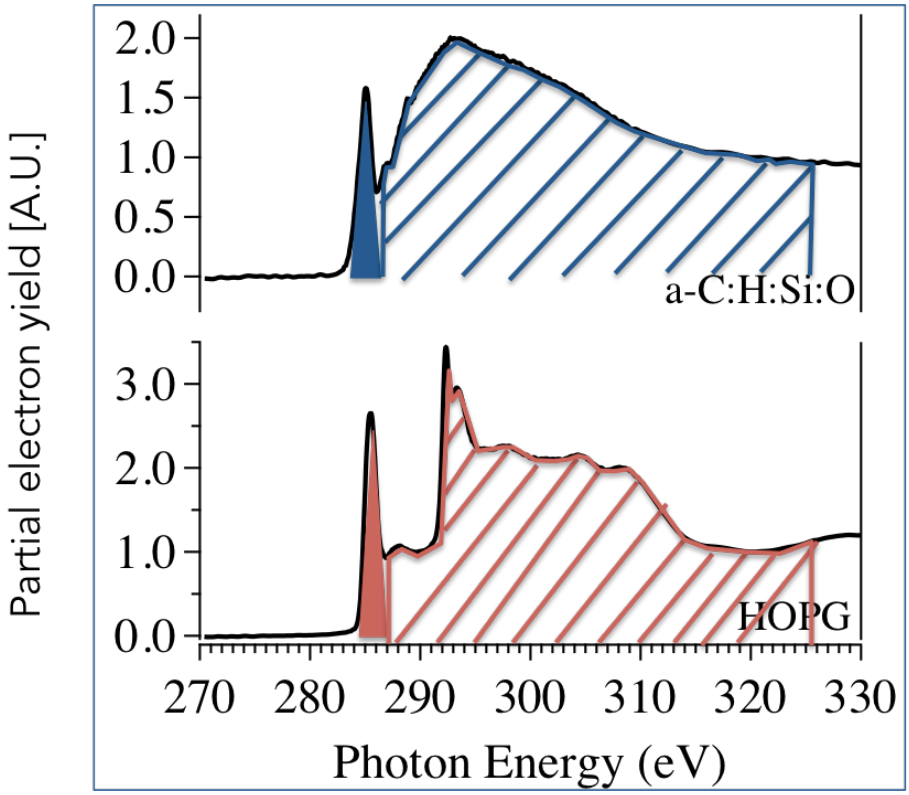


***Figure 2.18. Schematic of the calculation of $sp^2$ fraction from nefaxs spectra of the reference sample (HOPG) and a-C:H:Si:O***

The monochromator energy was calibrated using the carbon K-edge $\pi^*$ transition of freshly-cleaved highly ordered pyrolytic graphite (HOPG, grade 2, SPI Supplies, West Chester, PA, USA), located at 285.5 eV. All NEXAFS images were first normalized to the absorption current measured simultaneously from a gold mesh placed in the beamline upstream from the analysis chamber, and then normalized to the spectral intensity in the pre-edge region (intensity between 270 and 280 eV).

## 4. Summary

In this chapter we described the experimental approach that has been used to investigate the chemistry, composition and mechanical properties of a-C:H:Si:O as well as the environmental dependence of its tribological behavior, both at macro- and micro-scale. Macroscale environmental dependence experiments have been performed using an ambient air linear reciprocating tribometer equipped with a gas blowing system and a Controlled-Environment Analytical Tribometer. Analysis techniques used for the worn material, namely microscopy and x-ray based analytical techniques have also been presented.

# 5. Résumé Chapitre 2

Ce chapitre porte sur la description de l'approche expérimentale que nous avons adoptée pour répondre à la problématique soulevée par cette thèse : *la compréhension des phénomènes physico-chimiques qui interviennent entre un a-C:H:Si:O et son environnement de fonctionnement lors d'une sollicitation tribologique*.

Pour ce faire, le matériau qui a fait l'objet de ce travail a été développé par le Groupe Sulzer-Metco Inc. (Winterthur, Switzerland, now Oerlikon Metco) en utilisant un procédé de dépôt chimique en phase vapeur assisté par plasma (*Plasma-Enhanced Chemical Vapor Deposition* – PECVD). Une présentation des techniques et des procédures mises en œuvre pour une caractérisation complète de la couche mince avant et après essais tribologiques est présentée suivant deux axes :

- *Les techniques et procédures d'observation de la surface, la topographie et les propriétés mécaniques de la couche, avec notamment microscopie numérique, microscopie électronique à balayage, interférométrie en lumière blanche, microscopie à force atomique, microscopie à force de frottement et nanoindentation ;*
- *Les techniques et procédures d'analyse chimique et structurale du matériau initial et des surfaces après essais tribologiques, avec notamment la spectroscopie Raman à plusieurs longueurs d'onde, la spectroscopie de masse des ions secondaires (Secondary Ion Mass Spectroscopy – SIMS), la spectroscopie de rétrodiffusion Rutherford couplée à la spectroscopie de diffusion de l'hydrogène (Rutherford Backscattering Spectoscopy – RBS / Hydrogen Forward Scattering – HFS), la spectroscopie de photoélectrons (X-Ray Photoelectron Spectroscopy – XPS), ou encore la spectroscopie fine d'absorption des rayons X (Near-Edge X-ray Absorption Fine Structure – NEXAFS).*

Aussi, après une discussion du choix de la configuration des essais tribologiques, nous présentons dans ce chapitre les deux tribomètres utilisés dans cette étude :

- *Un tribomètre linéaire alternatif fonctionnant dans l'air ambiant et que nous avons équipé d'un système programmable de soufflage de gaz, permettant ainsi de changer rapidement l'environnement du contact ;*
- *Un tribomètre linéaire alternatif placé dans une chambre sous vide poussé ($<10^{-8}$ mbar) mais permettant aussi l'admission de gaz (oxygène, hydrogène ou vapeur d'eau dans notre cas) de manière contrôlée jusqu'à une pression de maximale de 2000 mbar.*

# 6.References


1. Neerinck, D. et al. Diamond-like nanocomposite coatings (a-C:H/a-Si:O) for tribological applications. Diam. Relat. Mater. **7,** 468–471 (1998).
2. Neerinck, D. et al. Diamond-like nanocomposite coatings for low-wear and low-friction applications in humid environments. Thin Solid Films **317,** 402–404 (1998).
3. Scharf, T. W., Ohlhausen, J. A., Tallant, D. R. & Prasad, S. V. Mechanisms of friction in diamondlike nanocomposite coatings. J. Appl. Phys. **101,** 063521–063521–11 (2007).
4. Prasad, S. V., Scharf, T. W., Kotula, P. G., Michael, J. R. & Christenson, T. R. Application of Diamond-Like Nanocomposite Tribological Coatings on LIGA Microsystem Parts. J. Microelectromechanical Syst. **18,** 695–704 (2009).
5. Venkatraman, C., Brodbeck, C. & Lei, R. Tribological properties of diamond-like nanocomposite coatings at high temperatures. Surf. Coat. Technol. **115,** 215–221 (1999).
6. Sudarshan, T. S., Khor, K. A., Jeandin, M. & Britain), I. of M. (Great. Surface modification technologies X: proceedings of the Tenth International Conference on Surface Modification Technologies held in Singapore, September 2-4, 1996. (Institute of Materials, 1997).
7. Konicek, A. R. Tribochemical studies of hard carbon films as a function of load and environment. Diss. Available ProQuest 1–218 (2010).
8. Holmberg, K., Andersson, P. & Erdemir, A. Global energy consumption due to friction in passenger cars. Tribol. Int. **47,** 221–234 (2012).
9. A Tribological Study of Retrieved Hip Prostheses. : Clinical Orthopaedics and Related Research. LWW at <http://journals.lww.com/corr/Fulltext/1992/03000/A_Tribological_Study_of_Retrieved_Hip_Prostheses_.15.aspx>
10. Gosvami, N. N. et al. Mechanisms of antiwear tribofilm growth revealed in situ by single-asperity sliding contacts. Science **348,** 102–106 (2015).
11. Tannous, J. et al. Understanding the Tribochemical Mechanisms of IF-MoS2 Nanoparticles Under Boundary Lubrication. Tribol. Lett. **41,** 55–64 (2010).
12. Lahouij, I. Mécanismes de lubrification des nanoparticules à structure Fullerène : approche multi-échelle. (Ecole Centrale de Lyon, 2012). at <https://tel.archives-ouvertes.fr/tel-00790813/document>
13. Springer Handbook of Mechanical Engineering | Springer. at <http://www.springer.com/us/book/9783540491316>
14. Randall, N. X. in Tribology for Scientists and Engineers (eds. Menezes, P. L., Nosonovsky, M., Ingole, S. P., Kailas, S. V. & Lovell, M. R.) 141–175 (Springer New York, 2013). at <http://link.springer.com/chapter/10.1007/978-1-4614-1945-7_4>
15. Belin, M. & Martin, J. M. Triboscopy, a new approach to surface degradations of thin films. Wear **156,** 151–160 (1992).
16. Philippon, D., Barros-Bouchet, M.-I. D., Lerasle, O., Mogne, T. L. & Martin, J.-M. Experimental Simulation of Tribochemical Reactions Between Borates Esters and Steel Surface. Tribol. Lett. **41,** 73–82 (2011).
17. Philippon, D. et al. Role of nascent metallic surfaces on the tribochemistry of phosphite lubricant additives. Tribol. Int. **44,** 684–691 (2011).
18. Matta, C. et al. Tribochemistry of tetrahedral hydrogen-free amorphous carbon coatings in the presence of OH-containing lubricants. Lubr. Sci. **20,** 137–149 (2008).
19. De Barros Bouchet, M.-I. et al. Friction of Diamond in the Presence of Water Vapor and Hydrogen Gas. Coupling Gas-Phase Lubrication and First-Principles Studies. J. Phys. Chem. C **116,** 6966–6972 (2012).
20. Martin, J.-M. et al. Gas-Phase Lubrication of ta-C by Glycerol and Hydrogen Peroxide. Experimental and Computer Modeling. J. Phys. Chem. C **114,** 5003–5011 (2010).
21. De Barros Bouchet, M. I. et al. Improved mixed and boundary lubrication with glycerol-diamond technology. Tribol. - Mater. Surf. Interfaces **1,** 28–32 (2007).
22. Wiora, D. G., Weber, M. & Chanbai, S. in Encyclopedia of Tribology (eds. Wang, Q. J. & Chung, Y.-W.) 2483–2488 (Springer US, 2013). at <http://link.springer.com.gate6.inist.fr/referenceworkentry/10.1007/978-0-387-92897-5_317>
23. Haugstad, G. Atomic Force Microscopy: Understanding Basic Modes and Advanced Applications. (John Wiley & Sons, 2012).
24. Enachescu, M. et al. Atomic Force Microscopy Study of an Ideally Hard Contact: The Diamond(111)/Tungsten Carbide Interface. Phys. Rev. Lett. **81,** 1877–1880 (1998).
25. Prokopovich, P. & Perni, S. Comparison of JKR- and DMT-based multi-asperity adhesion model: Theory and experiment. Colloids Surf. Physicochem. Eng. Asp. **383,** 95–101 (2011).
26. Bhushan, B. & Marti, O. in Nanotribology and Nanomechanics (ed. Bhushan, P. B.) 41–115 (Springer Berlin

Heidelberg, 2005). at <http://link.springer.com/chapter/10.1007/3-540-28248-3_2>
27. Cain, R. G., Biggs, S. & Page, N. W. Force Calibration in Lateral Force Microscopy. J. Colloid Interface Sci. **227,** 55–65 (2000).
28. Sader, J. E., Larson, I., Mulvaney, P. & White, L. R. Method for the calibration of atomic force microscope cantilevers. Rev. Sci. Instrum. **66,** 3789–3798 (1995).
29. Carpick, R. W. & Salmeron, M. Scratching the Surface: Fundamental Investigations of Tribology with Atomic Force Microscopy. Chem. Rev. **97,** 1163–1194 (1997).
30. Schwarz, U. D., Haefke, H., Reimann, P. & Güntherodt, H.-J. Tip artefacts in scanning force microscopy. J. Microsc. **173,** 183–197 (1994).
31. in Fracture Mechanics 339–352 (Springer Netherlands, 2005). at <http://link.springer.com.gate6.inist.fr/chapter/10.1007/1-4020-3153-X_13>
32. Loubet, J. L., Bauer, M., Tonck, A., Bec, S. & Gauthier-Manuel, B. in Mechanical Properties and Deformation Behavior of Materials Having Ultra-Fine Microstructures (eds. Nastasi, M., Parkin, D. M. & Gleiter, H.) 429–447 (Springer Netherlands, 1993). at <http://link.springer.com/chapter/10.1007/978-94-011-1765-4_28>
33. Bec, S., Tonck, A., Georges, J.-M., Georges, E. & Loubet, J.-L. Improvements in the indentation method with a surface force apparatus. Philos. Mag. A **74,** 1061–1072 (1996).
34. Guillonneau, G. Nouvelles techniques de nano-indentation pour des conditions expérimentales difficiles : très faibles enfoncements, surfaces rugueuses, température. (Ecully, Ecole centrale de Lyon, 2012). at <http://www.theses.fr/2012ECDL0048>
35. Cameron, A. The Principles of Lubrication. (Wiley, 1966).
36. Bec, S., Tonck, A. & Loubet, J. L. A simple guide to determine elastic properties of films on substrate from nanoindentation experiments. Philos. Mag. **86,** 5347–5358 (2006).
37. Demmou, K., Bec, S. & Loubet, J.-L. Effect of hydrostatic pressure on elastic properties of ZDTP tribofilms. ArXiv07064235 Phys. (2007). at <http://arxiv.org/abs/0706.4235>
38. Windom, B. C. & Hahn, P. D. W. in Encyclopedia of Tribology (eds. Wang, Q. J. & Chung, Y.-W.) 2742–2747 (Springer US, 2013). at <http://link.springer.com.gate6.inist.fr/referenceworkentry/10.1007/978-0-387-92897-5_1216>
39. Ferrari, A. & Robertson, J. Interpretation of Raman spectra of disordered and amorphous carbon. Phys. Rev. B **61,** 14095–14107 (2000).
40. Irmer, G. & Dorner-Reisel, A. Micro-Raman Studies on DLC coatings. Adv. Eng. Mater. **7,** 694–705 (2005).
41. Jana, S. et al. Effect of annealing on structural and optical properties of diamond-like nanocomposite thin films. Appl. Phys. A **114,** 965–972 (2014).
42. Casiraghi, C. Effect of hydrogen on the UV Raman intensities of diamond-like carbon. Diam. Relat. Mater. **20,** 120–122 (2011).
43. Sato, K. et al. D-band Raman intensity of graphitic materials as a function of laser energy and crystallite size. Chem. Phys. Lett. **427,** 117–121 (2006).
44. Casiraghi, C., Piazza, F., Ferrari, A. C., Grambole, D. & Robertson, J. Bonding in hydrogenated diamond-like carbon by Raman spectroscopy. Diam. Relat. Mater. **14,** 1098–1102 (2005).
45. Rose, F. et al. Complete characterization by Raman spectroscopy of the structural properties of thin hydrogenated diamond-like carbon films exposed to rapid thermal annealing. J. Appl. Phys. **116,** 123516 (2014).
46. Ferrari, A. C. & Robertson, J. Resonant Raman spectroscopy of disordered, amorphous, and diamondlike carbon. Phys. Rev. B **64,** 075414 (2001).
47. Casiraghi, C., Ferrari, A. C. & Robertson, J. Raman spectroscopy of hydrogenated amorphous carbons. Phys. Rev. B **72,** 085401 (2005).
48. Robertson, J. Diamond-like amorphous carbon. Mater. Sci. Eng. R Rep. **37,** 129–281 (2002).
49. Cui, W. G., Lai, Q. B., Zhang, L. & Wang, F. M. Quantitative measurements of sp3 content in DLC films with Raman spectroscopy. Surf. Coat. Technol. **205,** 1995–1999 (2010).
50. Sikora, A. et al. Structure of diamondlike carbon films deposited by femtosecond and nanosecond pulsed laser ablation. J. Appl. Phys. **108,** 113516 (2010).
51. Joo, S. & Liang, D. H. in Encyclopedia of Tribology (eds. Wang, Q. J. & Chung, Y.-W.) 2989–2994 (Springer US, 2013). at <http://link.springer.com/referenceworkentry/10.1007/978-0-387-92897-5_1218>
52. Benninghoven, A. Surface investigation of solids by the statical method of secondary ion mass spectroscopy (SIMS). Surf. Sci. **35,** 427–457 (1973).
53. Parkin, D. M. The displacement cascade in ceramic oxides. Nucl. Instrum. Methods Phys. Res. Sect. B Beam Interact. Mater. At. **46,** 26–35 (1990).
54. Atomic and Nuclear Analytical Methods. (Springer Berlin Heidelberg, 2006). at <http://link.springer.com/10.1007/978-3-540-30279-7>
55. Qu, D. J. & Iii, H. M. M. in Encyclopedia of Tribology (eds. Wang, Q. J. & Chung, Y.-W.) 4133–4138

(Springer US, 2013). at <http://link.springer.com.gate6.inist.fr/referenceworkentry/10.1007/978-0-387-92897-5_1222>
56. Andrade, J. D. in Surface and Interfacial Aspects of Biomedical Polymers (ed. Andrade, J. D.) 105–195 (Springer US, 1985). at <http://link.springer.com/chapter/10.1007/978-1-4684-8610-0_5>
57. Mangolini, F. et al. Angle-resolved environmental X-ray photoelectron spectroscopy: A new laboratory setup for photoemission studies at pressures up to 0.4 Torr. Rev. Sci. Instrum. **83,** 093112 (2012).
58. Shirley, D. A. High-Resolution X-Ray Photoemission Spectrum of the Valence Bands of Gold. Phys. Rev. B **5,** 4709–4714 (1972).
59. Lahouij, I., Vacher, B., Martin, J.-M. & Dassenoy, F. IF-MoS2 based lubricants: Influence of size, shape and crystal structure. Wear **296,** 558–567 (2012).
60. Njiwa, P. et al. Zinc Dialkyl Phosphate (ZP) as an Anti-Wear Additive: Comparison with ZDDP. Tribol. Lett. **44,** 19–30 (2011).
61. Hähner, G. Near edge X-ray absorption fine structure spectroscopy as a tool to probe electronic and structural properties of thin organic films and liquids. Chem. Soc. Rev. **35,** 1244–1255 (2006).
62. Persson, P., Lunell, S., Szöke, A., Ziaja, B. & Hajdu, J. Shake-up and shake-off excitations with associated electron losses in X-ray studies of proteins. Protein Sci. Publ. Protein Soc. **10,** 2480–2484 (2001).
63. Stöhr, J. NEXAFS Spectroscopy. (Springer Science & Business Media, 1992).
64. Genzer, J., Kramer, E. J. & Fischer, D. A. Accounting for Auger yield energy loss for improved determination of molecular orientation using soft x-ray absorption spectroscopy. J. Appl. Phys. **92,** 7070–7079 (2002).
65. Konicek, A. R. et al. Near-Edge X-ray Absorption Fine Structure Imaging of Spherical and Flat Counterfaces of Ultrananocrystalline Diamond Tribological Contacts: A Correlation of Surface Chemistry and Friction. Tribol. Lett. **44,** 99–106 (2011).
66. Mangolini, F., McClimon, J. B., Rose, F. & Carpick, R. W. Accounting for Nanometer-Thick Adventitious Carbon Contamination in X-ray Absorption Spectra of Carbon-Based Materials. Anal. Chem. (2014). doi:10.1021/ac503409c
67. Sumant, A. V. et al. Surface composition, bonding, and morphology in the nucleation and growth of ultra-thin, high quality nanocrystalline diamond films. Diam. Relat. Mater. **16,** 718–724 (2007).
68. Osswald, S., Yushin, G., Mochalin, V., Kucheyev, S. O. & Gogotsi, Y. Control of sp2/sp3 Carbon Ratio and Surface Chemistry of Nanodiamond Powders by Selective Oxidation in Air. J. Am. Chem. Soc. **128,** 11635–11642 (2006).

# *Chapter 3. Influence of environment on the tribological behavior of a-C:H:Si:O*

*This chapter focuses on the tribological behavior of a-C:H:Si:O coatings under different relative humidity levels in the sliding environment, in order to understand the role of water vapor on the friction mechanisms of a-C:H:Si:O. As discussed in chapter 2, the results presented herein were obtained using an ambient air linear reciprocating tribometer equipped with a gas flow system that allows a controlled gas flow in the contact, resulting in a quickly tunable RH of the sliding environment. We illustrated in chapter 1 that, even though the friction behavior of a-C:H:Si:O has been found to be less dependent on the relative humidity than the one of undoped DLC coatings[9], different values of the friction coefficient of a-C:H:Si:O have been reported depending on the relative humidity of the sliding environment[10,12,13,162]. Further investigations on the humidity dependence of the friction behavior of a-C:H:Si:O have been performed by Scharf et al.[96], who proposed a friction mechanism to account for such dependence. The main idea of this model is based on the shear strength[96] of the interfacial material (referred to as "tribofilm" in this document). According to Scharf's model, under humid environment a more silica-like and hard-to-shear tribofilm is generated, while under dry conditions, a rather carbon-like and easy-to-shear tribofilm is formed in the contact. The relatively high friction under humid conditions was then interpreted as a consequence of the high shear strength of the tribofilm (78 MPa)[96] and the low friction in dry conditions, to the low shear strength of the tribofilms (9 MPa)[96].*

*In the experiments performed in this chapter, we will first compare ambient air with dry sliding conditions by blowing different gases toward the contact (dry nitrogen, dry air, dry argon), under different normal loads. The goal of these experiments is to verify the shear*

*strength hypothesis and compare the chemical composition and structure of the obtained tribofilms. We will refer to this set of experiments as "constant environment".*

*In the second part of this chapter the gas flow will be switched on and off while sliding. The goal is to determine if the friction behavior is reversible when the environment varies from humid to dry or vice versa. This set of experiments will be labeled as "dynamic environment". We will also investigate the chemistry of the tribofilm when the environment is switched from humid to dry and from dry to humid in order to establish a relationship between the reversible friction behavior and the chemistry of the tribofilm.*

# Table of contents: Chapter 3. Influence of humidity on the tribological behavior of a-C:H:Si:O

# 1. Material Characterization

Rutherford backscattering spectrometry (RBS), and HFS (Hydrogen forwards Spectroscopy) were performed on the samples in collaboration with Evans Analytical Group, Sunnyvale, CA, USA. Briefly, the chemical composition of the films was: [C] = 57±3 at.%; [O] = 3±1 at.%; [Si] = 6±1 at.%; [H] = 34±3 at.%. The fraction of $sp^2$-bonded carbon in the as-deposited material was determined to be 0.54±0.02 using NEXAFS spectroscopy and 0.38±0.04 with multiwavelenght (MW) Raman spectroscopy. Knowing that NEXAFS probes the very surface of the material (3 nm)[157] whereas Raman probes deeper (250 nm),[163] these results are not incompatible since amorphous carbon coatings are known to have a more $sp^2$-bonded carbon-like surface layer. The root-mean square roughness of the as-received a-C:H:Si:O films was 1.3±0.1 nm (measured using contact mode AFM over an area of 1x1 $\mu m^2$). The Young's modulus and hardness of the film, measured with a MTS Nano Indenter XP using a continuous stiffness measurement (CSM) method with a Berkovich tip[164,165] were 142±2 GPa and 10±0.2 GPa respectively. Details of characterization results could be found in appendix 1.

Upon UHV annealing, the fraction of $sp^2$-bonded carbon increased to 0.73±0.02 and 0.78±0.04 respectively measured by NEXAFS and Raman. XPS analysis on the annealed sample also revealed an increased line shape asymmetry of the C1s peak, suggesting a progressive clustering and ordering of $sp^2$ carbon sites upon annealing. All the data can be found in appendix 2.

# 2.Tribological behavior of a-C:H:Si:O under constant environment

## 2.1. Role of humidity on the friction

Following the experimental procedure described in chapter 2 (section 1.2.2.2), tribological experiments were performed on a-C:H:Si:O under ambient air and under dry nitrogen, dry air or dry argon flows. As mentioned in the experimental part, while blowing gas toward the contact, the relative humidity RH decreases from about 35% down to less than 5%, independent of the gas.

On the first reference test performed under ambient air (23±1 °C and RH 35±1%), plotted in Figure 3.1.a, the friction starts at 0.30±0.01 and stabilizes at 0.18±0.01 after a running-in period of about 200 sliding cycles.

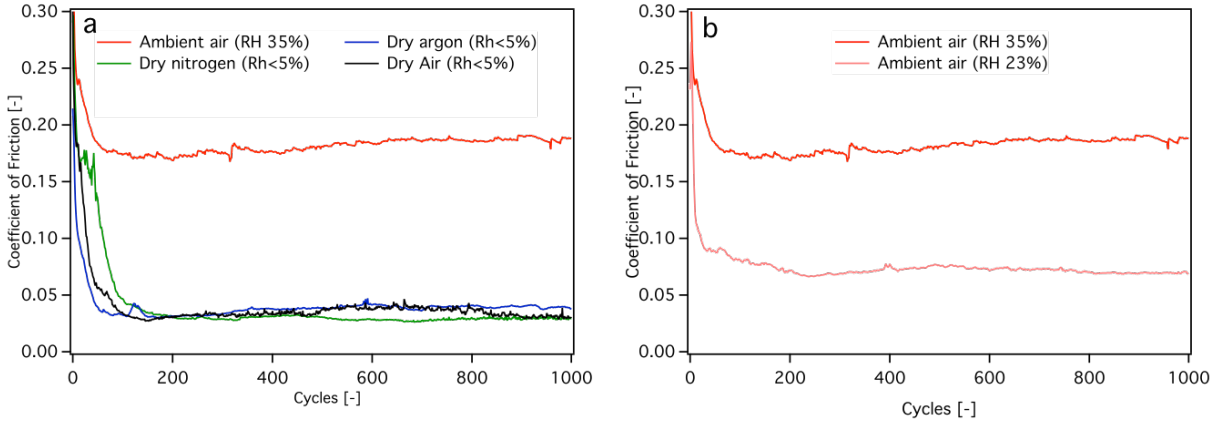


***Figure 3.1. Evolution of the coefficient of friction as a function of sliding cycles for a-C:H:Si:O under (a) ambient air and 5 l/min flows of dry nitrogen, dry argon and dry air (b)ambient air with different relative humidity.***

Under the gas flow (Figure 3.1.a), the initial value of the friction coefficient is comparable to the one in ambient air, but the steady-state friction coefficient is drastically reduced to around 0.03, *i.e.* 6 times lower than the one obtained under ambient air at 35% RH. This lower value is most probably due to the difference in the relative humidity between the two set of experiments. In fact, as discussed in the introduction and illustrated in Figure 3.1.b, lowering the relative humidity results in reducing the frictional response of a-C:H:Si:O. These results are consistent with Scharf's[96] findings. Since the decrease in friction is similar for all the gases blown toward the contact (inert ones, nitrogen or argon, as well as dry air), we can argue that this phenomenon is not related to the chemistry of the gas, but rather to the decrease in the relative humidity induced by the flow of gas around the contact.

## 2.2. Load dependence of the friction under a constant environment

In order to verify the shear strength hypothesis, as presented in the introduction, a set of load dependence friction experiments has been carried out under the four different environment conditions, namely ambient air, constant flow of dry nitrogen, dry air or dry argon, as reported on Figure 3.2. Loads of 1, 2 and 5 N, corresponding to a mean theoretical Hertzian pressure of respectively 380, 480 and 650 MPa, were used for each environment in

order to study the effect of the mean theoretical contact pressure on the friction. At each load, experiments were carried out three times for checking the reproducibility.

The shear strength of the tribofilm was then deduced from a linear fit of a contact mechanics model proposed by Singer *et al.*[77]. In this model, due to the pressure dependence of the mechanical properties of solids at high contact pressures, the shear strength $S$ can be considered as:

$$S = S_0 + \alpha P \qquad \textit{(Eq. 1)}$$

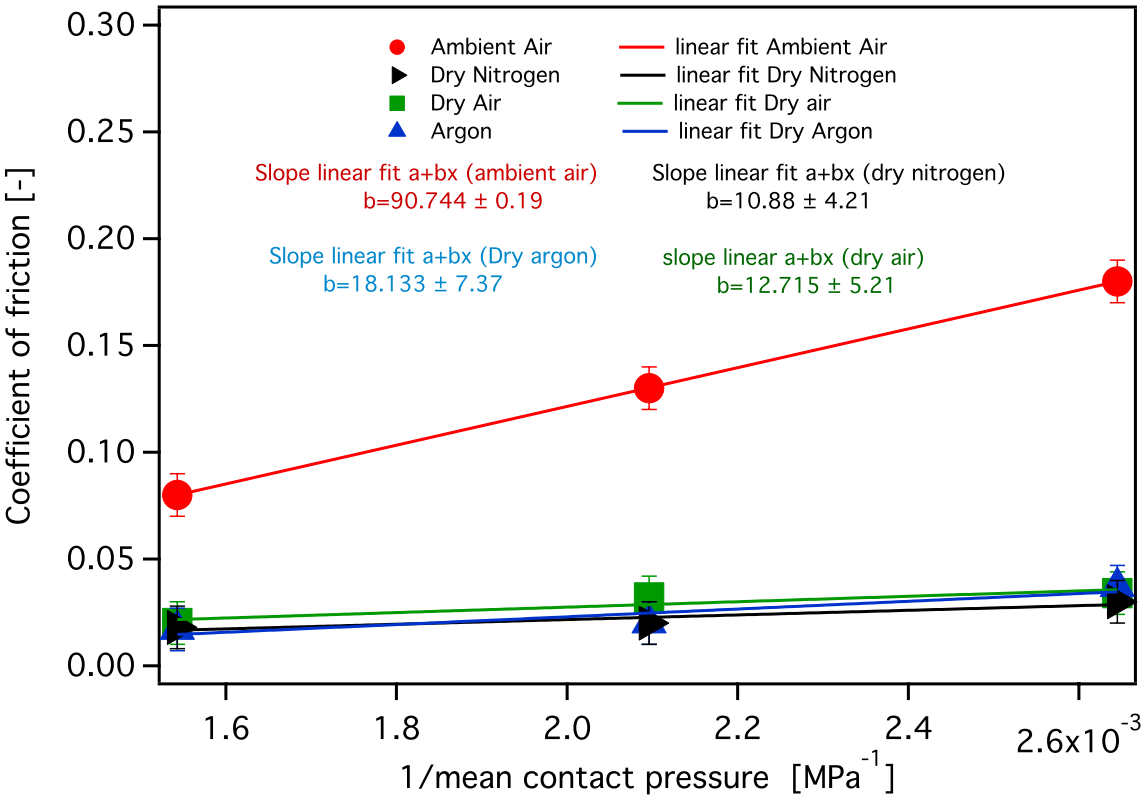


***Figure 3.2. Evolution of the coefficient of friction as a function of the inverse of the mean theoretical Hertzian pressure for a-C:H:Si:O under different environmental conditions, and corresponding linear fits.***

Knowing that the friction force $F_t$ can be reported as[77]:

$$F_t = A.S + F_p \qquad \textit{(Eq. 2)}$$

where $A$ is the contact area and $F_p$ the plowing contribution, which can be neglected in the case of hard materials. The coefficient of friction can then be written as follows:

$$\mu = \frac{F_t}{F_n} = \frac{A.S}{A.P} = \frac{S}{P} \qquad \textit{(Eq. 3)}$$

By combining equation 1 and 3, the load dependence of the coefficient of friction can be written as:

$$\mu = \frac{S_o}{P} + \alpha \qquad \textit{(Eq. 4)}$$

where $P$ is the mean contact pressure and $\alpha$ the pressure dependence of the shear strength.
This model supposes that an easily deformable interfacial material (the tribofilm) is able to distribute the load across the contact. The apparent contact area becomes thus the real contact area, meaning that the friction is mainly controlled by the Hertzian contact conditions[79]. The shear strength of the interface may then be determined by plotting the evolution of the coefficient of friction as a function of the mean contact pressure.
By fitting the pressure dependence of the stabilized friction data of Figure 3.2with equation (4), we were able to determine the shear strength of the tribofilm generated under the different environmental conditions. The shear strength of the tribofilm generated in ambient air was found to be almost 10 times higher than under the one generated under gas flows, namely 90.7±0.2 MPa, 18±7 MPa, 13±5 MPa, 11±4 MPa for respectively ambient air, dry argon, dry air and dry nitrogen. We can clearly notice the high shear strength of the tribofilm obtained under ambient air compared to the one of the tribofilms obtained under dry conditions imposed by the different gas flows. However, there is no difference considering the uncertainty in the shear strength of the tribofilms obtained under these three different gases. It is noticeable that the lowest attainable coefficient of friction deduced from the experiments in ambient air is evaluated at -0.06. This negative value can probably come from the error between the real contact area and the theoretical one that we used, and to a lower extent to subtle changes in the humidity in the room between the experiments at different loads. Also, one has to keep in mind that a relevant value of $\alpha$ is only obtained when the load goes to infinity, which is physically impossible.

From these calculations, we can argue that the tribofilm plays a major role in the decrease in friction of the a-C:H:Si:O films. The low coefficient of friction obtained under gas flows is thus believed, at this step of our investigations, to be a consequence of the low shear strength of the tribofilm. So far, these findings are in accordance with Scharf's[96] results namely the shear strength of a tribofilm obtained under humid environment is higher than the one of a tribofilm generated under dry conditions, resulting in high friction under humid environment and low friction in dry environment. Moreover, in our case, dry environment was distinctively obtained by blowing 3 different gases in the contact, while only dry nitrogen

was used in Scharf's[96] study, strengthening the contention that water vapor is primarily responsible for the modulation of friction.

In the following sections, we will investigate and compare the chemistry and structure of the different tribofilms obtained under different constant environments. Our goal is to provide evidence to support explanations for the different shear strengths that we estimated, and therefore the different coefficients of friction of a-C:H:Si:O in various environments.

## 2.3. Morphology and composition of the tribofilms

The morphology and composition were studied thanks to scanning electron microscopy (ESEM-FEG XL30, FEI-Philips, UK) equipped with energy dispersive X-ray spectroscopy (EDX, SDD Xmax 50 $mm^2$, Oxford Instruments, UK), as described in chapter 2 (section 1.3.1.1).

In Figure 3.3, carbon, silicon and oxygen incorporation in the tribofilm varies depending on the sliding environment. According to the EDX maps, the tribofilm obtained under ambient air is heterogeneous, containing mainly silicon and oxygen in the expected Hertzian contact area and surrounded by carbon, while the one obtained under dry nitrogen is homogeneous, mostly made of carbon with much less silicon and oxygen. So far, these results are consistent with Scharf's[96] findings.

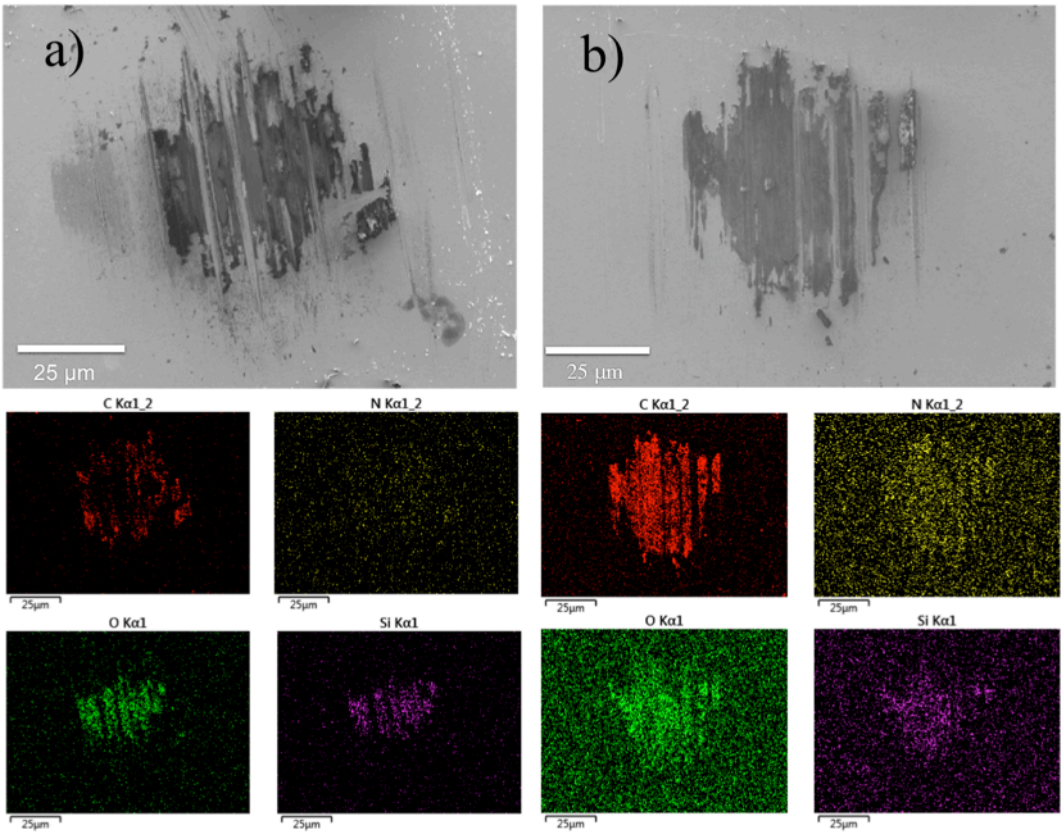


***Figure 3.3. SEM micrographs with the corresponding EDX maps of the tribofilms obtained (a) under ambient air and (b) under dry nitrogen flow.***

However, the EDX maps on tribofilms obtained under dry air or dry argon environment, on Figure 3.4, reveal that for both environmental conditions, the tribofilm is an intimate admixture of carbon, silicon and oxygen, with at least as much silicon and oxygen as in the tribofilm obtained under ambient air, despite very different friction evolutions.

It can also be noticed that the tribofilm obtained under dry air is much thicker than the one obtained under the other conditions and concentrated in the theoretical Herztian contact area. Assuming that the growth of the tribofilm is due to material removal from a-C:H:Si:O, the thick tribofilm obtained under dry air conditions seems to point towards a different wear rate in the case of dry air.

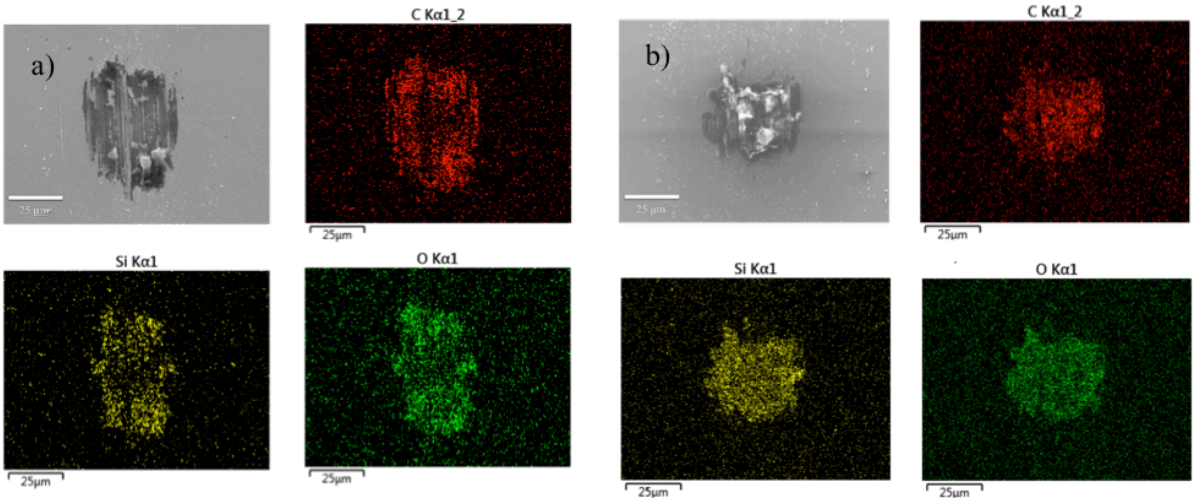


***Figure 3.4. SEM micrographs with the corresponding EDX maps of the tribofilms obtained (a) under argon flow and (b) under dry air flow.***

In summary, even though under dry argon and dry air, the relative humidity in the contact decreased down to less than 5%, like with dry nitrogen, there is a high amount of silicon and oxygen in the tribofilms. The amount of silicon and oxygen is close to the one obtained under ambient air, yet the shear strength of tribofilms obtained under dry argon flow and dry air flow is similar to the one of the tribofilm obtained under dry nitrogen flow and about a decade lower than the one of the tribofilm obtained under ambient air. Therefore, other facts than the composition must be considered to account for the observed shear strengths. Indeed, the structure of the carbon phase in the tribofilm is known to be critical in the frictional response of amorphous carbon films[54].

## 2.4. Structural changes in the carbon phase of the tribofilms and wear tracks

In order to investigate the structure of the carbon phase in the tribofilms obtained under different environments, we used UV Raman. Raman analyses were performed following the experimental approach described in chapter 2, section 1.3.2.1.2. All Raman analyses on the tribofilms were carried out at a single wavelength (325 nm) on the fact that Raman spectra acquired using UV wavelength are less affected by the photoluminescence background than the ones acquired using visible wavelengths. The wear tracks on the flat were analyzed using the four different wavelengths, allowing the computation of potential changes in the $sp^3$ fraction, using the procedure described in section 1.3.2.1.2 of chapter 2.

### 2.4.1. Analysis of the tribofilms and wear tracks by UV Raman

Figure 3.5 displays the Raman spectra acquired at 325 nm in the central and lateral parts of the different tribofilms, as well as the reference spectra acquired on the as-received and worn a-C:H:Si:O. The higher intensity of the spectra acquired inside and outside the wear track on the flat is mainly due to the higher Raman power that we applied as specified in chapter 2. From these spectra, it can be noticed that whatever the environment, there are significant differences between the tribofilm and the original or worn a-C:H:Si:O.

According to Casiraghi *et al.*[140], there are two reliable methods for fitting the Raman spectra in order to extract typical characteristics, such as the position of the D and G peak, their relative intensities, or the full width at half maximum (FWHM) of the G peak: the Gaussian fit and the Breit Wigen-Fano (BWF). Due to the significant photoluminescence background observed in the Raman spectra of a-C:H:Si:O, especially in visible Raman, BWF fitting method did not seem suitable for our data, since this method tends to adjust its asymmetry in order to recover a part of the photoluminescence[140]. We thus used a Gaussian fit of the G peak to extract its position, *Pos(G)*, from the Raman spectra acquired at 325 nm on the different tribofilms. The corresponding data are reported in Table 3.1.

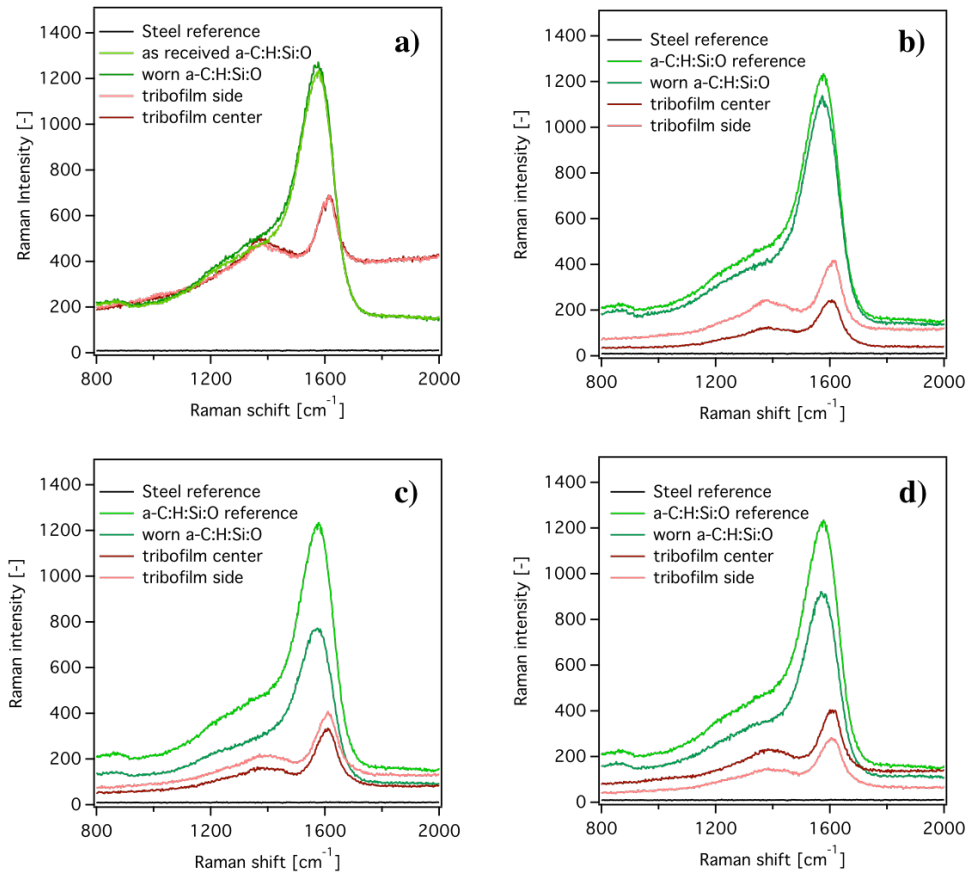


***Figure 3.5. Raman spectra at 325 nm wavelength, on as-received and worn a:C:H:Si:O and on the corresponding tribofilms, after tribological experiment against 52100 steel ball performed (a) under ambient air, (b) under dry nitrogen flow, (c) under dry air flow and (d) under dry argon flow.***

The values reported in table 3.1 show that the position of the G peak inside the a-C:H:S:O wear tracks obtained in ambient air, or under dry nitrogen, dry argon or dry air flows, doesn't change significantly. We can thus argue that there is no big structural difference between the worn and unworn material, in the volume probed by Raman. On the contrary, a significant drift of *Pos(G)* is observed toward higher wavenumbers in the tribofilms, which can be understood either as a clustering of the $sp^2$-bonded carbon atoms in the tribofilms or a decrease in $sp^3$ fraction followed by an increase in $sp^2$ chains and a decrease in bond disorder [10,133,138], as described in chapter 2, section 3.2.1.1.

| | *G peak position ($cm^{-1}$) Ambient air* | *G peak position ($cm^{-1}$) Dry nitrogen* | *G peak position ($cm^{-1}$) Dry air* | *G peak position ($cm^{-1}$) Argon* |
|---|---|---|---|---|
| *As received a-C:H:Si:O* | *1573.2±0.2* | *1573.2±0.2* | *1573.2±0.2* | *1573.2±0.2* |
| *Worn a-C:H:Si:O* | *1573.5±0.2* | *1572.8±0.2* | *1570±0.3* | *1572.4±0.2* |
| *Tribofilm center* | *1609.8±0.3* | *1602.5±0.2* | *1605.9±0.2* | *1607.7±0.2* |

***Table 3.1. G peak positions extracted by a Gaussian fit from Raman spectra on as-received a-C:H:Si:O, on worn a-C:H:Si:O and on the central part of the tribofilm, after tribological experiments under ambient air and under dry nitrogen, dry air and dry argon flows.***

At this stage, thanks to the Raman spectroscopy, we believe that the tribofilm is a material transferred from the worn region of a-C:H:Si:O to the steel ball, but having a different structure.

Nevertheless, the G peak position of the tribofilms after tribological experiments in the four different environmental conditions seems to be very close. This suggests that there is no significant difference in the size and shape distribution of the $sp^2$-bonded carbon clusters present in the tribofilm. Nevertheless, the differences in their calculated shear strengths suggest that their compositions and/or structures might be different.

Extending the Raman analysis to consider the intensity ratio between the D and G bands, and the FWHM of the G band allows a better characterization of the different tribofilms. Indeed, as detailed in chapter 2 section 2.3.2.1.1, it has been shown[139]that the ratio between the intensities of the two main bands I(D)/I(G) is related to the size of $sp^2$-bonded carbon atoms organized in rings[133,139,140]. The size of the excited $sp^2$-bonded ring-like carbon clusters is related to a given Raman excitation energy (the wavelength),*i.e.* small $sp^2$-bonded ring-like clusters are excited by low Raman wavelength and bigger clusters, by higher Raman excitation energy (higher wavelength). Thus, an increase in I(D)/I(G) is a signature of an increase in the size of the $sp^2$ ring-like carbon clusters and vice-versa.

On the other hand, the FWHM of the G band is a measurement of the structural disorder, in bond lengths and in bond angles[133,138–140]. Thus, low values of the FWHM of the G band could be understood as defect free or unstrained $sp^2$ clusters whereas high values of FWHM of the G band reveal a high bond length and bond angle disorder of the $sp^2$ bonded carbon atoms, *ie*, strained $sp^2$ ring-like carbon atoms. Figure 3.6 shows an example of a typical Gaussian fit of the Raman spectra on the tribofilm obtained under dry nitrogen.

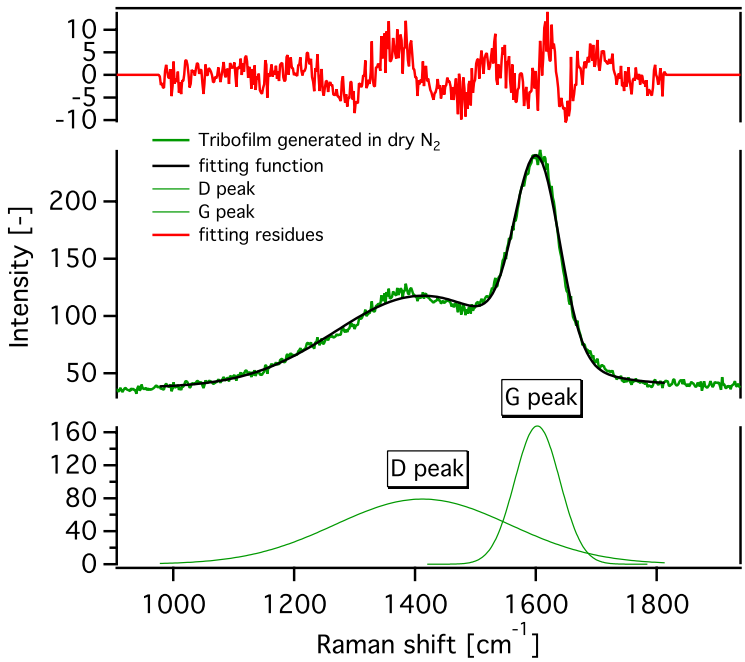


***Figure 3.6. Gaussian fit of a Raman spectrum acquired at 325 nm on a tribofilm obtained after sliding a-C:H:Si:O against a 52100 steel ball under dry nitrogen flow.***

Figure 3.7 reports the FWHM of the G band and the I(D)/I(G) ratio for the tribofilms obtained under various environmental conditions. From these plots, we can notice a high FWHM of the G peak for all the tribofilms obtained under gas flow compared to the one obtained under ambient air. Tribofilms obtained under dry conditions also exhibit a relatively lower I(D)/I(G). In summary, under dry conditions, the $sp^2$-bonded ring-like carbon clusters in the tribofilm are relatively smaller and more strained than the ones found in the tribofilm obtained under ambient air.

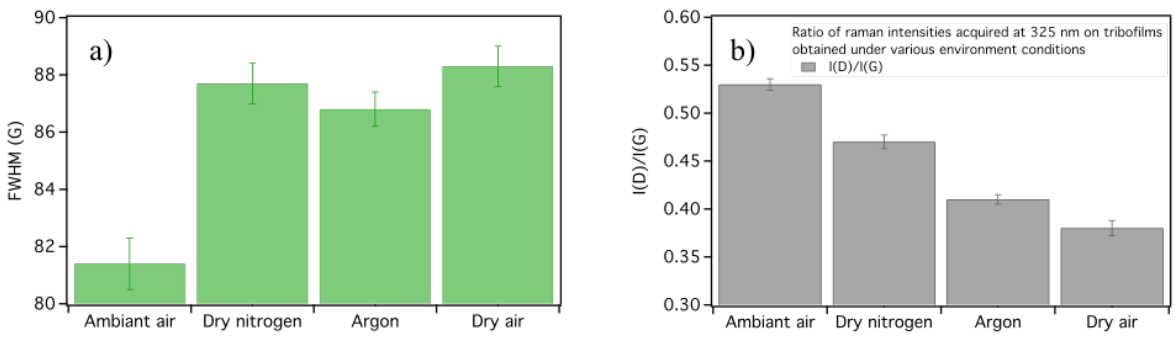


***Figure 3.7. FWHM (G) and I(D)/I(G) extracted from a Gaussian fit of the Raman spectra on tribofilms obtained under ambient air, dry nitrogen, argon and dry air at 325 nm.***

### 2.4.2. Analysis of the wear tracks on a-C:H:Si:O by Multi-Wavelength Raman

Using Multi-Wavelength Raman with the Gaussian fitting procedure described above, we were able to extract the *Pos(G)* for each of the 4 Raman wavelengths from UV to near infrared, and this, for as-received a-C:H:Si:O and for the wear tracks obtained on it after sliding in ambient air and under dry nitrogen, dry argon and dry air flows.

Following the methodology described by Rose *et al.*[138], we deduced the dispersion of the G peak, *Disp(G)* ($cm^{-1}$/nm), by quantifying the slope of a linear fit of the G peak position, *Pos(G),* as a function of the wavelength. The standard deviations of the Pos(G) were 0.2, 0.5, 0.5 and 0.7 for 325 nm, 442nm, 488nm and 633nm Raman wavelengths respectively.

The fraction of $sp^3$-bonded carbon atoms, $f_{sp3}$, was then deduced from the empirical formula proposed by Cui *et al.*[142] for hydrogenated DLC coatings, which is as follows:

$$\boldsymbol{f_{sp^3} = -0.07 + 2.5 \times Disp(G) \pm 0.06} \qquad \textit{(Eq. 5)}$$

The last term of the equation is the standard deviation related to the linear fit as deduced from the empirical method used by Cui *et al.*[142].

Figure 3.8 shows the linear fit results of *Pos(G)* for the wear tracks obtained under the four different environments and the corresponding values of *Disp(G)*. These values and the corresponding $sp^3$-bonded carbon fractions are gathered on Table 3.2, for as-received a-C:H:Si:O and the wear tracks obtained after sliding in ambient air and under dry nitrogen, dry air and dry argon.

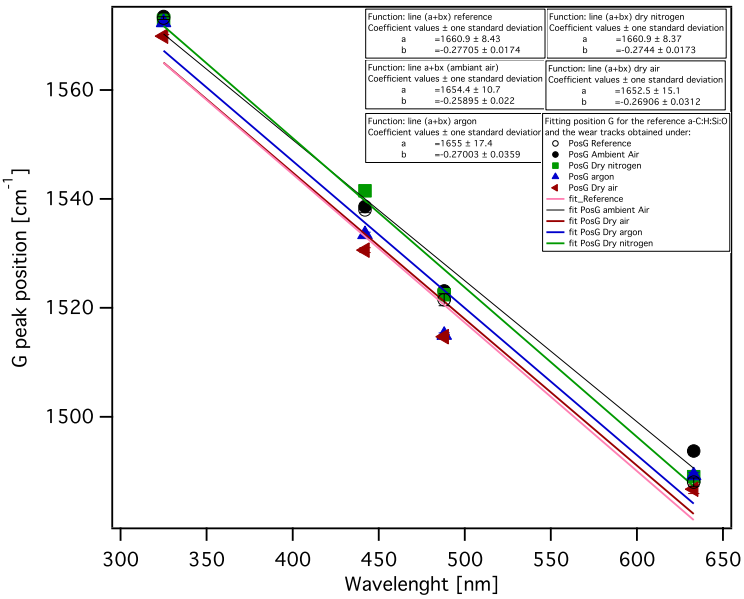


***Figure 3.8. Calculation of* Disp(G) *from the linear fit of* Pos(G) *for spectra acquired at 325, 442, 488 and 633 nm, on as-received a-C:H:Si:O sample and on the wear tracks obtained after sliding in ambient air and under dry nitrogen, dry air and dry argon flows***

| | *Reference* | *Ambient air* | *Dry nitrogen* | *Dry air* | *Dry argon* |
|---|---|---|---|---|---|
| *Disp (G)* | *0.2770±0.0174* | *0.2589±0.0220* | *0.2744±0.0173* | *0.2690±0.0312* | *0.2700±0.0359* |
| $f_{sp}^3$ | *62±4* | *58±5* | *62±4* | *60±7* | *60±8* |

***Table 3.2. Summary of disp(G) and the fraction of sp$^3$-bonded carbon atoms calculated using MW Raman on the reference a-C:H:Si:O as well as inside the wear track obtained after the friction test under ambient air, dry nitrogen, dry air and dry argon.***

For the as-received a-C:H:Si:O sample, the sp$^3$-bonded carbon fraction is evaluated at 62±4% using MW Raman. Such value is not in agreement with the one obtained by NEXAFS spectroscopy, at 46±2%. Two reasons can be brought forward to account for such discrepancy:

- *Heterogeneity in the film: indeed, NEXAFS spectroscopy probes the very surface of the coating (approximately the first 3 nm[157]) while Raman probes deeper in the coating (with an optical mean free path of approximately 250 nm[163]);*
- *The role of additional elements on the measured values: the method we used for estimating the sp$^3$-bonded carbon fraction from MW Raman data was developed for pure hydrogenated amorphous carbon coatings, without any additional element.*

Despite these uncertainties, we estimated the $sp^3$-bonded carbon fraction after sliding in ambient air and under dry nitrogen, dry air and dry argon flows, as reported in Table 3.2. As discussed in chapter 1, by using both molecular dynamic simulations and experiments, several authors[39,65,71,166–169] have reported that for carbon-based amorphous materials, a stress-induced conversion from $sp^3$- to $sp^2$-bonded carbon occurs upon sliding. In our case, for a-C:H:Si:O sliding under the four different environmental conditions, we could only notice a very small difference in the *Disp(G)* values. As it can be seen on Figure 3.9. Calculated $sp^3$-bonded carbon fraction on the as-received a-C:H:Si:O and inside the wear tracks obtained in ambient air and under dry nitrogen, dry air and dry argon flow., no clear tendency on the amount of $sp^3$-bonded carbon could be extracted from these results.

This suggests that any potential friction-induced structural change that might have occurred is below the resolution of Raman analysis, *i.e.* such structural changes would be in the very surface region that only a very surface sensitive analysis could reveal.

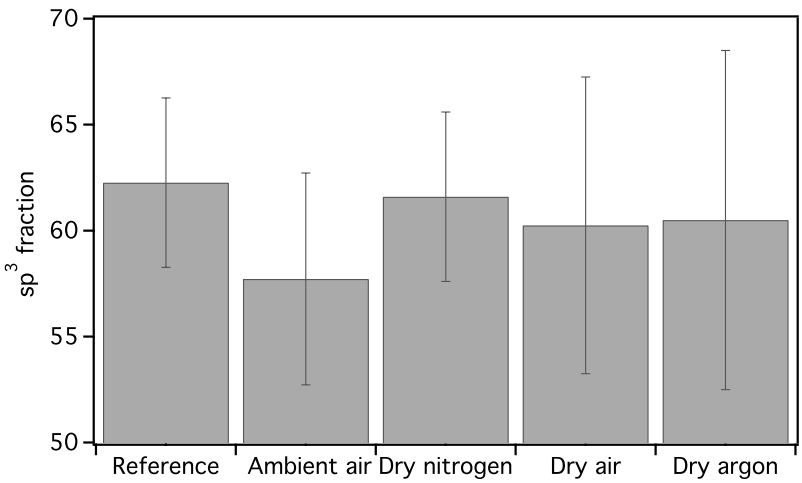


***Figure 3.9. Calculated $sp^3$-bonded carbon fraction on the as-received a-C:H:Si:O and inside the wear tracks obtained in ambient air and under dry nitrogen, dry air and dry argon flow.***

## 2.5. Quantifying the wear by optical interferometry and AFM

White light interferometry was used to study the morphology of the wear tracks produced by the tribological experiments run in ambient air and under dry nitrogen, dry air and dry argon flows following the experimental details given in chapter 2, section 3.1.2. However, to ensure that the potential stress-induced phase transformation from $sp^3$- into $sp^2$-bonded carbon, and the consequences in the optical gap[3] that it can generate, doesn't induce

errors in the measurements, these wear tracks were also observed by Atomic Force Microscopy (AFM) in contact mode.

On Figure 3.10 AFM and interferometry images of the wear tracks, obtained under the different environments, are compared. From each image, we extracted a relative depth profile taken at the middle of the wear tracks. These depth profiles are gathered in Figure 3.11

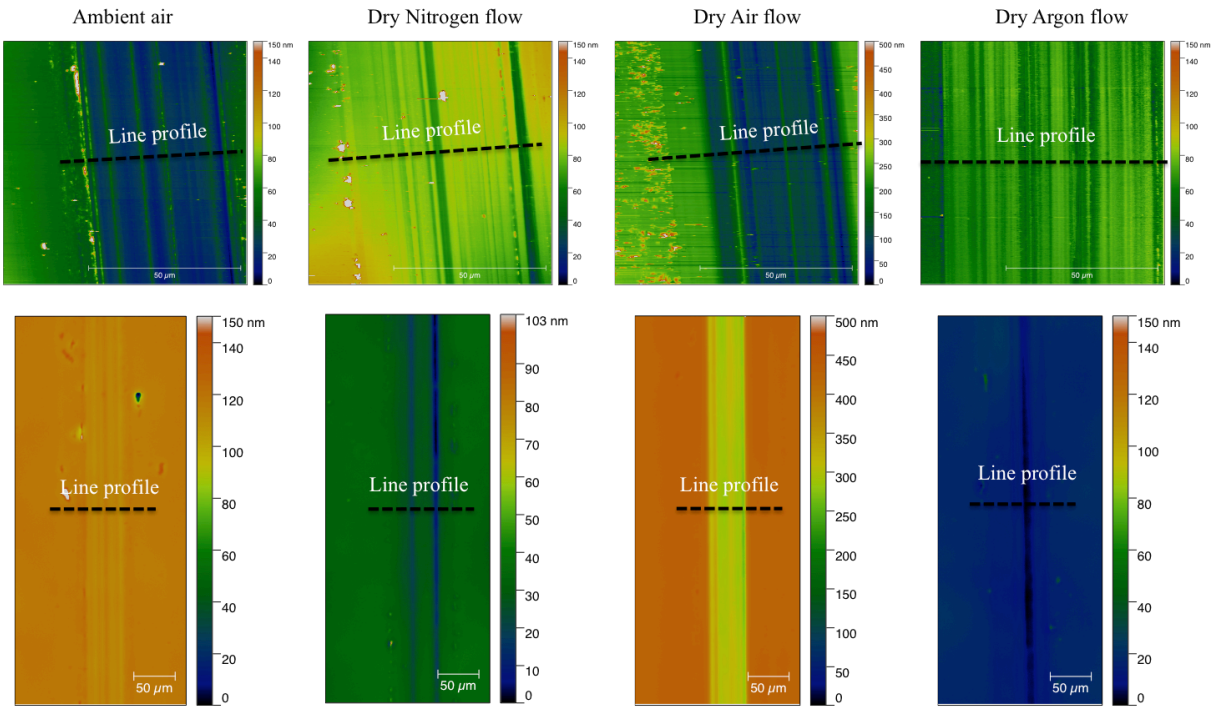


***Figure 3.10. Comparison of AFM (left) and white light interferometry (right) images of the wear tracks obtained on a-C:H:Si:O after sliding under various environmental conditions.***

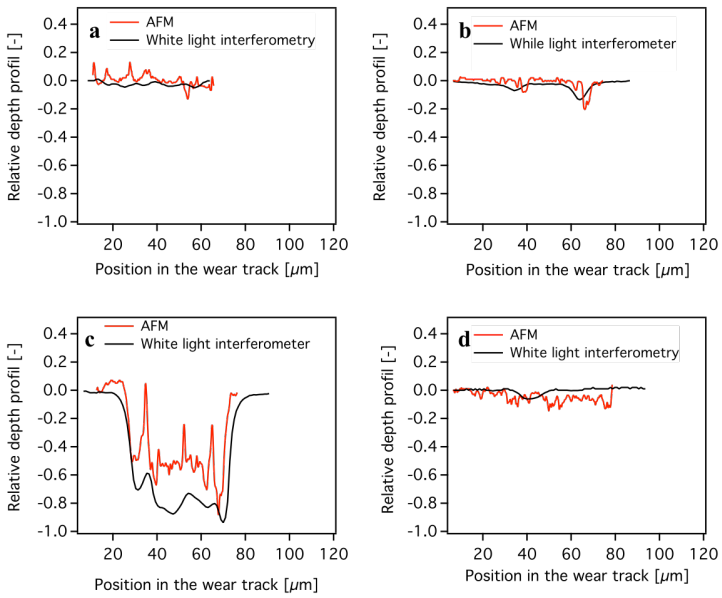


***Figure 3.11. Comparison of the relative depth profiles, measured by AFM and white light interferometry, of the wear tracks obtained on a-C:H:Si:O after sliding (a) in ambient air, and under (b) dry nitrogen flow, (c) dry air flow and (d) dry argon flow***

From Figure 3.10 and Figure 3.11 it can be clearly seen that there is very low wear of the coating when sliding in ambient air or under dry nitrogen or dry argon flows. On the contrary, drastic wear can be observed under dry air flow. This higher wear seems thus related to the thicker tribofilm observed in section 1.3.4. Knowing that the amount of oxygen in the contact while blowing dry air is higher than the one under dry nitrogen and dry argon, we can argue that in dry conditions, oxygen promotes a higher wear of a-C:H:Si:O coating. A careful analysis of the role of oxygen in the tribological behavior of a-C:H:Si:O will be presented in chapter 4.

Thanks to this systematic study of the wear tracks, we can compare the two techniques: AFM and white light interferometry. Better lateral resolution of the AFM images may help in quantifying the worn volumes more accurately. However, the results of white light interferometry are not too far from the AFM ones, and this technique is much faster to implement and allows the sampling of a representative fraction of the wear track volume, which allows the measurement of a considerable number of wear tracks in a reasonable time. In the remainder of this document, we will only use white light interferometry for wear characterization.

# 3. Reversible friction behavior of a-C:H:Si:O coatings in dynamic environments

## 3.1. Tribological behavior of a-C:H:Si:O in dynamic environment

From the static environment analysis, we were able to demonstrate that the shear strength of the tribofilm is mainly controlled by the carbon amount in the tribofilm and its structure. We were also able to show that the carbon amount and its coverage in the tribofilm increase while switching the environment from humid to dry. In this section, we will address two key questions:

- *What would be the frictional response of a-C:H:Si:O when the environment is quickly changed from humid to dry and reverse?*
- *What are the chemical and structural changes occurring in the tribofilm upon a quick change of the sliding environment?*

Figure 3.12 presents the evolution of the friction coefficient of a-C:H:Si:O sliding against 52100 steel under dynamic gas flows. When the friction experiment starts in ambient air (red curve), the running-in period lasts about 400 sliding cycles before reaching a steady-state friction at ~ 0.1. Then, each time the nitrogen gas is blown in the contact, the friction coefficient decreases from ~ 0.1 to ~ 0.04 within about 40 sliding cycles, and remains at this low value until the nitrogen flow stops. When the friction experiment starts in dry nitrogen (pink curve) the running-in period lasts about 40 cycles before reaching a steady-state friction at ~0.04. When the nitrogen flow stops, the friction coefficient increases to reach ~ 0.1 and is stabilized at this value until the nitrogen flow restarts. Each time the nitrogen flow stops, a fast increase of the friction coefficient, back to ~ 0.1 within about 40 cycles, is observed. These alternating phases for the friction coefficient last until the end of the friction test (3000 sliding cycles).

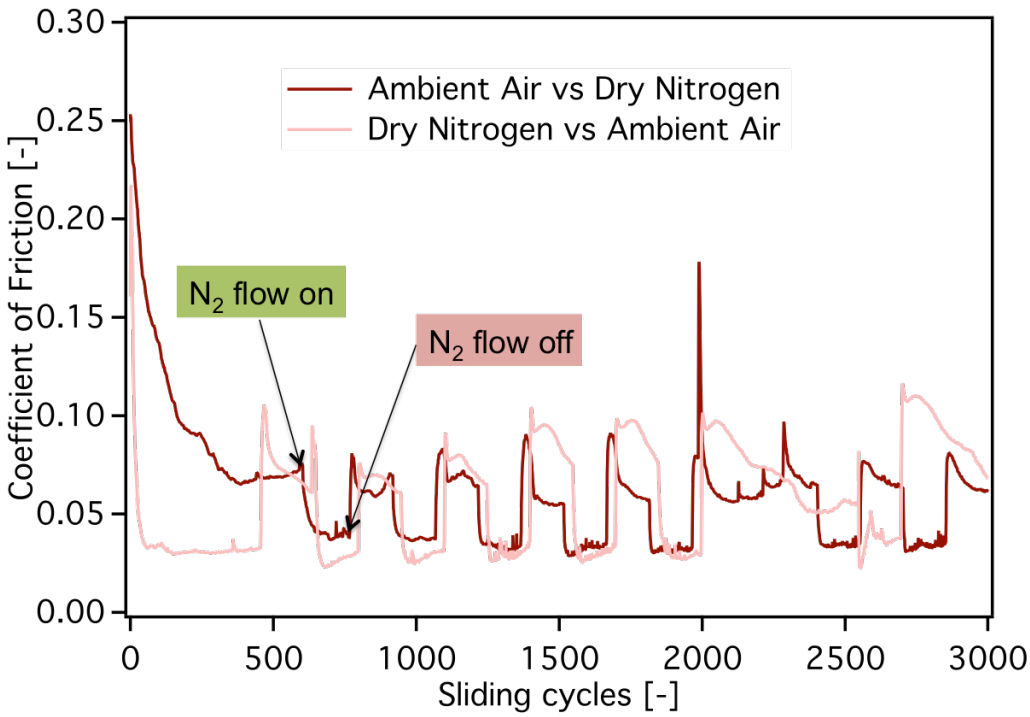


***Figure 3.12. Evolution of the coefficient of friction for a-C:H:Si:O sliding against 52100 steel under dynamic flow of nitrogen gas, the experiments starting either in ambient air (red curve) or in dry nitrogen (pink curve).***

Notice that upon a sudden change of the environment, an accommodation time is needed before reaching a steady-state friction and this explains the "shoulders" that can be observed in the friction behavior every time the environment is changed.

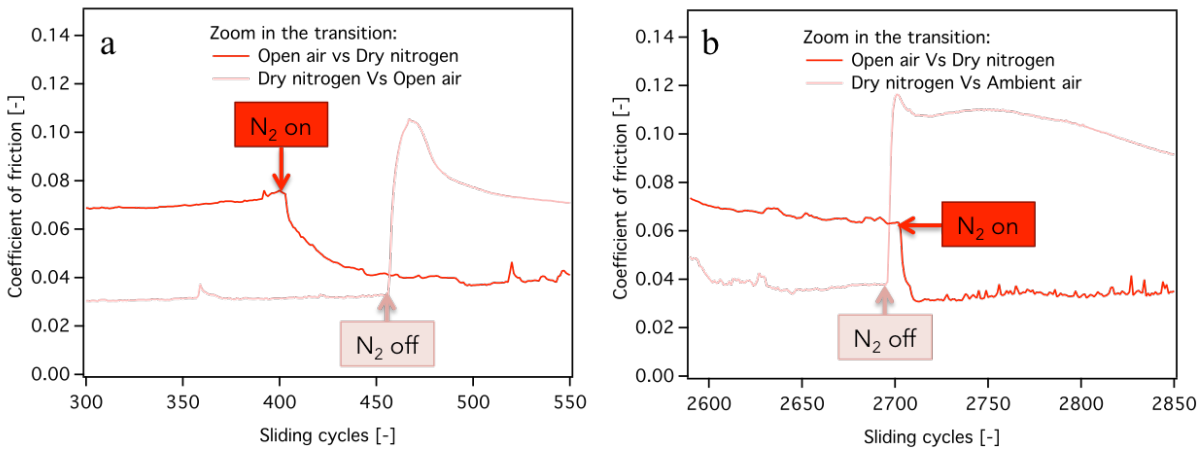


***Figure 3.13. Detailed evolution of coefficient of friction for a-C:H:Si:O sliding against 52100 steel under a dynamic nitrogen flow (from Figure 12), (a) transition between high and low friction regimes for friction test started in ambient air (red) and dry nitrogen (pink) early in test. (b) transition at the end of the experiments.***

One transition (Figure 3.13.a) early in the friction experiments (from 300 to 550 cycles) shows that when nitrogen is blown into the contact sliding in ambient air, the transition from high (0.1) to low friction (0.04) requires around 80 sliding cycles while when near the end of the experiment (Figure 3.13.b), the transition requires only 15 sliding cycles.

A similar observation can be made for the friction test started in dry nitrogen. When the nitrogen flow is stopped near the beginning of the friction test, it requires about 40 sliding cycles to increase from low friction (0.04) to high friction (0.1). Near the end of the test, the transition time decreased down to 15 sliding cycles.

Knowing that near the end of the friction test (from 2600 to 2850 sliding cycles) the sliding environment becomes dryer due to the long time exposure of the contact to the gas flow, we can argue that the transition time required to switch from high to low friction regime and the reverse is shorter in relatively dry conditions. This means that the structural and chemical phenomena that might induce this reversible friction behavior occur faster in dry environment than in ambient.

The reversible friction behavior tests have been performed 3 times in order to check the reproducibility and in all cases, this effect on the friction has been confirmed throughout the whole duration of the test (3000 cycles). Likewise, as reported on Figure 3.14 the same phenomena have been observed when using dry argon or dry air.

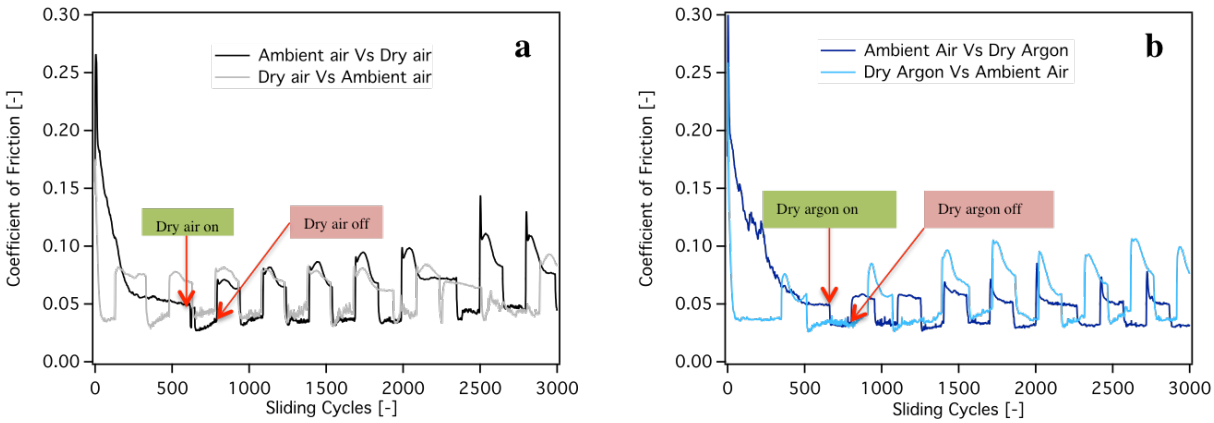


***Figure 3.14. Evolution of coefficient of friction for a-C:H:Si:O sliding against 52100 steel under (a) a dynamic argon gas flow and (b) a dynamic dry air flow.***
***Black curve and dark blues curves correspond to experiments starting in ambient air, while gray and blue curve correspond to experiments starting under gas flow.***

In order to track any tribochemical reaction that may account for the humidity induced reversible friction behavior of a-C:H:Si:O, experiments were performed while alternating the environment only once or twice (Figure 3.15), in order to end the experiment in each environment. An experiment was thus started in ambient air, and switched to nitrogen gas flow after the running-in period, resulting in low stabilized friction at the end of the experiment. We will refer to this experiment in the following as *"ambient air vs. dry nitrogen bottom"*. An experiment was performed in the same way, but was continued by a switch back to ambient air environment, resulting in high stabilized friction at the end of the experiment. We will refer to this experiment as *"Ambient air vs. dry nitrogen top"*. Two additional experiments were performed, in ambient air and under dry nitrogen flow, for 1000 cycles, as references (not shown).

In order to limit the amount of experiments and the corresponding chemical analysis, the "bottom" and "top" friction tests were performed only with dry nitrogen flow. Experiments were performed under a relative humidity in the experimental room of 32±1%, at 25±1°C.

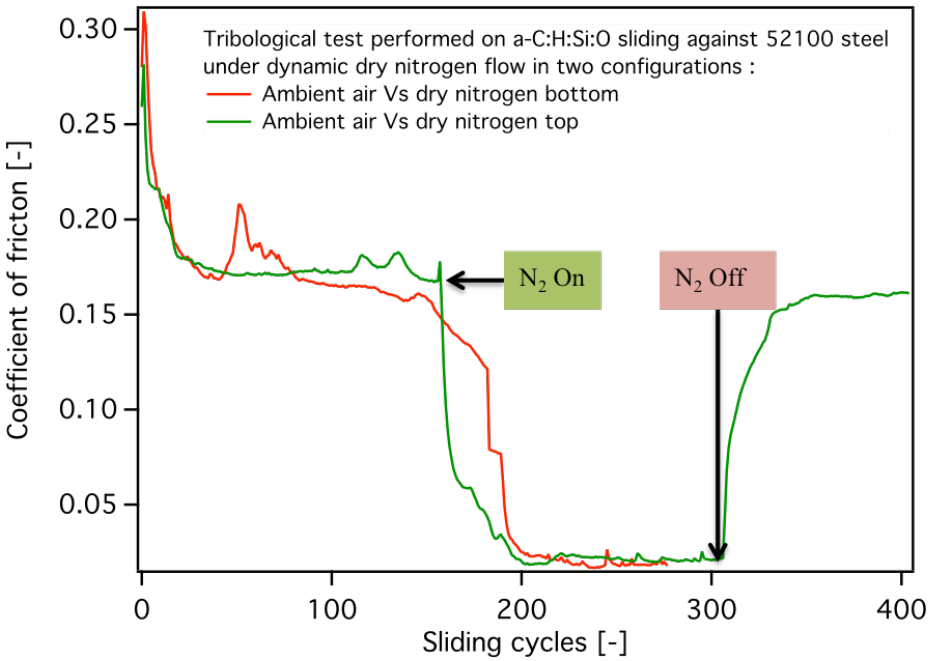


***Figure 3.15. Evolution of coefficient of friction for a-C:H:Si:O sliding against 52100 steel under a dynamic nitrogen flow. Two cases are plotted: bottom (green) and up (red).***

For both cases, "bottom" and "top", the friction coefficient reached its steady state after about 200 sliding cycles in ambient air, before nitrogen was blown toward the contact, thus resulting in the decrease in the friction down to ~ 0.03.

## 3.2. Investigating the structure of the tribofilms obtained in "bottom" and "top" configurations

### 3.2.1. Morphology and composition of the tribofilms

As illustrated in Figure 3.16 below, SEM and EDX observations reveal that the tribofilms generated in "bottom" and "top" configurations are made of carbon, silicon and oxygen, as expected. In the "top" configuration, carbon is being pushed out of the contact area where silicon and oxygen signals are strong and the carbon signal is weak. In the bottom configuration, there is no clear separation of the elements in the central part of the tribofilm, but rather an intimate mixture.

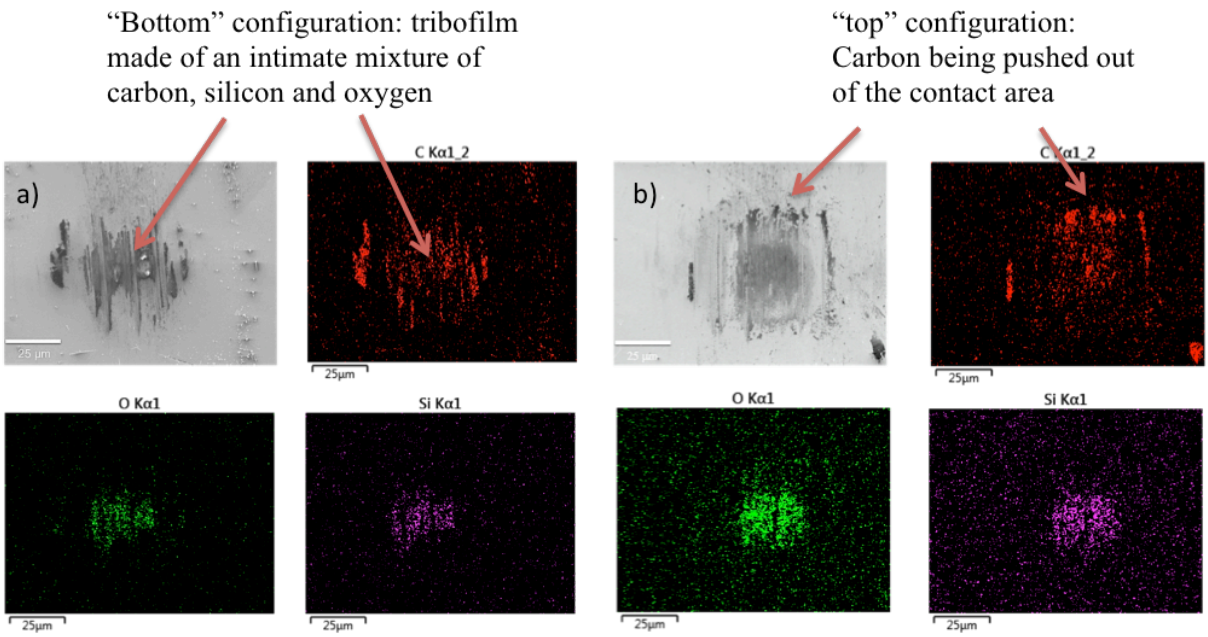


***Figure 3.16. SEM observations and EDX analysis on the tribofilms generated (a) in bottom and (b) in top configurations.***

This suggests that during the transition time of 40 sliding cycles between the "bottom" configuration and the "top" configuration, the friction varies from ~ 0.03 to ~ 0.18 concomitantly with the removal of carbon from the central part of the tribofilm.

### 3.2.1. Structural characterization of the tribofilms by UV Raman

Figure 3.17 shows the Raman spectra acquired at 325 nm on the tribofilms obtained under bottom and top configurations compared to the two references (ambient air and dry nitrogen). It can be noticed that the *Pos(G)* did not change for the 4 different tribofilms. Nevertheless, there is a difference in the photoluminescence background that may depend on different parameters, including a different organization of the $sp^2$-bonded carbon ring clusters[138].

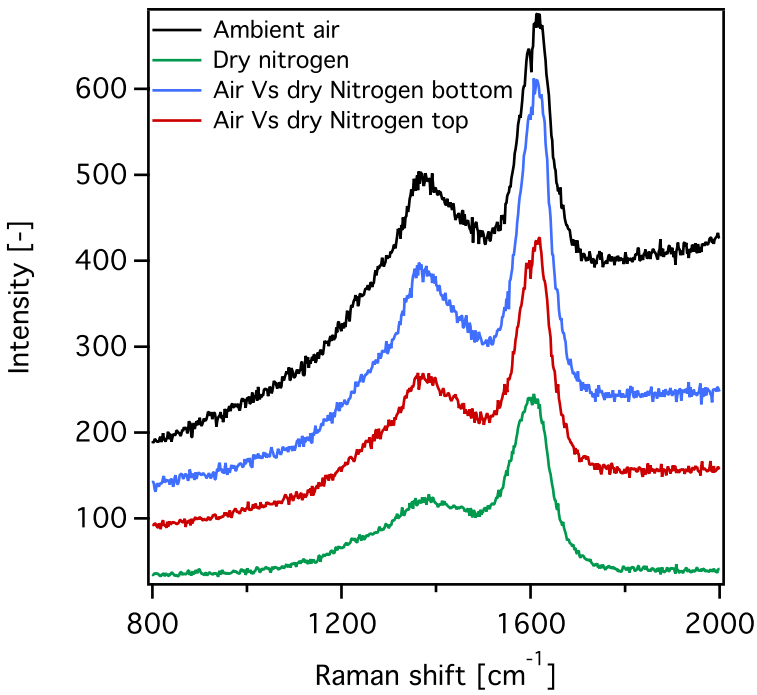


***Figure 3.17. Raman spectra acquired at 325 nm on the tribofilms obtained in bottom and up configurations, in ambient air and under constant dry nitrogen flow.***

Further Raman analysis have been performed on the tribofilms obtained in "bottom" and "top" configurations by analyzing the Full Width at Half Maximum (FWHM) of the G peak and the I(D)/I(G) as illustrated in Figure 3.18. These analyses could not provide us with any information on the differences between the two corresponding tribofilms since both their FWHM of G peak and I(D)/I(G) are very close. Nevertheless, the values obtained for FWHM of G peak and I(D)/I(G) for bottom and top configuration are close to the one of the test performed under constant nitrogen flow. This may suggest that the overall structure of the $sp^2$-bonded carbon atoms in the tribofilms generated under dry nitrogen flow is close to the one of "bottom" and "top" configurations.

Knowing that the data is a normalized signal issued from the probed volume by Raman, we believe that there might be some changes in the tribofilms' structure as suggested by the EDX analysis but these differences might be under the resolution of the UV Raman. We used then XPS to analyze the four different tribofilms.

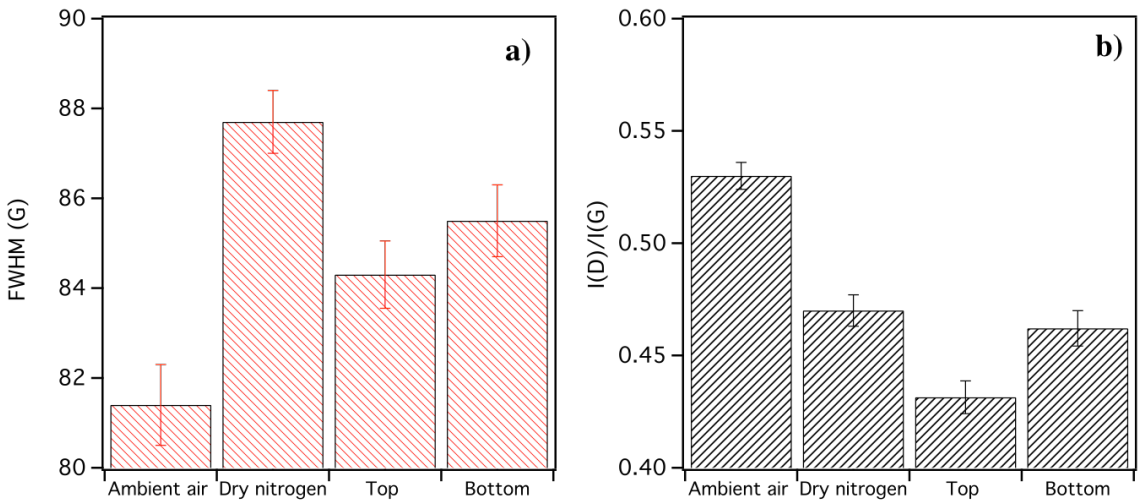


***Figure 3.18. (a) FWHM of the G peak and (b) I(D)/I(G) ratio from Raman spectra of the tribofilms obtained under ambient air, dry nitrogen, bottom and up conditions.***

### 3.2.3. Surface analysis of the tribofilms by XPS

The tribofilms produced by the tribological experiments in "bottom" and "top" configurations were analyzed using the Quantera PHI XPS apparatus described in chapter 2. The measurements were performed under UHV (<$10^{-7}$ Pa) with a depth sensitivity lower than 10 nm, as described elsewhere[108,152,153]. One must underline the fact that the spot size used for the XPS was only 20 µm while the tribofilm covers all the contact area (diameter of 60 µm) and beyond, *i.e.* these measurements may not be representative of the entire tribofilm. Nevertheless, we were able to quantify the atomic concentrations of carbon, nitrogen, oxygen, silicon and iron on the surface of the different tribofilms, as shown in Figure 3.19.

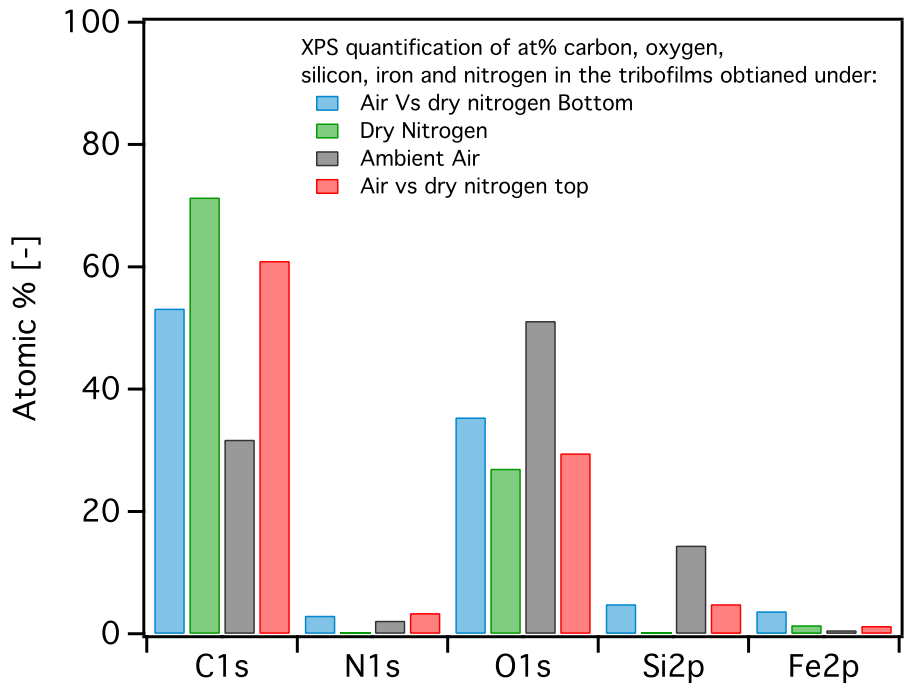


***Figure 3.19. XPS quantification of carbon, oxygen, silicon, nitrogen and iron content in the tribofilms obtained under various environmental conditions.***

The XPS quantification shows a clear delineation in tribofilm compositions. In ambient air, the surface of the tribofilm is a mixture of silicon, oxygen and carbon while the one obtained under dry nitrogen flow is mostly made of carbon. This result supports the previous ones obtained using EDX and explained in section 3.2.1. Only very few differences between the tribofilms obtained upon sliding in "bottom" and "top" configurations can be noticed. There are no big differences in carbon, oxygen and silicon amount for the two tribofilms but their overall composition is closer to the one of the tribofilm obtained under dry nitrogen.

In this section, by means of SEM/EDX, UV Raman and XPS analysis of the tribofilms generated under "bottom" and "top" configuration, we were able to highlight the fact that the presence of carbon in the Hertzian contact area is related to a decrease of the friction coefficient. The low coefficient of friction obtained under dry environment correlates with an abundance of carbon in the contact area while under humid condition, the relatively high coefficient of friction correlates with a special segregation of carbon towards the sides of the contact.

# 4. Summary

Thanks to constant environment friction tests, especially the one performed under dry air, we were able to point out in this chapter that in absence of water vapor, oxygen promotes the wear of a-C:H:Si:O resulting is the generation of a thick tribofilm on the steel counterbody. Dynamic friction tests allowed us to highlight the predominant role of water vapor in controlling the frictional response of a-C:H:Si:O upon sliding against 52100 steel. We also underlined the fact that the amount of silicon and oxygen in the tribofilm does not seem to be crucial for controlling the frictional response of a-C:H:Si:O coatings as suggested by the main existing work[96] that focused on the fundamental mechanisms of friction of a-C:H:Si:O films. In fact we were able to show that only the presence of carbon in the contact area and its structure modulates the shear strength of the tribofilm and thus the coefficient of friction. Both EDX and XPS performed on "bottom" and "top" tribofilms revealed that, in ambient conditions, carbon is being pushed out of the Herztian contact area, while in dry conditions there is an abundance of carbon in the contact area. The higher amount of carbon in dry condition as well as its structure (small and strained $sp^2$ clusters) seems to be more favorable for obtaining low friction. In brief, the role of oxygen and water vapor in the tribological response of a-C:H:Si:O has been highlighted in this chapter. In the following chapter, we will focus on the fundamental mechanisms occurring upon sliding a-C:H:Si:O against steel in oxygen, water vapor and hydrogen environment using Controlled-Environment Analytical Tribometer.

# 5. Résumé Chapitre 3

Le chapitre 3 intitulé « *influence de l'environnement sur les propriétés tribologiques des a-C:H:Si:O* » présente les résultats de l'analyse du revêtement utilisé ainsi que des essais réalisés sur le tribomètre alternatif fonctionnant sous air ambiant et équipé du système de soufflage de gaz, introduit dans le chapitre précédent.

Les analyses ont permis une caractérisation structurale précise du revêtement, en déterminant précisément la fraction de carbone $sp^2$ présente (54±2%). Les mesures RBS (*Rutherford Backscattering Spectroscopy*) et HFS (*Hydrogen Forward Scattering*) couplées aux profils SIMS (*Secondary Ions Mass Spectroscopy*) ont, quant à elles, permis de déterminer avec précision la composition chimique du revêtement ([C] = 57±3 % at., [O] = 3±1 % at., [Si] = 6±1 % at., [H] = 34±3 % at.). Les propriétés mécaniques et la topographie, mesurées respectivement par nanoindentation et microscopie à force atomique ont révélé une dureté d'environ 10 GPa et une rugosité de 1.4±0.1 nm (mesurée sur un carré de 2 µm de côté).

Quant aux essais tribologiques, la procédure qui consistait à souffler du gaz autour du contact nous a permis de permuter rapidement la quantité de vapeur d'eau et d'oxygène présent dans l'environnement du contact.

Dans ce chapitre nous revenons sur les explications fournies par d'autres groupes de recherche, en particulier Scharf *et al.*[96], concernant le rôle de la vapeur d'eau dans le comportement tribologique des couches a-C:H:Si:O. Le mécanisme proposé par Scharf *et al.*[96] est basé sur la variation de composition du tribofilm et de son taux de cisaillement en fonction du taux de vapeur d'eau dans l'environnement. Ils ont montré qu'en environnement humide, le tribolfilm généré est constitué essentiellement de silicium et d'oxygène et que son taux de cisaillement est 10 fois supérieur à celui obtenu en environnement sec. Le tribofilm généré sous environnement sec (essais réalisés dans une enceinte remplie d'azote) était quant à lui essentiellement constitué de carbone. Ceci expliquerait donc le coefficient de frottement élevé en environnement humide et faible en environnement sec.

Dans nos travaux, nous avons considéré deux configurations d'essais :

- ***Les essais à environnement constant.***

Dans cette configuration nous avons réalisé trois types d'essais :

  - *à air ambiant (environnement humide correspondant au taux d'humidité dans la salle d'expérimentation) ;*

- *avec soufflage de 5 l/min d'azote sec ou d'argon pour diminuer le taux de vapeur d'eau et d'oxygène dans l'environnement du contact ;*
- *avec soufflage de 5 l /min d'air sec pour diminuer le taux de vapeur d'eau mais maintenir constante, le taux d'oxygène dans l'environnement de contact.*

- ***Les essais à environnement dynamique***

Ici nous avons fait alternativement évoluer l'environnement d'un état humide à sec et vice-versa pour évaluer la réversibilité du rôle de la vapeur d'eau dans le comportement tribologique des a-C:H:Si:O.

Ces expériences nous ont permis de confirmer le bas coefficient de frottement obtenu sous flux de gaz sec en environnement constant et un coefficient de frottement reversible en environnement dynamique.

Après essais tribologiques, les différents tribofilms ont été analysés par Raman à plusieurs longueurs d'onde, par EDX et par XPS. Le Raman a permis d'évaluer toute modification structurale éventuelle du revêtement survenue pendant les essais tribologiques et de comprendre la structure des tribofilms générés dans les différentes configurations choisies. Nous avons ainsi montré que l'abondance et la structure du carbone (petits clusters de $sp^2$ contraints) dans le tribofilm généré en environnement sec est favorable à l'obtention du bas frottement.

Les données EDX et XPS ont quant à elles révélé que la composition chimique du tribofilm n'explique pas à elle seule la différence du taux de cisaillement de l'interface lors du frottement.

En effet, les analyses EDX ont montré que les teneurs en silicium et en oxygène dans le tribofilm généré lors du frottement en environnement sec (en soufflant de l'air sec ou de l'argon) sont similaires à ceux du tribofilm généré en environnement humide. Toutefois, les taux de cisaillement de l'interface en environnement sec sont 10 fois inferieurs à ceux calculés en environnement humide.

Ceci montre donc que la composition chimique du tribofilm n'est pas nécessairement corrélée au taux de cisaillement de l'interface, comme proposé par Scharf *et al*[96]. En outre, les analyses élémentaires quantitatives par XPS des tribofilms générés lors des essais en environnement dynamique corrobore cette conclusion.

Le mécanisme principal élucidé dans ce chapitre est ainsi que la vapeur d'eau agit comme un « film protecteur » de la couche de a-C:H:Si:O contre l'usure, bien qu'elle ne soit pas favorable à l'obtention d'un bas frottement. La présence d'oxygène, quant à elle, conduit à

une usure importante du revêtement, mais permet l'obtention de bas niveaux de frottement.

# 6. References.


1. Neerinck, D. *et al.* Diamond-like nanocomposite coatings for low-wear and low-friction applications in humid environments. *Thin Solid Films* **317,** 402–404 (1998).
2. Yang, W. J., Sekino, T., Shim, K. B., Niihara, K. & Auh, K. H. Microstructure and tribological properties of SiOx/DLC films grown by PECVD. *Surf. Coat. Technol.* **194,** 128–135 (2005).
3. Yang, W. J. *et al.* Structural characteristics of diamond-like nanocomposite films grown by PECVD. *Mater. Lett.* **57,** 3305–3310 (2003).
4. Scharf, T. W. & Singer, I. L. Monitoring Transfer Films and Friction Instabilities with In Situ Raman Tribometry. *Tribol. Lett.* **14,** 3–8 (2003).
5. Kester, D. J., Brodbeck, C. L., Singer, I. L. & Kyriakopoulos, A. Sliding wear behavior of diamond-like nanocomposite coatings. *Surf. Coat. Technol.* **113,** 268–273 (1999).
6. Scharf, T. W., Ohlhausen, J. A., Tallant, D. R. & Prasad, S. V. Mechanisms of friction in diamondlike nanocomposite coatings. *J. Appl. Phys.* **101,** 063521–063521–11 (2007).
7. Genzer, J., Kramer, E. J. & Fischer, D. A. Accounting for Auger yield energy loss for improved determination of molecular orientation using soft x-ray absorption spectroscopy. *J. Appl. Phys.* **92,** 7070–7079 (2002).
8. Scharf, T. W. & Singer, I. L. Thickness of diamond-like carbon coatings quantified with Raman spectroscopy. *Thin Solid Films* **440,** 138–144 (2003).
9. Hochstetter, G., Jimenez, A. & Loubet, J. L. Strain-rate effects on hardness of glassy polymers in the nanoscale range. Comparison between quasi-static and continuous stiffness measurements. *J. Macromol. Sci. Part B* **38,** 681–692 (1999).
10. Demmou, K., Bec, S., Loubet, J.-L. & Martin, J.-M. Temperature effects on mechanical properties of zinc dithiophosphate tribofilms. *Tribol. Int.* **39,** 1558–1563 (2006).
11. Singer, I. L. in *Fundamentals of Friction: Macroscopic and Microscopic Processes* (eds. Singer, I. L. & Pollock, H. M.) 237–261 (Springer Netherlands, 1992). at <http://link.springer.com/chapter/10.1007/978-94-011-2811-7_13>
12. Singer, I. L., Dvorak, S. D., Wahl, K. J. & Scharf, T. W. Role of third bodies in friction and wear of protective coatings. *J. Vac. Sci. Technol. A* **21,** S232–S240 (2003).
13. Erdemir, A. & Donnet, C. Tribology of diamond-like carbon films: recent progress and future prospects. *J. Phys. Appl. Phys.* **39,** R311 (2006).
14. Casiraghi, C., Ferrari, A. C. & Robertson, J. Raman spectroscopy of hydrogenated amorphous carbons. *Phys. Rev. B* **72,** 085401 (2005).
15. Rose, F. *et al.* Complete characterization by Raman spectroscopy of the structural properties of thin hydrogenated diamond-like carbon films exposed to rapid thermal annealing. *J. Appl. Phys.* **116,** 123516 (2014).
16. Ferrari, A. & Robertson, J. Interpretation of Raman spectra of disordered and amorphous carbon. *Phys. Rev. B* **61,** 14095–14107 (2000).
17. Ferrari, A. C. & Robertson, J. Resonant Raman spectroscopy of disordered, amorphous, and diamondlike carbon. *Phys. Rev. B* **64,** 075414 (2001).
18. Cui, W. G., Lai, Q. B., Zhang, L. & Wang, F. M. Quantitative measurements of sp3 content in DLC films with Raman spectroscopy. *Surf. Coat. Technol.* **205,** 1995–1999 (2010).
19. Konicek, A. R. *et al.* Origin of Ultralow Friction and Wear in Ultrananocrystalline Diamond. *Phys. Rev. Lett.* **100,** 235502 (2008).
20. Konicek, A. R. *et al.* Influence of surface passivation on the friction and wear behavior of ultrananocrystalline diamond and tetrahedral amorphous carbon thin films. *Phys. Rev. B* **85,** 155448 (2012).
21. Kunze, T. *et al.* Wear, Plasticity, and Rehybridization in Tetrahedral Amorphous Carbon. *Tribol. Lett.* **53,** 119–126 (2014).
22. 'Tribochemical studies of hard carbon films as a function of load and e' by Andrew Robert Konicek. at <http://repository.upenn.edu/dissertations/AAI3447631/>
23. Pastewka, L., Moser, S. & Moseler, M. Atomistic Insights into the Running-in, Lubrication, and Failure of Hydrogenated Diamond-Like Carbon Coatings. *Tribol. Lett.* **39,** 49–61 (2010).
24. Romero, P. A., Pastewka, L., Lautz, J. V. & Moseler, M. Surface passivation and boundary lubrication of self-mated tetrahedral amorphous carbon asperities under extreme tribological conditions. *Friction* **2,** 193–208 (2014).
25. Pastewka, L., Moser, S., Gumbsch, P. & Moseler, M. Anisotropic mechanical amorphization drives wear in

diamond. *Nat. Mater.* **10,** 34–38 (2011).
26. Robertson, J. Diamond-like amorphous carbon. *Mater. Sci. Eng. R Rep.* **37,** 129–281 (2002).
27. Tannous, J. *et al.* Understanding the Tribochemical Mechanisms of IF-MoS2 Nanoparticles Under Boundary Lubrication. *Tribol. Lett.* **41,** 55–64 (2010).
28. Lahouij, I., Vacher, B., Martin, J.-M. & Dassenoy, F. IF-MoS2 based lubricants: Influence of size, shape and crystal structure. *Wear* **296,** 558–567 (2012).
29. Njiwa, P. *et al.* Zinc Dialkyl Phosphate (ZP) as an Anti-Wear Additive: Comparison with ZDDP. *Tribol. Lett.* **44,** 19–30 (2011).

# *Chapter 4. Influence of hydrogen, oxygen, and water vapor on the tribological behavior of a-C:H:Si:O*

*In the previous chapter, we were able to show that the amount of water vapor and oxygen in the sliding environment plays a key role in controlling the tribological response of a-C:H:Si:O upon sliding against 52100 steel. A precise control of the environmental conditions is thus required for a fundamental understanding of the influence of the gaseous species on the tribological response of a-C:H:Si:O. For that aim, in the results herein presented, we employed the Controlled-Environment Analytical tribometer (CEAT) extensively described in chapter 2 section 2.2.3.1. The device allows performing tribological experiments in a wide range of environmental conditions from high vacuum to elevated pressures of different gases. Experiments were carried out under high vacuum as well as in presence of water vapor, oxygen and hydrogen (up to 2000 mbar). The subsequent characterization of both the a-C:H:Si:O coatings and the steel countersurface by multiple analytical techniques (interferometry, SEM/EDX, Raman and NEXAFS) allowed elucidating the structural transformations and chemical reactions that occurred upon sliding, and understanding the origin of the environmental dependence of the friction force.*

# Table of contents: Chapter 4. Influence of hydrogen, oxygen and water vapor on the tribological behavior of a-C:H:Si:O

# 1.Tribological investigations under different environmental conditions

## 1.1. Tribological behavior of a-C:H:Si:O in high vacuum

Figure 4.1 displays the evolution of the coefficient of friction while sliding a-C:H:Si:O against 52100 steel under high vacuum (HV, i.e., $2.10^{-7}$ mbar). The coefficient of friction starts at an initial value around 0.3 and rapidly increases to reach values around 1.2 after few numbers of cycles (6-10). The experiment was thus stopped to avoid damaging of the tribometer's force sensor and to preserve the worn surfaces from heavy damage.

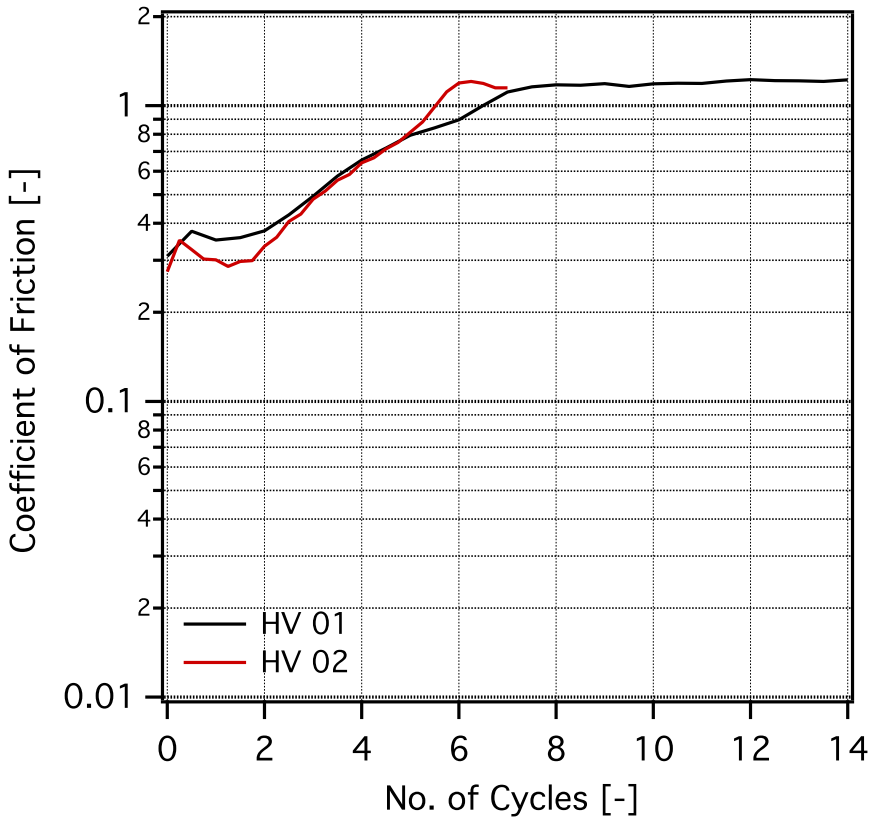


***Figure 4.1. Evolution of the coefficient of friction vs. sliding cycles during tribological tests performed on a-C:H:Si:O sliding against 52100 steel pin under HV***

## 1.2. Tribological behavior of a-C:H:Si:O in presence of hydrogen

Figure 4.2 illustrates the evolution of the coefficient of friction as a function of the number of cycles during tribological experiments performed on a-C:H:Si:O under different environmental conditions, ranging from HV to elevated pressures of hydrogen. To facilitate visualization of the results, only a few curves (corresponding to an hydrogen pressure of 0.01, 50, 100, 200 and 2000 mbar) are reported in Figure 4.2. Several additional experiments were performed at other hydrogen pressures and the results are collectively displayed in Figure 4.5. Under low hydrogen pressure (*i.e.*< 50 mbar), the friction coefficient has an evolution similar to the one in HV, *i.e.* it increases rapidly with the number of cycles, thus resulting in a very high value (>1) within less than 15 sliding cycles. For hydrogen pressures above 50 mbar, the coefficient of friction starts also at around 0.3 but after a running-in period it eventually stabilizes at low values (<0.1). Also, the running-in period is progressively reduced: it lasted 100 cycles at 50 mbar, 80 cycles at 100 mbar, 50 cycles at 200 mbar, and 20 cycles at 2000 mbar. It clearly appears that increasing hydrogen promotes low steady-state friction and decreases the running-in period. As for the friction tests performed below 50 mbar of hydrogen pressure, the experiments were stopped on purpose to avoid damaging of the tribometer's force sensor and to preserve the worn surfaces from heavy damage.

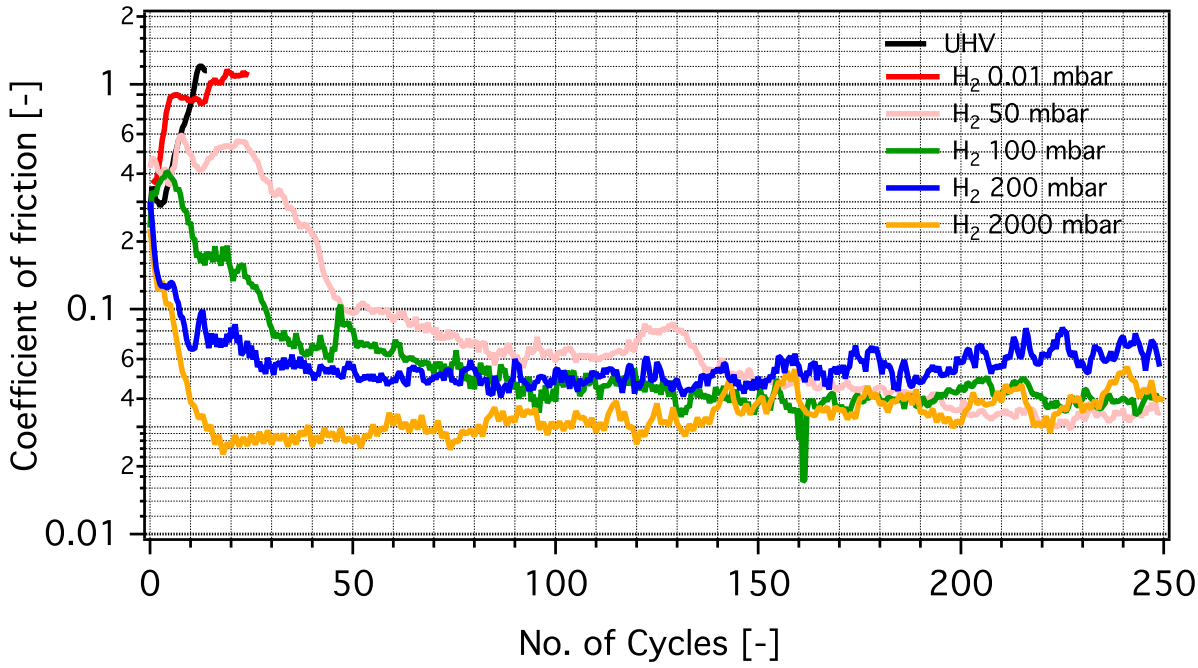


***Figure 4.2. Evolution of the coefficient of friction vs. sliding cycles during tribological tests performed on a-C:H:Si:O sliding against 52100 steel pin under various hydrogen pressures (from high vacuum to 2000 mbar)***

## 1.3. Tribological behavior of a-C:H:Si:O in presence of oxygen

In Figure 4.3 the evolution of the coefficient of friction with sliding cycles in presence of different pressure of oxygen is displayed. Experiments were carried out on a wide range of oxygen pressures but only the data corresponding to an oxygen pressure of 0.01, 14, 100, 500, and 1000 mbar are reported in Figure 4.3 to facilitate the visualization of the experimental results. In the presence of low pressure of oxygen (i.e., < 14 mbar), the friction increases and reaches the same values as under HV, (>1) after only 15 sliding cycles.

Unlike under HV or low oxygen pressure, upon increasing oxygen pressure up to 1000 mbar, the coefficient of friction decreases during a running-in period and got stabilized at low values (<0.1). In contrast to the experiments performed in the presence of hydrogen, no clear tendency was observed in the evolution of the running-in period with increasing oxygen pressure. The lowest steady state friction was obtained under 14 mbar of oxygen at 0.02±0.01. Beyond this pressure, the friction progressively increases to reach its highest value (0.06±0.01) at 1000 mbar.

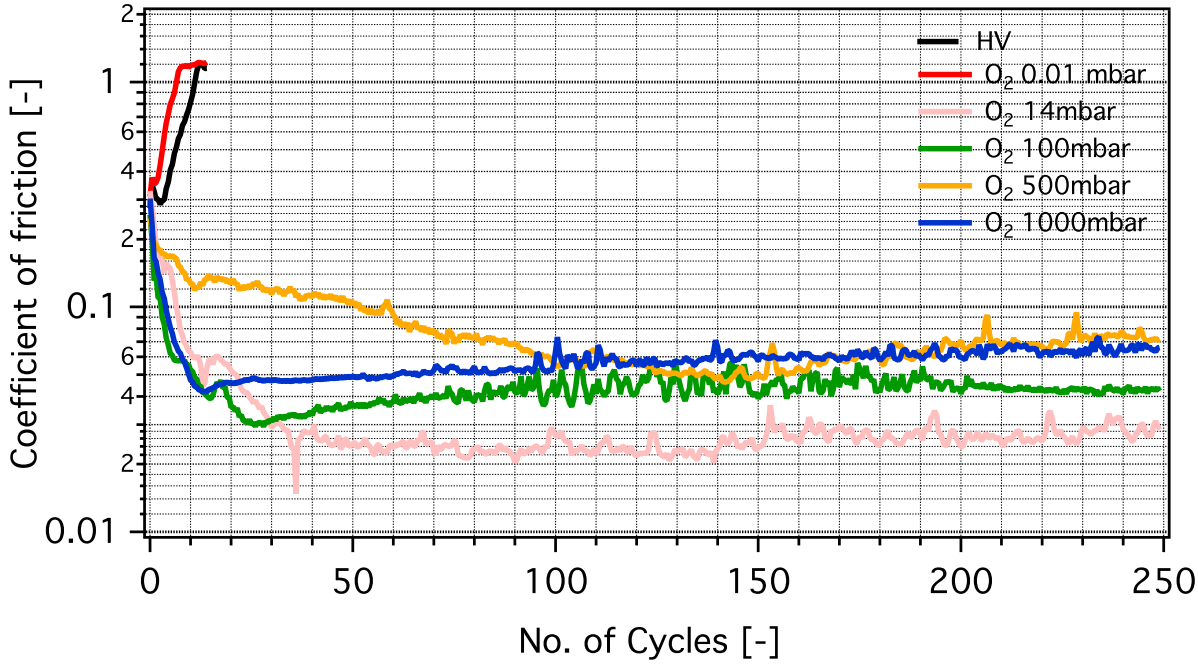


***Figure 4.3. Evolution of the coefficient of friction vs. sliding cycles during tribological tests performed on a-C:H:Si:O sliding against 52100 steel pin under various environmental conditions (from high vacuum to 1000 mbar of oxygen)***

## 1.4. Tribological behavior of a-C:H:Si:O in presence of water vapor

Figure 4.4 shows the evolution of the coefficient of friction of a-C:H:Si:O upon sliding under different pressures of water vapor. Only the data obtained for a pressure of water vapor of 0.01 mbar (~ 0.04% RH), 1 mbar (~ 0.4% RH), 5 mbar (~ 18% RH), 10 mbar (~ 35% RH), 16 mbar (~ 60% RH), and 28 mbar (~ 100% of RH) are presented.

Below 1 mbar (~ 0.4% RH) of water vapor, the friction coefficient behaves as in the previous cases of low gas pressure or <HV, *i.e.*, it increases rapidly to reach 0.7±0.1.

For higher water vapor pressure, a decrease in the coefficient of friction is observed until a threshold is reached, followed by an increase with increasing water vapor pressure.

At 1 mbar (~ 4% RH), the steady state friction reaches its lowest value at 0.05±0.01.

For water vapor pressure > 1 mbar (~ 4% RH), the stabilized coefficient of friction increases with the pressure of water vapor up to a maximum value of 0.17±0.02 at 28 mbar (~100% RH).

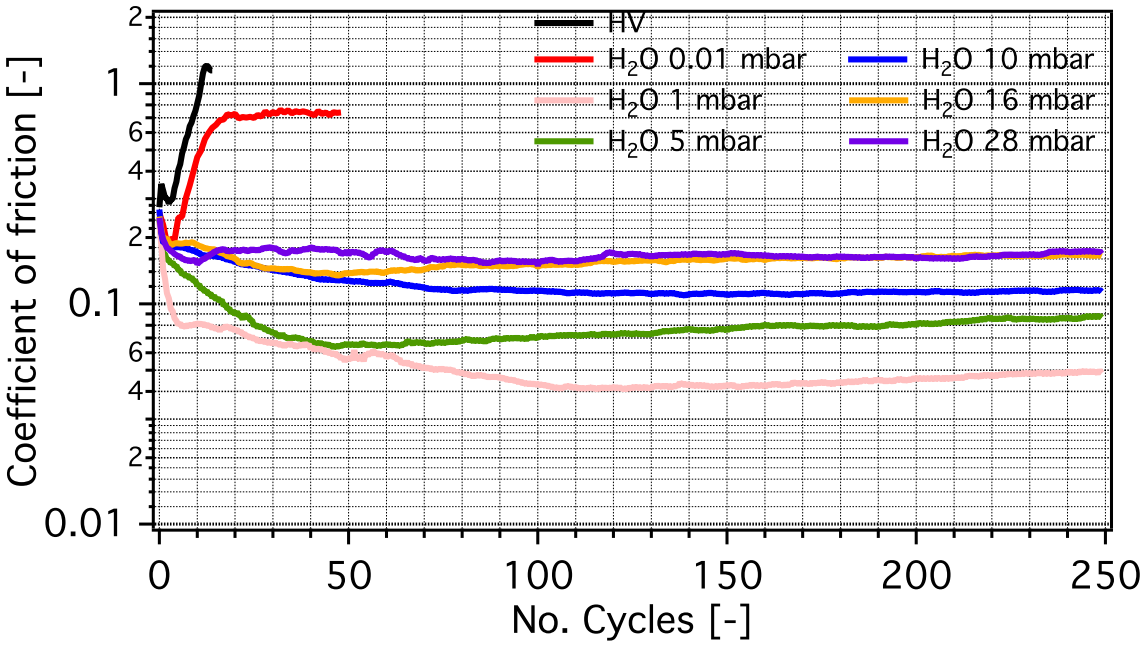


***Figure 4.4. Evolution of the coefficient of friction vs. sliding cycles during tribological tests performed on a-C:H:Si:O sliding against 52100 steel pin under various environmental conditions (from high vacuum to 28 mbar of water vapor)***

## 1.5. Summary of the environmental dependence of the tribological behavior of a-C:H:Si:O

Figure 4.5 displays the dependence of the steady-state coefficient of friction on the pressure of hydrogen, oxygen, and water vapor. The steady-state coefficient of friction was calculated by averaging the coefficient of friction values over the last 200 sliding cycles. For the case of the tests performed under gas pressures lower than 1 mbar of water vapor, 10 mbar of oxygen and 50 mbar of hydrogen, the average coefficient of friction was calculated considering all data points. The corresponding standard deviation is reported in Figure 4.5, as well.

Upon increasing the gas pressure in the chamber, a threshold between high and low stabilized friction coefficients is evidenced for hydrogen, oxygen or water vapor.

In hydrogen, the threshold in coefficient of friction occurs between 10 and 50 mbar. Upon further increasing hydrogen pressure, the coefficient of friction kept on decreasing and reached its lowest value (0.02±0.01) at 1000 mbar followed by a slight increase at 2000 mbar (0.04±0.01), which might be due to non reproducibility related to the high pressure applied on the mechanical parts of the tribometer.

In case of oxygen, the threshold in the coefficient of friction (0.02±0.01) occurs between 12 and 14 mbar and then slightly increases to reach 0.06±0.01 for a maximum pressure of 1000 mbar.

Under water vapor, the threshold in the coefficient of friction, was reached between 0.5 and 1 mbar (~ 4% RH) and further increases of the pressure leads to an increase of the friction coefficient from 0.05±0.01 at 1 mbar (~ 4% RH) until its highest value, 0.17±0.02 at 28 mbar (~100% RH).

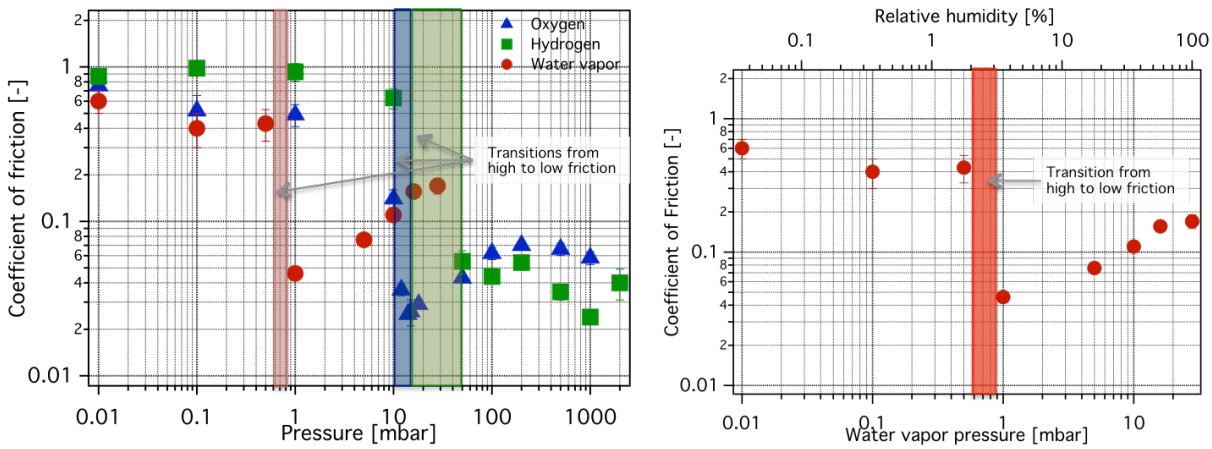


***Figure 4.5. (a)Average stabilized coefficient of friction as a function of the hydrogen, oxygen and water vapor pressure in the tribometer chamber. (b) Highlight of steady-state coefficient of friction as function of water vapor pressure and RH.***

# 2. Investigation of material transfer phenomena triggered by the environment

## 2.1. Analysis of the worn material generated in HV and low gas pressure

Figure 4.6 shows the electron dispersive X-ray analysis on the wear track obtained after sliding a-C:H:Si:O against 52100 steel under 0.01 mbar of oxygen. The grey spots that can be observed on surface of the flat are made of iron. Since the source of iron in the tribosystem is the steel counterbody, this finding clearly indicates that a preferential transfer of materials from the steel pin to the a-C:H:Si:O flat occurs under a oxygen pressure of 0.01 mbar. Very similar results (not shown) were also observed for wear tracks obtained upon sliding under HV, a low pressure of oxygen (<10 mbar), hydrogen (<50 mbar), or water vapor (<1 mbar). We can thus argue that upon friction experiments under HV or low gas pressure, a transfer of

material occurs from the steel counterbody to a-C:H:Si:O flat and much less transfer from the flat to the pin.

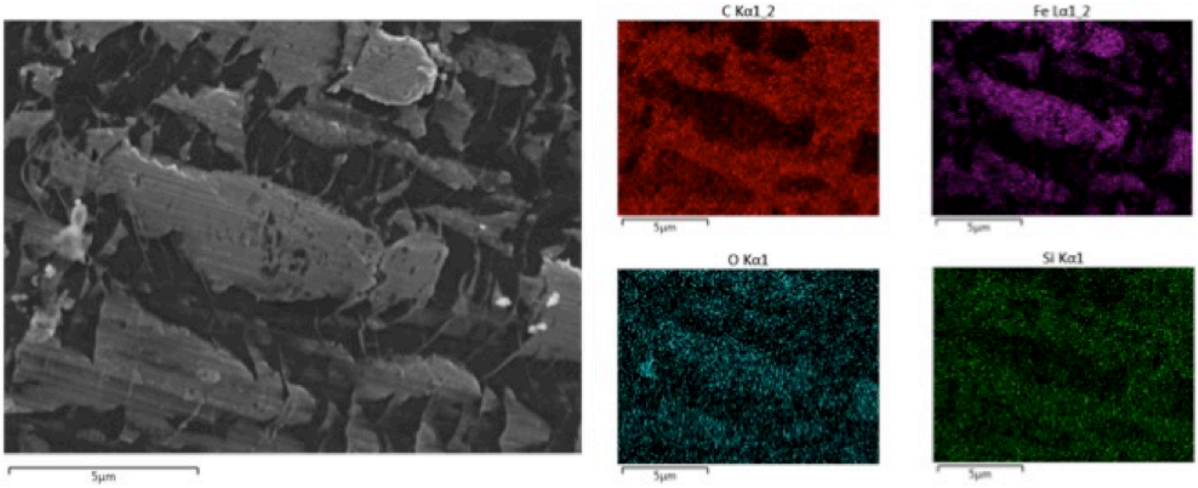


***Figure 4.6. SEM micrograph (left) with the corresponding EDX maps (right) of a-C:H:Si:O after tribological testing at 0.01 mbar of oxygen***

## 2.2. Analysis of the worn material generated under intermediate and high gas pressure

At intermediate and high gas pressure there is no more transfer occurring from the steel to a-C:H:Si:O flat but rather a transfer from the flat to the steel pin as illustrated by SEM/EDX analysis of the wear track obtained after sliding under 100 mbar of oxygen is (Figure 4.7).

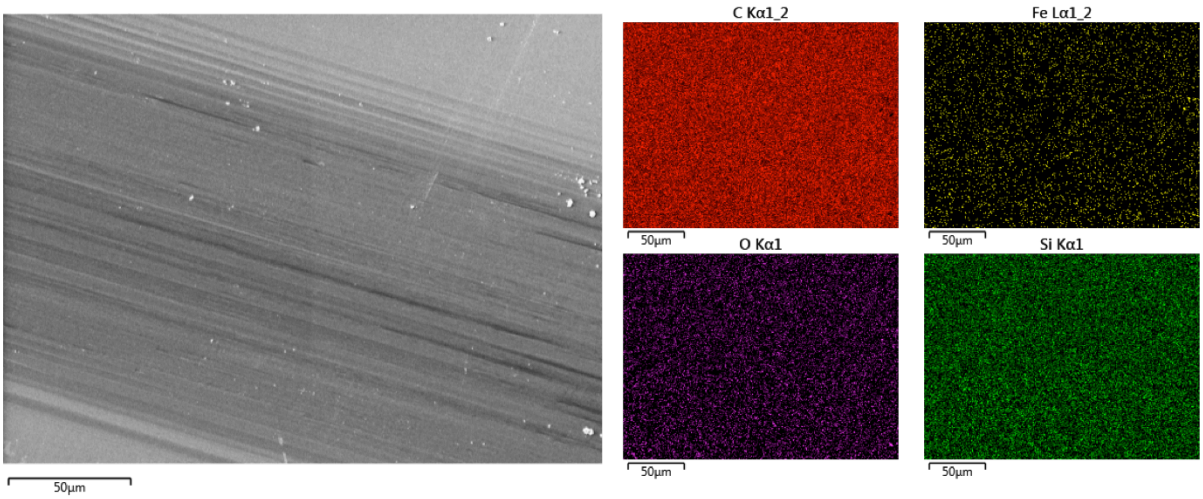


***Figure 4.7. SEM micrograph (left) with the corresponding EDX maps (right) of a-C:H:Si:O after tribological testing at 100 mbar of oxygen***

The following figures illustrate SEM micrographs of material transferred on top of the steel pin.

Figure 4.8 shows the SEM micrographs of the tribofilms corresponding to wear tracks obtained under hydrogen. It can be noticed that upon increasing the gas pressure, the thickness of the tribofilm decreases. In other words, less material is transferred from a-C:H:Si:O to the steel pin as the hydrogen pressure increases (above 50 mbar).

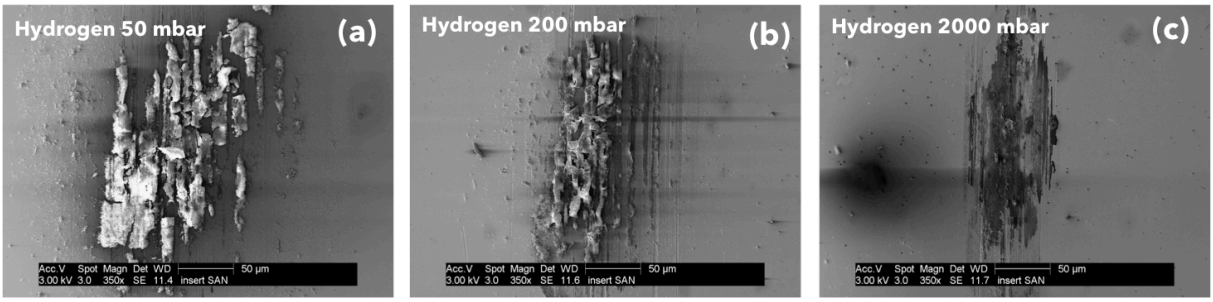


***Figure 4.8. SEM micrographs of tribofilms on the steel counterbody formed after sliding against a-C:H:Si:O at (a)50 mbar, (b) 200 mbar and (c) 2000 mbar of hydrogen***

In case of oxygen (Figure 4.9) the presence of a tribofilm on the steel counterbody is also observed, suggesting the same transfer phenomenon as in case of hydrogen. No clear evolution of the thickness of the tribofilm with oxygen gas pressure was observed.

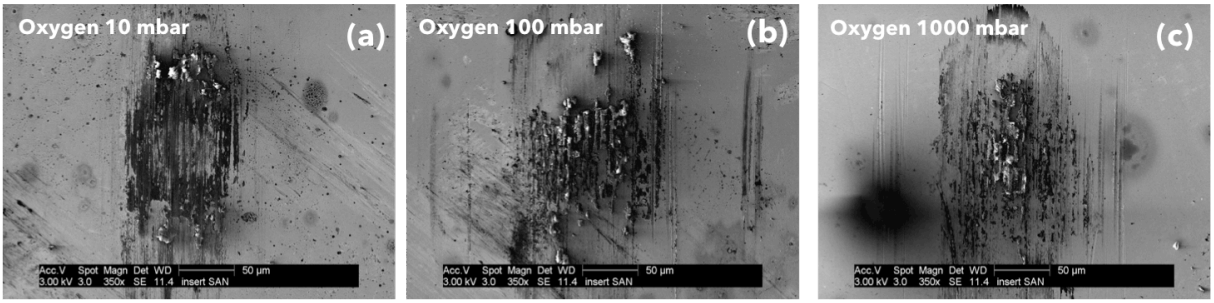


***Figure 4.9. SEM analysis of the tribofilms formed on the steel counterbody upon sliding against a-C:H:Si:O under (a)10 mbar, (b)100 mbar and (c) 1000 mbar of oxygen***

In Figure 4.10 the SEM micrographs of the tribofilms formed on steel pin after sliding under 1 mbar, 10 mbar and 28 mbar of water vapor are displayed. A tribofilm is also systematically observed but its relatively small amount suggests a lower wear of a-C:H:Si:O than in hydrogen or oxygen environment.

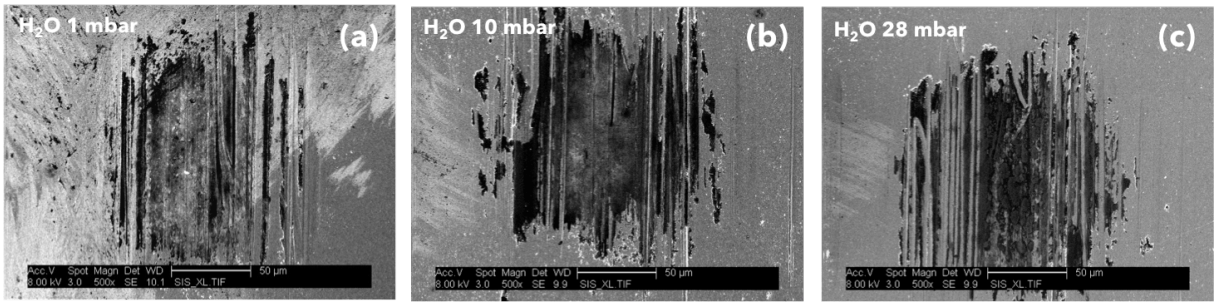


***Figure 4.10. SEM analysis of the tribofilms formed on the steel counterbody upon sliding against a-C:H:Si:O under (a) 1 mbar, (b) 10 mbar and (c) 28 mbar of water vapor***

EDX analysis on the steel pin used for running tribological tests at the transition pressure between high and low friction regime, namely 50 mbar of hydrogen, 10 mbar of oxygen and 1 mbar of water vapor (Figure 4.11), indicates that the tribofilm formed on the pin is composed of carbon, oxygen and silicon, thus suggesting a transfer from the a-C:H:Si:O flat to the steel pin. No transfer has been observed from the steel pin to the flat. The formation of tribofilms composed of carbon, oxygen, and silicon on steel pins was also observed for all tribotests carried out at gas pressures higher than the threshold mentioned above. This finding suggests that the transfer of iron to the flat ceases upon increasing the gas pressure in the chamber above to 1 mbar of water vapor, 10 mbar of oxygen and 50 mbar of hydrogen. These pressure values are the same ones at which a drastic reduction in friction was observed.

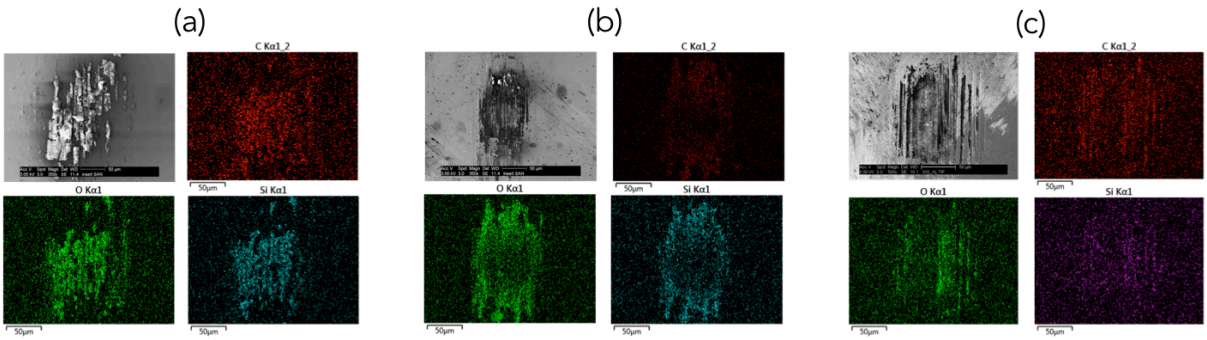


***Figure 4.11. EDX analysis of the tribofilm formed on the steel counterbody upon sliding against a-C:H:Si:O at (a) 50 mbar of hydrogen, (b)10 mbar of oxygen and (c) 1 mbar of water vapor***

## 2.3. Main tribological process of a-C:H:Si:O: Abrasion vs. adhesion

The friction results presented in section 2 reveal that the tribological behavior of a-C:H:Si:O films strongly depends on the sliding environment, *i.e.*, the amount and nature of gas introduced in the vacuum chamber. Under HV or low gas pressure, the coefficient of friction increases rapidly and reaches values >1 just after few sliding cycles. The transfer of iron from the steel pin to the a-C:H:Si:O film after tribotests under HV or low gas pressure, revealed by SEM/EDX analyses, indicates that strong adhesion occurred between a-C:H:Si:O and steel (*i.e.* formation of bonds across the sliding interfaces, in agreement with Gao *et al.*[61,63]), followed by a breaking of the adhesive junctions on the steel side. The close hardness values of the steel pin and the a-C:H:Si:O (9±1 GPa and 10±1GPa, respectively) and the relative smoothness of the surfaces (rms =1.3±0.1 nm and < 30 nm for the a-C:H:Si:O coating and the steel pin respectively measured on a area of 5*5 $\mu m^2$) indicate that this transfer phenomenon is a consequence of adhesion, rather than abrasion of the steel by the a-C:H:Si:O followed by an accumulation of the abrasive debris on a-C:H:Si:O film's surface. This is consistent with Fontaine *et al.*[170], who showed that while sliding a very smooth a-C:H film against a steel counterbody, adhesion occurs between the flat and the pin by starting at some key locations on the flat and spread to the whole wear track. Molecular dynamics simulations of such systems indeed find that the generation of covalent bonds through the interface induces an increase in friction upon sliding[63,171].

A relatively small, yet significant, pressure of water vapor, oxygen or hydrogen gas is required to transition from the high friction regime to the relatively low friction regime: 1 mbar of water vapor, 10 mbar of oxygen gas or 50 mbar of hydrogen gas. This indicates that the reduction of friction is due to tribochemical reactions, which require a sufficiently abundant source of gas molecules to achieve and maintain low friction.

In addition, at these intermediate and higher gas pressures (>1 mbar water vapor, 10 mbar oxygen, >50 mbar hydrogen), there is no more transfer from the steel pin to the film as observed under HV. Rather, there is transfer in the other direction: from the a-C:H:Si:O to the steel pin (Figure 4.7). The gas thus plays a key role in determining the friction response by inducing tribochemical reactions that prevent the mechanical transfer of steel to a-C:H:Si:O film, observed under HV. In light of this, the transfer phenomena observed in the experiments can be interpreted as a consequence of the creation of adhesive junctions between the two surfaces and not because of abrasion.

# 3. Analysis of the environment dependence of the wear kinetics

## 3.1. Interferometry observation of the wear track on a-C:H:Si:O

The following figures represent interferometry images of the wear tracks obtained under different sliding environments. The theoretical Hertz contact diameter is displayed for reference. These images were extracted from the central part of every track. As illustrated in Figure 4.12, after friction tests under vacuum conditions, additional material adheres on the worn region of a-C:H:Si:O flat, which makes unfeasible any measurement of the volume of a-C:H:Si:O material removed. This confirms the SEM measurements, which show material transfer from steel to a-C:H:Si:O under HV or low gas pressure.

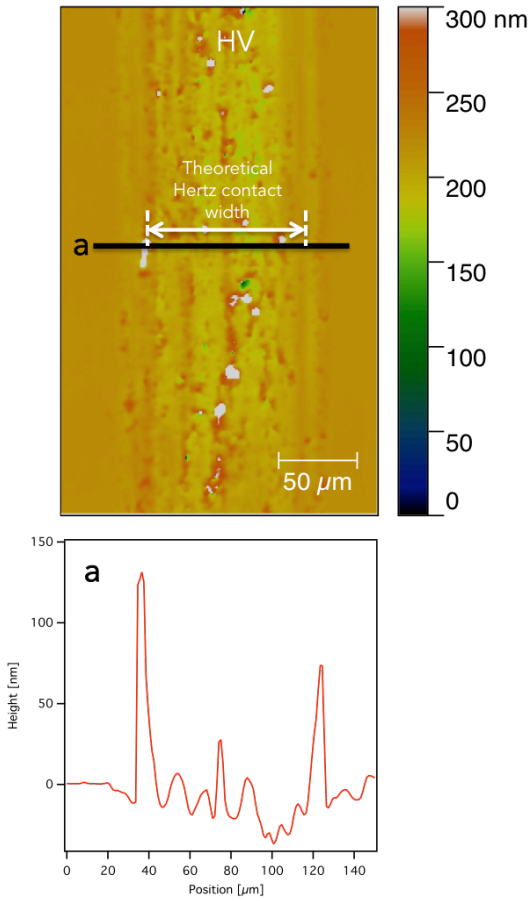


***Figure 4.12. Scanning white light interferometry measurements on the wear track obtained after friction test of a-C:H:Si:O against 52100 steel in HV***

Figure 4.13 compares the wear tracks generated on a-C:H:Si:O after sliding at increasing hydrogen pressure (50 mbar, 200 mbar and 2000 mbar). Upon increasing the hydrogen pressure, the wear track becomes narrower, suggesting a decrease in wear.

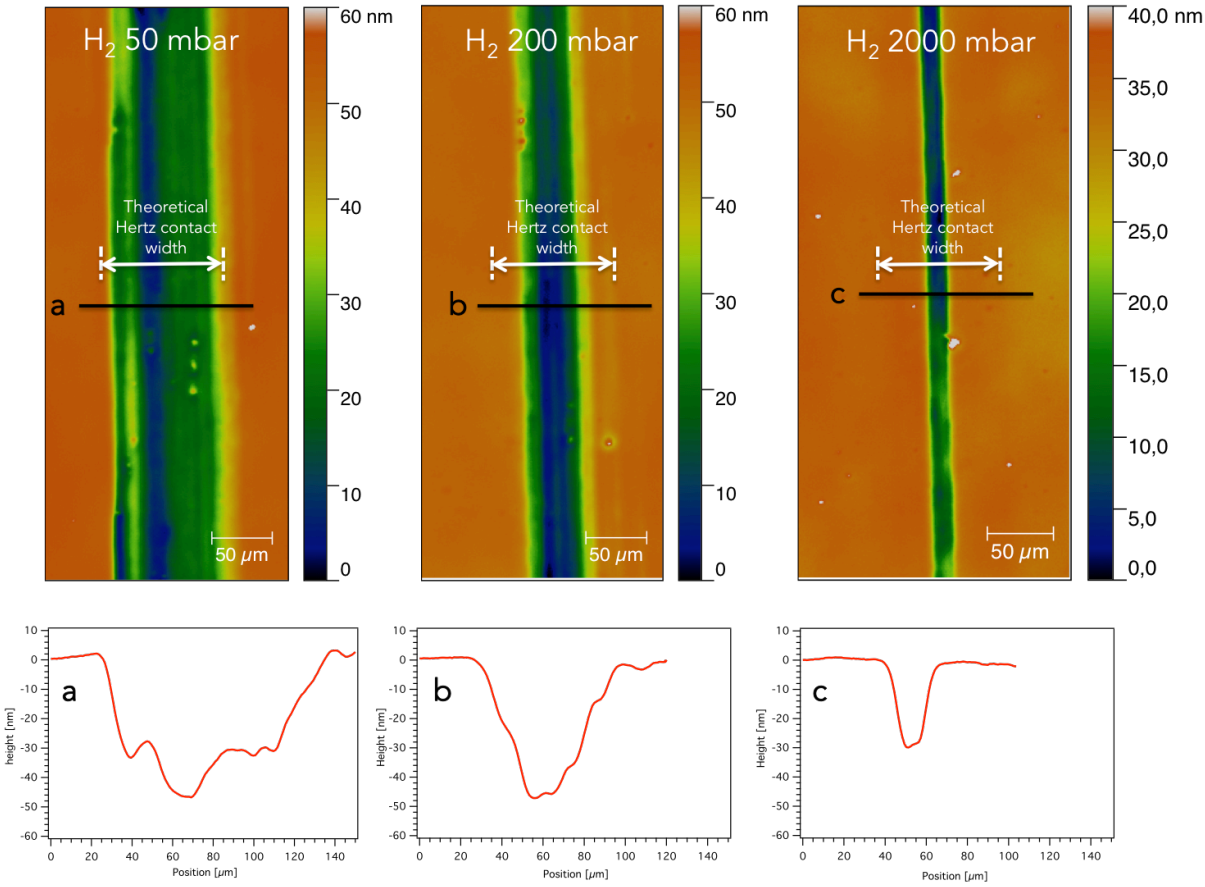


***Figure 4.13. Scanning white-light interferometry measurements of the wear tracks obtained after friction test of a-C:H:Si:O against 52100 steel under (a) 50 mbar, (b) 200 mbar, (c) 2000 mbar of hydrogen with the corresponding depth profile.***

Figure 4.14 illustrates the wear tracks formed on a-C:H:Si:O after sliding under different oxygen pressures (10 mbar, 100 mbar, and 1000 mbar). When increasing oxygen pressure, a deeper wear tracks are generated, suggesting a higher material removal from a-C:H:Si:O contrary to increasing hydrogen pressure.

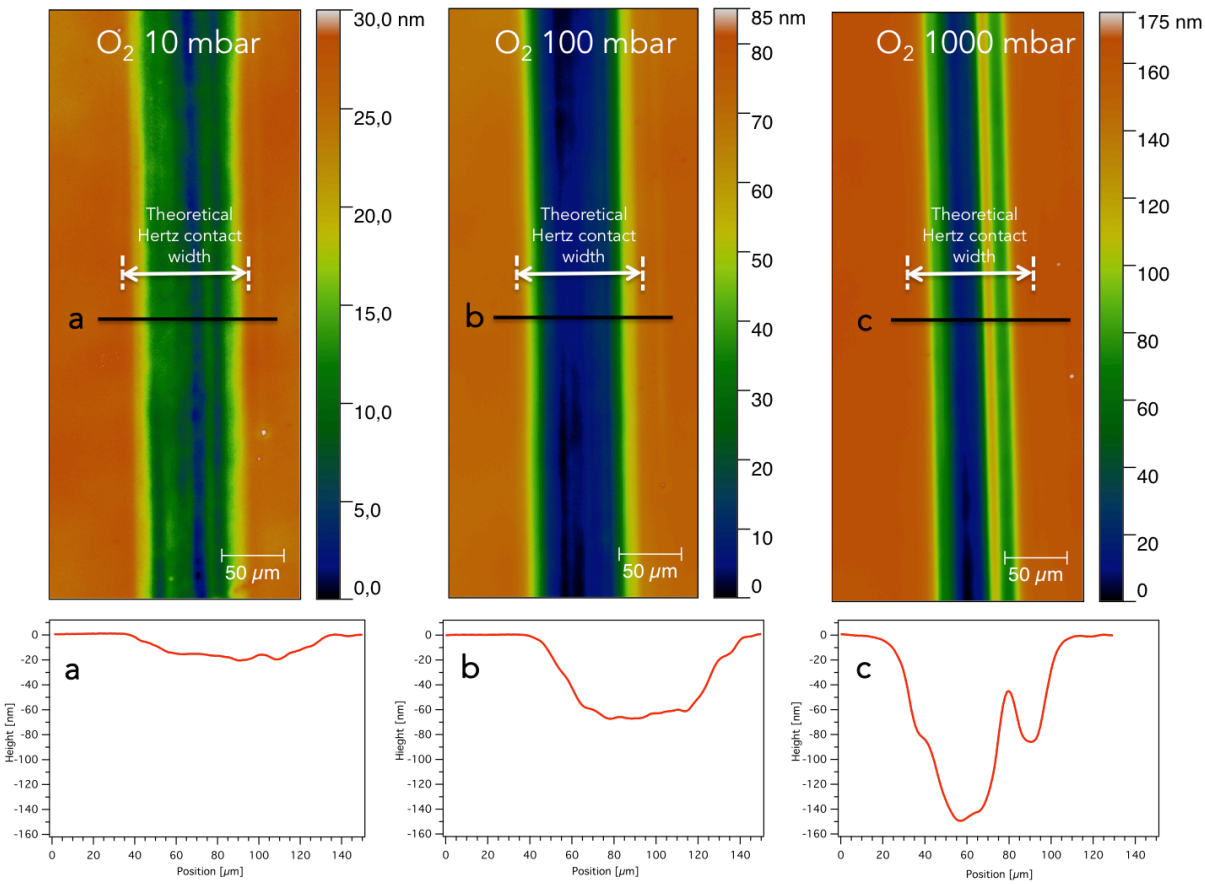


***Figure 4.14. Scanning white-light interferometry measurements of the wear tracks obtained after friction test of a-C:H:Si:O against 52100 steel under (a) 10 mbar, (b) 100 mbar, (c) 1000 mbar of oxygen with the corresponding depth profile.***

In Figure 4.15 the interferometric images of the wear tracks generated on a-C:H:Si:O after sliding in presence of 1 mbar (~ 4% RH), 10 mbar (~ 35% RH), and 28 mbar (~ 100% RH) of water vapor. There seems not to be is big differences in the wear for different water vapor pressures. Further interferometric computation of the wear provided a clear tendency of increasing wear with increasing water vapor pressure as discussed in the next section.

It can be underlined that for the tracks obtained under water vapor, the wear is much lower than in case hydrogen or oxygen or gas.

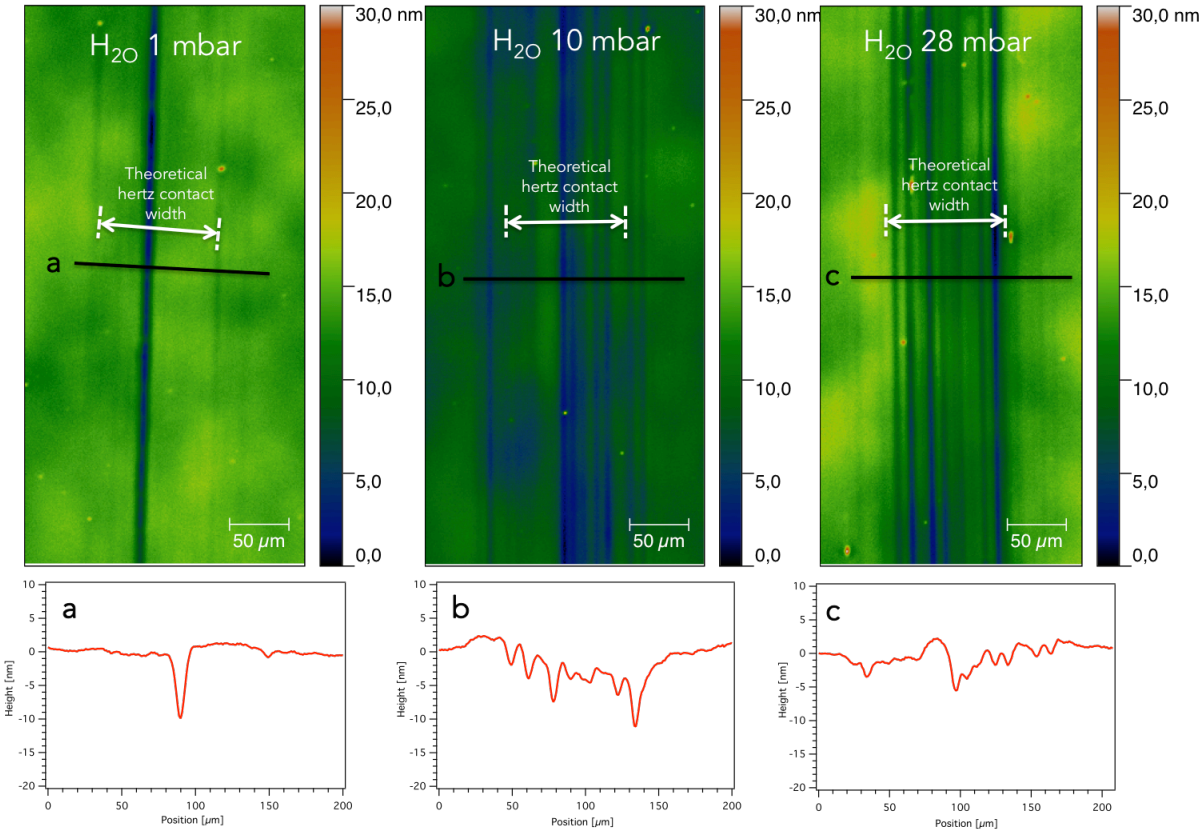


***Figure 4.15 Scanning white-light interferometry measurements of the wear tracks obtained after friction test of a-C:H:Si:O against 52100 steel under (a) 1 mbar, (b) 10 mbar and (c) 28 mbar of water vapor n with the corresponding depth profile.***

## 3.2. Summary of the wear process of a-C:H:Si:O in presence of hydrogen, oxygen and water vapor

Figure 4.16 displays the wear rates of a-C:H:Si:O after friction test under different pressures of hydrogen (50 mbar, 200 mbar, 2000 mbar), oxygen (10 mbar, 100 mbar, 1000 mbar), and water vapor (1 mbar, 10 mbar, 28 mbar). The wear rate decreases with increasing hydrogen pressure, while it increases with oxygen or water vapor pressure. Among the three different environments, the lowest wear rate was achieved upon sliding in the presence of water vapor while oxygen environment leads to the highest wear. This finding can explain the higher wear obtained in case of dry air flow reported in the previous chapter compared to the results of tribological tests performed in the presence of inert gases or ambient air.

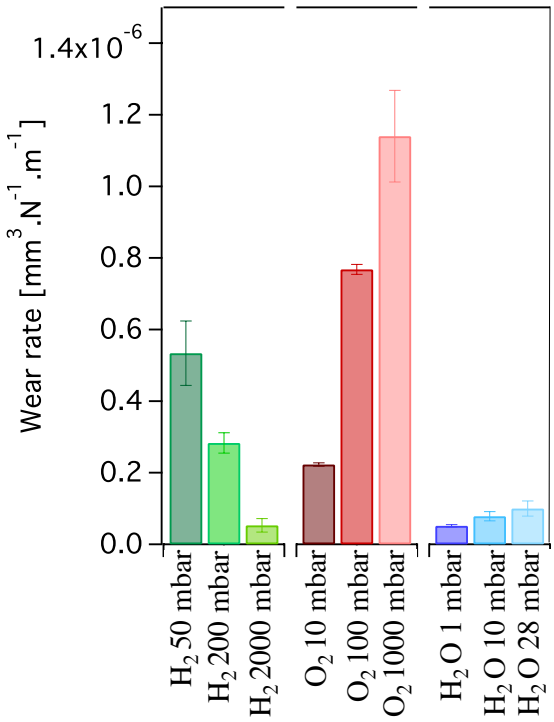


***Figure 4.16. Wear rate of a-C:H:Si:O after sliding under different pressure of hydrogen (green), oxygen (red) and water vapor (blue)***

Figure 4.17 reports the worn volume, total dissipated energy and the specific wear energy for tribological tests performed under hydrogen (50 mbar, 200 mbar, 2000 mbar), oxygen (10 mbar, 100 mbar, 1000 mbar) and water vapor (1mbar, 10 mbar, 28 mbar) following the calculations described in Chapter 2, section 4.1.2. The computed total dissipated energy (Figure 4.17) reveals that less energy is dissipated when increasing the pressure of hydrogen, while it increases with the oxygen and water vapor pressure.

From the computed specific wear energy (the energy needed to wear out a unit volume of a-C:H:Si:O under a defined environmental condition) (Figure 4.17) it can be understood that wearing a-C:H:Si:O requires much more energy in presence of water vapor than in hydrogen or oxygen environments. Increasing the hydrogen or water vapor pressure seems to increase the specific wear energy for a-C:H:Si:O. In other words, the presence of oxygen facilitates the wear process of a-C:H:Si:O, while this is the opposite case for hydrogen and water vapor.

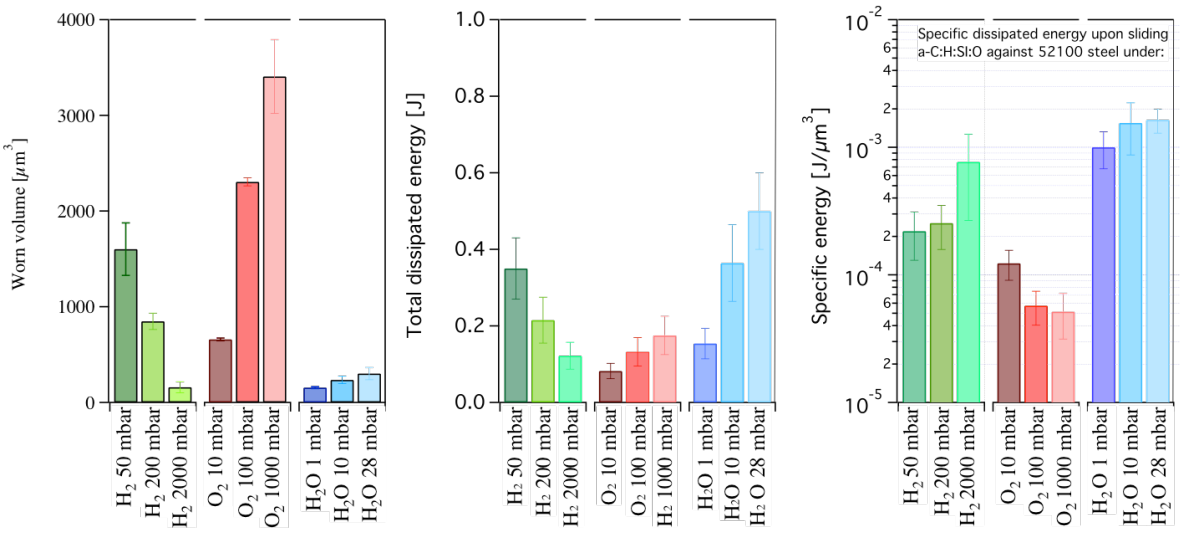


***Figure 4.17. (a) measured wear volume, (b) calculated total dissipated energy and (c) specific wear energy (b) when sliding a-C:H:Si:O against a steel pin in the presence of hydrogen, oxygen, or water vapor.***

# 4. Tribologically-induced chemical and structural changes of a-C:H:Si:O

To gain insights of the fundamental mechanisms responsible for the friction and wear results presented in the previous sections (dependence of the frictional behavior of a-C:H:S:O on the amount of gas in the vacuum chamber, wear process etc) it is paramount to study the potential mechanically-induced chemical and structural analysis of the worn material. Raman and NEXAFS were used and the results are discussed in this section.

## 4.1. Structural analysis of the worn material: Raman spectroscopy

To gain insights into the structural changes occurring in a-C:H:Si:O upon sliding as well as into the structure of the tribofilm formed on the steel pin, Raman analyses were performed (Figure 4.18). The spectra were acquired on tribofilms generated in the low friction regime (*i.e.* at 100 mbar of hydrogen, 15 mbar of oxygen).

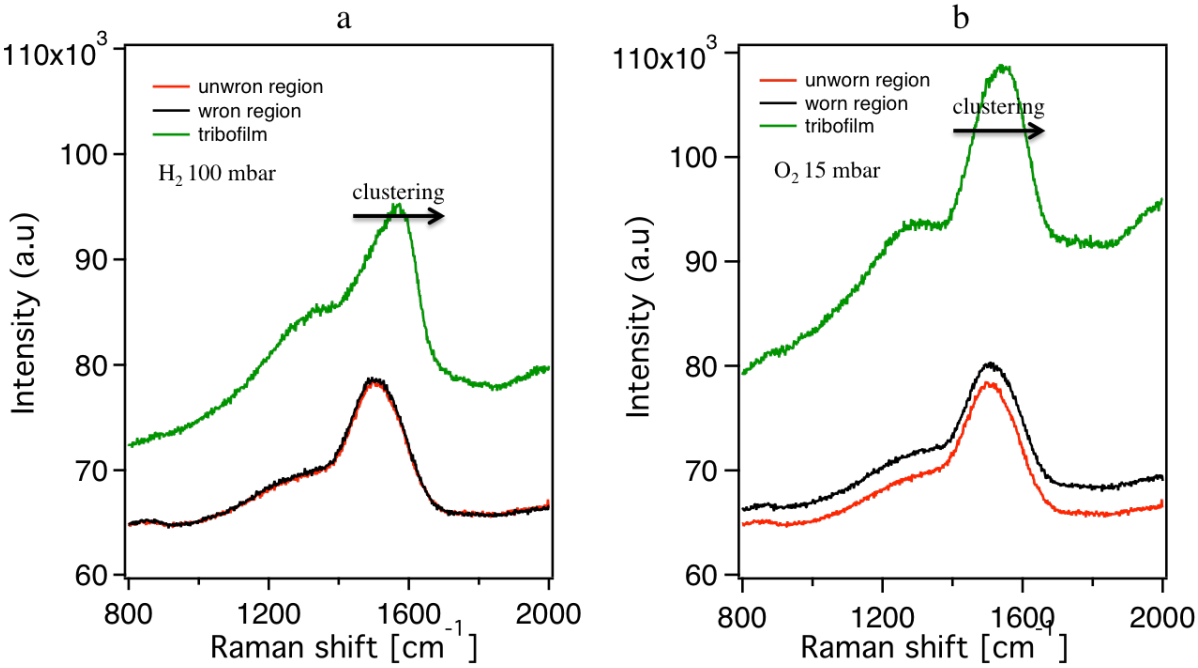


***Figure 4.18. Visible Raman spectra acquired on worn and unworn regions of a-C:H:Si:O as well as on the tribofilm formed on 52100 steel pin after sliding at (a)100 mbar of hydrogen and (b) 15 mbar of oxygen***

Due to instrument availability limitations, visible Raman measurements were carried out for the experiments performed in hydrogen and oxygen, while the worn material generated under 1 mbar of water vapor was analyzed by UV Raman (Figure 4.19).

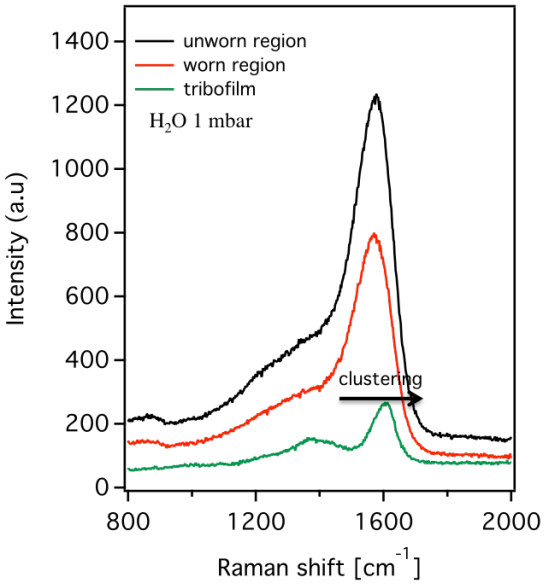


***Figure 4.19. UV Raman spectra acquired on worn and unworn regions of a-C:H:Si:O as well as on the tribofilm formed on 52100 steel pin after sliding at 1 mbar of water vapor***

As already mentioned in Chapter 3, the Raman spectra of amorphous carbon-based materials is dominated by the signal originating from $sp^2$-hybridized carbon, since the scattering cross section of π states is more than 50 times higher than that of σ states[133,138,140,172].

The characteristic Raman spectrum of unworn a-C:H:Si:O (from the as-grown, non-contact region) exhibits the characteristic broad envelope for amorphous hydrogenated carbon-based materials[137,172,173]. After sliding under oxygen or hydrogen environments, no significant changes in the Raman spectra of a-C:H:Si:O were observed, regardless of the gas pressure. Under water vapor, even though the Pos(G) stays constant (1573±1 $cm^{-1}$ and 1570±1 $cm^{-1}$ respectively for unworn and worn region) there is as slight shift in the photoluminescence background. These could be related either to a presence of carbon-hydrogen bonds or to the clustering of the $sp^2$-bonded carbon phase in the worn region[138].

As for the Raman measurements on the tribofilms generated in the three different environmental conditions, the spectra exhibited clear differences compared to the spectrum of as-received a-C:H:Si:O: the G band shifts towards higher wavenumbers, the ratio between the D and G band increases, and the photoluminescence background intensity increases. These results indicate that the tribofilms generated are rich in $sp^2$-bonded carbons in ring-like structure.

These findings suggest that no significant structural changes occurred in a-C:H:Si:O upon sliding under either oxygen, water vapor, or hydrogen environment, in the volume probed by the Raman experiments (the optical mean free path of a-C:H:Si:O films has been reported by Scharf *et al.*[163] to be 245±26 nm). In contrast, the Raman analysis of the wear particles and the tribofilms formed on steel pins clearly indicates the occurrence of a structural reorganization of the $sp^2$ carbon phase, forming a material with $sp^2$-hybridized carbon organized in clusters to a greater extent than in the as-grown film.

## 4.2. Chemical analysis of the wear tracks of a-C:H:Si:O using near edge adsorption fine structure spectroscopy (NEXAFS)

### 4.2.1. Chemistry and structure of the worn material at threshold for oxygen and hydrogen

To further investigate the structural transformations and surface reactions occurring on a-C:H:Si:O upon sliding under different environmental conditions, imaging near edge X-ray absorption fine structure spectroscopy (NEXAFS) measurements were performed on a-C:H:Si:O samples with wear tracks formed under HV conditions, 15 mbar of oxygen and 100 mbar of hydrogen (note: two different samples were used for NEXAFS and SEM observation to avoid carbon contamination from electron beam exposure in SEM, and X-ray induced sample modification in NEXAFS). NEXAFS measurements are highly surface sensitive (for electron yield NEXAFS spectroscopy of low atomic number elements, the information depth, which is the specimen thickness measured normal to the surface from which a specified percentage of typically 95% of the detected signal originates, is usually less than 5 nm)[156],. A typical carbon K-edge NEXAFS image is reported in Figure 4.20. a.

Figure 4.20.b illustrates the NEXAFS spectra extracted from the corresponding C K-edge image. The characteristic absorption features for amorphous carbon materials are observed at 285.0±0.1 eV (due to the C1s→π* transition for disordered carbon-carbon bonds), ~ 286.5 eV (due to the C1s→π* transition for carbonyl groups), 287.5±0.1 eV (assigned to the C1s→$\sigma^*$ transition for carbon-hydrogen bonds), and 288.9±0.1 eV (assigned to the C1s→ σ* transition for carbon-oxygen and carbon-silicon bonds, as well as to the C1s→ π* transition for carboxyl groups)[156,174]. These assignments are summarized in Table 4.1.

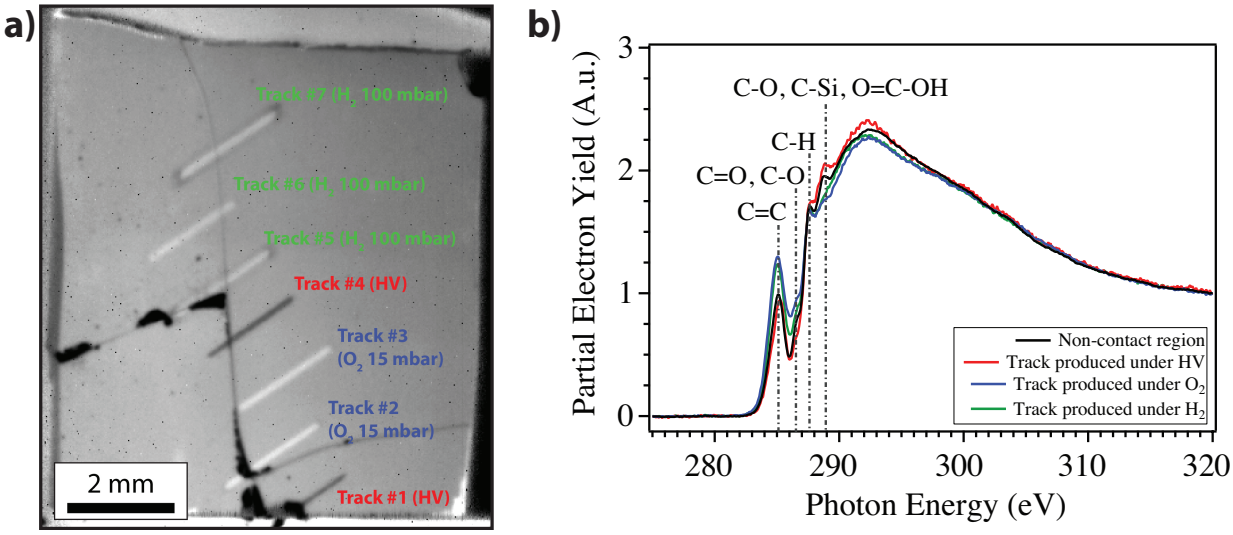


***Figure 4.20. a) NEXAFS partial electron yield image of a-C:H:Si:O after tribological experiments under high vacuum, oxygen (15 mbar), and hydrogen (100 mbar) environments. The image is the sum of the images acquired at photon energies between 282 and 330 eV. Brighter colors correspond to higher intensity. The sample was cracked during sample handling and mounting; b) NEXAFS spectra extracted from region of interests (i.e., inside and outside the wear tracks)***

| *Peak Position (eV)* | *Assignment* |
|---|---|
| *285.0±0.1* | *C1s→π* for disordered C=C bonds* |
| *~286.5* | *C1s→π* transition for C=O groups* |
| *287.5±0.1* | *C1s→σ* transition for C-H bonds* |
| *288.9±0.1* | *C1s→σ* transition for C-O and C–Si bonds; C1s→π* transition for O=C–OH* |

***Table 4.1. Summary of the carbon K-edge characteristic absorption features and the corresponding assignment, from[175,176]***

Similarly, NEXAFS spectra were extracted from the wear tracks. To compare the worn regions of a-C:H:Si:O with the unworn region, a pre- and post-edge normalization was performed (Figure 4.21, upper right inset. A larger plot of the NEXAFS spectra extracted from the corresponding C K-edge image is reported in Figure 4.20. In this way, variations in spectral intensity only arise from chemical changes and are independent of the total carbon content. In addition, to more easily investigate the structural transformations occurring in the near-surface region of a-C:H:Si:O upon sliding, the difference between spectra obtained from

the worn and unworn a-C:H:Si:O regions was calculated (Figure 4.21). Computing these difference spectra also allows eliminating the contribution of the carbonaceous contamination layer present on the sample surface due to its exposure to air to (this is valid under the assumption that the adventitious contamination layer is laterally homogeneous in composition, density, and thickness across both worn and unworn regions, *i.e.* is due to ambient exposure after the tribotesting; this approach avoids the need for correcting the as-acquired spectra for the presence of an adventitious carbonaceous contamination using a reference sample[159]). Since significant transfer of material from the steel pin to the a-C:H:Si:O surface occurs under HV or low gas pressures, the difference spectrum cannot be employed to elucidate the transformations occurring in the material in these cases. As for the tests performed under 15 mbar of oxygen and 50 mbar of hydrogen, the intensity of the C1s→$\pi^*$ transition for disordered carbon-carbon bonds at 285.0 eV significantly increased, thus demonstrating a significant conversion from $sp^3$- to $sp^2$-bonded carbon. Furthermore, a decrease in the signal at 288.9±0.1 eV (assigned to the C1s→$\sigma^*$ transitions for C–O and C–Si bonds, as well as to the C1s→$\pi^*$ transition for O=C–OH groups) was observed. Finally, an intense peak at 286.0 eV (due to the C1s→$\pi^*$ transition for carbonyl groups)[156,175] was detected in the difference spectrum obtained from the track produced under oxygen environment. This peak is also detected (with much less intensity) from the track produced under hydrogen, which can be due to some residual oxygen in the vacuum chamber.

To quantify the change in the carbon hybridization state upon sliding, the relative variation of the fraction of threefold-coordinated carbon atoms was calculated as follows (Equation.4.1):

$$\Delta f sp^2 = 100 * \frac{f_{sp^2_{Worn\ region}} - f_{sp^2_{unworn\ region}}}{f_{sp^2_{unworn\ region}}} \qquad (Eq.4\ 1.)$$

The results are displayed as a function of the entrance grid bias (EGB) voltage in the lower inset of Figure 4.21 (increasing the EGB voltage allows NEXAFS measurements with higher surface sensitivity to be performed[157]).

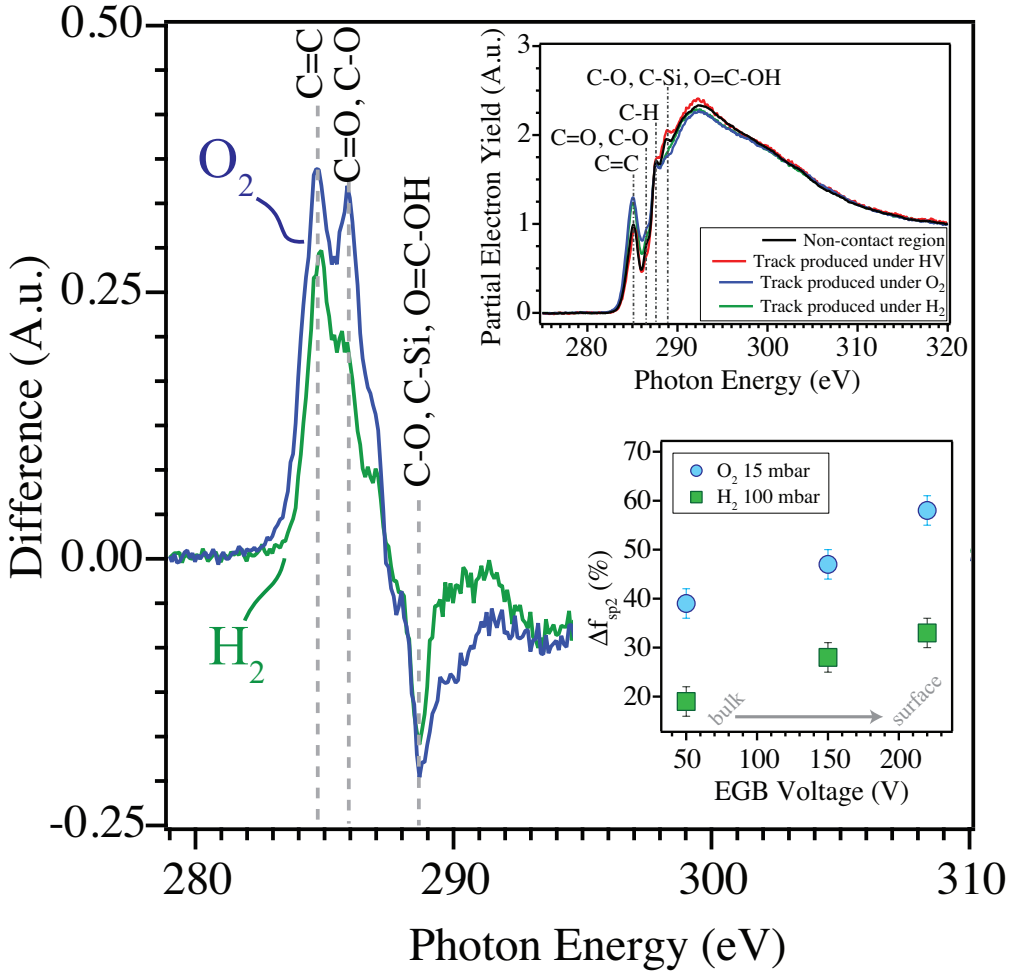


***Figure 4.21. Difference in the NEXAFS partial electron yield spectra between worn and unworn regions of a-C:H:Si:O*** **Green curve*****: difference between a spectrum taken from the wear track generated upon sliding in hydrogen (100 mbar) and a spectrum from unworn a-C:H:Si:O;*** **Blue curve*****: difference between a spectrum taken from the wear track generated upon sliding in oxygen (15 mbar) and a spectrum from unworn a-C:H:Si:O. The*** **upper** ***inset recall figure 15 (b) for comparison. The*** **lower inset** ***shows the relative variation of the fraction of sp$^2$-bonded carbon for the track generated in hydrogen (100 mbar) or oxygen (15 mbar) as a function of the entrance grid bias (EGB) voltage (the surface sensitivity increases with the EGB voltage).***

Upon increasing the EGB voltage, a higher fraction of sp$^2$-bonded carbon was detected independently of the gas environment. This finding suggests the formation of a gradient in carbon bonding configuration, with even more conversion to sp$^2$-bonded carbon occurring in the near-surface region of a-C:H:Si:O during sliding.

### 4.2.2. Chemical and structural evolution of the worn material with increasing oxygen and hydrogen pressure

To investigate the effect of gas pressure on the structural and chemical changes occurring on a-C:H:Si:O, NEXAFS measurements were performed on wear tracks obtained under different pressures of oxygen (10, 100 and 1000 mbar) and hydrogen (50, 200 and 2000 mbar). Figure 4.22.a shows the chemical NEXAFS maps at the carbon K-edge corresponding to four different spectral features (C=C, C–H, C=O, and C–O/C–Si/COOH).

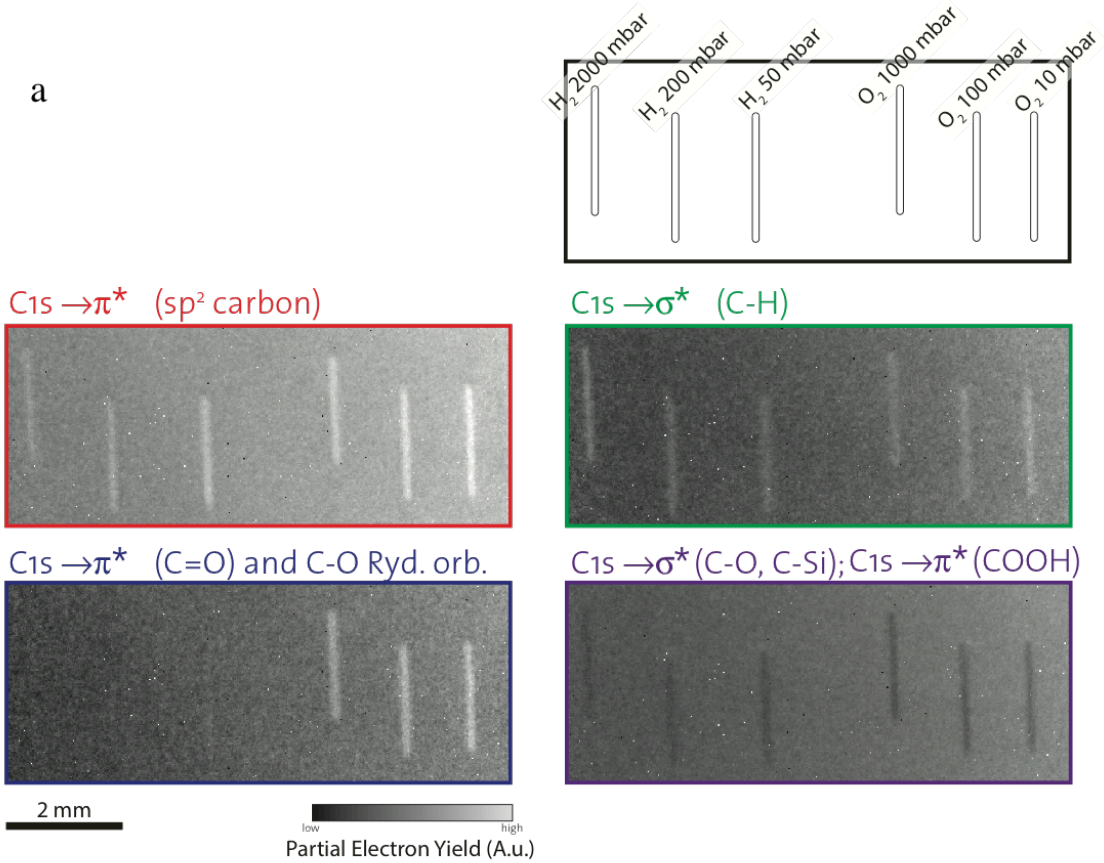

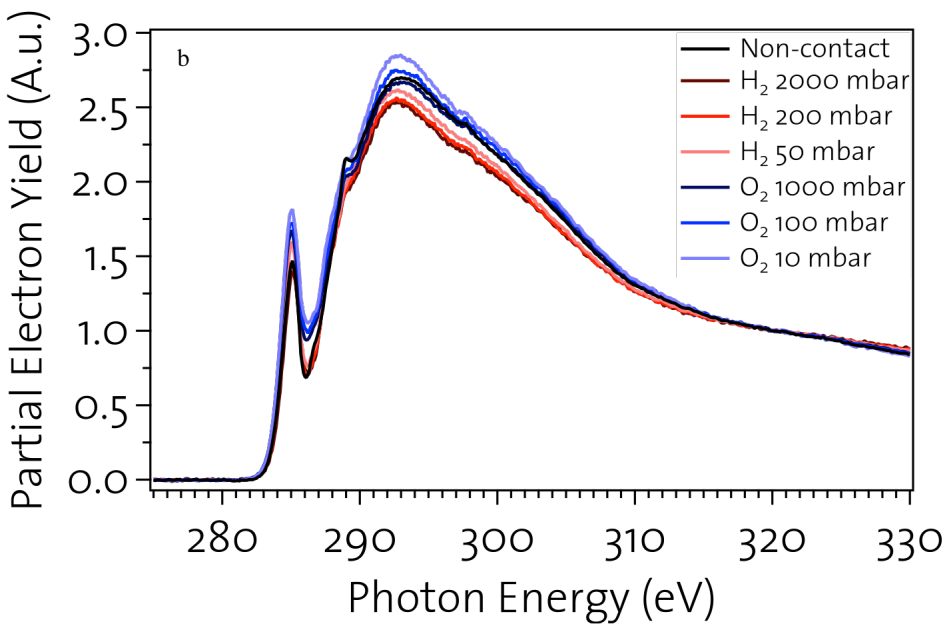


***Figure 4.22. NEXAFS partial electron yield image of a-C:H:Si:O after tribological experiments under hydrogen (50, 200, 2000 mbar) and oxygen (10, 100, 1000 mbar) gas pressure. (a) The image is the sum of the images acquired at photon energies between 282 and 330 eV. Brighter colors correspond to higher intensity; (b) NEXAFS spectra extracted from region of interests (i.e. inside and outside the wear tracks)***

Six tracks can be observed in the maps, three obtained after sliding in oxygen at 10, 100, and 1000 mbar, and three generated after sliding in hydrogen (50, 200, and 2000 mbar). The color contrast in the maps displayed in Figure 4.22.a clearly indicates the occurrence of structural and chemical changes upon sliding in the presence of oxygen and hydrogen. The spectra extracted from the NEXAFS maps are displayed in Figure 4.22.b. Since subtle differences between the spectra can be noticed on Figure 4.22.b, the difference spectra between worn and unworn region were computed to highlight structural and chemical variations induced by the sliding process (Figure 4.23).

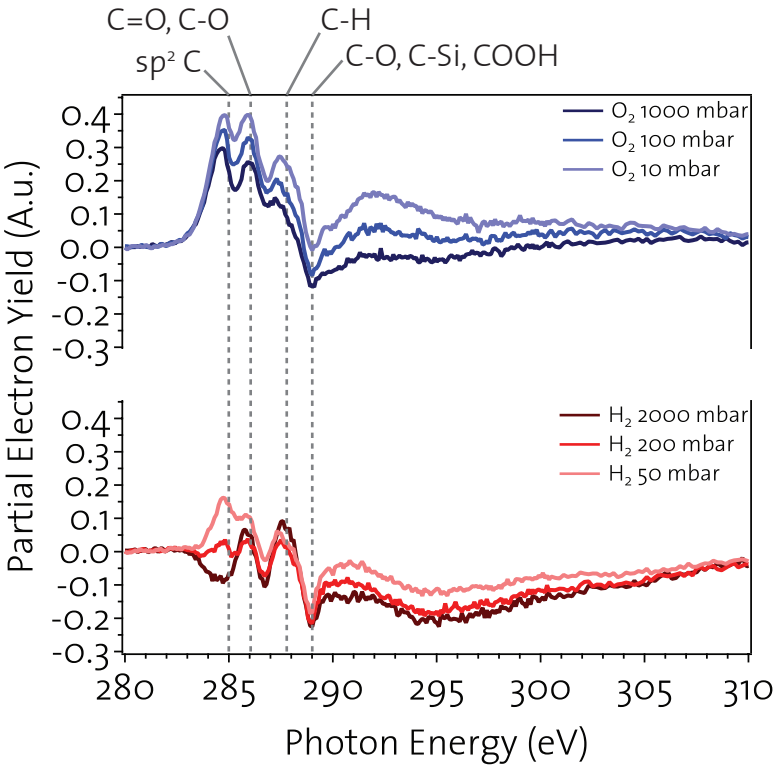


***Figure 4.23. Difference in the NEXAFS partial electron yield spectra between worn and unworn regions of a-C:H:Si:O*** **Red series curves*: difference between a spectrum taken from the wear track generated upon sliding in hydrogen (50, 200 and 2000 mbar) and the spectrum from unworn a-C:H:Si:O;*** **Blue series curves*: difference between a spectrum taken from the wear track generated upon sliding in oxygen (10, 100 and 1000 mbar) and the spectrum from unworn a-C:H:Si:O.***

From Figure 4.23, we can confirm that upon sliding under hydrogen or oxygen:

- *The intensity of C1s→π* transition for disordered carbon-carbon bonds at 285.0 eV significantly increased upon sliding, thus demonstrating a significant conversion from $sp^3$- to $sp^2$-bonded carbon as observed in the previous section. In case of hydrogen, there is a clear gradient in the C1s→π* peak of $sp^2$-bonded carbon with increasing pressure (namely, upon increasing the hydrogen pressure, less $sp^2$-bonded carbon is present on the sample surface), while under oxygen, such a difference is less pronounced;*
- *The intensity of C1s→π* transition for C=O and C–O Rydberg orbitals at 285.9±0.1 eV increased upon sliding, both in oxygen and hydrogen. The detection of this feature upon sliding in hydrogen might be due to some residual oxygen in the chamber;*

- *The intensity of C1s→$\sigma^*$ transition for C–H at 287.8±0.1 eV slightly increased, especially upon sliding at 2000 mbar of hydrogen. The relative ratio between C–H and C=O depends on the sliding environment, ($I_{C\text{-}H}/I_{C=O}$ under hydrogen > $I_{C\text{-}H}/I_{C=O}$ under oxygen);*
- *Furthermore, a decrease in the signal at 289±0.1 eV (assigned to the C1s→$\sigma^*$ transitions for C–O and C–Si bonds, as well as to the C1s→ $\pi^*$ transition for O=C–OH groups) was observed independently on the sliding environment. The main origin of this spectral feature is assigned to C–Si, since the calculation of the difference spectra most likely allows the removal of any contribution of the adventitious carbon contamination layer (which contains C–O, C=O, and COOH species).*

The relative change in the fraction of $sp^2$-bonded carbon calculated using equation 1 is displayed in Figure 4.24 as a function of the pressure of hydrogen and oxygen and of the EGB voltage. On Figure 4.24.a, it can be noticed that independently of the gas pressure, the worn material generated upon sliding under oxygen contains more $sp^2$-bonded carbon in their near-surface region than in the wear tracks generated under hydrogen environment. For both oxygen and hydrogen environment, when increasing the gas pressure (Figure 4.24.a), the fraction of $sp^2$-bonded carbon decreases.

The fraction of $sp^2$-bonded carbon increases with increasing surface sensitivity for all wear tracks generated under oxygen and hydrogen environment independently of the gas pressure (Figure 4.24.b). This finding indicates the formation of a $sp^2$-bonded carbon-rich layer on a-C:H:Si:O upon sliding independently of the gas and its pressure.

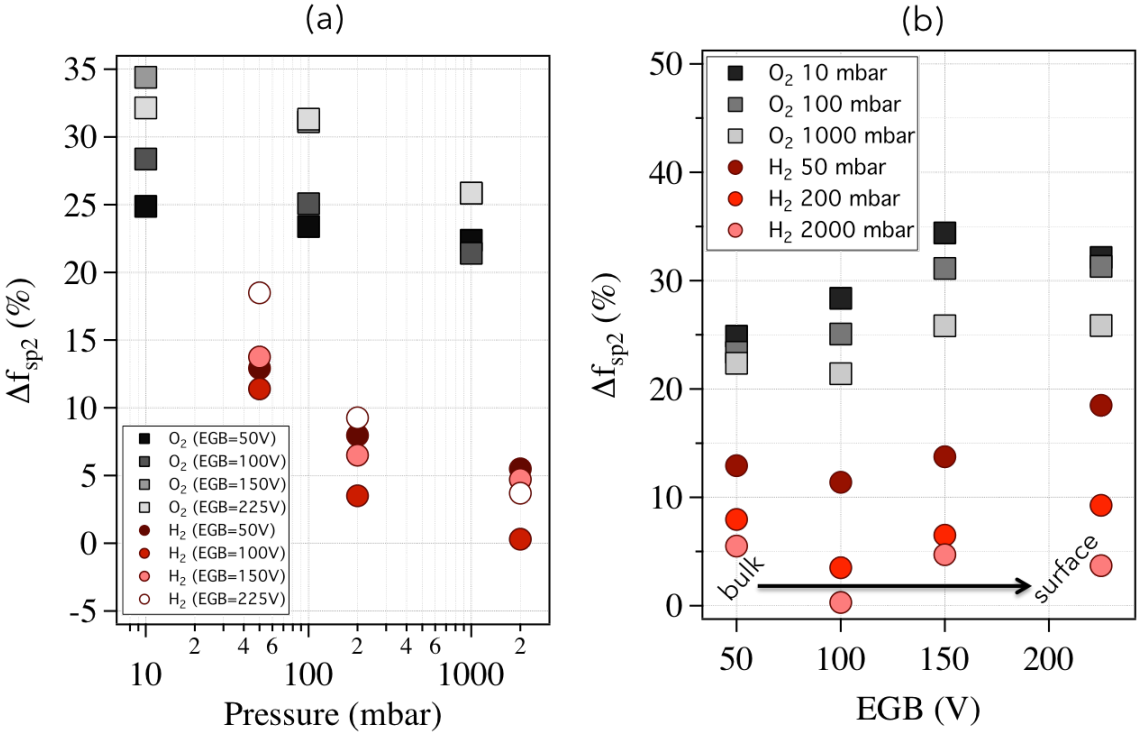


***Figure 4.24. Relative variation of the fraction of sp$^2$-bonded carbon for the track generated in hydrogen (50, 200 and 2000 mbar) or oxygen (10, 100, and 1000 mbar) as (a) function of the gas pressure and (b) the entrance grid bias (EGB) voltage (b)***

# 5. Discussion: Surface passivation vs. rehybridization in determining the friction response of a-C:H:Si:O

NEXAFS spectra (Figure 4.21, Figure 4.23 and Figure 4.24) acquired inside the worn region after tribotests performed either under oxygen or hydrogen revealed the presence of an sp$^2$-bonded carbon rich surface layer, with an increasing sp$^2$ concentration towards the surface. This is in agreement with Le Huu *et al.*, who have shown a transformation of sp$^3$- to sp$^2$-bonded carbon upon sliding. This rehybridization phenomenon is also supported by experimental data from self-mated sliding studies of diamond and tetrahedral amorphous carbon (ta-C) films[44,64] and molecular dynamics simulations of sliding of hydrogenated and hydrogen-free amorphous carbon films[63,65].

In addition, according to NEXAFS analysis, the wear track produced when sliding in oxygen environment exhibited carbon-oxygen bonds in the near-surface region of a-C:H:Si:O. This increase in intensity of the signal assigned to carbon-oxygen bonds (286.0 eV) could be interpreted as the dissociative reaction of oxygen molecules with strained sp$^2$–hybridized C-C

bonds, which are produced upon sliding[65]. This reaction results in the formation of an oxygen-passivated layer on a highly $sp^2$-bonded carbon surface produced by sliding on a-C:H:Si:O in oxygen.

However, according to the NEXAFS analysis, the wear track produced in hydrogen environment did not lead to a higher increase in C–H bonds at the surface (a slight increase was observed only at 2000 mbar of hydrogen) than in the wear tracks generated in oxygen environment. In addition, the near-surface region of this track exhibits much less $sp^2$-bonded carbon than the wear track produced under oxygen environment (note: the tribological conditions used for performing experiments were the same for the different environments). This suggests that either hydrogen is favoring the breakage of a-C:H:Si:O thanks to the newly generated strained $sp^2$ carbon rich layer to form a tribofilm on the steel countersurface, or the carbon atoms react with hydrogen to generate volatile hydrocarbon fragments. This finding is different than results reported by Fontaine *et al.*[66], Donnet *et al.*[67], and Erdemir *et al.*[68] who studied hydrogenated amorphous carbon films under HV and in presence of hydrogen or in dry environment. Matta *et al*.[69] also studied tetrahedral hydrogen free amorphous carbon films in presence of OH-containing environments. They all explained the decrease of the friction in the presence of hydrogen or –OH elements respectively, as a consequence of the passivation of the $sp^2$ bonded carbon by either hydrogen of –OH groups.

# 6. Summary

In this Chapter, the tribological response of a-C:H:Si:O film under different environmental conditions, ranging from high vacuum to elevated hydrogen, oxygen and water vapor pressures, was investigated. Three major conclusions can be drawn on the basis of the results presented in this Chapter:

1. By using a Controlled Environment Analytical Tribometer from high vacuum up to two atmospheres, we were able to determine, for the first time, a threshold in water vapor (1 mbar), oxygen (10 mbar) or hydrogen gas pressure (50 mbar), necessary to switch from a high friction regime to a low friction regime. This indicates that the reduction of friction is due to tribochemical reactions, which require a sufficiently abundant source of gas molecules to achieve and maintain low friction. Even though water is more reactive than oxygen and hydrogen (only 1 mbar of water vapor is needed to switch from high to low friction regime whereas 10 or 50 mbar is required for oxygen and hydrogen respectively), the energy required to wear a-C:H:Si:O in

presence of water vapor is higher than the one required for the same process under oxygen or hydrogen;

2. Under high vacuum and low gas pressure (P < 1 mbar of water vapor, P < 10 mbar of oxygen or P < 50 mbar of hydrogen), transfer of material from the steel pin to the a-C:H:Si:O flat was observed. In contrast, above 1 mbar of water vapor, 10 mbar of oxygen and 50 mbar hydrogen, transfer of material takes place from the a-C:H:Si:O flat to the steel pin, resulting in the formation of a tribofilm on the steel countersurface. This latter tribofilm has a low shear strength thus favoring low friction;
3. The NEXAFS characterization of a-C:H:Si:O after the tribological tests revealed that upon sliding under oxygen (P > 10 mbar) or hydrogen (P > 50 mbar) environments, a surface layer with a higher fraction of $sp^2$-bonded carbon atoms compared to the unworn material is formed on a-C:H:Si:O.

# 7. Résumé Chapitre 4

Dans ce chapitre intitulé « *influence de l'hydrogène, de l'oxygène et de la vapeur d'eau sur le comportement tribologique des a-C:H:Si:O* », nous approfondissons les résultats du chapitre précédent, en travaillant sous un environnement bien mieux contrôlé, mais par conséquent statique. À la vapeur d'eau et l'oxygène abordé précédemment, nous ajoutons l'hydrogène, bien connu pour son rôle majeur dans la réduction du frottement des couches minces DLC.

Pour ce faire, nous avons utilisé un tribomètre linéaire alternatif placé dans une chambre mise sous vide poussé, telle que décrite dans le chapitre deux. Les pressions d'oxygène et d'hydrogène considérées varient entre 0,01 et 2000 mbar, et les pressions de vapeur d'eau entre 0,01 et 20 mbar (correspondant respectivement à 0,04% et 100% d'humidité relative). Ces essais montrent que les a-C:H:Si:O présentent un mauvais comportement tribologique intrinsèque (sous vide), avec des coefficients de frottement autour de 1. En conduisant des essais à différentes pressions de gaz dans la chambre, nous avons quantifié, pour la première fois, les pressions exactes d'hydrogène, d'oxygène et de vapeur d'eau nécessaires à la transition entre un régime de frottement élevé et un régime de frottement faible, pour un contact entre une couche mince a-C:H:Si:O et un antagoniste en acier 100Cr6. Ces seuils sont de 50 mbar d'hydrogène, 10 mbar d'oxygène et 1 mbar de vapeur d'eau.

Lorsque les essais tribologiques sont menés en dessous de ce seuil, non seulement le frottement est très élevé, mais il se produit en outre, un transfert de l'acier vers le revêtement. Comme la dureté de la couche mince a-C:H:Si:O est très légèrement supérieure à celle de l'acier, ce comportement s'explique par une usure adhésive de l'acier.

Pour des pressions de gaz supérieures à ce seuil, le transfert de matière se produit dans le sens inverse, du a-C:H:Si:O vers l'acier, avec formation d'un tribofilm adhérent à l'acier.

Une analyse approfondie des processus d'usure du revêtement en fonction de l'environnement de fonctionnement confirme la tendance trouvée au chapitre trois. En effet, l'oxygène agit comme un « accélérateur » dans le processus d'usure de l'a-C:H:Si:O, alors que la vapeur d'eau constitue un « film protecteur » qui inhibe l'usure du revêtement.

Les données Raman recueillies sur les tribofilms montrent, quant à elles, que les tribofilms carbonés générés dans les différents environnements sont riches en clusters de carbone $sp^2$.

En effectuant des analyses de spectroscopie d'absorption des rayons X (NEXAFS), nous montrons pour la première fois sur les revêtements a-C:H:Si:O que lors d'un essai

tribologique en présence de quantité suffisante de gaz (au delà des pressions seuil identifiées), un changement structural des carbone $sp^3$ en $sp^2$ intervient en extrême surface du revêtement, avec un gradient décroissant vers le cœur.

Ces analyses montrent également une passivation de la surface par l'oxygène environnant. Par ailleurs, plus la pression de gaz environnant est élevée, plus la fraction de carbone $sp^2$ dans la zone de frottement diminue et plus le tribofilm obtenu sur l'antagoniste en acier est épais. Tous ces éléments permettent de confirmer et clarifier les mécanismes de lubrification des couches a-C:H:Si:O en présence d'oxygène, d'hydrogène et de vapeur d'eau.

# 8. References


1. Gao, G. T., Mikulski, P. T. & Harrison, J. A. Molecular-Scale Tribology of Amorphous Carbon Coatings: Effects of Film Thickness, Adhesion, and Long-Range Interactions. J. Am. Chem. Soc. **124,** 7202–7209 (2002).
2. Schall, J. D., Gao, G. & Harrison, J. A. Effects of Adhesion and Transfer Film Formation on the Tribology of Self-Mated DLC Contacts. J. Phys. Chem. C **114,** 5321–5330 (2010).
3. Fontaine, J., Belin, M., Le Mogne, T. & Grill, A. How to restore superlow friction of DLC: the healing effect of hydrogen gas. Tribol. Int. **37,** 869–877 (2004).
4. Gao, G. T., Mikulski, P. T. & Harrison, J. A. Molecular-scale tribology of amorphous carbon coatings: effects of film thickness, adhesion, and long-range interactions. J. Am. Chem. Soc. **124,** 7202–7209 (2002).
5. Rose, F. et al. Complete characterization by Raman spectroscopy of the structural properties of thin hydrogenated diamond-like carbon films exposed to rapid thermal annealing. J. Appl. Phys. **116,** 123516 (2014).
6. Ferrari, A. C. & Robertson, J. Resonant Raman spectroscopy of disordered, amorphous, and diamondlike carbon. Phys. Rev. B **64,** 075414 (2001).
7. Casiraghi, C., Ferrari, A. C. & Robertson, J. Raman spectroscopy of hydrogenated amorphous carbons. Phys. Rev. B **72,** 085401 (2005).
8. Ferrari, A. & Robertson, J. Interpretation of Raman spectra of disordered and amorphous carbon. Phys. Rev. B **61,** 14095–14107 (2000).
9. Ferrari, A. C. & Robertson, J. Interpretation of Raman spectra of disordered and amorphous carbon. Phys. Rev. B **61,** 14095–14107 (2000).
10. Casiraghi, C., Piazza, F., Ferrari, A. C., Grambole, D. & Robertson, J. Bonding in hydrogenated diamond-like carbon by Raman spectroscopy. Diam. Relat. Mater. **14,** 1098–1102 (2005).
11. Scharf, T. W. & Singer, I. L. Thickness of diamond-like carbon coatings quantified with Raman spectroscopy. Thin Solid Films **440,** 138–144 (2003).
12. Stöhr, J. NEXAFS Spectroscopy. (Springer Science & Business Media, 1992).
13. Robin, M. B., Ishii, I., McLaren, R. & Hitchcock, A. P. Fluorination effects on the inner-shell spectra of unsaturated molecules. J. Electron Spectrosc. Relat. Phenom. **47,** 53–92 (1988).
14. Ishii, I. & Hitchcook, A. P. The oscillator strengths for C1s and O1s excitation of some saturated and unsaturated organic alcohols, acids and esters. J. Electron Spectrosc. Relat. Phenom. **46,** 55–84 (1988).
15. Stöhr, J. NEXAFS Spectroscopy. (Springer Science & Business Media, 1992).
16. Mangolini, F., McClimon, J. B., Rose, F. & Carpick, R. W. Accounting for Nanometer-Thick Adventitious Carbon Contamination in X-ray Absorption Spectra of Carbon-Based Materials. Anal. Chem. (2014). doi:10.1021/ac503409c
17. Genzer, J., Kramer, E. J. & Fischer, D. A. Accounting for Auger yield energy loss for improved determination of molecular orientation using soft x-ray absorption spectroscopy. J. Appl. Phys. **92,** 7070–7079 (2002).
18. Konicek, A. R. et al. Influence of surface passivation on the friction and wear behavior of ultrananocrystalline diamond and tetrahedral amorphous carbon thin films. Phys. Rev. B **85,** 155448 (2012).
19. Konicek, A. R. et al. Origin of Ultralow Friction and Wear in Ultrananocrystalline Diamond. Phys. Rev. Lett. **100,** 235502 (2008).
20. Kunze, T. et al. Wear, Plasticity, and Rehybridization in Tetrahedral Amorphous Carbon. Tribol. Lett. **53,** 119–126 (2014).
21. Fontaine, J., Le Mogne, T., Loubet, J. L. & Belin, M. Achieving superlow friction with hydrogenated amorphous carbon: some key requirements. Thin Solid Films **482,** 99–108 (2005).
22. Donnet, C., Fontaine, J., Grill, A. & Mogne, T. L. The role of hydrogen on the friction mechanism of diamond-like carbon films. Tribol. Lett. **9,** 137–142 (2001).
23. Erdemir, A. The role of hydrogen in tribological properties of diamond-like carbon films. Surf. Coat. Technol. **146–147,** 292–297 (2001).
24. Matta, C. et al. Tribochemistry of tetrahedral hydrogen-free amorphous carbon coatings in the presence of OH-containing lubricants. Lubr. Sci. **20,** 137–149 (2008).

# *Chapter 5. Influence of environment and structural evolutions on the tribological behavior of a-C:H:Si:O: proposition of a model*

*In this chapter, the effect of annealing induced structural changes on the tribological properties of a-C:H:Si:O in dry conditions as well as the main scientific outcomes of the experimental work presented in the previous Chapters (environmental dependence of tribological behavior) are summarized and discussed. A thorough discussion of the results obtained from the experiments with previously published, state-of-the-art works will be made. Finally, a model that describes the fundamental mechanisms behind the tribological response of a-C:H:Si:O in different environments is proposed and discussed.*

# Table of contents: Chapter 5. Influence of environment and structural evolutions on the tribological behavior of a-C:H:Si:O: proposition of a Model

# 1. Effect of structural changes on the tribological behavior of a-C:H:Si:O

As demonstrated in chapter 4, stress-induced rehybridization (conversion from $sp^3$ to $sp^2$-bonded carbon) plays a major role in the overall friction response of a-C:H:Si:O. Changing the initial $sp^2$-bonded carbon fraction in the coating by annealing of a-C:H:Si:O has been achieved. Upon annealing a-C:H:Si:O under UHV, an increase in the fraction of $sp^2$ bonded carbon with increasing temperature has been verified by NEXAFS and Raman spectroscopic measurements, following the procedure described in chapter 2 session 4.2. Below an annealing temperature of 450°C, NEXAFS and Raman results are in slight disagreement (Figure 5.1.) which might be due to the difference in the information depth probed by the two techniques (~5 nm for NEXAFS[157] and ~ 300 nm for Raman[163]) and to the presence of a surface gradient in the structure of the material (meaning that the near-surface region is richer in $sp^2$-bonded carbon). At 450 °C, the good agreement between Raman and NEXAFS spectroscopic measurements suggests that the structure of the material is homogeneous within the volume probed by Raman. Despite these structural changes, SIMS analyses (Appendix A.2) indicated the absence of any significant composition change upon annealing.

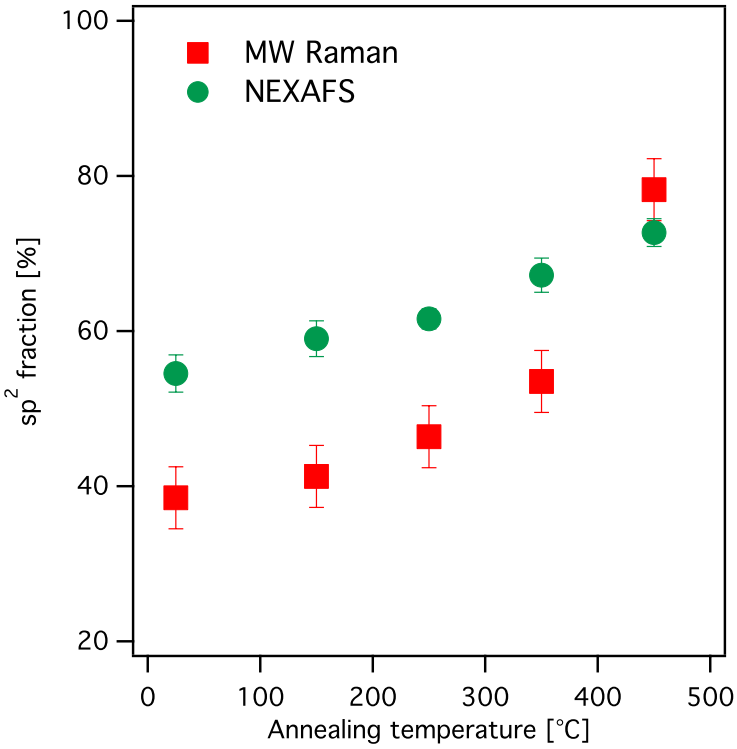


***Figure 5.1. $sp^2$-bonded carbon fraction in a-C:H:Si:O upon UHV annealing measured by MW Raman (red) and NEXAFS (green)***

Using the linear reciprocating tribometer equipped with the gas blowing system extensively described in chapter 2, session 3.2.1, tribological experiments performed on samples annealed in UHV under dry nitrogen flow (Figure 5.2) indicate that there is no significant difference in the steady-state frictional response between annealed samples and as received material (the coefficient of friction got stabilized at ~0.03 for annealed sample as well as the as-received one). Differences might be present in the duration of the running-in period, but a careful statistical evaluation of the running-in duration requires more extensive work to be performed. This finding suggest, for the first time, that under dry conditions the steady-state frictional response is not significantly affected by the structure of the coating.

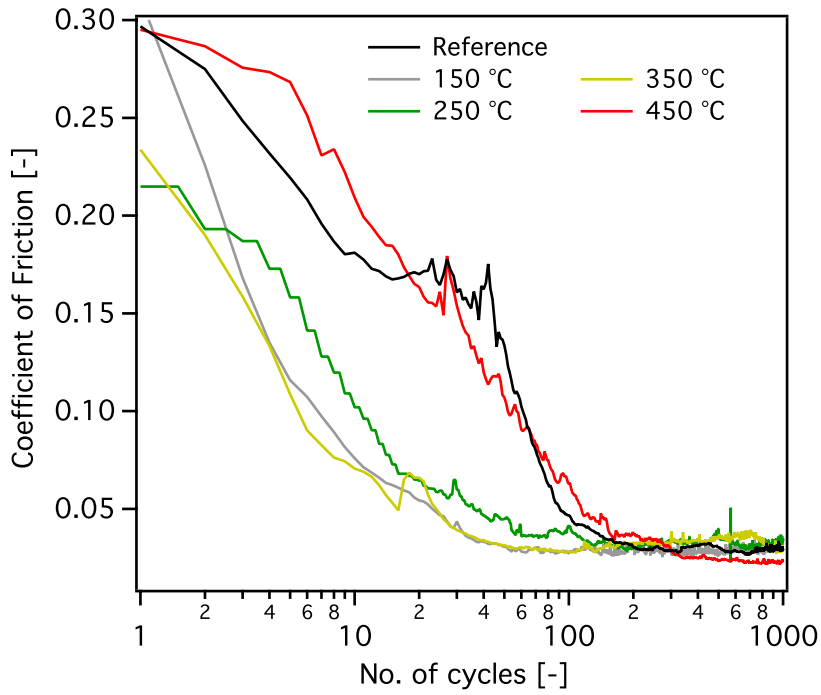


***Figure 5.2. Evolution of coefficient of friction vs. cycles of annealed a-C:H:Si:O sliding against 52100 steel under dry nitrogen flow***

# 2. Effect of water vapor and oxygen on the tribological behavior of a-C:H:Si:O

## 2.1. Effect of water vapor on the frictional response of a-C:H:Si:O

As discussed in Chapters 3 and 4, and herein illustrated (Figure 5.3) water vapor plays a major role in controlling the frictional response of a-C:H:Si:O. For water vapor pressures lower than 1 mbar (~ 4% RH) high friction is achieved, while at this threshold, the lowest coefficient of friction (0.02±0.01) was reached. Above 1 mbar of water vapor, the coefficient of friction starts increasing again (Figure 5.3.a). Comparing these results to the ones obtained with the ambient air linear tribometer equipped with the gas blowing system, it can be noticed that the friction response of a-C:H:Si:O in dry environment (dry nitrogen, dry argon or dry air flow (<5% RH), Figure 5.3.b) is equivalent to the one obtained at 1 mbar, namely 0.04±0.01. Also, the coefficient of friction values obtained in ambient air (35% RH at 27 °C or 13 mbar partial pressure of water vapor, Figure 5.3.c) with the linear reciprocating tribometer is not

significantly different from the one obtained with Environment Controlled Analytical tribometer (15 mbar of water vapor or 50% RH at 24 °C), *i.e.*, 0.18±0.01.

Even though a correlation between the results obtained with the two experimental methods employed in the study can be performed, it has to be underlined that the environmental conditions are not exactly the same. In facts, while the partial pressure of water matches between the two experimental methodologies, during tribological experiments performed in ambient air while blowing gas, some residual gaseous species such as oxygen, nitrogen or carbon dioxide are still present in the environment. On the contrary, in the Controlled Environment Analytical Tribometer, leaking specific gases in the HV chamber allows having only one gas species at the time. However, the fact that it is possible to correlate the tribological results obtained as a function of water vapor partial pressure with the two experimental apparatuses clearly suggest that the residual species in air (oxygen, carbon dioxide, and nitrogen) do not play a major role in affecting the frictional response of a-C:H:Si:O. In other words, water vapor has a higher reactivity with a-C:H:Si:O compared to the other gaseous species. This is also in agreement with the higher threshold found for oxygen (14 mbar) and hydrogen (50 mbar) while the one of water vapor is 1 mbar.

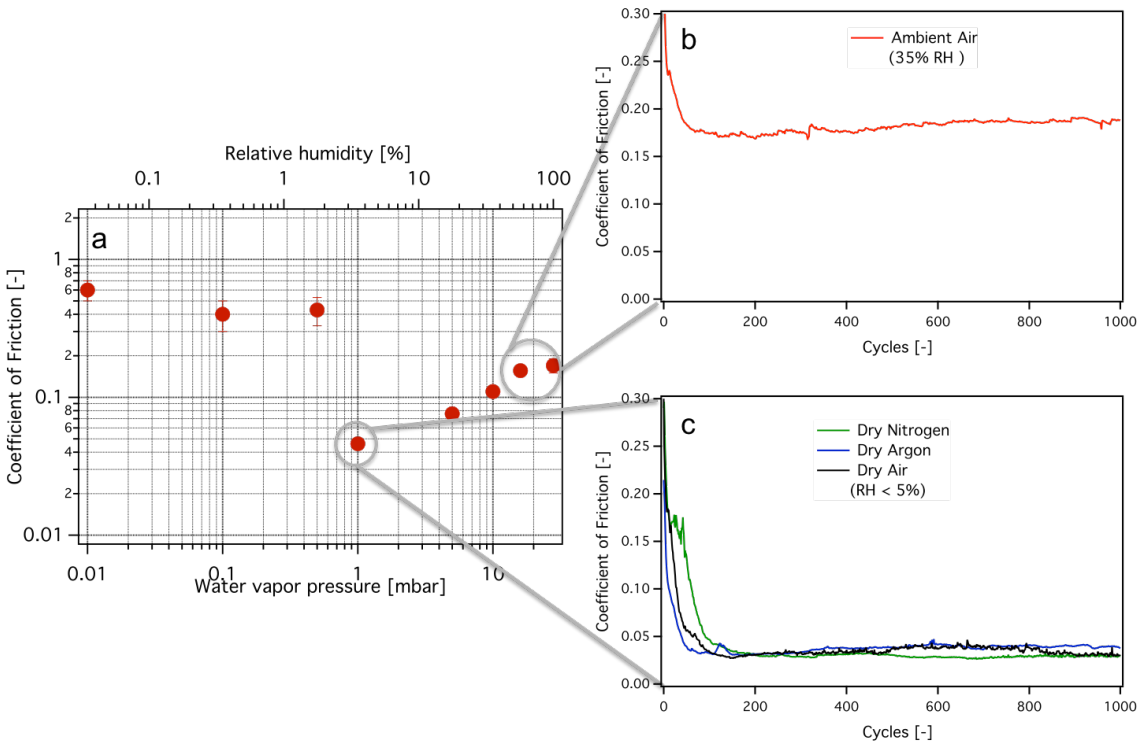


***Figure 5.3. Correlation between the results obtained with the Environment Controlled Analytical Tribometer and the ambient air tribometer (CEAT) equipped with gas blowing system. Evolution of the coefficient of friction vs. sliding cycles with (a) various partial pressure of water vapor, (b) in ambient air (RH 35%), (c) under dry nitrogen, dry argon or dry air flow (RH<5%).***

## 2.2. Effect of oxygen on the wear of a-C:H:Si:O

As mentioned in chapter 3, blowing dry air in the contact in order to lower the relative humidity down to RH < 5% and thus decrease the steady-state coefficient of friction, results in generating more wear than under ambient air (RH 35%), dry nitrogen flow or dry argon flow (RH <5%) as illustrated in Figure 5.4.a.

Figure 5.4.b shows the relative wear of a-C:H:Si:O in presence of oxygen (1000 mbar), hydrogen (2000 mbar) or water vapor (28 mbar). The higher wear of a-C:H:Si:O was obtained in oxygen environment.

Coupling CEAT wear results together with the ones obtained under dry air flow and keeping in mind that under dry air flow, the residual oxygen in the sliding environment is higher than under dry nitrogen and dry argon, we can argue that oxygen is the main gaseous element responsible for the wear of a-C:H:Si:O.

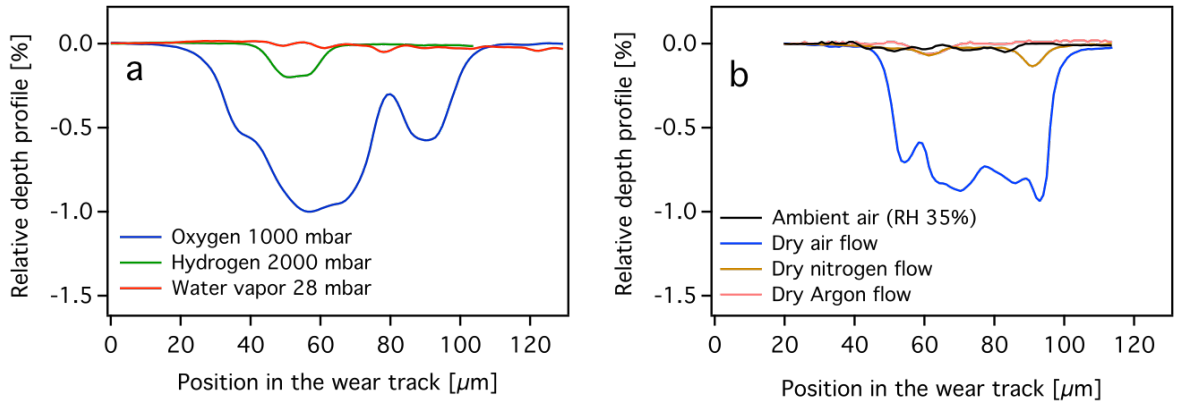


***Figure 5.4. Relative depth profile of the wear tracks obtained on a-C:H:Si:O after tribological experiments performed using (a) CEAT in oxygen (1000 mbar), hydrogen (2000 mbar) and water vapor (28 mbar) or (b) open air tribometer equipped with gas flow system in ambient air, dry air, dry nitrogen and dry argon.***

## 3. Tribological behavior of a-C:H:Si:O under HV and in presence of oxygen, hydrogen and water vapor: a new model

On the basis of the results presented in Chapter 3 and 4, we were able to propose a model depicted in Figure 5.5 for explaining the frictional response of a-C:H:Si:O under different environmental conditions.

- **Stage 1**: Initial state without applying any mechanical stress;
- **Stage 2**: Upon sliding, asperities come into contact. As shown by several authors[59,65], carbon rehybridization (stress-induced conversion from $sp^3$- to $sp^2$-bonded carbon) occurs within the contact area. The initial and newly-generated $sp^2$-bonded carbon is highly strained and thus prone to react with the environment[69];
- **Stage 3, under HV and low gas pressure**: Upon further sliding, the reactive $sp^2$ bonded carbon atoms at the surface interact with the steel counterbody and create adhesive junctions. The interaction of carbon $sp^2$ orbitals under HV has been also observed by Donnet *et al.*[67];
- **Stage 4, under HV and low gas pressure**: Some adhesive bonds are stronger than the metallic bonds in the steel countersurface, thus leading to a transfer of steel onto the a-C:H:Si:O. The large amount of energy required for breaking metallic bonds in steel results in high friction under HV conditions and low gas pressure.

➢ **Stage 3', under intermediate and high gas pressure**: The observed transfer of material from the coating to the steel pin indicates that interfacial adhesion, as described at Stage 3 (under HV and low gas pressure), still occurs. However, the direction of the material transfer is changed: carbon, silicon, and oxygen are observed transferred to the steel countersurface (hydrogen is presumed to be transferred as well), whereas no iron is transferred to a-C:H:Si:O. Based on NEXAFS data, a layer with a higher fraction of $sp^2$-hybridized carbon is formed during sliding, similar to simulations and experiments for self-mated sliding of diamond and ta-C films[44,64,65]. In the presence of highly reactive gases, the strained $sp^2$ carbon-carbon bonds can easily break, thus leading to transfer of material to the steel countersurface and leaving behind a passivated highly-$sp^2$-bonded carbon surface. The increase of C=O peak intensity at 286.0 eV in the track obtained upon sliding under oxygen supports this. The fact that the C-H peak does not increase in intensity for sliding in hydrogen environments may be due to the highly favorable reaction of hydrogen molecules with strained $sp^2$ carbon-carbon bonds, resulting in either an easier removal of material from the wear track or the formation of volatile short-chain hydrocarbon fragments. More work is required to have insights into the dominant tribochemical reaction(s). The etching of the softer, disordered, highly-$sp^2$-bonded carbon layer is supported by the fact that the absolute values of the variation in the fraction of $sp^2$-bonded carbon in the near-surface region of the wear track created upon sliding under hydrogen environment is lower than upon sliding in oxygen (chapter 4, lower inset, Figure 4.16).

➢ **Stage 4'**, **under intermediate and high gas pressure**: Under the combined effect of a larger total sliding distance of the steel pin (higher than the worn region of the a-C:H:Si:O flat) and the applied load and stress, the transferred $sp^2$ hybridized carbon-rich top layer on the steel pin, has enough energy to reorganize itself into larger aromatic clusters, leading then to a $sp^2$ layer rich in ring-like structures between the steel pin and the flat, as indicated by Raman spectroscopic measurements explained in chapter 4, session 5.1. Nevertheless, once the modified carbon tribofilm is generated in the contact, the friction will no longer only depend on the way the adhesive junctions are released (the energy that is needed to break the bonds in the steel side or in the a-C:H:Si:O) but also on the shear strength of this tribofilm. In fact, as shown by Scharf *et al.*[96], the shear strength of tribofilms generated when sliding against a-C:H:Si:O depends on its chemical composition, which is a function of the sliding

environment. This might explain differences in the friction coefficients obtained under water vapor, oxygen gas or hydrogen gas.

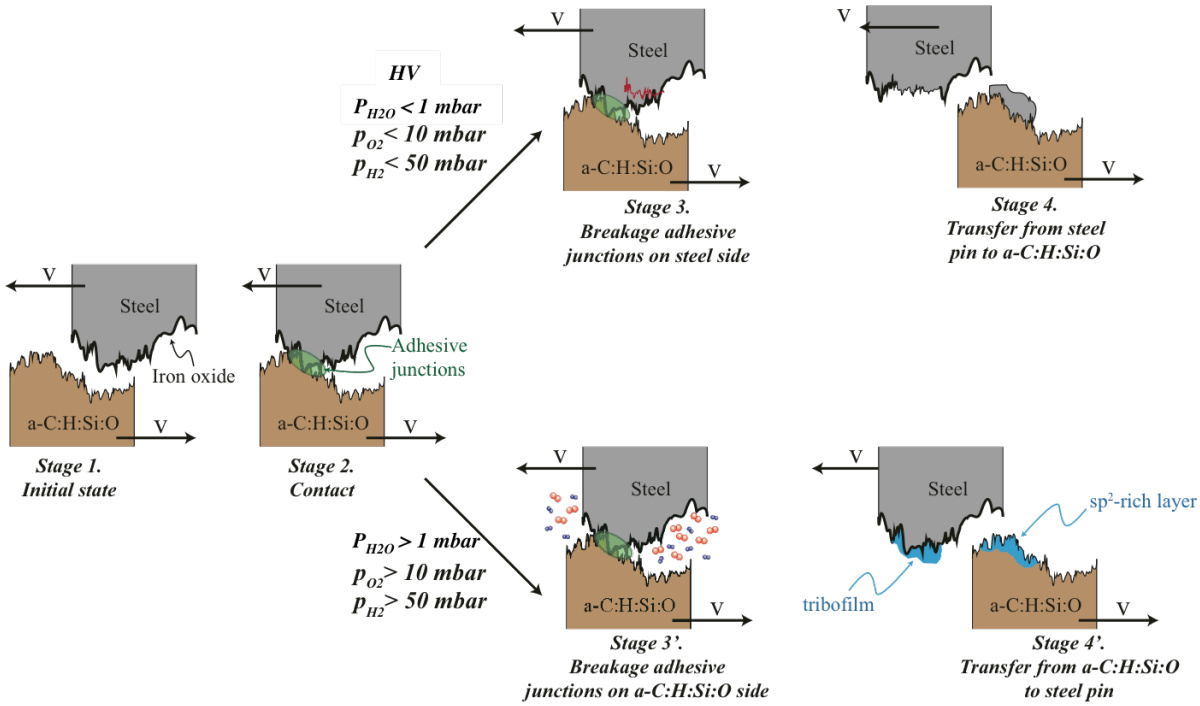


***Figure 5.5. Schematic model for describing the friction properties of an a-C:H:Si:O vs. steel tribosystem sliding under different environmental conditions.***

# 4. Summary

The tribological response of a-C:H:Si:O film was investigated under different environmental conditions, ranging from humid and dry sliding environment to high vacuum or elevated water vapor, oxygen and hydrogen pressures. Four major conclusions can be drawn on the basis of the results presented in this work:

- *We were able to establish a direct relationship between the amount of water vapor in the sliding environment and the frictional response of a-C:H:Si:O, thanks to an ambient air tribometer equipped with a gas flow system and the Controlled Environment Analytical Tribometer (CEAT). It has also been possible to demonstrate that oxygen is the main gaseous elements responsible for the wear of a-C:H:Si:O.*
- *We were able to determine, for the first time, a threshold in water vapor (1 mbar), oxygen (10 mbar) or hydrogen gas pressure (50 mbar), necessary to switch from a high friction regime to a low friction regime by using an CEAT from high vacuum up to elevated pressures of hydrogen, oxygen, or water vapor. This indicates that the reduction of friction is due to tribochemical reactions, which require a sufficiently abundant source of gas molecules to achieve and maintain low friction. The difference in the threshold values also reflects a different reactivity of the gases, i.e., reactivity of water vapor > reactivity of oxygen > reactivity of hydrogen;*
- *Under high vacuum and low gas pressure ($p < 1$ mbar of water vapor, 10 mbar of oxygen or $p < 50$ mbar of hydrogen), transfer of material from the steel pin to the a-C:H:Si:O flat was observed. In contrast, above 1 mbar of water vapor, 10 mbar of oxygen and 50 mbar hydrogen, transfer of material takes place from the a-C:H:Si:O flat to the steel pin, thus building a tribofilm on the steel countersurface. This latter tribofilm has a low shear strength;*
- *The NEXAFS characterization of a-C:H:Si:O after the tribological tests revealed that upon sliding under oxygen ($p > 10$ mbar) or hydrogen ($p > 50$ mbar) environments, a surface layer with a higher fraction of $sp^2$-bonded carbon atoms compared to the unworn material is formed on a-C:H:Si:O.*

The outcomes of the present thesis suggest that the build-up and release of adhesive junctions between steel and a-C:H:Si:O strongly depends on the environment. In particular, the tribochemical changes occurring in a-C:H:Si:O upon sliding in the presence of water vapor (1 mbar), oxygen (p > 10 mbar) or hydrogen (p > 50 mbar) indicate, for the first time, that these gases favor the release of the chemical bonds by dissociatively reacting with the mechanically-stressed $sp^2$ carbon-rich surface layer in the near-surface of a-C:H:Si:O.

# 5. Résumé Chapitre 5

Du fait de l'importance des modifications chimiques et structurales mises en évidence dans le chapitre quatre, nous abordons dans ce chapitre des investigations complémentaires concernant l'influence de modifications chimiques et structurales du revêtement sur le comportement tribologique de ce dernier. Pour ce faire, nous nous intéressons à des échantillons ayant subi un traitement thermique sous vide à 150°C, 250°C, 350°C et 450°C.

Après analyses structurales (NEXAFS et Raman à plusieurs longueurs d'onde) et mécanique (nanoindentation) du revêtement après traitement thermique, une étude de l'effet synergique de la modification structurale et de l'influence de la vapeur d'eau et de l'oxygène sur la réponse tribologique du revêtement a été menée. Nous avons ainsi montré que même si l'enrichissement de la surface de la couche en carbone $sp^2$ ne modifie pas de façon notoire, le coefficient de frottement stabilisé de la couche, l'oxygène accélère l'usure de la couche alors que la vapeur d'eau semble jouer le rôle d'un élément anti usure comme c'est le cas pour la couche n'ayant pas subi de traitement thermique.

Ce dernier chapitre propose ensuite – à la lumière de tous les résultats présentés dans le manuscript– un modèle expériemental expliquant les interactions physico-chimiques entre l'environnement et les revêtements a-C:H:Si:O en contact avec un antagoniste en acier 100Cr6. Ce modèle est résumé dans la figure ci-dessous.

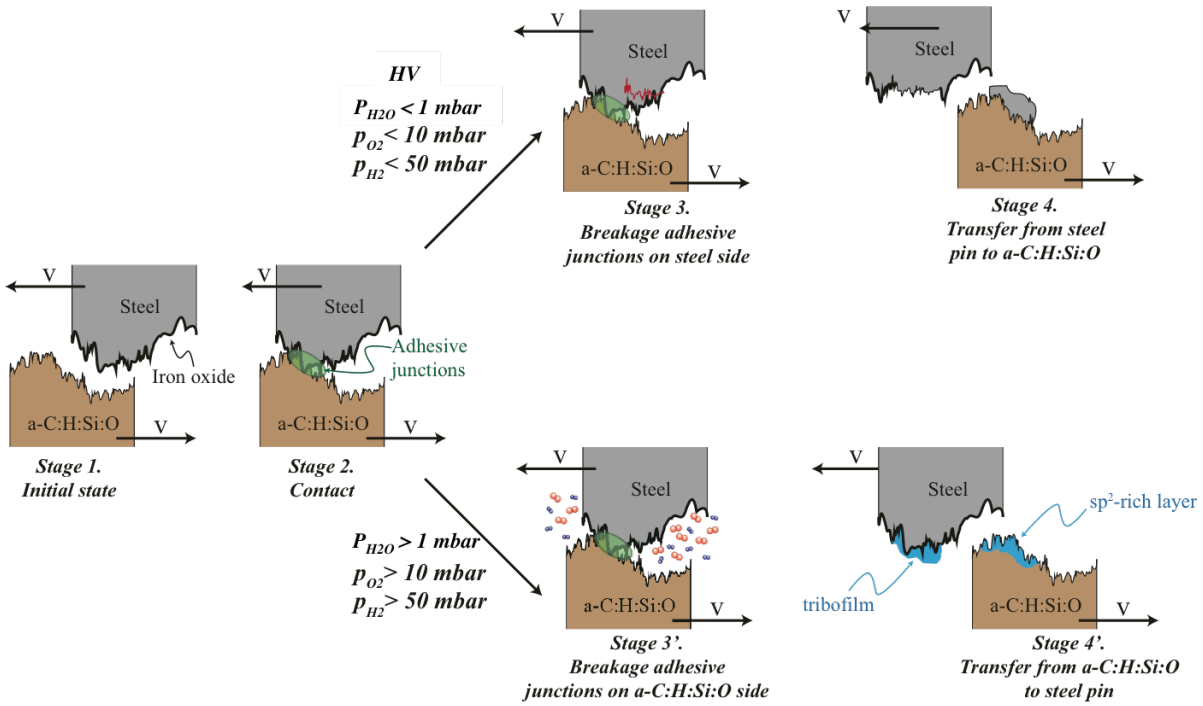


**Modèle schématique décrivant l'évolution d'un contact a-C:H:Si:O / acier 100Cr6 en fonction de l'environnement (hydrogène, oxygène, vapeur d'eau) et les phénomènes locaux correspondants**

# 6. References


1. Genzer, J., Kramer, E. J. & Fischer, D. A. Accounting for Auger yield energy loss for improved determination of molecular orientation using soft x-ray absorption spectroscopy. J. Appl. Phys. **92,** 7070–7079 (2002).
2. Scharf, T. W. & Singer, I. L. Thickness of diamond-like carbon coatings quantified with Raman spectroscopy. Thin Solid Films **440,** 138–144 (2003).
3. Kunze, T. et al. Wear, Plasticity, and Rehybridization in Tetrahedral Amorphous Carbon. Tribol. Lett. **53,** 119–126 (2014).
4. Le Huu, T., Zaidi, H., Paulmier, D. & Voumard, P. Transformation of sp3 to sp2 sites of diamond like carbon coatings during friction in vacuum and under water vapour environment. Thin Solid Films **290–291,** 126–130 (1996).
5. Matta, C. et al. Tribochemistry of tetrahedral hydrogen-free amorphous carbon coatings in the presence of OH-containing lubricants. Lubr. Sci. **20,** 137–149 (2008).
6. Donnet, C., Fontaine, J., Grill, A. & Mogne, T. L. The role of hydrogen on the friction mechanism of diamond-like carbon films. Tribol. Lett. **9,** 137–142 (2001).
7. Konicek, A. R. et al. Origin of Ultralow Friction and Wear in Ultrananocrystalline Diamond. Phys. Rev. Lett. **100,** 235502 (2008).
8. Konicek, A. R. et al. Influence of surface passivation on the friction and wear behavior of ultrananocrystalline diamond and tetrahedral amorphous carbon thin films. Phys. Rev. B **85,** 155448 (2012).
9. Scharf, T. W., Ohlhausen, J. A., Tallant, D. R. & Prasad, S. V. Mechanisms of friction in diamondlike nanocomposite coatings. J. Appl. Phys. **101,** 063521–063521–11 (2007).

# Conclusion and outlook

# *Conclusion*

Diamond-Like Carbon (DLC) thin films are a class of solid lubricant with a wide range of technological applications from automotive industries to cutting tools and biomedical prosthesis. Different additional elements can be incorporated into this amorphous carbon network in order to enhance some specific properties while maintaining the amorphous structure. Silicon-oxide doped amorphous hydrogenated carbon coatings are a variant of DLC, known for their higher thermal stability and tribological properties, which are less dependent on the sliding environment than pure DLC coatings.

This thesis aims to understanding the fundamental mechanical, physical and chemical interactions occurring between a-C:H:Si:O and environmental constituents upon sliding against 52100 steel and their consequences for the overall tribological response. Thanks to annealing-induced structural changes of a-C:H:Si:O, effect of structural evolutions on the tribological behavior of a-C:H:Si:O have been also studied.

Since the tribological behavior of DLC coatings is a global response due to both intrinsic and extrinsic factors, as described in this thesis, a complete characterization of the material has been carried out prior to tribological experiments. Multi-Wavelength Raman spectroscopy, coupled with Near-Edge X-ray Absorption Fine Structure (NEXAFS) spectroscopy, confirmed the amorphous structure of the material of interest, while Rutherford Backscattering Spectroscopy (RBS) coupled with Hydrogen Forward Scattering (HFS), together with depth profiling Secondary Ions Mass Spectroscopy (SIMS), provided a precise chemical composition of the a-C:H:Si:O. The mechanical properties and the surface topography were measured by nanoindentation and AFM, respectively.

Experiments using an ambient air linear reciprocating tribometer that we equipped with a gas blowing system, revealed that water vapor and oxygen play a key role respectively in the frictional response and in the wear of a-C:H:Si:O,. Thanks to the static and dynamically-controlled variation of the humidity of the sliding environment, we were able to show that the friction response of a-C:H:Si:O is governed by the amount of carbon in the tribofilm generated at the sliding interface and its structure, which in turn, depends on the amount of water vapor in the environment. In dry conditions, there is a high fraction of carbon in the tribofilm – small and strained aromatic carbon clusters – while in humid conditions the

lower fraction of carbon are primarily segregated to regions outside of the theoretical Hertzian contact area.

A more precisely controlled examination of the environmental dependence of the tribological response was then performed using a Controlled Environment Analytical Tribometer (CEAT) that allowed performing experiments in a wide range of conditions; from HV to elevated pressures of water vapor, oxygen and hydrogen (0.01 mbar up to 2000 mbar).
For low water vapor, oxygen and hydrogen pressures (P<1, P<10 and P<50 mbar respectively, a transfer of material occurs from steel to a-C:H:Si:O resulting in high friction. For intermediate and high gas pressures (P>1, P>10 and P>50 mbar of water vapor, oxygen and hydrogen respectively) transfer occurs in the opposite direction from a-C:H:Si:O to steel resulting in low friction.
We were thus able to define precisely, for the first time, the minimum amount of water vapor, oxygen or hydrogen needed to achieve low friction while sliding a-C:H:Si:O against 52100 steel. For gas pressures bellow the threshold, transfer of material occurs from the steel to a-C:H:Si:O, resulting in high friction while above the threshold, the transfer occurs from a-C:H:Si:O to steel, resulting in low friction.

Furthermore, based on detailed surface analysis using NEXAFS together with extensive Raman spectroscopy and SEM/EDX observations, we proposed a new model describing the fundamental friction mechanism of a-C:H:Si:O in the presence of oxygen and hydrogen. This mechanism is based on the build-up and release of adhesive junctions through the sliding interface. For oxygen and hydrogen pressures lower than 10 and 50 mbar respectively, adhesive junctions are broken inside the steel, resulting in a transfer of iron on top of a-C:H:Si:O. Due to the strength of the metallic bonds between the steel and the transferred, the friction coefficient in this range of gas pressure was as high as ~ 1.2. For oxygen and hydrogen pressure higher than 10 and 50 mbar respectively, adhesive junctions are released inside the a-C:H:Si:O promoting a lower coefficient of friction.
Thanks to chemical mapping using NEXAFS, we were able to show that, when sliding in the presence of gases, rehybridization (the transition from $sp^3$- to $sp^2$-bonded carbon) occurs in the near-surface region of a-C:H:Si:O, as suggested by several molecular dynamics simulation works.

Increasing oxygen or hydrogen pressure in the sliding environment favors a decrease of $sp^2$-bonded carbon formation in the near surface region, suggesting that either gaseous species preferentially break strained $sp^2$ carbon bonds in the near surface region, followed by a transfer to the steel counterbody, as verified by Raman either in presence of gas less

adhesive junctions are created and broken. Passivation of the remaining dangling carbon bonds in the worn region was observed in oxygen environment while no significant increase in C–H was observed in the wear track, even at 2000 mbar of hydrogen. The total amount of hydrogen in the wear track being the same, one could be tempted to think that passivation does not occur upon sliding under hydrogen. Nevertheless it is also plausible that environmental hydrogen acts as a permanent reservoir as discussed in chapter 1, thus compensating the amount of hydrogen "leaked out" from a-C:H:Si:O. Further experiments using deuterium and Tof-SIMS analysis could be of a good interest in determining weather or hydrogen identified in the wear track comes from the environment, i.e. weither or not passivation occurs

Under UHV annealing, a-C:H:Si:O evolves towards a more $sp^2$-bonded carbon-like structure. The tribological response of this new material appeared unchanged compared to the one of as-received a-C:H:Si:O. This implies that under dry conditions, the tribological response a-C:H:Si:O does not seem to be controlled by the fraction of $sp^2$-bonded carbon in the initial state, but rather by the chemistry and structure of the tribofilm.

# *Outlooks*

Although this thesis contributes to the fundamental understanding of the tribogocial behavior of a-C:H:Si:O solid lubricants in various environmental conditions by shedding light on the mechanical, physical and chemical interactions that occur upon sliding a-C:H:Si:O films against 52100 steel, there are still different interesting aspects that could be explored for further understanding of the tribological behavior of these coatings. Here are some ideas for future work:

- ***Varying the composition of the material***

In order to confirm the beneficial effect of the presence of silicon in the amorphous carbon network on the tribological behaviour of a-C:H:Si:O, performing experiments on films with different silicon contents would be helpful, and would allow a better understanding of its actual role.

- ***Improving experimental conditions while using the ambient air reciprocating tribometer equipped with the gas flow system***

As discussed in chapter 3, the steady-state coefficient of friction strongly depends on the amount of water vapor in the sliding environment. Relative humidity (RH) controls thus the stabilized coefficient of friction that can be obtained prior to the gas flow. As mentioned in chapter 3, session 3.1, RH and temperature in the sliding environment can be very dispersed depending on the weather conditions, affecting thus the stabilized coefficient of friction prior to the gas flow. For a better control of this stabilized friction, prior to the gas flow, the device could be introduced in a glove box.

- ***Further surface analysis by PhotoEmission Electron Microscopy***

Due to the strong magnetic field in the synchrotron end station's analyzing chamber, we were not able to analyze the material transferred on the steel counterbody. Investigating the structural changes occurring in the near surface region has thus been carried out only in the worn region of a-C:H:Si:O. Nevertheless, as suggested by all our results, the chemistry and structure of the tribofilm play a major role in the overall tribological response of a-C:H:Si:O. Analyzing the tribofilm transferred on the steel counterbody using PhotoEmission Electron Microscopy (PEEM) could be of a good contribution in bridging the gap between the chemistry and structure of the tribofilm and the tribological behavior of a-C:H:Si:O. For that aim, a proposal that we submitted to "Synchrotron soleil" (Saint Aubin, France) has been accepted and beam time granted. PEEM experiments should be thus conducted in the upcoming months.

- ***Controlled environment FFM (Friction Force Microscopy)***

As described in supplementary material S.3, results obtained using FFM in humid and dry conditions correlate with macroscale measurements (lower friction obtained under dry condition than in humid air). There still is a lot of investigations than could be carried out in order to understand the fundamental microscale tribolofigical mechanisms of a-C:H:Si:O and hopefully, at the scale of a single asperity.

# Conclusion et Perspectives

Les films minces DLC représentent une classe de lubrifiants solides aux domaines d'application multiples pouvant aller de l'industrie automobile aux outils de coupe et aux applications biomédicales. Différents éléments peuvent être incorporés dans le réseau de carbone amorphe de ces revêtements en couche mince afin de les « fonctionnaliser » pour une application cible, tout en maintenant leur structure amorphe. L'incorporation de silicium et d'oxygène dans le réseau amorphe de carbone permet d'obtenir des revêtements dénommés a-C:H:Si:O, connus pour leur meilleure stabilité thermique et la faible dépendance environnementale de leurs performances tribologiques, comparativement aux revêtements DLC « purs ». La compréhension fondamentale des phénomènes responsables de ces différences de comportement permettrait de concevoir des matériaux à base carbone aux propriétés tribologiques optimales pour différents environnements.
Le but de ce travail de thèse était ainsi d'élucider les phénomènes fondamentaux impliqués dans la réponse tribologique de revêtements *a-C:H:Si:O,* tant du point de vue de la mécanique que des interactions physico-chimiques avec l'environnement et/ou leur antagoniste (en acier 100Cr6). En outre, afin de répondre à la problématique de la stabilité thermique de ces revêtements, nous avons pu étudier l'effet des changements structuraux induits par traitement thermique sur leur réponse tribologique.

Il est bien établi dans la littérature que le comportement tribologique des revêtements DLC en général est une réponse globale conjuguant à la fois les facteurs intrinsèques et extrinsèques, tel que présenté dans le premier chapitre de ce manuscrit.

Nous avons donc procédé à une analyse complète des revêtements a-C:H:Si:O avant essais tribologiques, exposée dans le chapitre 2, notamment par des mesures Raman à plusieurs longueurs d'ondes couplées avec de la spectroscopie NEXAFS (*Near-Edge X-Ray Absorption Fine Structure*).

Nous avons menés des essais tribologiques, à pression atmosphérique, sur un tribomètre linéaire alternatif, que nous avons équipé d'un système de soufflage de gaz, permettant de changer l'environnement du contact de l'air ambiant à l'air sec, l'azote sec ou l'argon sec (Chapitre 3). Ces essais ont révélé que la vapeur d'eau et l'oxygène jouent un rôle clé respectivement sur le coefficient de frottement et sur le taux d'usure du revêtement a-C:H:Si:O. Ce dispositif nous a également permis de varier de façon dynamique l'environnement du contact. Il nous a ainsi été possible de démontrer que la réponse en frottement du revêtement est contrôlée par la réponse mécanique de l'interface (structure et composition du tribofilm, taux de cisaillement de l'interface), elle-même dépendante du taux de vapeur d'eau dans l'environnement. Cette variation de la réponse en frottement en fonction du taux d'humidité s'avère réversible. Ces expériences à pression atmosphérique ont aussi permis de mettre en évidence le rôle prépondérant de l'oxygène dans l'accélération de l'usure des revêtements a-C:H:Si:O.

Afin de mieux comprendre le rôle de l'environnement sur la réponse tribologique des a-C:H:Si:O, nous avons mené des essais sur un tribomètre analytique en environnement contrôlé (Chapitre 4), fonctionnement depuis un vide poussé jusqu'à des pressions élevées de vapeur d'eau, d'oxygène ou d'hydrogène. Ces expériences ont révélé que les revêtements a-C:H:Si:O tribologiques intrinsèques médiocres (essais sous haut vide ou à faible pression de gaz, c'est à dire P<1 mbar de vapeur d'eau, P<10 mbar d'oxygène, P<50 mbar d'hydrogène). Néanmoins à partir et au-delà de ces pressions seuil, on obtient un faible coefficient de frottement.

Une analyse plus approfondie des surfaces antagonistes après essais tribologiques (trace d'usure et tribofilms) par NEXAFS et spectroscopie Raman ainsi que par microscopie électronique en Balayage couplée à l'analyse EDX (*Electron Dispersive X-Ray Spectroscopy*) nous ont permis de proposer un modèle expérimental décrivant globalement les mécanismes fondamentaux qui interviennent entre les revêtements a-C:H:Si:O et leur environnement lorsqu'ils sont soumis à des sollicitations tribologiques (Chapitre 5). Ce modèle est basé sur la formation et la dissociation de jonctions adhésives créées à l'interface entre le revêtement et l'acier. En effet, sous vide poussé ou sous faible pression de gaz (régime de haut coefficient de frottement), un phénomène de transfert de matière se produit de l'acier vers le revêtement, alors qu'à pression de gaz suffisamment élevée (régime de faible coefficient de frottement), le phénomène de transfert a lieu en sens opposé, du revêtement vers l'acier.

Ces analyses structurales en extrême surface du revêtement a-C:H:Si:O nous ont également permis de donner pour la première fois, une preuve expérimentale du phénomène de ré-hybridation du carbone, généré par les sollicitations tribologiques, phénomène largement étudié dans le cas d'autres familles de couches minces à base carbone. La formation de

carbone $sp^2$ en extrême surface des traces d'usure serait donc le résultat de la rupture des jonctions adhésives dans la couche à base carbone. Nous avons ainsi pu démontrer l'existence d'une réaction dissociative entre les gaz environnants (oxygène et hydrogène) et les liaisons carbone contraintes dans le revêtements suite aux sollicitations mécaniques, favorisant la rupture des liaisons C–C et *in fine* des jonctions adhésives.

Les essais tribologiques réalisés sur des revêtements ayant subi une transformation structurale par traitement thermique sous ultra vide ont aussi montré qu'une plus importante fraction initiale de carbone $sp^2$ en extrême surface du revêtement *a-C:H:Si:O* ne prédispose pas à l'obtention d'un bas coefficient de frottement.

**Perspectives**

En apportant de nouveaux éclairages sur les interactions mécaniques et physico-chimiques intervenant entre les revêtements à base de carbone amorphe contenant du silicium et de l'oxygène (*a-C:H:Si:O*) et leur environnement lorsqu'ils sont soumis à des sollicitations tribologiques, ce travail de thèse a contribué à la compréhension fondamentale des performances tribologiques des couches minces à base carbone. Différents aspects restent toutefois, à explorer, notamment :

- ***La variation de la composition du revêtement***

Afin de confirmer l'effet bénéfique de la présence du silicium et de l'oxygène dans la stabilité thermique et la moindre dépendance environnementale des propriétés tribologiques des a-C:H:Si:O, de nouvelles campagnes d'essais avec des revêtements à taux de silicium et d'oxygène variable pourraient être envisagées.

- ***Améliorer l'installation du tribomètre à air ambiant et son dispositif de changement rapide d'environnement***

Comme évoqué au Chapitre 3, à air ambiant, le coefficient de frottement stabilisé dépend fortement de l'humidité relative et donc des conditions climatiques au sein du laboratoire. Afin de permettre une meilleure reproductibilité des résultats, il serait envisageable d'introduire le dispositif dans une boite à gants, permettant en particulier un contrôle de l'humidité ambiante.

- ***Davantage d'analyses structurale des différents tribofilms générés***

Du fait de la forte force magnétique appliquée dans la chambre d'analyse de la ligne du synchrotron lors des analyses NEXAFS, il nous a été impossible de procéder à une analyse de

la structure et de l'hybridation des tribofilms formés sur les pions en acier. Il n'en demeure pas moins que la chimie et la structure du tribofilm peuvent nous renseigner davantage sur la de la corrélation entre la réponse tribologique des revêtements amorphes à base carbone et la nature de l'environnement. Dans cet ordre d'idée, une demande de temps d'analyses par PEEM (PhotoEmission Electron Microscopy) a été soumise et acceptée par le synchrotron SOLEIL (ligne HERMES). Les analyses des tribofilms par PEEM viendront donc compléter les résultats ici présentés dans les mois à venir.

- ***Essais tribologiques en environnement contrôlé à nano-échelle par FFM (Friction Force Microscopy)***

Comme présenté dans l'annexe S.3, les résultats obtenus par FFM en environnement humide (RH = 50%) ou sec (RH<1%) en utilisant des colloïdes d'acier collés sur des leviers d'AFM sont en adéquation avec ceux obtenus à macro échelle. Davantage d'investigations pourront être menées afin de comprendre les mécanismes de lubrification solide des couches minces à base carbone à nano échelle.

# *Appendix*

# Appendix A.1. Characterization of the as received material

## A.1.1. Film thickness, topography and mechanics

### A.1.1.1. Film thickness: cross section SEM

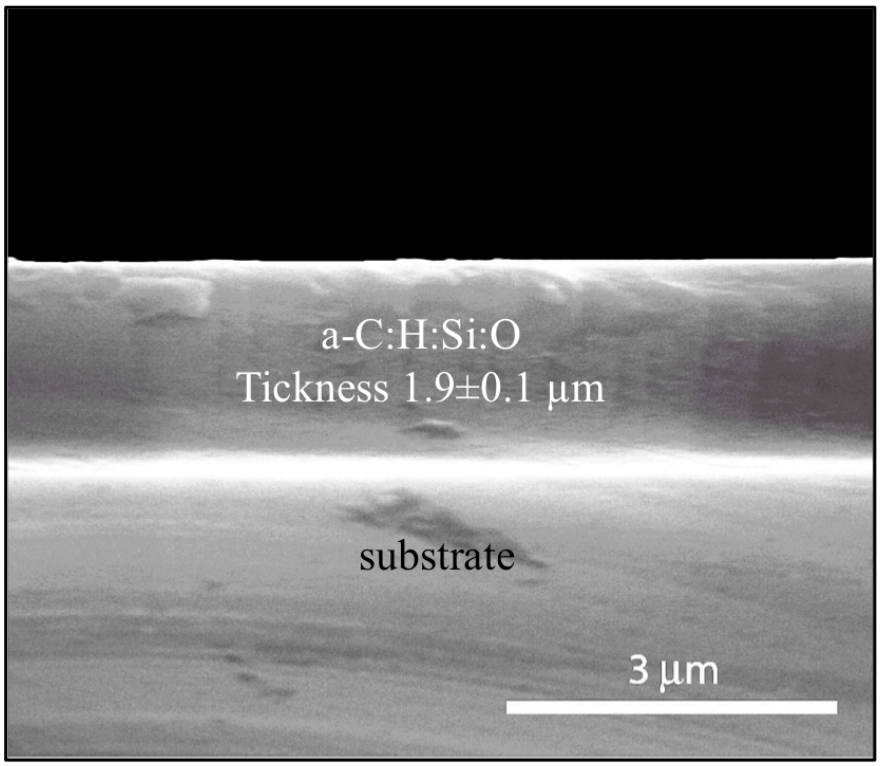


***Figure A.1. Cross section SEM micrograph of as received a-C:H:Si:O***

### A.1.1.2. Surface roughness: AFM measurements

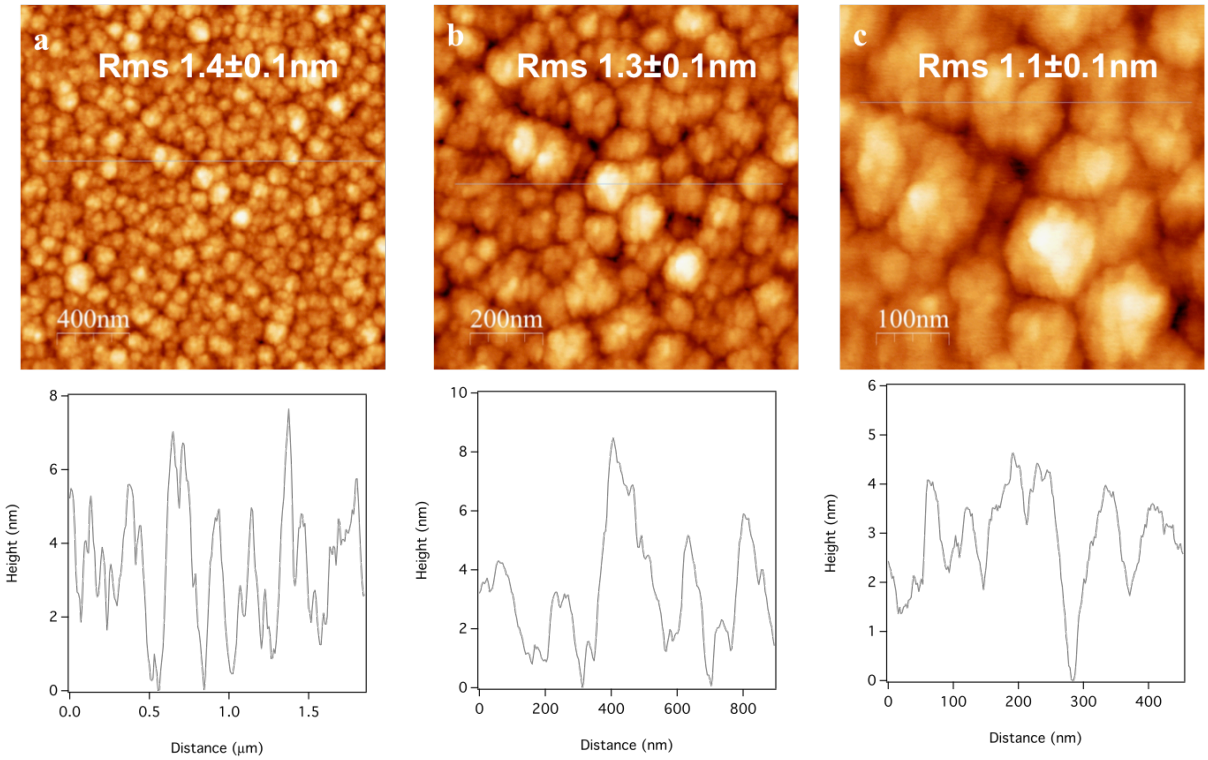


***Figure A.2. rms roughness of a-C:H:Si:O measured by AFM an area of (a) 2*2 µm$^2$, (b) 1*1 µm$^2$ and (c) 500*500 nm$^2$***

### A.1.1.3. Mechanical properties: Nanoindentation

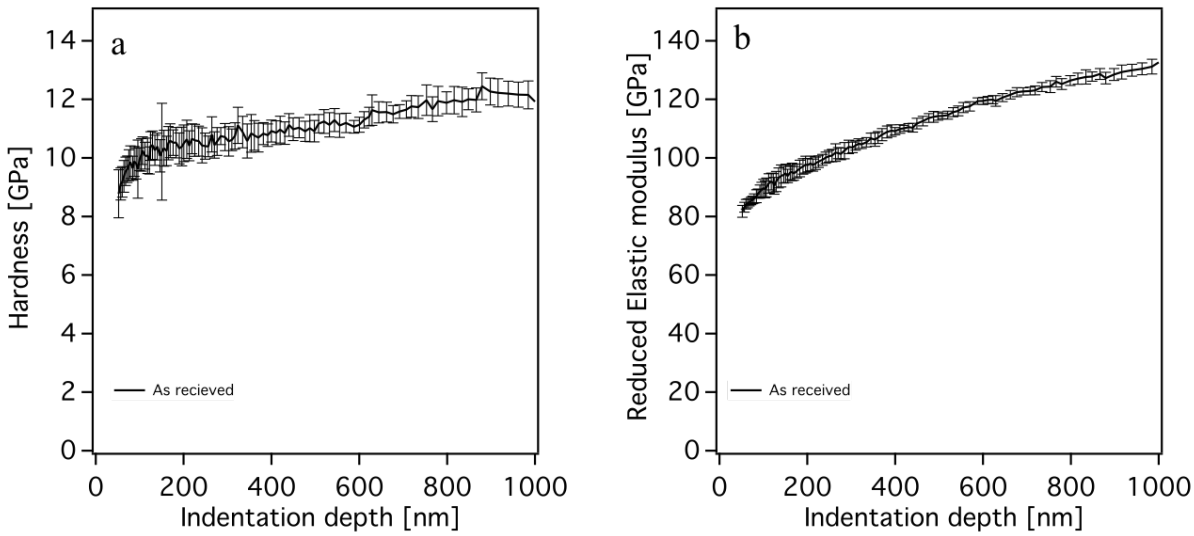


***Figure A.3. (a) Hardness and (b) Elastic modulus of a-C:H:Si:O measured by nanoindentation***

## A.1.2. Chemical characterization

### A.1.2.1. Composition: RBS/HFS and SIMS

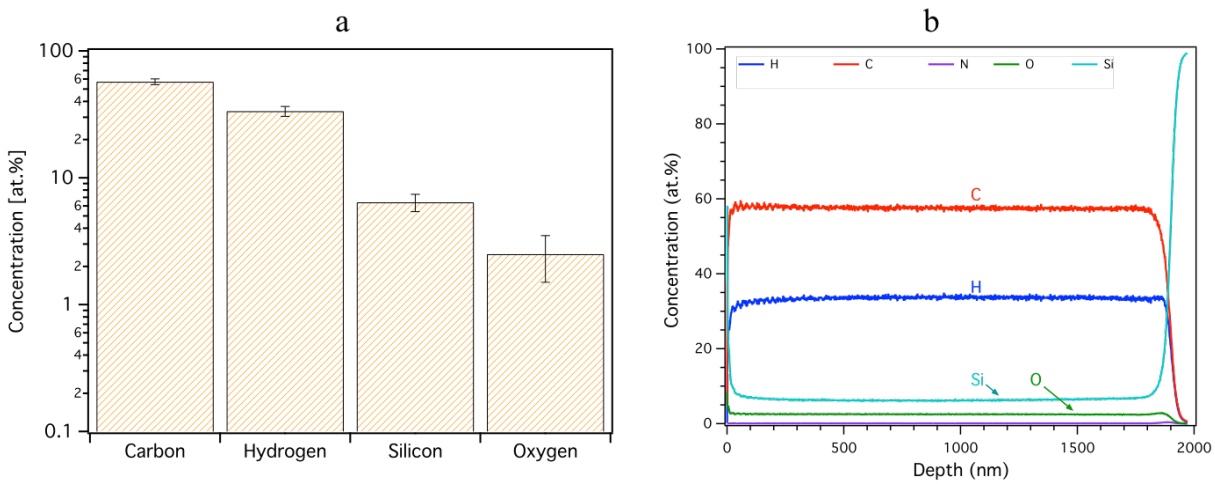


***Figure A.4. (a) RBS and (b) SIMS characterization of as-received a-C:H:Si:O. Data acquired by Evans Analytical Group.***

### A.1.2.2. Surface analysis: NEXAFS

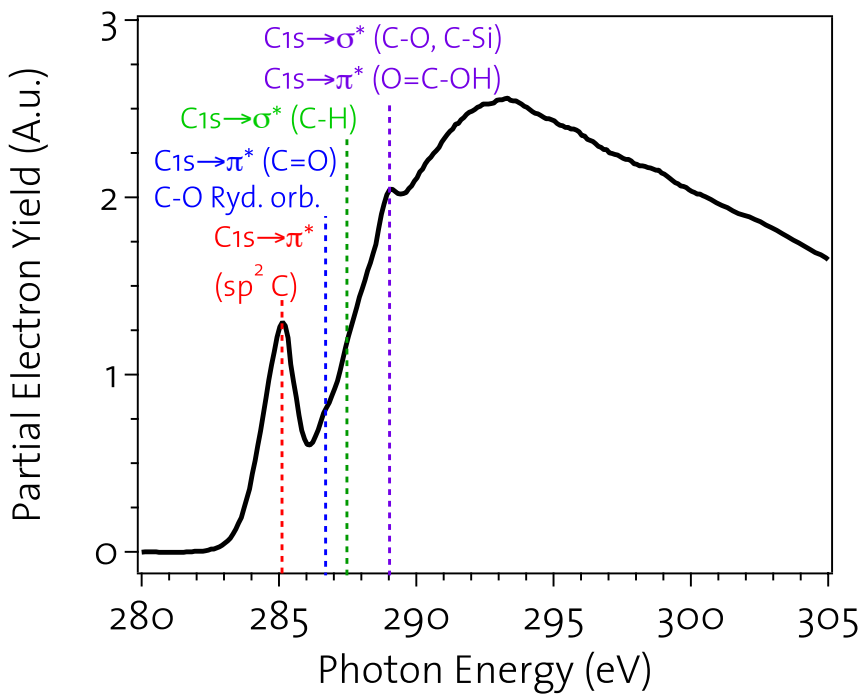


***Figure A.5. NEXAFS spectra with peak assignment for as recieved a-C:H:Si:***

# A.2. Characterization of UHV annealed sample

## A.2.1. Mechanical properties: Nanoindentation

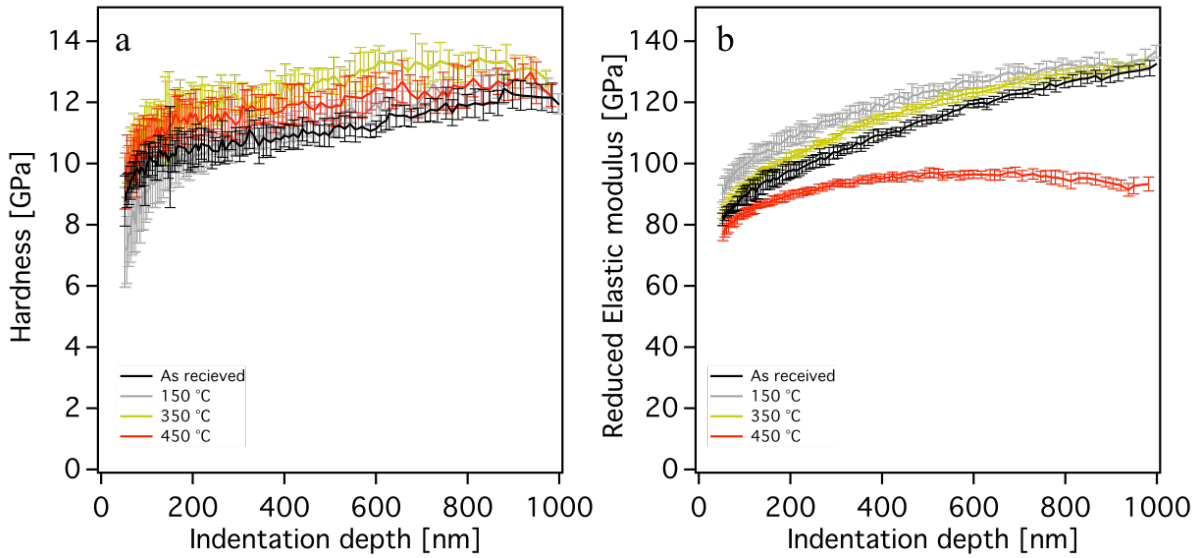


***Figure A.6. (a) Hardness and (b) Elastic modulus measurement on ultra high vacuum annealed a-C:H:Si:O at 150, 250 and 450°C for one hour.***

## A.2.2. Chemical characterization: SIMS

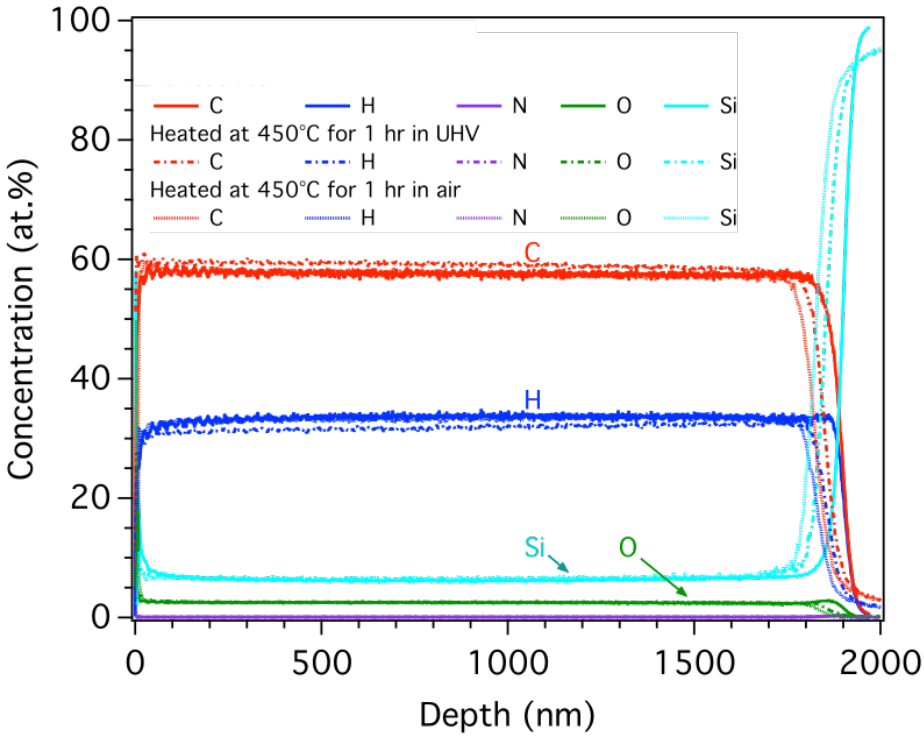


***Figure A.7. SIMS analysis of a-C:H:Si:O after annealing at 450°C under ultra-High vacuum conditions***

## A.2.3. Surface analysis

### A.2.3.1. XPS

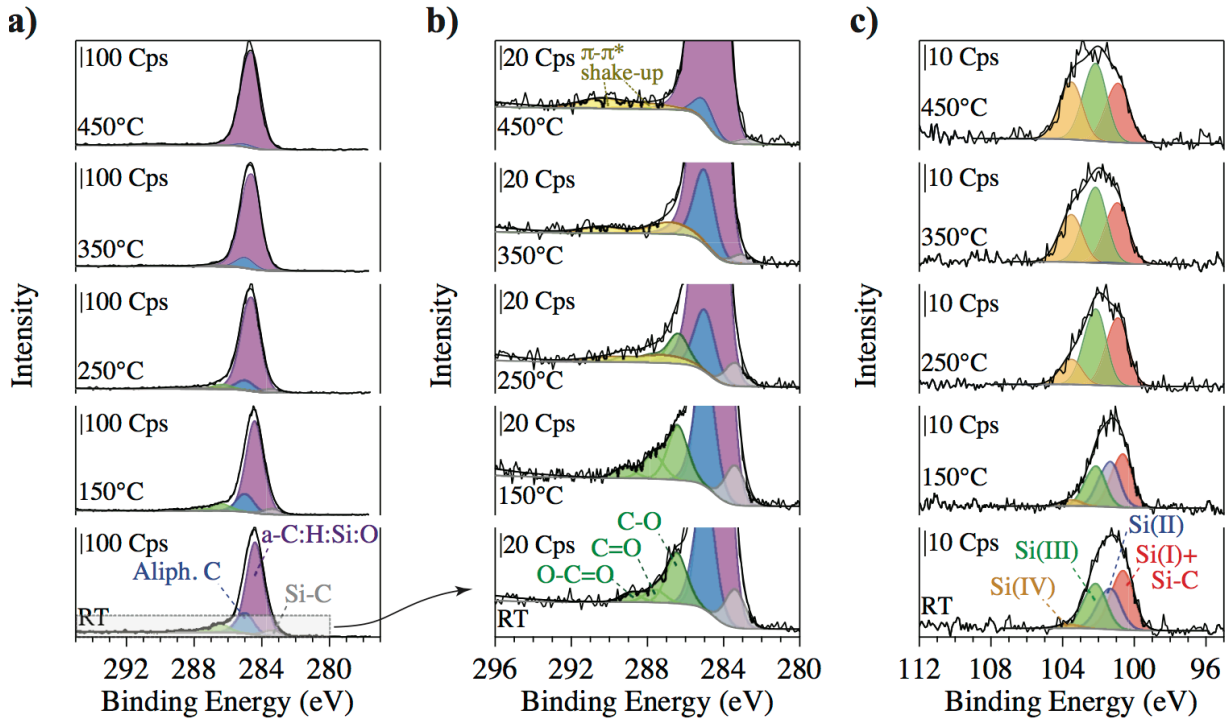


***Figure A.8. High-resolution XPS spectra ((a) and (b) C1s, (c) Si2p) of a-C:H:Si:O acquired before annealing and after annealing at different temperatures under ultra high vacuum condition. Colored lines are curve fits. (c) composition calculated from XPS data of the near-edge surface region of a-C:H:Si:O as function of annealing temperature. Data were acquired by Dr. F. Mangolini.***

### A.2.3.2. NEXAFS

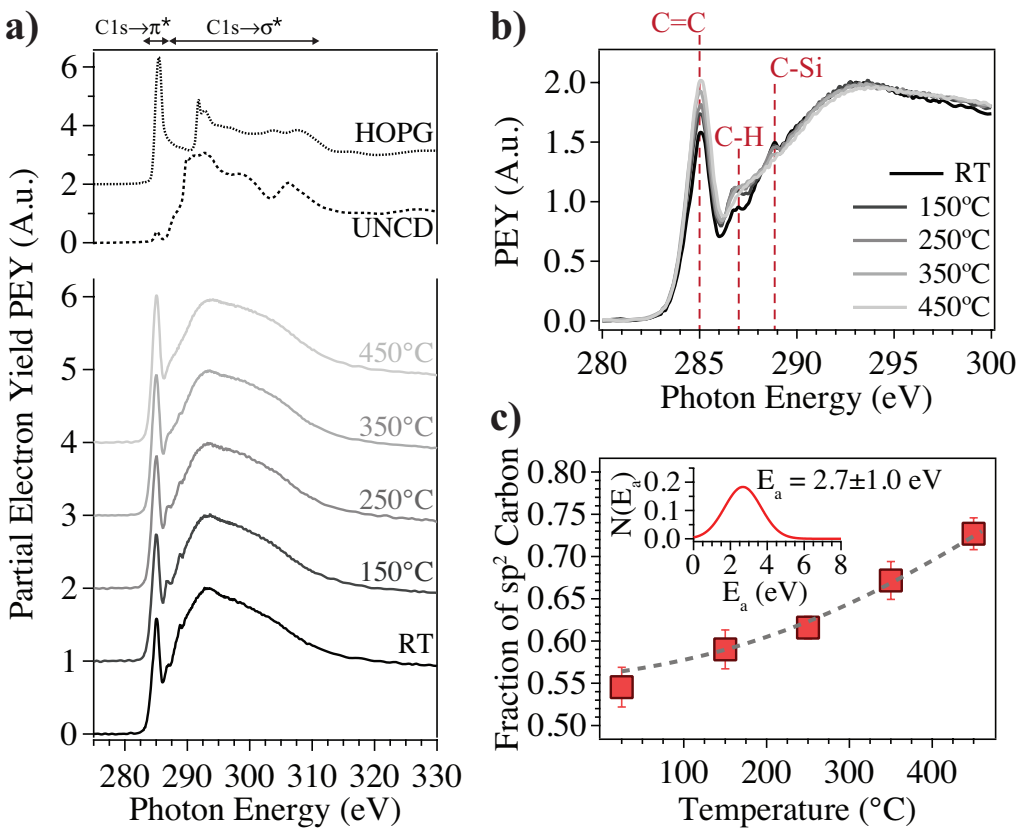


***Figure A.9. (a) C-K edge NEXAFS spectra of a-C:H:Si:O acquired before and after annealing at different temperatures under ultra-high vacuum conditions. The C K-edge spectra of reference sample (i.e. HOPG and UNCD) are also displayed (dashed lines). Spectra are presented and post-edge normalized as well as offset for clarity; (b) zoomed view of the absorption edge region of C K-edge NEXAFS spectra. Spectra displayed without any offset to allow for comparisons; (c) fraction of $sp^2$-hybridized carbon vs. annealing temperature calculated from NEXAFS spectra. Data were acquired by Dr. F. Mangolini.***

## Appendix A.3. Effect of environment on microscale tribological behavior of a-C:H:Si:O

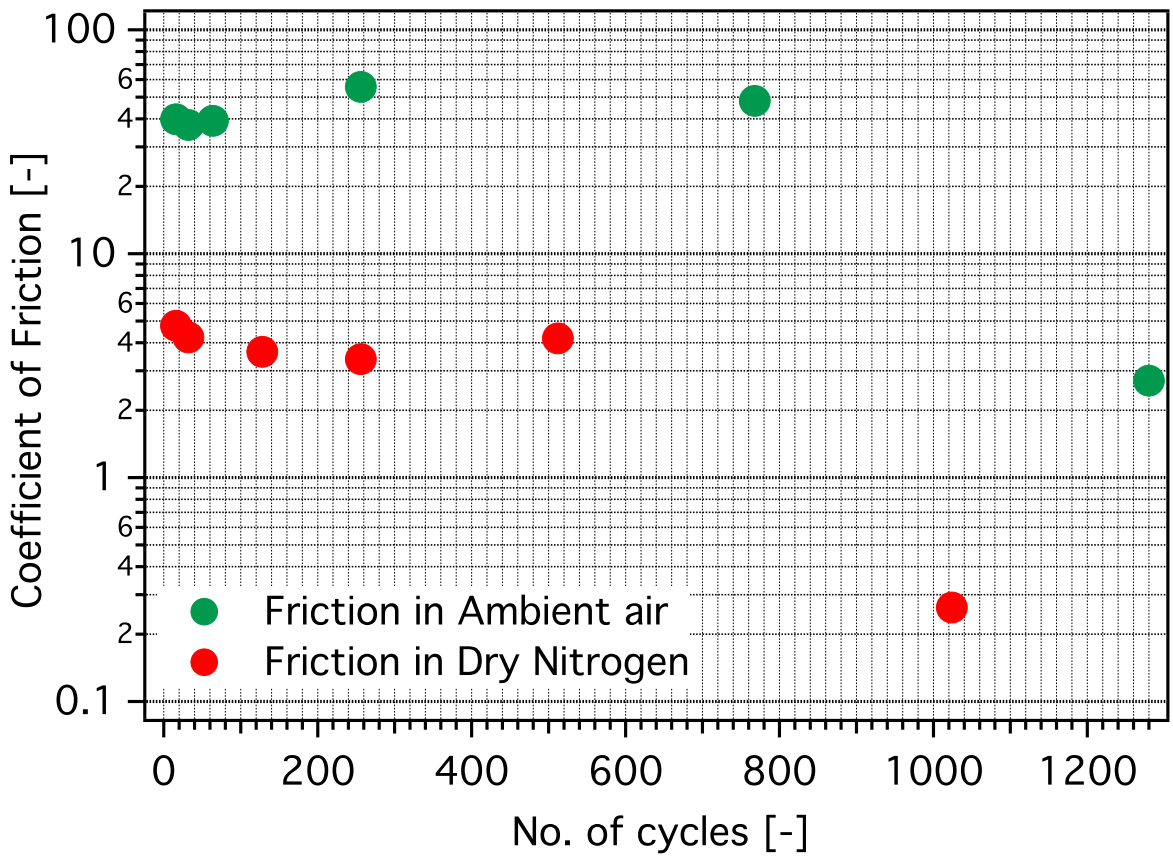


***Figure A.10. Microscale coefficient of friction of a-C:H:Si:O sliding against steel colloidal probe . Red measurements acquired in dry conditions (RH<1%), green: measurements acquired in humid conditions (RH 50%).***

*dernière page de la thèse*

# AUTORISATION DE SOUTENANCE

Vu les dispositions de l'arrêté du 7 août 2006,

Vu la demande du Directeur de Thèse

Monsieur F. DASSENOY

et les rapports de

Monsieur J. DENAPE
Professeur - Ecole Nationale d'Ingénieurs de Tarbes - 47 avenue d'Azereix - BP 1629
65016 TARBES cedex

Et de

Monsieur S. MISCHLER
Docteur - Ecole Polytechnique de Lausanne (EPFL) SCI STI SM - MXC 210 (Bâtiment MXC) station 12
CH-1015 Lausanne

**Monsieur KOSHIGAN Komlavi Dzidula**

est autorisé à soutenir une thèse pour l'obtention du grade de **DOCTEUR**

**Ecole doctorale MATERIAUX**

Fait à Ecully, le 24 septembre 2015

P/Le directeur de l'E.C.L.
La directrice des Etudes

ECOLE CENTRALE DE LYON
Service Scolarité
ECULLY

M-A. GALLAND

## Abstract

Silicon oxide-containing hydrogenated amorphous carbon (a-C:H:Si:O) is a class of solid lubricants from the family of Diamond-Like Carbon (DLC) coatings that exhibit outstanding mechanical properties, thermal stability and tribological performance. It is well established that the frictional and wear performances of a-C:H:Si:O are less dependent on environment than that of pure hydrogenated amorphous carbon (a-C:H). However the fundamental mechanisms accounting for such excellent tribological behavior of a-C:H:Si:O are still not fully understood. The present work, which is part of a collaboration between the Laboratoire de Tribologie et Dynamique des Systèmes of Ecole Centrale de Lyon and the department of Mechanical Engineering and Applied Mechanics of University of Pennsylvania, consists in using a multi-scale, multidisciplinary and multi-technique experimental approach for understanding the influence of environment on the tribological response of a-C:H:Si:O.

A wide rang of complementary techniques, including nanoindentation, Atomic Force Microscopy (AFM), Friction Force Microscopy (FFM), optical and electron microscopy, Raman, X-ray Photoelectron Spectroscopy (XPS) and near edge x-ray absorption fine structure spectroscopy (NEXAFS), have thus been used to fully characterize the structure, composition and mechanics of the studied material, as deposited as well as after tribological testing. Control of the environment has been achieved first thanks to an open air linear reciprocating tribometer that we equipped with a gas blowing system, thus allowing a quick change of the sliding environment, and a environment-controlled analytical tribometer operating from high vacuum to elevated pressures of desired gases.

We were able to evidence the strong influence of the amount of water vapor in the environment on the friction behavior of a-C:H:Si:O, with a reversible behavior when abruptly changing the environment. Contrary to water vapor, oxygen promotes the wear of a-C:H:Si:O. SEM observations revealed that while sliding a-C:H:Si:O against 52100 steel, the frictional response is controlled by the build-up and the release of adhesive junctions within the interface. Under high vacuum and below a threshold pressure of water vapor (1 mbar), oxygen (10 mbar) and hydrogen (50 mbar), adhesive junctions are released in the steel, resulting in a transfer of material from steel to a-C:H:Si:O and in a high coefficient of friction ($\mu \approx 1.2$). However, as the gas pressure is increased above the threshold, the adhesive junctions break on the a-C:H:Si:O side, leading to a material transfer in the opposite direction, from the a-C:H:Si:O to the steel. NEXAFS spectroscopy revealed that a dissociative reaction occurs between the gaseous species and the strained C–C atoms in the near surface region ofa-C:H:Si:O, thus resulting in a drastic decrease of the steady state coefficient of friction by at least an order of magnitude.

In light of these observations, an analytical model has been proposed to describe the fundamental interaction mechanisms between the environment and the a-C:H:Si:O/steel tribopairs.



**Keywords:** Solid lubricants, Diamond-like Carbon, a-C:H:Si:O, surface analysis, XPS, NEXAFS, Raman, nanoindentation, environment-controlled tribology, tribofilms, re-hybridization.



## Résumé

Les revêtements de carbone amorphe hydrogéné (a-C:H) avec incorporation de silicium et d'oxygène (a-C:H:Si:O) sont une catégorie de lubrifiants solides, de la famille des Diamond-Like Carbon (DLC), présentant aussi bien de bonnes propriétés mécaniques que tribologiques et une bonne stabilité thermique. Bien qu'il soit établi que le comportement tribologique de ces couches est moins dépendant de l'environnement que celui des couches a-C:H, sans éléments d'addition, l'origine physico-chimique de ce comportement reste à élucider. Ce travail de thèse s'inscrit dans le cadre une collaboration internationale entre le Laboratoire de Tribologie et Dynamique des Systèmes de l'Ecole Centrale Lyon et le département de Génie Mécanique et Mécanique Appliquée de l'Université de Pennsylvanie, et a pour objectifs d'apporter des réponses à ces questions ouvertes.

Un large éventail de techniques expérimentales complémentaires, notamment la nanoindentation, la microscopie à force atomique (AFM), la microscopie à mesure de force (FFM), la microscopie optique et électronique, le Raman, la spectroscopie de photoélectron X (XPS) et la spectroscopie de structure près du front d'absorption de rayons X (NEXAFS) a été mis en œuvre pour non seulement établir une carte d'identité mécanique, structurale et chimique du revêtement initial, mais aussi comprendre les modifications structurelles induites par le frottement. Afin de contrôler l'environnement au cours des essais tribologiques, nous avons utilisé d'une part un tribomètre linéaire alternatif, que nous avons équipé d'un système de soufflage de gaz permettant de changer rapidement l'environnent au cours des essais, et d'autre part un tribomètre analytique à environnement contrôlé autorisant des expérimentations tant sous vide poussé qu'à pression élevée de gaz.

Ainsi, nous avons pu montrer que le coefficient de frottement augmente avec le taux de vapeur d'eau dans l'environnement et cela est réversible lorsqu'on diminue brusquement l'humidité. En outre, la vapeur d'eau protège la couche de l'usure alors que la présence d'oxygène la favorise.

Grace aux observations en microscopie électronique, nous avons pu prouver que le comportement tribologique des couches a-C:H:Si:O, lors d'un frottement contre de l'acier 100Cr6, est essentiellement contrôlé par la formation de jonctions adhésives dans l'interface.

Sous vide poussé ou à faible pression de gaz (<1 mbar de vapeur d'eau, <10 mbar d'oxygène ou <50 mbar d'hydrogène), la rupture de ces jonctions adhésives a lieu dans l'acier, résultant en un transfert de matériau de l'acier vers l'a-C:H:Si:O s'accompagnant d'un coefficient de frottement élevé ($\mu \approx 1.2$). Au delà de ces pressions seuils de gaz, les jonctions adhésives se rompent du côté du a-C:H:Si:O, le transfert de matière s'opérant alors dans la direction opposée, du revêtement vers l'acier. Des analyses NEXAFS ont révélé que ce phénomène s'expliquait par une réaction dissociative entre les éléments du gaz environnant et les liaisons carbone C–C contraintes, favorisée par la sollicitation mécanique en extrême surface de l'a-C:H:Si:O. Ceci résulte en une diminution drastique du coefficient de frottement à des valeurs d'un ordre de grandeur inférieures à celles obtenues dans la configuration précédente.

L'ensemble de ces résultats nous a ainsi permis de développer un modèle expérimental expliquant les mécanismes fondamentaux d'interaction entre l'environnement et les lubrifiants solides du type a-C:H:Si:O.



**Mots clés :** Lubrification solide, Diamond-Like Carbon, a-C:H:Si:O, analyse de surface, XPS, NEXAFS, Raman, nanoindentation, tribologie en environnement contrôlé, tribofilms, ré-hybridation.